



UNIVERSITÉ CATHOLIQUE DE LOUVAIN  
ÉCOLE POLYTECHNIQUE DE LOUVAIN  
ICTEAM INSTITUTE  
PÔLE EN INGÉNIEURIE ÉLECTRIQUE

# PARAMETER ESTIMATION FOR ULTRA WIDEBAND BASED POSITIONING

**Achraf Mallat**

Thesis submitted in partial fulfillment  
of the requirements for the degree of  
*Docteur en sciences de l'ingénieur*

Dissertation committee:

Prof. L. Vandendorpe (ICTEAM, UCLouvain, Belgium), advisor  
Prof. C. Craeye (ICTEAM, UCLouvain, Belgium), member  
Prof. J. Louveaux (ICTEAM, UCLouvain, Belgium), member  
Prof. D. Dardari (DEI, University of Bologna, Italy), member  
Prof. V. Poor (Princeton University, USA), member  
Prof. M. Verleysen (ICTEAM, UCLouvain, Belgium), President

July 3, 2013



---

# PARAMETER ESTIMATION FOR ULTRA WIDEBAND BASED POSITIONING

---

**Achraf Mallat**

Ecole Polytechnique de Louvain

ICTEAM Institute

Pôle en ingénierie électrique

---

**UCL**

**Université  
catholique  
de Louvain**

Université catholique de Louvain

Louvain-la-Neuve (Belgium)



*To my parents,  
to Rana,  
and to Fatima and Maryam*



# CONTENTS

---

List of Figures	xi
List of Tables	xv
Acknowledgments	xvii
Abstract	xxi
Acronyms	xxiii
Author's Publication List	xxvii
<b>1 Introduction</b>	<b>1</b>
1.1 UWB-based positioning	1
1.1.1 UWB signals	2
1.1.2 UWB channels	4
1.1.3 Positioning systems	5
1.1.4 TOA estimation via UWB signals	7
1.2 Organization of the thesis	11
<b>2 Non-linear estimation: MLE Statistics, approximate bounds, and optimal signal design</b>	<b>13</b>
2.1 Statistics of the MLE and approximate upper and lower bounds	14
2.1.1 System model	17
2.1.2 Threshold and ambiguity phenomena	22
2.1.3 Approximation of the MLE statistics	25
2.1.4 Approximate lower bounds based on Ziv and Zakai method	33
2.1.5 Alternate MSE approximations and approximate bounds	38
2.1.6 Numerical results and discussion	41
2.2 Threshold computation	47
2.2.1 System model, MSE approximations, and approximate lower bounds	48
2.2.2 Threshold computation	51
	<b>vii</b>

2.2.3	Numerical results on thresholds	57
2.3	Signal design for minimum MSE on TOA estimation	62
2.3.1	Waveform with spectrum falling in a given frequency band	63
2.3.2	Waveform with spectrum falling in a given frequency band and having a given bandwidth	69
2.4	Conclusion	70
<b>3</b>	<b>New TOA estimators</b>	<b>73</b>
3.1	Delaying-and-multiplying receiver	75
3.1.1	System model	75
3.1.2	CR receiver and delaying-and-multiplying receiver	76
3.1.3	Local statistics and probabilities of error	78
3.1.4	Global statistics and probabilities of error	84
3.2	Maximum delaying-and-multiplying estimator	88
3.2.1	The estimator	89
3.2.2	Asymptotic performances	89
3.2.3	Approximation of the local MSE	91
3.2.4	Numerical results and discussion	92
3.3	DFT-based estimators	94
3.3.1	System model	95
3.3.2	Statistics of the unwrapped phase	97
3.3.3	Phase-slope-based and absolute-phase-based local TOA estimators	103
3.3.4	Phase-slope-based and absolute-phase-based global TOA estimators	105
3.3.5	DFT-based estimation in multipath channels	109
3.4	Conclusion	110
<b>4</b>	<b>TOA estimation in multiuser systems using TH-IR-UWB signals</b>	<b>111</b>
4.1	Multiuser system model and joint MLE and CRLBs	112
4.1.1	Time-hopping waveforms	112
4.1.2	Joint MLE and CRLBs for the multiuser gain and TOA	115
4.2	MSE approximations and approximate lower bounds	121
4.3	TOA estimation with single-user	127
4.3.1	Maximum-correlation estimator	128
4.3.2	Maximum-delaying-and-multiplying estimator	133
4.3.3	Summary	135
4.4	TOA estimation with multiuser interference	136

4.4.1	Deterministic multiuser interference	136
4.4.2	Random multiuser interference	145
4.5	THMA codes with minimum CCR and sidelobe ACR	148
4.5.1	THMA code with chip separation and minimum CCR and sidelobe ACR	149
4.5.2	THMA code with chip separation and minimum circular CCR and sidelobe ACR	152
4.5.3	THMA code without chip separation and with minimum CCR and sidelobe ACR	154
4.5.4	THMA code without chip separation and with minimum circular CCR and sidelobe ACR	155
4.5.5	THMA codes with variable length	157
4.5.6	Numerical results	158
4.6	Conclusion	163
<b>5</b>	<b>CRLBs for position estimation and joint TOA and AOA estimation in MIMO and UWB systems</b>	<b>165</b>
5.1	CRLBs for UWB-based positioning using AOA and hybrid TOA-AOA techniques	166
5.1.1	System model	167
5.1.2	Non-overlapping assumption	169
5.1.3	CRLBs for the joint estimation of the direct path TOA and AOA	170
5.1.4	FIM transformation formula	174
5.1.5	CRLBs for AOA-based positioning	175
5.1.6	CRLBs for hybrid TOA-AOA based positioning	176
5.1.7	Comparison of the exact AOA CRLB and the CRLB obtained with the narrowband assumption	177
5.1.8	Numerical results and discussion	179
5.2	CRLBs for joint TOA and AOA estimation in wideband MISO and MIMO systems	184
5.2.1	System model	185
5.2.2	CRLBs for the joint estimation of the TOA and the AOA	187
5.2.3	Comparison of SISO, SIMO, MISO and MIMO configurations	191
5.2.4	Numerical results and discussion	192
5.3	CRLBs for UWB channel estimation with overlapping MPCs	195
5.3.1	System model	196

5.3.2	Channel statistical model	198
5.3.3	Probability of overlapping between neighboring MPCs	199
5.3.4	Fisher information matrix for multipath channel parameter estimation	200
5.3.5	CRLBs for channel parameter estimation	202
5.3.6	Average CRLBs	206
5.4	Conclusion	209
<b>6</b>	<b>Testbed for IR-UWB based ranging and positioning</b>	<b>211</b>
6.1	TH-IR-UWB generator	212
6.1.1	Monopulse and single-user TH-IR-UWB generation	213
6.1.2	Multiuser TH-IR-UWB waveforms generation	215
6.1.3	Pulse shaping	217
6.2	The testbed	221
6.3	Signals characteristics	223
6.4	Channel model and TOA estimator	225
6.5	Ranging	227
6.6	Positioning	229
6.7	Conclusion	233
<b>7</b>	<b>Conclusions</b>	<b>235</b>
<b>Appendix A: Curvatures of the autocorrelation function and of its envelope</b>		<b>239</b>
<b>Appendix B: Inertia of a regular antenna array</b>		<b>241</b>
<b>Appendix C: FIM for joint TOA and AOA estimation in MIMO systems</b>		<b>243</b>
<b>Bibliography</b>		<b>245</b>

# LIST OF FIGURES

---

1.1	FCC emission masks for indoor UWB systems.	2
1.2	Pure IR-UWB pulses.	3
1.3	UWB statistical channel model.	4
1.4	AOA and TDOA techniques.	6
1.5	MF, energy and DT receivers.	8
2.1	Threshold and ambiguity regions.	15
2.2	ML samples for different pulse shapes.	23
2.3	Subdomain probability for an unmodulated pulse.	28
2.4	Subdomain probability for a modulated pulse.	29
2.5	Subdomain variance for unmodulated and modulated pulses.	33
2.6	Two-hypothesis decision problem.	37
2.7	MSE approximations for an unmodulated pulse.	42
2.8	MSE approximations for a modulated pulse.	44
2.9	Thresholds for an unmodulated pulse.	58
2.10	Thresholds for a modulated pulse.	60
2.11	Feasible region for optimal waveform design.	63
2.12	Optimal spectrum and minimum MSE.	68
3.1	DM and CR receivers, MME and MCE estimators.	76
3.2	Useful DM and CR observations.	82
3.3	Local statistics (DM and CR receivers).	83
3.4	Global statistics (DM and CR receivers).	88

3.5	Local achieved MSE (MME and MCE).	93
3.6	Wrapped and unwrapped phases.	100
3.7	Marginal PDF of the unwrapped phase.	101
3.8	MSE of the unwrapped phase.	102
3.9	MSEs of the local DFT-based estimators.	105
3.10	MSEs of the global DFT-based estimators.	107
4.1	Circular ACR.	130
4.2	Minimum probability of error.	131
4.3	MSE achieved by the MCE (single-user).	132
4.4	MSE achieved by the MME (single-user).	135
4.5	Reference case for deterministic MUI.	137
4.6	Deterministic MUI (Case 1).	139
4.7	Deterministic MUI (Case 2).	140
4.8	Deterministic MUI (Case 3).	141
4.9	Deterministic MUI (Case 4).	142
4.10	Deterministic MUI (Case 5).	143
4.11	Deterministic MUI (Case 6).	144
4.12	Random MUI.	148
4.13	THMA Code 1.	158
4.14	THMA Code 2.	159
4.15	THMA Code 3.	160
4.16	THMA Code 4.	161
4.17	THMA Code 5.	162
5.1	Positioning based on AOA and hybrid TOA-AOA techniques.	167
5.2	Narrowband to UWB AOA-CRLBs ratio.	178
5.3	Triangular array and polar and Cartesian bounds.	179
5.4	CRLBs for AOA-based positioning (two arrays).	181
5.5	CRLBs for AOA-based positioning (four arrays).	182

5.6	CRLBs for hybrid positioning (one array).	183
5.7	CRLBs for hybrid positioning (four arrays).	184
5.8	MIMO system model.	185
5.9	CRLBs (SISO $1 \times 1$ , SIMO $1 \times 2$ , MISO $2 \times 1$ , MIMO $2 \times 2$ ).	193
5.10	CRLBs (SISO $1 \times 1$ , SIMO $1 \times 4$ , MISO $4 \times 1$ , MIMO $4 \times 4$ ).	195
5.11	Link budget.	197
5.12	Probability of overlapping.	200
5.13	CRLBs for a block of one MPC.	203
5.14	CRLBs for a block of two MPCs.	205
5.15	CRLBs for a block of three MPCs.	206
5.16	Average CRLBs.	208
6.1	Xilinx ML505 development board.	213
6.2	LVDS driver with two complementary outputs.	214
6.3	Single-user TH-IR-UWB waveforms.	215
6.4	Multuser TH-IR-UWB waveforms.	217
6.5	Antenna based shaping.	218
6.6	Equipment for antenna and complementary-output shaping.	219
6.7	Complementary-output based shaping (first example).	220
6.8	Complementary-output based shaping (second example).	221
6.9	Oscilloscopes and characterization room.	222
6.10	Signals characteristics.	224
6.11	Frequency response between the generated and received pulses.	225
6.12	Ranging performances.	228
6.13	Positioning setup (positions of Tx, Rx1, Rx2 and Rx3).	229
6.14	False MPC detection.	231
6.15	Positioning performances.	232



# LIST OF TABLES

---

2.1	ML samples for different pulse shapes.	24
5.1	Parameters of the IEEE 802.15.4a LOS “Residential” and “Office” environments.	170
5.2	Parameters of the IEEE 802.15.4a LOS “Residential”, “Office”, “Outdoor” and “0–4m” environments.	198



# ACKNOWLEDGMENTS

---

In the Name of God, the Most Gracious, the Most Merciful

All praise and thanks are due to God, Lord of the world, and His peace and blessings be upon all His prophets and messengers.

I would like to thank those who can never be thanked enough; my dear mother Sonia Al-Khatib and my beloved father Hassan Mallat. Thank you, for everything you have done for me since the second I came to this world. Your tireless, passionate and endless work is very much appreciated. Your selfless and boundless love encourages me beyond expression. May you both be rewarded in this life and the next. I would also like to thank my grandparents, Wahiba Jourad, Fatima Assoukiya, Ahmed Mallat and Mohamad Kamal Al-Khatib. A warm thanks for my mother in law, Fatma Jiblawi for never giving up and for her words of wisdom, reminding me of the story of Joseph (peace be upon him) and to hold tightly on the rope of God. Despite the many miles away from Belgium to Australia her words were so very close and near. I do not know how to express my thanks to my wife Rana Zeidan and my daughters Fatima and Maryam for their love, support and encouragement during all the years of my PhD. It should be said that this thesis would not be finished without their prayers, patience and endurance. I thank my wife for pushing me and believing in me and never losing hope. She stood by my side and was always there to listen and give me her advice. Thank you Rana, for providing the peace and stability I needed to finish this Phd. I thank all my sisters and brothers for their encouragement and especially Sara and Khadijah for their love and continuous prayers, and Amjad for his support and care. Special thanks to my uncles and especially my uncle Ahmad Al-Khatib for his support during my engineering studies and my uncle Nasser Al-khatib for his continuous encouragement and advice.

I would like to express my gratitude and thankfulness to my advisor, Prof. Luc Vandendorpe. It was very generous of him to give me the opportunity to accomplish my PhD under his supervision. He warmly welcomed me in his team. I fully appreciate his scientific skills, rigorousness and perseverance in research. I have realized this from the hundreds of hours of discussions led by him during these years. I thank him for his sympathy, support and valuable advice. He boosted my confidence at a time when I needed it. His enthusiasm is very inspiring.

I am very thankful to Prof. Jérôme Louveaux and Prof. Christophe Craeye who kindly accepted to be in my PhD supervising committee. I thank Prof. Louveaux for his fruitful collaboration especially at the beginning of the PhD. I also thank him for coauthoring some of my publications and for his valuable

comments. I thank Prof. Craeye as well for his fertile cooperation and for the discussions we had during all the years of my PhD. I particularly thank him for his proposal of the subdomain method that I have improved and widely employed in my thesis. I will not forget his support during and after my private defense.

I would like to sincerely thank Prof. Davide Dardari, Prof. Vincent Poor and Prof. Michel Verleysen for accepting to be in the Jury. I thank them for the long time they spent on reading my thesis, and for the advice, comments and corrections they proposed during my private defense. I especially thank Prof. Vincent Poor for the very valuable reference that he suggested me to consider. I widely benefited from his publications in the field of positioning and UWB. Special thanks to Prof. Michel Verleysen for presiding my jury.

Also, I thank Prof. Dardari, Prof. Sinan Gezici and all the NEWCOM++ WPR.B partners: Prof. Marco Luise, Prof. Monica Nicoli, Emanuela Faletti, Francesco Sottile, Giacomo Bacci, Prof. Montse Nájjar. I should say that the background I have now about positioning and UWB is due to all of them. I would like to express again my appreciation to Prof. Dardari and Prof. Gezici for the very fruitful discussions we had, the key references they suggested to me, especially among their own papers, and for coauthoring two of my ongoing articles. I also thank Prof. Luise and Dr. Mario Di Dio for their cooperation and the joint papers we wrote together. I cannot forget to thank Prof. Alain Genz for giving me the programs he developed for the computation of the multi-variate-normal cumulative probability. Special thanks to Prof. Claude Oestges, Prof. Denis Flandre and Mohammad Al-Kadi Jazairli for the fruitful cooperation and the joint papers.

My sincere appreciation for Pierre Gérard for his cooperation, for the different solutions he investigated for the realization of an IR-UWB generator, for having the idea of using an FPGA as generator, and finally for putting the generator in turn. Special thanks and appreciation for Maxime Drouguet for his continuous help and for the long hours he spent on writing the Labview and Matlab acquisition codes for the UWB and the Radar testbeds. I express my gratitude and thankfulness to Pascal Simon, the technical manager of the WELCOME platform. I thank him for his continuous help and assistance (troubleshooting, preparing the equipments for measurement, entrainment, etc.). Special thanks for Xavier Wautelet and Vincent Nicolas for their past computer assistance. I sincerely thank Christian Kinon for his assistance and fabricating the antennas. My special thanks also go to François Hubin the actual administrator, for his patience and continuous assistance. I would also like to thank Marie-Hélène Dewael. My very special and sincere thanks for Jean Deschuyter for his patience, continuous assistance, and especially his kindness.

I will not forget the nice moments I spent with the actual and previous members of the DIGICOM team: Xavier Jaspard, Bertrand Devillers, Harold Sneessens, Xavier Wautelet, Vaibhav Bhatnagar, André Lebacqz, Onur Oguz, Aissa Ikhlef, Zohaib Awan, Mohieddine El Soussi, Ivan Stupia. I specifically

thank my previous colleagues in my office Brah Félix, Ali Kalakech and Adrià Amigó Gusi. Special thanks to Abdellatif Zaidi for encouraging me when I was preparing my private defense.

I sincerely thank Prof. Abdelaati Daouia for reading this thesis towards its end and for his corrections. I would like to thank Dr Mostafa Emam as well for his help, assistance and advise in writing my thesis. Special thanks to my professors in the Faculty of Engineering in Lebanon Prof. Haissam Ziadé, Bachar El-Hassan and Khaled Mouchref. I specially thank Prof. Ziadé for his support, kindness and unstopped encouragement since my engineering studies until this day. I will never forget my dear brother and colleague in the faculty of engineering in Lebanon, Niazi Darwich. Thank you very much for your precious support during my engineering studies.

Last but not least, special thanks go to all my friends and their families for being a second family for my wife and me in a land so far away from home. Thank you for making Belgium our second home. Thank you for your support, friendship, care and love. Abdel Hakim, Youcef, Abdallah, Malek, Kahlid, Nouredine, Omar, Abdul Hamid, Karim, Hassan, Othman, Saed, Ahmed, Jalal, Mohammad and once again Mostafa, to name a few.

Achraf Mallat

July 3, 2013



# ABSTRACT

---

Positioning an unknown location node can be performed either directly from the signals received at/from the reference nodes, or by estimating some position-related parameters in a first step, and then combining them in an optimal way to get the desired position in a second step. In two-step positioning strategies, different types of parameters can be considered such as the time of arrival (TOA) and the angle of arrival (AOA). On the other hand, Impulse radio (IR) ultra wideband (UWB) signals are characterized by their pulses shorter than 2 ns (bandwidth larger than 500 MHz). Such signals represent an excellent candidate for highly accurate positioning when the TOA technique is employed.

In this thesis we consider the problem of parameter estimation for positioning using IR-UWB signals.

We treat the general setting of non-linear estimation, study the threshold and ambiguity phenomena, propose some approximations of the statistics of the maximum likelihood estimator (MLE), and derive some approximate upper and lower bounds of the mean squared error (MSE). The obtained results are applied in the context of TOA estimation using IR-UWB signals, and exploited in the design of the pulses that achieve the lowest attainable MSE.

We deal with TOA estimation in multiuser time-hopping IR-UWB systems. We introduce a new receiver that we call “delaying-and-multiplying” receiver, and propose a new estimator based on that receiver and named it “maximum delaying-and-multiplying estimator”. We compute the asymptotic, local and global performances of the proposed estimator and compare it with some existing benchmark estimators. We study the potential of the proposed estimator in the presence of deterministic and random multiuser interference. We also propose a family of TOA estimators based on the discrete Fourier transform of the received signal for both AWGN and multipath channels.

We derive the Cramer-Rao lower bounds (CRLB) for joint TOA and AOA estimation, for AOA based positioning, and for hybrid TOA-AOA based positioning, in UWB multipath channels. We investigate the impact of the overlapping between the different multipath components (MPC) on the joint estimation of the MPCs gains and TOAs. We also derive the CRLBs for the joint estimation of the TOA and the AOA in single-input-single-output (SISO), single-input-multiple-output (SIMO), multiple-input-single-output (MISO) and multiple-input-multiple-output (MIMO) systems.

We present a testbed that we realized at Université catholique de Louvain (UCL) for ranging and positioning by using IR-UWB signals based and employ-

ing the TOA technique. Two TOA estimators are considered: the MLE and a threshold-based estimator. We have studied from measurement data the impact of the multipath aspect of the channel and that of the shape of the transmitted pulses on the positioning performances. The obtained results are compared with the theoretical limits.

# ACRONYMS

---

ACR	Autocorrelation
AOA	Angle of arrival
ATBW	A priori time bandwidth product
AWGN	Additive white Gaussian noise
BK	Block of overlapping MPCs
BLB	Barankin lower bound
BPF	Band-pass filtering
BTLB	Bellini-Tartara lower bound
CCR	Crosscorrelation
CR	Correlation
CRLB	Cramer-Rao lower bound
DFT	Discrete Fourier transform
DM	Delaying-and-multiplying
DS	Direct sequence
DT	Dirty-template
EC	Commission of the European communities
ECRLB	Envelope Cramer-Rao lower bound
EMQBW	Envelope mean quadratic bandwidth
ESD	Energy spectral density
FCC	Federal communications commission
FIM	Fisher information matrix
FPGA	Field-programmable gate array
IBERT	Integrated bit error ratio tester
IFBW	Inverse fractional bandwidth
IR	Impulse radio
JBSF	Jump Back and Search Forward
LOS	Line of sight
LVDS	Low voltage differential signaling

MCE	Maximum correlation estimator
MF	Matched filter
MIMO	Multiple-input-multiple-output
MISO	Multiple-input-single-output
ML	Maximum likelihood
MLE	Maximum likelihood estimator
MME	Maximum delaying-and-multiplying estimator
MP	Multipath
MPC	Multipath component
MQBW	Mean quadratic bandwidth
MSE	Mean squared error
MU	Multiuser
MUI	Multiuser interference
MUSIC	Mutiple signal classification
NOLA	Non overlapping assumption
NWR	Narrowband to UWB CRLBs ratio
PAM	Pulse amplitude modulation
PDF	Probability density function
PPM	Pulse position modulation
PSD	Power spectral density
Ref	Reference node
RSS	Received signal strength
Rx	Receive antenna
SBS	Serial Backward Search
SBSMC	Serial Backward Search for Multiple Clusters
SIMO	Single-input-multiple-output
SINR	Signal-to-interference-plus-noise ratio
SISO	Single-input-single-output
SNR	Signal to noise ratio
TDOA	Time difference of arrival
TH	Time hopping
THMA	Time-hopping multiple access
TOA	Time of arrival
Tx	Transmit antenna

UCL	Université catholique de Louvain
Unk	Unknown location node
UWB	Ultra wideband
ZZLB	Ziv-Zakai lower bound



# AUTHOR'S PUBLICATION LIST

---

## Journal papers

- [1] A. Mallat, J. Louveaux, L. Vandendorpe, M. Di Dio, and M. Luise, "Discrete fourier transform-based TOA estimation in UWB systems," *EURASIP Journal on Wireless Communications and Networking*, vol. 2012, no. 1, pp. 1–9, 2012. [Online]. Available: <http://dx.doi.org/10.1186/1687-1499-2012-3>

## Book chapters

- [2] A. Mallat, C. Oestges, and L. Vandendorpe, "CRBs for for UWB multipath channel estimation: Impact of the overlapping pulses," in *Satellite and Terrestrial Radio Positioning Techniques: A signal processing perspective*, D. Dardari, M. Luise, and E. Falletti, Eds. Elsevier, 2012.
- [3] A. Mallat, J. Louveaux, and L. Vandendorpe, "TOA estimators operating in the frequency domain," in *Satellite and Terrestrial Radio Positioning Techniques: A signal processing perspective*, D. Dardari, M. Luise, and E. Falletti, Eds. Elsevier, 2012.
- [4] A. Mallat and L. Vandendorpe, "CRB for the joint estimation of TOA and AOA in MIMO systems," in *Satellite and Terrestrial Radio Positioning Techniques: A signal processing perspective*, D. Dardari, M. Luise, and E. Falletti, Eds. Elsevier, 2012.

## Conference proceedings

- [5] A. Mallat, J. Louveaux, and L. Vandendorpe, "UWB based positioning: Cramer rao bound for angle of arrival and comparison with time of arrival," in *2006 Symposium on Communications and Vehicular Technology*, November 2006, pp. 65–68.
- [6] —, "UWB based positioning in multipath channels: CRBs for AOA and for hybrid TOA-AOA based methods," in *IEEE International Conference on Communications (ICC 2007)*, June 2007, pp. 5775–5780.
- [7] A. Mallat, C. Oestges, and L. Vandendorpe, "CRBs for UWB multipath channel estimation: Impact of the overlapping between the MPCs on MPC gain and TOA estimation," in *IEEE International Conference on Communications (ICC 2009)*, June 2009, pp. 1–6.

- [8] A. Mallat and L. Vandendorpe, "CRBS for the joint estimation of TOA and AOA in wideband MISO and MIMO systems: Comparison with SISO and SIMO systems," in *IEEE International Conference on Communications (ICC 2009)*, June 2009, pp. 1–6.
- [9] A. Mallat, P. Gerard, M. Drouguet, F. Keshmiri, C. Oestges, C. Craeye, D. Flandre, and L. Vandendorpe, "Testbed for IR-UWB based ranging and positioning: Experimental performance and comparison to CRLBs," in *5th IEEE International Symposium on Wireless Pervasive Computing (ISWPC 2010)*, May 2010, pp. 163–168.
- [10] M. Jazairli, A. Mallat, L. Vandendorpe, and D. Flandre, "An ultra-low-power frequency-tunable UWB pulse generator using 65nm CMOS technology," in *IEEE International Conference on Ultra-Wideband (ICUWB 2010)*, vol. 1, September 2010, pp. 1–4.
- [11] A. Amigo, A. Mallat, and L. Vandendorpe, "Multiuser and multipath interference mitigation in UWB TOA estimation," in *IEEE International Conference on Ultra-Wideband (ICUWB 2011)*, September 2011, pp. 465–469.
- [12] A. Mallat, P. Gerard, and L. Vandendorpe, "Multi-user time-hopping IR-UWB generator based on FPGA with high-speed serial module," in *2011 18th IEEE International Conference on Electronics, Circuits and Systems (ICECS 2011)*, December 2011, pp. 615–618.

**To submit soon**

- [13] A. Mallat, S. Gezici, D. Dardari, C. Craeye, and L. Vandendorpe, "Statistics of the MLE and approximate upper and lower bounds – part 1: Application to TOA estimation using UWB signals," *IEEE Transactions on Signal Processing*.
- [14] A. Mallat, S. Gezici, D. Dardari, and L. Vandendorpe, "Statistics of the MLE and approximated upper and lower bounds – part 2: Threshold computation and optimal signal design for minimum achievable MSE," *IEEE Transactions on Signal Processing*.

# CHAPTER 1

---

## INTRODUCTION

---

THE unlicensed use of the ultra wideband (UWB) spectrum has been allowed in May 2002 by the U.S. federal communications commission (FCC) [1].

A signal is considered as UWB if its fractional bandwidth (i.e. bandwidth to central frequency ratio) is larger than 0.2 or its bandwidth is greater than 500 MHz. For most UWB applications (see [1] for more details), emission is allowed in the band between 3.1 and 10.6 GHz at a very low power spectral density (PSD) level of -41.3 dBm/MHz. For example, the FCC emission masks for indoor UWB systems are depicted in Fig. 1.1.

Five years later (in February 2007), the unlicensed use of the UWB spectrum has been allowed in Europe by the commission of the European communities (EC) at the same PSD level as by the FCC but in the frequency band between 6 and 8.5 GHz [2, 3].

### 1.1 UWB-BASED POSITIONING

Thanks to the ultra wideband and/or the ultra short pulses (shorter than 2 ns) used in UWB signals, UWB technology can serve for highly accurate positioning by employing the time of arrival (TOA) technique [4]. From the different advantages of UWB-based positioning it will suffice to mention [5–7]:

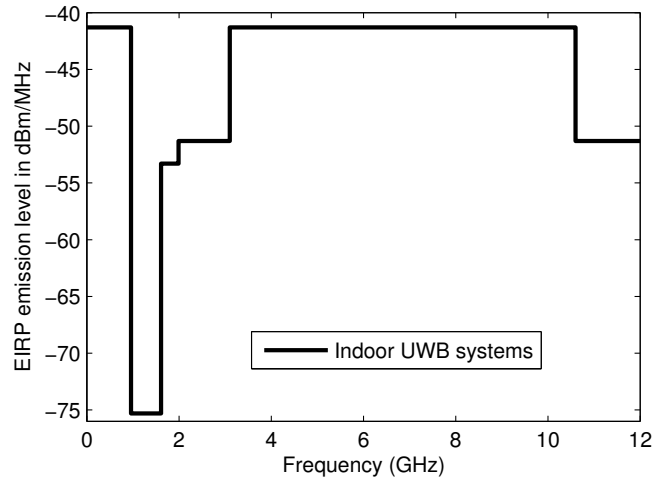


Fig. 1.1.: FCC emission masks for indoor UWB systems.

- Accurate positioning.
- Secure communication.
- Penetrability through obstacles.
- Low cost, low power, and low size chips.

For a very nice introduction on positioning using UWB signals, we refer the reader to [5].

### 1.1.1 UWB signals

UWB signals can be divided into two main categories [4, 6–8]:

- Multi-band UWB signals.
- Impulse radio (IR) UWB signals.

IR-UWB signals consist of trains of ultra short pulses modulated using pulse amplitude modulation (PAM) and/or pulse position modulation (PPM). Thanks to their very low duty cycle, and because it is easier to estimate the TOA with pulsed signals, IR-UWB signals are preferred in positioning applications. According to the method used to make the spectrum of the transmitted UWB pulses falling in the target band (from 3.1 to 10.6 GHz in U.S.A and from 6 to 8.5 GHz in Europe), we distinguish:

- Pure IR-UWB signals.

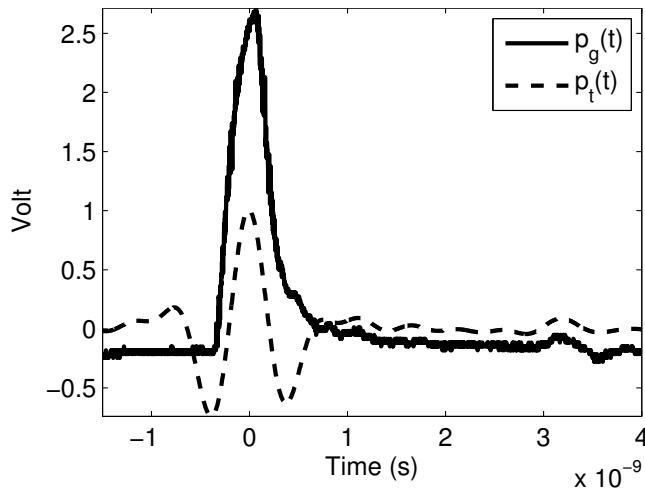


Fig. 1.2.: Pure IR-UWB;  $p_g(t)$ : rectangular pulse shaped by the circuit low-pass filtering effects applied to an UWB transmit antenna;  $p_t(t)$ : transmitted pulse.

- Carrier-based IR-UWB signals.

With carrier-based IR-UWB, the generated baseband pulse (e.g, Gaussian pulse, root raised cosine, etc.) is modulated by a carrier in order to move its spectrum to the target band. However, with pure IR-UWB, the spectrum of the transmitted pulse naturally falls in the band of interest. Thanks to the constant shape of their pulses (i.e. there is no carrier phase uncertainty due to the mixing stage like with carrier-based IR-UWB), pure IR-UWB signals can easily benefit from the super accuracy on TOA estimation furnished by the passband frequency components.

A simple example for transmitting a pure IR-UWB pulse consists on generating a very short rectangular pulse then applying it directly to an UWB transmit antenna. In fact, due to the low-pass filtering effects of the circuit, the rectangular pulse becomes a Gaussian-like pulse, then once applied to the transmit antenna the generated pulse will be shaped by the antenna frequency response. Fig. 1.2 illustrates the Gaussian-like pulse  $p_g(t)$  (generated by a digital circuit, see more details in Chap. 6) at the input of an UWB transmit antenna, and the corresponding transmitted pulse  $p_t(t)$ .

Both spread-spectrum and multiple-user-access can be ensured with IR-UWB signals by using direct sequence (DS) and/or time-hopping (TH) codes. The generic DS/TH-PAM/PPM-IR-UWB signal transmitted by the  $k$ th user can be

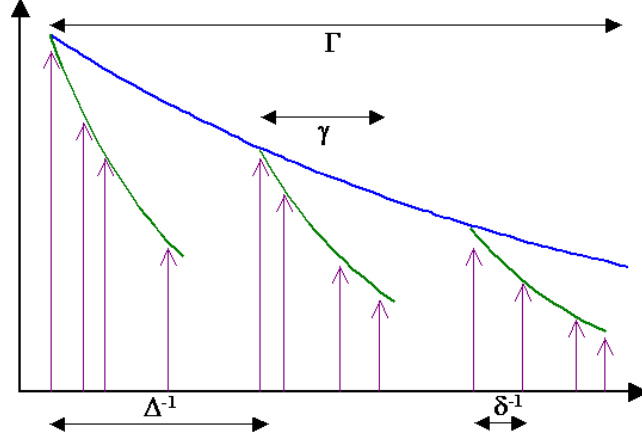


Fig. 1.3.: Impulse response of an UWB channel: The MPCs arrive grouped in consecutive clusters ( $\Delta^{-1}$ : average cluster rate of arrival,  $\delta^{-1}$ : average MPC rate of arrival within a cluster,  $\Gamma$ : cluster exponential decay constant,  $\gamma$ : MPC exponential decay constant within a cluster).

written as:

$$s^{(k)}(t) = \sum_{i=-\infty}^{+\infty} a_i^{(k),PAM} \sum_{n=0}^{N_c-1} c_n^{(k),DS} p(t - iT_s - nT_c - c_n^{(k),TH}T_h - a_i^{(k),PPM}\epsilon) \quad (1.1)$$

where  $p(t)$  denotes the IR-UWB pulse,  $T_s$  and  $T_c = T_s/N_c$  the symbol and chip periods respectively ( $N_c$  chips/pulses per symbol),  $a_i^{(k),PAM}$  and  $a_i^{(k),PPM}$  the PAM and PPM modulating symbols, ( $c_n^{(k),DS} \in \{+1, -1\}$ ) and ( $c_n^{(k),TH} \in \{0, \dots, N_h - 1\}$ ) the DS and TH codes of length  $N_c$ ,  $T_h = T_c/N_h$  the time-hop ( $N_h$  time-hops per chip), and  $\epsilon$  the PPM time shift.

### 1.1.2 UWB channels

UWB channels are characterized by their multipath (MP) aspect. According to the IEEE802.15.3a [7] and IEEE802.15.4a [9] UWB statistical channel models, the MP components (MPC) of an UWB channel arrive grouped in consecutive clusters.

Both the cluster TOA and the MPC TOA within a cluster follow Poisson processes, and both the average power per cluster and the average power per MPC within a cluster vanish with time according to an exponential decay. The general allure of an UWB channel impulse response is illustrated in Fig. 1.3.

UWB statistical channel models are considered in more details in Chap. 5.

### 1.1.3 Positioning systems

Depending on whether the unknown location nodes are locating themselves, positioning systems can be divided into three categories [10–12]:

- Network-based positioning (called “remote-positioning” in [5]) (e.g, cellular networks): where the network (e.g, base stations) locates the unknown location nodes (e.g, mobiles); the unknown location nodes are not involved in the positioning process.
- Mobile-based positioning (called “self-positioning” in [5]) (e.g, global positioning system, GPS): where the unknown location nodes are locating themselves.
- Mobile-assisted positioning: where the unknown location nodes cooperate with the network to estimate their positions (e.g, cooperative localization networks).

According to the strategy adopted to estimate the position from the received signals, positioning techniques can be divided into two types [5, 13]:

- Direct positioning: where the position of the unknown location node is directly estimated from the signals received at (or from) the different reference nodes.
- Two-step positioning: in the first step we estimate some parameters related to the unknown position; then in the second step, called sometimes “data fusion” [11], we combine in an optimal way the parameters gathered in the first step in order to find the desired position. In geometric positioning techniques [5], the position related parameters are the TOA, the angle of arrival (AOA), the time difference of arrival (TDOA) and the received signal strength (RSS). Hybrid techniques where various types of information are merged together (e.g, TOA with AOA) can also be employed.

We can also consider anchor-based and anchor-free positioning systems relying on the availability of reference nodes in the network. More classes of positioning techniques (e.g, geometric, statistical, and mapping/fingerprinting techniques) counting on the type of the dependency between the useful observation and the unknown position, and on the availability of statistical information about the noise corrupting the useful observation are investigated in [5].

Both the TOA and the RSS determine the distance between the node to locate and the reference nodes, so three reference nodes are sufficient to find a two-dimensional (2D) position without ambiguity (the intersection of three circles). Two nodes are sufficient using the AOA information (intersection of two rays, see more details about the required number of reference nodes for 2D AOA-based positioning in 5.1.8.2), whereas three nodes are not always sufficient using

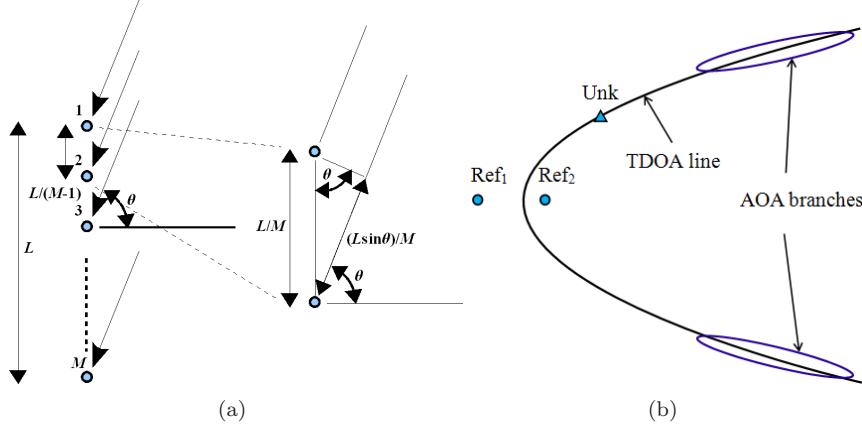


Fig. 1.4.: (a) Uniform linear array (ULA) of  $M$  elements for AOA estimation (b) Hyperbola corresponding to the TDOA between two reference nodes ( $\text{Ref}_1$  and  $\text{Ref}_2$ ); when  $\text{Unk}$  is very far from  $\text{Ref}_1$  and  $\text{Ref}_2$ , the TDOA measure determines the AOA with ambiguity (two branches).

the TDOA [5] (intersection of hyperbolas). Note that with AOA, every reference node should be equipped with an antenna array (see Fig. 1.4(a)).

In practice, the lines (i.e. the circles, rays and hyperbolas) obtained from the estimated parameters do not intersect at one point due to the estimation errors. Therefore, the data fusion step consists on estimating the position by minimizing a given error function. As example, the unknown position can be estimated using the TOA technique as:

$$(\hat{x}, \hat{y}) = \underset{(x, y)}{\operatorname{argmin}} \sum_{i=1}^I \frac{[\hat{d}_i - d_i(x, y)]^2}{2\sigma_{\hat{d}_i}^2}$$

where  $(x, y)$  and  $(x_i, y_i)$  denote the positions of the unknown location node ( $\text{Unk}$ ) and  $i$ th reference node ( $\text{Ref}_i$ ) respectively,  $d_i(x, y) = \sqrt{(x - x_i)^2 + (y - y_i)^2}$  the distance between  $\text{Unk}$  and  $\text{Ref}_i$ ,  $(\hat{x}, \hat{y})$  and  $\hat{d}_i = c\hat{\tau}_i$  the estimated position and distance ( $c$  denotes the speed of the light, and  $\tau_i$  and  $\hat{\tau}_i$  the true and the estimated time of flight between  $\text{Unk}$  and  $\text{Ref}_i$ ), and  $\sigma_{\hat{d}_i}^2$  the variance of  $\hat{d}_i$  (assumed unbiased). Note that  $\text{Unk}$  and  $\text{Ref}_i$  should be synchronized for the estimation of  $\tau_i$  (TOA technique). However, with TDOA only the reference nodes should be synchronized, and with AOA the elements of each antenna array.

When positioning is performed by way of UWB signals, TOA technique is much more accurate than both RSS [5] and AOA (see the comments on Fig. 5.6(a) and Fig. 5.6(b) in Sec. 5.1.8.3) techniques. Furthermore, TOA is more accurate

than TDOA. For setups where Unk is surrounded by the different  $\text{Ref}_i$ , the accuracy achieved by TDOA is comparable to that achieved by TOA. However if Unk moves away from all  $\text{Ref}_i$ , then TDOA becomes unable to estimate the position, whereas TOA will be still able to do it; TDOA will be only able to provide the AOA (see Fig. 1.4(b)) of Unk with respect to the array composed from the different  $\text{Ref}_i$ ; in that case, the estimated position accuracy achieved by TOA will be equal to that achieved by hybrid TOA-AOA technique based on the array just mentioned (see Sec. 5.1.8.3 for the accuracy achieved by one array using hybrid TOA-AOA). Finally, we can deduce TOA then TDOA are the most promising techniques for highly accurate positioning via UWB signals.

#### 1.1.4 TOA estimation via UWB signals

Depending on whether the transmitter and receiver clocks are synchronized, two approaches can be considered for the estimation of the TOA [14, 15]:

- One-way delay: where the receiver finds from the transmission time, assumed known, and the estimated TOA, the time of flight corresponding to the distance. With this approach both the transmitter and the receiver should have the same time reference.
- Two-way delay: where the transmitter sends a signal at a given time; when the receiver receives the signal, it waits for a duration known by the transmitter, then resend a reply signal to the transmitter; finally, from the time of transmission of the first signal, the waited duration at the receiver side, and the estimated TOA of the reply signal, the transmitter can estimate the duration of the round-trip flight. This approach suffers from the errors introduced by the time drift at the receiver side if the waited duration is very long.

TOA estimation suffers from many undesirable effects, mainly [5, 11, 14]:

- Low signal to noise ratios (SNR).
- MP aspect of the channel.
- Multiuser interference (MUI).
- Non-line of sight (NLOS) conditions.
- The very high sampling frequency required in “all digital” receivers.

In additive white Gaussian noise (AWGN) channels, the maximum likelihood estimator (MLE) (which is the optimal estimator) consists on maximizing either the output of the filter matched to the transmitted signal (see Fig. 1.5(a)) or the crosscorrelation (CCR) of the received signal and a delayed template of the transmitted signal. The main challenge facing the realization of this estimator is the need of either sampling the matched filter (MF) output at an ultra high

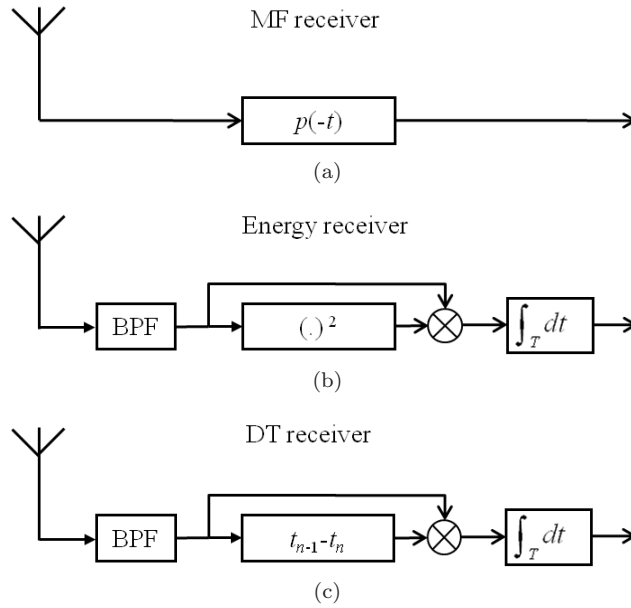


Fig. 1.5.: (a) Filter matched to the transmitted pulse  $p(-t)$  (b) Energy receiver (c) DT receiver ( $t_n - t_{n-1}$  is the relative delay between two consecutive pulses).

rate (greater than or equal to the Nyquist rate equal to  $2 \times 10.6$  GHz for a signal fulfilling the FCC band), or implementing a huge number of correlation (CR) branches (due to the spectrum and the very low duty cycle of IR-UWB signals).

As analog analog-to-digital converters (ADC) operating at the required rate do not exist [5], various solutions such as frequency-domain channelization [16, 17] and subsampling techniques [18, 19] have been considered. Another solution for this problem consists on using threshold-based estimators; the main two benefits of this approach are the high achievable accuracy (when CR or MF receivers are used) and the possible analog implementation [14, 15]. Thresholding can also be performed with non-coherent receivers (as done in [20–22] with an energy receiver). Simple estimators can be implemented using low-complexity receivers (i.e. relatively low sampling rate can be considered), such as the energy [20, 21, 23–26] and the dirty-template (DT) [27–31] receivers. However, these estimators are less accurate than CR/MF based estimators because non-coherent receivers are employed. As depicted in Fig. 1.5(b) and Fig. 1.5(c), respectively, an energy receiver consists on passing the received signal through a band-pass filter (BPF), applying the squaring operator, then integrating over a window of fixed length  $T$ , whereas a DT receiver consists on applying the BPF, multiplying each symbol [28] or pulse [27, 29–31] by the previous one, then integrating. Both receiver types

can be employed in MP channels in order to capture the maximum useful energy carried by the MPCs. The DT receiver has the advantage of benefiting from the total energy of the distorted pulse if the used delay lines are sufficiently accurate (a challenge of the DT receivers). The integration time  $T$  should be optimized to obtain the maximum SNR (tradeoff between the integrated noise and MPC energies); in [27], the optimal  $T$  in a DT receiver is calculated for both AWGN and MP channels. In [23], the TOA is estimated in AWGN and MP channels by considering parallel energy integrators starting at different moments. By making use of low-complexity receivers (e.g, threshold, energy, DT) we can realize the MLE by proceeding in two steps; in the first step we find a coarse estimate of the TOA by employing one of the receivers just mentioned; then in the second step, a fine estimate is obtained based on the CR receiver; such an estimator is optimal and easy to implement.

In MP channels, the MLE of the first MPC consists on maximizing the CCR of the received signal and a delayed version of the MP useful signal (the transmitted signal filtered by the channel impulse response); as the channel is itself unknown, this estimator is impossible to compute. In such a case the optimal estimator consists on jointly estimating, using the joint MLE, the number  $L$  of MPC, and the gains and the delays of all MPCs; this estimator is very complex to realize because it consists on varying the candidate number of MPCs  $L'$ , and minimizing for each considered  $L'$  an objective function in a  $2L'$  dimensional space. In channels with resolvable (i.e. non-overlapping) MPCs, a search over a  $2L'$  dimensional space is no longer required and the estimation process becomes much easier; as the first MPC is not necessarily the strongest one now, the main task consists on detecting the portion of the observation (e.g, MF, energy and DT signals) corresponding to the first MPC.

An algorithm to estimate the TOA  $\tau^{(1)}$  of the first MPC based on the joint approach is proposed in [32]; it detects the strongest MPC, and then the earlier MPCs one by one; this algorithm requires to set, based on the statistics of the channel, two thresholds determining the search-space of  $\tau^{(1)}$  and a lower bound of  $\alpha^{(1)}$  (gain of the first MPC), respectively. Two other estimators called “Search and subtract” and “Search subtract and readjust” are proposed in [33] based on the joint approach. Both estimators assume that the first MPC belongs to the set of the  $N$  strongest MPCs, where  $N$  has to be fixed before running the algorithms. Obviously, the choice of  $N$  is very crucial; bad values of  $N$  can cause large errors due to early/late detections; in [33], the optimal  $N$  is computed based on measurement data. When the MPCs are resolvable, the last two mentioned algorithms give the same result as the “Single search” algorithm (very simple) also proposed in [33]. The fourth algorithm proposed in [33] (two-step algorithm) finds a coarse estimation of  $\tau^{(1)}$  by comparing the output of the MF to a fixed threshold, then finds a fine estimate by maximizing the output of the MF within a window of length equal to the pulse width; in turn, the choice of the threshold is very critical. In [33], the optimal threshold has been computed based on measurement data; However, it is calculated in [22] from the statistics

of the channel for both MF and energy receivers. The main drawback of the estimators proposed in [32, 33] (except the thresholding one) is the very high required sampling rate.

In [20], two algorithms called (in [15]) “Jump Back and Search Forward” (JBSF) and “Serial Backward Search” (SBS) are proposed for the detection of the first MPC. They both use an energy receiver, start by detecting the strongest MPC, then compare the observation to a threshold to identify the first MPC. An improved version of JBSF named (in [15]) “Serial Backward Search for Multiple Clusters” (SBSMC) is proposed in [21] to take into account the clustered aspect of the UWB channels (see Sec. 1.1.2 and Fig. 1.3); in fact, the use of SBS may cause large errors due to false cluster detection when the first and the strongest MPCs do not fall in the same cluster.

In [25, 26, 34], three two-step estimators are proposed. They all use the energy receiver in the first step. However in the second step, the fine estimate is obtained in [26] by comparing the MF output to a threshold. In [34], the received signal is correlated with a set of delayed versions of the transmitted signal corresponding to the number  $N_h$  of time-hops (of length assumed equal to the pulse width) per chip (the so-called here “time-hop” and “chip” are named in [34] “chip” and “frame” respectively, see Eq. 1.1); then, the optimal time-hop is obtained using the method of moments. In [25], the second step is also based on the energy receiver. We have already mentioned that a two-step TOA estimator based on the MF is proposed in [33]; it consists on performing thresholding in the first step, and a maximum search in the second step. In [35, 36], we have proposed a two-step TOA estimator for MP channels. In the first step, we find coarse estimates of the TOAs of the different MPCs by using a threshold estimator based on the baseband CR receiver; then in the second step, we find the fine estimates by employing the discrete Fourier transform (DFT) of the received signal. This estimator is the scope of Sec. 3.3 in Chap. 3.

We have already mentioned that MUI is one of the most challenging problems for TOA estimation via IR-UWB signals. According to [15], relatively few publications address this problem [37, 38]. However, MUI in IR-UWB systems is widely investigated in the literature for demodulation and symbol detection under the assumption of perfect synchronization [39–43]. In [39] the MUI is modeled as an AWGN and the  $N_c$  pulses composing a given symbol (see Eq. 1.1) are equally weighted like in the case of single user (i.e. the receiver depicted in Fig. 3.1(b) in Chap. 3). The effect of MUI is mitigated in [40] by keeping the pulses crossing a given threshold and discarding the other pulses, and in [41] by keeping the pulses non-colliding with the interfering user pulses. The performance of the latter approach depends on the useful energy received by/from the user of interest and the probability of collision. In [42], a weighted combining scheme of the different pulses is proposed in order to maximize the signal-to-interference-plus-noise ratio (SINR). The latter method is improved in [43] to perform optimal combining of the received MPCs as well. Some other materials on time-hopping-multiple-access (THMA) and MUI can be found in [44–47].

Regarding the estimation of the TOA in MP channels in the presence of MUI, an iterative joint estimator based on successive cancellation is derived in [48]; it has been shown from simulation that the proposed estimator achieves the Cramer-Rao lower bound (CRLB) at high SNRs. In [37], the proposed estimator employs an energy receiver; the row vector containing the  $N_c N_{sam}$  samples per symbol ( $N_{sam}$  is the number of samples per chip) is converted into a  $N_c \times N_{sam}$  matrix (the  $n$ th row contains the  $N_{sam}$  samples of the  $n$ th chip, see Eq. 1.1); a non-linear transformation is applied to each column in order to mitigate the MUI components; the matrix is then converted into a  $1 \times N_{sam}$  vector by adding the different rows; the TOA is estimated from the latter vector like in the case of single-user. This method is improved later in [38] by applying a differential filter to each row before adding the rows to each other; the goal of this operation is to emphasize the beginning of the different clusters (see Fig. 1.3).

All estimators described above are based on the time-domain (except the one in [35, 36] which is based on both the time-domain and the frequency-domain). Some other estimators for either electromagnetic or acoustic signals are employing the DFT of the received signal [35, 36, 49–56]. In [56], a “super-resolution” TOA estimator is proposed; first, an estimate of the frequency response of the MP channel is obtained from the DFT of the received signal; then the multiple signal classification (MUSIC) algorithm is employed to estimate the TOAs of the different MPCs. The MUSIC algorithm assumes that the number of the sources (MP scatterers in our case) is known, and that the corresponding signals are uncorrelated (not applicable if the MPCs are overlapping); the determination of the number of MPCs is also investigated in [56]. Note that in the case of unresolvable MPCs (correlated signals) the estimates obtained from the algorithm in [56] can be considered as coarse estimates; the fine estimates can be obtained from another algorithm that approximates the joint MLE like the successive cancellation [48], the alternating maximization and the gradient algorithms (see [57] for the problem of AOA estimation). We have already mentioned that our estimator proposed in [35, 36] will be considered in Sec. 3.3; therein, we briefly compare it to the other DFT-based estimators.

## 1.2 ORGANIZATION OF THE THESIS

We present here the organization of our thesis.

In Chap. 2, we consider the general case of non-linear estimation of deterministic parameters. We study the impacts of the threshold and ambiguity phenomena on the performances of the estimation. We derive some approximations of the statistics of the MLE based on the so-called “subdomain method”, and some approximate upper and lower bounds for the mean squared error (MSE). We apply the derived approximations and approximate bounds on the problem of TOA estimation based on IR-UWB signals. Using the derived MSE approximations we compute, with respect to some features of the transmitted signal, the SNR required to achieve the CRLB. These results are employed to optimize the

spectrum of the transmitted signal with respect to the available SNR in order to achieve the lowest attainable MSE.

In Chap. 3, we propose a new receiver for TH-IR-IWB signals, and a new TOA estimator based on that receiver. We compute some statistics related to the proposed receiver. We calculate the asymptotic MSE achieved by the new TOA estimator, and derive some approximations of the local MSE and two approximate lower bounds. The new estimator is compared with the MLE. We also propose some TOA estimators based on the DFT of the received signal. We compute the statistics of the proposed estimators.

In Chap. 4, we deal with TOA estimation in multiuser (MU) TH-IR-UWB systems. We consider the new estimator introduced in Chap. 3 and another estimator based on the CR receiver. For both estimators, we derive some approximations of the global MSE and some approximate lower bounds. We investigate the cases of single-user and multiuser. We analyze the performances of the two estimators by considering deterministic MUI and random MUI.

In Chap. 5, we derive the CRLBs for the joint estimation of the TOA and the AOA, and for the estimation of the position based on the AOA technique and based on the hybrid TOA-AOA technique. UWB signals and MP channels have been considered. Then, we calculate the CRLBs for the joint estimation of the TOA and the AOA in multiple-input-single-output (MISO) and multiple-input-multiple-output (MIMO) systems. We compare with single-input-single-output (SISO) and single-input-multiple-output (SIMO) systems. Wideband signals and AWGN channels have been considered. Finally, we consider the estimation of UWB channels. We derive the CRLBs for the joint estimation of the gains and the TOAs of the different MPCs. We study the impact of the overlapping among the different MPCs on the estimation performance. Average CRLBs have been computed.

In Chap. 6, we present a testbed realized at Université catholique de Louvain (UCL) for IR-UWB based ranging and positioning. We describe a TH-IR-UWB generator based on a field-programmable gate array (FPGA) with high-speed serial module. Two methods for IR-UWB pulse shaping are proposed and discussed. For our experiments, we consider one setup for ranging and another for positioning. Ranging and positioning are performed by employing the TOA technique. The MLE and a threshold-based estimator are investigated. We study the impacts of the MP channel and the shape of the transmitted pulse on the performances of both estimators.

In Chap. 7, we summarize the contributions of this thesis and draw out some interesting problems for future investigation.

## CHAPTER 2

---

# NON-LINEAR ESTIMATION: STATISTICS OF THE MLE, APPROXIMATE UPPER AND LOWER BOUNDS, AND OPTIMAL SIGNAL DESIGN

---

NONLINEAR estimation problems, like position estimation, TOA estimation, AOA estimation and many other estimation problems, suffer from the threshold effect which means that for a SNR above a given threshold, estimation can achieve the CRLB (minimum mean square error achievable by an unbiased estimator), whereas for SNRs lower than that threshold, estimation deteriorates drastically until the estimator becomes uniformly distributed in the *a priori* domain of the unknown parameter. The behavior of the threshold effect is determined by the shape of the autocorrelation (ACR) of the observation carrying the information on the unknown parameter. It also depends on another phenomenon, that is the ambiguity phenomenon. Due to the threshold effect, the exact evaluation of the statistics of most estimators like the MLE has been considered as a prohibitive task. In order to be used as benchmarks, and to judge the performances of the estimators proposed for the different estimation problems, many lower and upper bounds have been derived in literature.

In Sec. 2.1 we study the threshold and ambiguity phenomena for a general deterministic nonlinear estimation problem. We approximate the statistics of the MLE. We propose some approximate upper bounds and lower bounds for the MSE. Some approximate lower bounds are based on the binary detection principle, which has been firstly used by Ziv and Zakai [58] to derive lower bounds for Bayesian estimation. We apply the derived approximations of the

MSE and the approximate upper and lower bounds on the problem of TOA estimation using UWB signals.

In Sec. 2.2 we consider TOA estimation based UWB signals. We use the MSE approximations and the approximate upper and lower bounds derived in Sec. 2.1 to compute the SNR thresholds of the regions, where the estimation is useless, where it achieves an intermediate accuracy, and where it achieves the CRLB. The thresholds are computed with respect to some features of the transmitted signal, and analytic expressions are also obtained.

Based on the results obtained about the thresholds, we consider in Sec. 2.2 the optimization, with respect to the available SNR, of the spectrum of the transmitted signal in order to attain the minimum achievable MSE. We consider the cases of signals with spectrum falling in a given frequency band, and of signals with spectrum falling in a given frequency band and having a given bandwidth.

## 2.1 STATISTICS OF THE MLE AND APPROXIMATE UPPER AND LOWER BOUNDS

Nonlinear estimation suffers from the threshold effect [58–67]. In deterministic estimation (i.e. the unknown parameter has one deterministic value which is unknown), this effect means that for a SNR above a given threshold, the estimation can achieve the CRLB, whereas for SNRs below that threshold, the estimation deteriorates remarkably until the estimator becomes uniformly distributed in the *a priori* domain of the unknown parameter. In Bayesian estimation (i.e. the unknown parameter follows a given *a priori* distribution), the Bayesian CRLB is achieved at sufficiently high SNRs, and the estimator follows the *a priori* distribution at low SNRs. In this work we only consider the case of deterministic estimation.

As depicted in Fig. 2.1(a), the SNR axis can be in general split into three regions according to the achieved MSE:

1. *A priori* region: the region where the estimation becomes uniformly distributed in the *a priori* domain of the unknown parameter (region of low SNRs). In this region, the estimation becomes useless.
2. Threshold region: the region of transition between the *a priori* and the asymptotic regions (region of medium SNRs).
3. Asymptotic region: the region where the CRLB can be achieved (region of high SNR).

As illustrated in Fig. 2.1(a), these regions are delimited by the *a priori*  $\rho_{pr}$  and asymptotic  $\rho_{as}$  thresholds.

If the ACR of the signal carrying the information on the unknown parameter is oscillating, then the estimation will be affected by the ambiguity phenomenon.

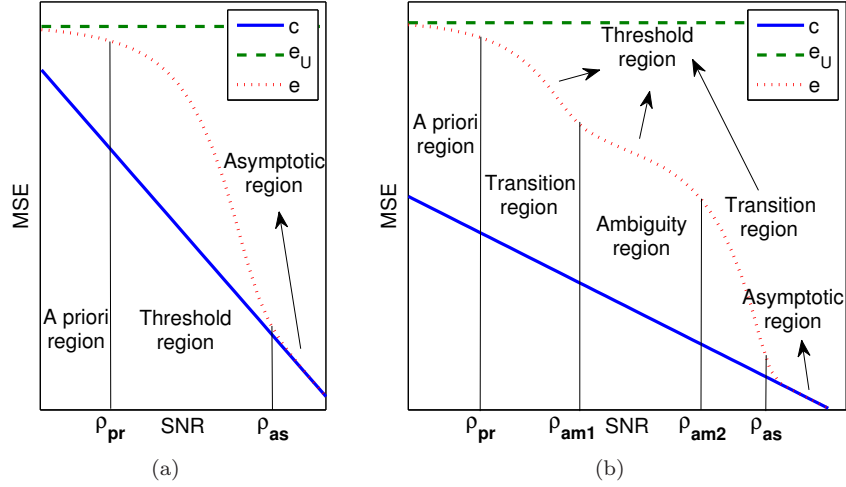


Fig. 2.1.: SNR regions (a) *A priori*, threshold and asymptotic regions for non-oscillating ACR (b) *A priori*, ambiguity and asymptotic regions for oscillating ACR ( $c$ : CRLB,  $e_U$ : MSE of uniform distribution in the *a priori* domain,  $e$ : achievable MSE,  $\rho_{pr}$ ,  $\rho_{am1}$ ,  $\rho_{am2}$ ,  $\rho_{as}$ : *a priori*, begin-ambiguity, end-ambiguity and asymptotic thresholds).

Due to this phenomenon a new region (the ambiguity region) appears in the threshold region. The MSE achieved in this region is determined by the curvature of the envelope of the ACR. Accordingly, the SNR axis can be split into five regions as depicted in Fig. 2.1(b):

1. *A priori* region.
2. *A priori*-ambiguity transition region: the region of transition between the *a priori* and the ambiguity regions.
3. Ambiguity region.
4. Ambiguity-asymptotic transition region: the region of transition between the ambiguity and the asymptotic regions.
5. Asymptotic region.

As shown in Fig. 2.1(b), these regions are delimited by the *a priori*  $\rho_{pr}$ , begin-ambiguity  $\rho_{am1}$ , end-ambiguity  $\rho_{am2}$  and asymptotic  $\rho_{as}$  thresholds.

The exact evaluation of the statistics, in the threshold region, of some estimators like the MLE has been considered as a prohibitive task. Many lower bounds have been derived for both deterministic and Bayesian estimation in order to be used as benchmarks and to describe the behavior of the MSE in

the threshold region [68] (very nice survey in French on the different families of deterministic and Bayesian lower bounds). Some upper bounds have been also derived like the Seidman [69] and McAulay [70] bounds. It will suffice to mention here the CRLB, Bhattacharyya, Chapman-Robbins, Barankin (BLB) and Abel lower bounds for deterministic estimation, the Bayesian Cramer-Rao [71], Bayesian Bhattacharyya [71], Bobrovsky-Zakai [72], Bobrovsky-MayerWolf-Zakai [73], and Weiss-Weinstein [74] lower bounds for Bayesian estimation, and the Ziv-Zakai lower bound (ZZLB) [58] with its improved versions: Bellini-Tartara [60], Chazan-Ziv-Zakai [75], Weinstein [76] (approximation of Bellini-Tartara), and Bell-Steinberg-Ephraim-VanTrees [77] (generalization of Ziv-Zakai and Bellini-Tartara) lower bounds for Bayesian estimation too, and finally the Reuven-Messer lower bound for simultaneously deterministic and Bayesian estimation. It has been shown in [68] that the deterministic bounds mentioned above can be seen as different versions of one unified bound, similarly for the ZZLB and its improved versions, and as well as for the Bayesian Cramer-Rao, Bayesian Bhattacharyya, Bobrovsky-MayerWolf-Zakai, Bobrovsky-Zakai, and Weiss-Weinstein lower bounds.

The CRLB [78, pp. 53-56] gives the minimum MSE achievable by an unbiased estimator. However, it is very optimistic for low and moderate SNRs and does not indicate the presence of threshold and ambiguity regions. The BLB [79] gives the greatest lower bound of an unbiased estimator. However, its general form is not easy to compute for most interesting problems. A useful form of this bound, which is much tighter than the CRLB, and which shows clearly the threshold and ambiguity regions, is derived by McAulay and Seidman in [80] and generalized to vector cases in [81]. Still, the bound in [80] is too optimistic so the threshold, ambiguity and asymptotic regions (see Fig. 2.1(a) and Fig. 2.1(b)) are detected much earlier (i.e. at lower SNRs) than the corresponding regions given by the MSE truly achieved in practice. Some applications to BLB can be found in [59, 61, 64, 65, 82, 83].

The Bayesian Ziv-Zakai lower bound family [58, 60, 75–77] is based on the minimum probability of error of a binary detection problem (i.e. detection problem with two hypotheses). The Ziv-Zakai bounds are very tight, show clearly the presence of the threshold and the ambiguity regions and detect accurately the asymptotic region. Some applications to the Ziv-Zakai bounds, discussions and comparison to other bounds can be found in [14, 15, 22, 66, 67, 84–88].

In [89, pp. 627-637], a method is proposed by Wozencraft to approximate the MSE of the MLE, applied therein on TOA estimation using particular waveforms (Cardinal sine), and used in [59] as reference to judge some upper and lower bounds. The same method is used by McAulay in [70] to derive an approximate upper bound that can be used with any type of waveforms. As shown in [84], the proposed bound is very tight and can be used to accurately estimate the threshold of the asymptotic region. Wozencraft method consists on splitting the *a priori* domain of the unknown parameter into subdomains and computing the

probability of each subdomain and the statistics of the MLE in each subdomain. Some applications to this method can be found in [90–92].

In this work employ the method of Wozencraft [89] and the approach of McAulay [70] to propose different approximations of the statistics (probability density function, mean and MSE) of the MLE, and to derive two approximate upper bounds. We derive an approximate lower bound tighter than the CRLB using Taylor series expansion of noise limited to second order. The derived approximations of the MSE are highly accurate (tighter than the Ziv-Zakai and the approximate McAulay [70] bounds) and follow closely the truly achieved MSE. By making use of the method proposed by Ziv and Zakai [58] to derive lower bounds for Bayesian estimation, we get some approximate lower bounds for deterministic estimation. We discuss the precision and the tightness of the derived approximations of the MSE and the obtained approximate upper and lower bounds by applying them to the problem of TOA estimation based on UWB waveforms.

In Sec. 2.1.1 we describe the system model. In Sec. 2.1.2 we discuss the threshold and ambiguity phenomena. In Sec. 2.1.3 we derive the first approximation of the MLE statistics. In Sec. 2.1.4 we propose some approximate lower bounds using the method of Ziv and Zakai. In Sec. 2.1.5 we derive two other approximations of the MLE statistics, two approximate upper bounds, and an approximate lower bound. In Sec. 2.1.6 we apply the approximations of the MSE and the approximate upper and lower bounds on TOA estimation using UWB waveforms and discuss the obtained results.

### 2.1.1 System model

In this subsection we describe our system model. In Sec. 2.1.1.1 we consider a general deterministic nonlinear estimation problem and in Sec. 2.1.1.2 we consider the particular case of TOA estimation.

#### 2.1.1.1 Deterministic nonlinear estimation

We describe now the system model of a general deterministic nonlinear estimation problem. Denote by  $\Theta$  the unknown parameter to estimate with  $D_\Theta = [\Theta_1, \Theta_2]$  being its *a priori* domain. We can write the observed signal as:

$$r(t) = \alpha s(t; \Theta) + \tilde{w}(t) \quad (2.1)$$

where  $s(t; \Theta)$  is the signal carrying the information on  $\Theta$ ,  $\alpha$  a known gain, and  $\tilde{w}(t)$  an AWGN of two-sided PSD of  $\frac{N_0}{2}$ .

From Eq. 2.1 we can write the log-likelihood function of  $\Theta$  as:

$$\Lambda(\theta) = -\frac{1}{N_0} \int_{-\infty}^{+\infty} \left\{ r(t) - \alpha s(t; \theta) \right\}^2 dt \quad (2.2)$$

$$= -\frac{1}{N_0} \left\{ E_r + \alpha^2 E_s(\theta) - 2\alpha X_{s,r}(\theta) \right\} \quad (2.3)$$

where  $\theta \in D_\Theta$  denotes a variable associated with the unknown parameter  $\Theta$ ,  $E_r = \int_{-\infty}^{+\infty} r^2(t)dt$  and  $E_s(\theta) = \int_{-\infty}^{+\infty} s^2(t;\theta)dt$  the energies of  $r(t)$  and  $s(t;\theta)$  respectively, and

$$X_{s,r}(\theta) = \int_{-\infty}^{+\infty} s(t;\theta)r(t)dt = \alpha R_s(\theta, \Theta) + w(\theta) \quad (2.4)$$

the CCR of  $s(t;\theta)$  and  $r(t)$  with respect to  $\theta$ , with

$$R_s(\theta, \theta') = \int_{-\infty}^{+\infty} s(t;\theta)s(t;\theta')dt \quad (2.5)$$

the ACR of  $s(t;\theta)$  with respect to  $(\theta, \theta')$  and

$$w(\theta) = \int_{-\infty}^{+\infty} s(t;\theta)\tilde{w}(t)dt \quad (2.6)$$

a colored zero-mean Gaussian noise of covariance given by ( $\mathcal{E}\{\cdot\}$  denotes the expectation operator):

$$C_w(\theta, \theta') = \mathcal{E}\{w(\theta)w(\theta')\} = \frac{N_0}{2}R_s(\theta, \theta'). \quad (2.7)$$

By assuming  $E_s(\theta) = E_s$  Eq. 2.3 independent of  $\theta$  (true for most estimation problems) we can write the MLE of  $\Theta$  as:

$$\hat{\Theta} = \underset{\theta}{\operatorname{argmax}} \{X_{s,r}(\theta)\} \quad (2.8)$$

and the CRLB of  $\Theta$  from Eq. 2.2 and Eq. 2.3 as [78, pp. 39]:

$$c(\Theta) = \frac{-1}{\mathcal{E}\{\ddot{\Lambda}(\theta)|_{\theta=\Theta}\}} = \frac{N_0/2}{\alpha^2 E_s(\Theta)} = \frac{-N_0/2}{\alpha^2 \ddot{R}_s(\Theta, \Theta)} \quad (2.9)$$

where  $\dot{s}(t;\theta)$  denotes the first derivative of  $s(t;\theta)$  with respect to  $\theta$ ,  $\ddot{\Lambda}(\theta)$  and  $\ddot{R}_s(\theta, \Theta)$  the second derivatives of  $\Lambda(\theta)$  and  $R_s(\theta, \Theta)$  respectively, and  $E_{\dot{s}}(\Theta) = \int_{-\infty}^{+\infty} \dot{s}^2(t;\theta)dt$  the energy of  $\dot{s}(t;\theta)$ . Unlike  $E_s(\Theta)$ ,  $E_{\dot{s}}(\Theta) = -\ddot{R}_s(\Theta, \Theta)$  may depend on  $\Theta$  for many estimation problems (e.g. angle estimation [93]).

The CRLB in Eq. 2.9 is inversely proportional to the curvature of the ACR function  $R_s(\theta, \Theta)$  at  $\theta = \Theta$ . Sometimes  $R_s(\theta, \Theta)$  is oscillating with respect to  $\theta$ . Then, if the SNR is sufficiently high (resp. relatively low) the maximum of the CCR function  $X_{s,r}(\theta)$  Eq. 2.4 will fall around the global maximum (resp. the local maxima) of  $R_s(\theta, \Theta)$  and the MLE  $\hat{\Theta}$  Eq. 2.8 of  $\Theta$  will (resp. will not) achieve the CRLB. We will see later in Sec. 2.1.6 that the MSE achieved at relatively low (i.e. medium) SNRs is inversely proportional to the curvature of the envelope of the ACR instead of the curvature of the ACR itself. To be able to characterize this phenomenon, known as ambiguity phenomenon, we define

the envelope CRLB (ECRLB, not necessarily a CRLB of an existing estimation problem) as:

$$c_e(\Theta) = -\frac{N_0/2}{\alpha^2 \Re\{\ddot{e}_{R_s}(\Theta, \Theta)\}} \quad (2.10)$$

where  $\Re\{\cdot\}$  denotes the real part operator,  $e_{R_s}(\theta, \Theta)$  the complex envelope of  $R_s(\theta, \Theta)$  with respect to its mean frequency  $\varphi_c(\Theta)$  in the frequency domain relative to  $\theta$  (dimension of  $\frac{1}{\theta}$ ), and  $\ddot{e}_{R_s}(\theta, \Theta)$  its second derivative. We can write:

$$\begin{aligned} R_s(\theta, \Theta) &= \Re\left\{e^{j2\pi(\theta-\Theta)\varphi_c(\Theta)} e_{R_s}(\theta, \Theta)\right\} \\ \varphi_c(\Theta) &= \frac{\int_0^{+\infty} \varphi \Re\{\mathcal{F}_{R_s}(\varphi)\} d\varphi}{\int_0^{+\infty} \Re\{\mathcal{F}_{R_s}(\varphi)\} d\varphi} \\ \mathcal{F}_{R_s}(\varphi) &= \int_{\Theta_1}^{\Theta_2} R_s(\theta, \Theta) e^{-j2\pi\varphi(\theta-\Theta)} d\theta \end{aligned} \quad (2.11)$$

with  $\mathcal{F}_{R_s}(\varphi)$  the Fourier transform of  $R_s(\theta, \Theta)$  with respect to  $\theta - \Theta$ . In Appendix A we show that we can write the curvature of  $R_s(\theta, \Theta)$  with respect to that of its envelope as:

$$-\ddot{R}_s(\Theta, \Theta) = -\Re\{\ddot{e}_{R_s}(\Theta, \Theta)\} + 4\pi^2 \varphi_c^2(\Theta) E_s. \quad (2.12)$$

Finally, we write the CRLB and the ECRLB of  $\Theta$  from Eq. 2.9, Eq. 2.10 and Eq. 2.12 as:

$$c(\Theta) = \frac{1}{\rho \beta_s^2(\Theta)} \quad (2.13)$$

$$c_e(\Theta) = \frac{1}{\rho \beta_e^2(\Theta)} \quad (2.14)$$

where

$$\rho = \frac{\alpha^2 E_s}{N_0/2} \quad (2.15)$$

$$\beta_s^2(\Theta) = \frac{E_s(\Theta)}{E_s} = -\frac{\ddot{R}_s(\Theta, \Theta)}{E_s} \quad (2.16)$$

$$\beta_e^2(\Theta) = -\frac{\Re\{\ddot{e}_{R_s}(\Theta, \Theta)\}}{E_s} \quad (2.17)$$

denote the SNR, and the normalized curvatures of  $R_s(\theta, \Theta)$  and  $e_{R_s}(\theta, \Theta)$  respectively. We have from Eq. 2.12:

$$\beta_s^2(\Theta) = \beta_e^2(\Theta) + 4\pi^2 \varphi_c^2(\Theta). \quad (2.18)$$

Consider now the BLB derived by McAulay and Seidman in [80]. It can be written as:

$$c_B = (\underline{\Theta} - \Theta)^T D^{-1} (\underline{\Theta} - \Theta) \quad (2.19)$$

where

$$\begin{aligned}
\Theta &= (\theta_{n_1} \cdots \theta_{-1} \ 1 + \Theta \ \theta_1 \cdots \theta_{n_2})^T \\
D &= (d_{i,j})|_{i,j=n_1, \dots, n_2} \\
d_{0,0} &= \frac{\alpha^2 E_s(\Theta)}{N_0/2} = \frac{1}{c(\Theta)} \\
d_{0,i} &= d_{i,0} = \frac{\alpha^2}{N_0/2} [\dot{R}_s(\Theta, \theta_i) - \dot{R}_s(\Theta, \Theta)] \\
d_{i,j} &= \frac{\alpha^2}{N_0/2} [R_s(\theta_i, \theta_j) - R_s(\theta_i, \Theta) - R_s(\theta_j, \Theta) + E_s]
\end{aligned}$$

where  $\theta_{n_1}, \dots, \theta_{n_2}$  ( $\theta_0 = \Theta$ ,  $n_1 \leq 0$ ,  $n_2 \geq 0$ ) denote  $N = n_1 - n_2 + 1$  testpoints to be chosen in the *a priori* domain of  $\Theta$ , and  $\dot{R}_s(\theta, \Theta)$  the derivative of  $R_s(\theta, \Theta)$  with respect to  $\theta$ . The term  $d_{0,0}$  is equal to the inverse of the CRLB  $c(\Theta)$  Eq. 2.9. Note that the testpoint  $\theta_0$  is equal to  $\Theta$  and that  $i, j \neq 0$  in the expressions of  $d_{0,i}$  and  $d_{i,j}$ .

Similarly to [15, 85] we assume that the maximum MSE is achieved when the estimator becomes uniformly distributed in the *a priori* domain  $D_\Theta = [\Theta_1, \Theta_2]$ . We can write:

$$\begin{aligned}
e_U &= \sigma_U^2 + (\Theta - \mu_U)^2 & (2.20) \\
\mu_U &= \frac{\Theta_1 + \Theta_2}{2} \\
\sigma_U^2 &= \frac{(\Theta_2 - \Theta_1)^2}{12}.
\end{aligned}$$

where  $e_U$ ,  $\mu_U$  and  $\sigma_U^2$  denote the MSE, mean and variance of a uniform distribution in  $D_\Theta$  respectively. For more information on maximum variance, we refer the reader to [94, 95].

### 2.1.1.2 TOA estimation

We consider here the special case of TOA estimation. The signal  $s(t; \Theta)$  Eq. 2.1 carrying the information on  $\Theta$  is given by:

$$s(t; \Theta) = s(t - \Theta)$$

where  $\alpha$  Eq. 2.1 and  $\Theta$  denote now the gain and delay introduced by the channel respectively, and  $s(t)$  the transmitted signal. Accordingly, we can write  $R_s(\theta, \theta')$  Eq. 2.5,  $X_{s,r}(\theta)$  Eq. 2.4 and  $C_w(\theta, \theta')$  Eq. 2.7 as:

$$\begin{aligned}
R_s(\theta, \theta') &= R_s(\theta - \theta') \\
X_{s,r}(\theta) &= \alpha R_s(\theta - \Theta) + w(\theta) \\
C_w(\theta, \theta') &= \frac{N_0}{2} R_s(\theta - \theta') = C_w(\theta - \theta')
\end{aligned} \tag{2.21}$$

where

$$R_s(\theta) = \int_{-\infty}^{+\infty} s(t+\theta)s(t)dt$$

denotes the ACR of  $s(t)$ . The CRLB Eq. 2.13, ECRLB Eq. 2.14, mean frequency  $\varphi_c(\Theta)$  Eq. 2.11 (denoted here by  $f_c$ ), and  $E_{\dot{s}}(\Theta)$ ,  $\ddot{R}_s(\Theta, \Theta)$ ,  $\beta_s^2(\Theta)$  Eq. 2.16,  $\ddot{e}_{R_s}(\Theta, \Theta)$  and  $\beta_e^2(\Theta)$  Eq. 2.17 become now independent of  $\Theta$ :

$$c = \frac{1}{\rho\beta_s^2} \quad (2.22)$$

$$c_e = \frac{1}{\rho\beta_e^2} \quad (2.23)$$

$$\beta_s^2 = \frac{E_{\dot{s}}}{E_s} = \frac{-\ddot{R}_s(0)}{E_s} = \frac{\int_{-\infty}^{+\infty} 4\pi^2 f^2 |\mathcal{F}_s(f)|^2 df}{\int_{-\infty}^{+\infty} |\mathcal{F}_s(f)|^2 df} \quad (2.24)$$

$$\beta_e^2 = \frac{\int_{-\infty}^{+\infty} 4\pi^2 f^2 |\mathcal{F}_{e_s}(f)|^2 df}{\int_{-\infty}^{+\infty} |\mathcal{F}_{e_s}(f)|^2 df} \quad (2.25)$$

$$\beta_s^2 = \beta_e^2 + 4\pi^2 f_c^2 \quad (2.26)$$

$$f_c = \frac{\int_0^{+\infty} f |\mathcal{F}_s(f)|^2 df}{\int_0^{+\infty} |\mathcal{F}_s(f)|^2 df} \quad (2.27)$$

where  $f$  denotes the frequency relative to time, and  $\mathcal{F}_s(f)$  and  $\mathcal{F}_{e_s}(f)$  the Fourier transforms of  $s(t)$  and its envelope  $e_s(t)$  given by  $s(t) = \Re\{e^{j2\pi f_c t} e_s(t)\}$ . In the special case of TOA estimation, the envelope of the ACR of a given signal is equal to ACR of its envelope. Furthermore,  $\beta_s^2$  and  $\beta_e^2$  denote now the mean quadratic bandwidth (MQBW) of  $s(t)$  and that of its envelope (EMQBW).

We have already mentioned TOA estimation will be performed using UWB signals. We have already mentioned as well that the unlicensed use of the UWB spectrum from 3.1 to 10.6 GHz at a PSD level of -41.3 dBm/MHz has been authorized by the FCC in May 2002 [1], and in Europe by the EC in February 2007 from 6 to 8.5 GHz at the same PSD level [2, 3]. In both the FCC and the EC bands, the CRLB  $c$  Eq. 2.22 is much smaller than the ECRLB  $c_e$  Eq. 2.23 because the MQBW  $\beta_s^2$  Eq. 2.26 is much larger than the EMQBW  $\beta_e^2$  Eq. 2.25. In fact, for a signal occupying the whole FCC band ( $f_c = 6.85$  GHz and bandwidth  $B = 7.5$  GHz), we obtain  $\beta_e^2 = \frac{\pi^2 B^2}{3} \approx 185$  GHz<sup>2</sup> (largest  $\beta_e^2$ ),  $4\pi^2 f_c^2 \approx 10\beta_e^2$ ,  $\beta_s^2 \approx 11\beta_e^2$  and  $c \approx \frac{c_e}{11}$ . Therefore, estimation seriously deteriorates at relatively low SNR when the ECRLB is achieved instead of the CRLB due to ambiguity. As  $\beta_e^2 \ll 4\pi^2 f_c^2$ , the super accuracy provided by  $c$  is mainly due to the mean frequency  $f_c$ . Accordingly,  $\beta_s^2$  Eq. 2.26 can be approximated by:

$$\beta_s^2 = \beta_e^2 + 4\pi^2 f_c^2 \approx 4\pi^2 f_c^2. \quad (2.28)$$

Note that to benefit from this super accuracy at sufficiently high SNR, the sufficient condition to satisfy is that the phase of the transmitted signal should not

be modified across the communication channel (e.g. due to fading), regardless whether the signal is pure impulse-radio UWB (carrier-less), carrier-modulated with known phase (e.g. in monostatic radar), or carrier-modulated with unknown phase (e.g. in most communication systems). In fact, with the latter (worse case with non arbitrary signals) the phase can be jointly estimated with the TOA (from the carrier and the envelope) in order to obtain a finer estimate of the latter.

### 2.1.2 Threshold and ambiguity phenomena

In this section we explain the physical origin of threshold and ambiguity phenomena by considering TOA estimation with UWB waveforms. The transmitted waveform  $s(t)$  is a Gaussian pulse of width  $T_w$  modulated by carrier  $f_c$ :

$$s(t) = e_s(t) \cos(2\pi f_c t) \quad (2.29)$$

$$e_s(t) \propto e^{-2\pi \frac{t^2}{T_w^2}} \quad (2.30)$$

where  $e_s(t)$  is the envelope of  $s(t)$  with respect to  $f_c$  equal to the mean frequency in Eq. 2.27.

We recall that the MLE  $\hat{\Theta}$  Eq. 2.8 of  $\Theta$  is the abscissa of the CCR  $X_{s,r}(\theta)$  Eq. 2.21 of the received signal  $r(t)$  Eq. 2.1 and the candidate signal  $s(t - \theta)$ . In our simulation, we consider three values of the carrier ( $f_c = 0, 4$  and  $8$  GHz) and three values of the SNR ( $\rho = 10, 15$  and  $20$  dB) per considered  $f_c$ . We take  $\Theta = 0$ ,  $T_w = 0.6$  ns, and  $D_\Theta = [-1.5, 1.5]T_w$ . In Fig. 2.2(a), Fig. 2.2(b) and Fig. 2.2(c) we show the normalized ACR Eq. 2.21:

$$R(\theta - \Theta) = \frac{R_s(\theta - \Theta)}{E_s}$$

for  $f_c = 0$  (unmodulated pulse),  $4$  and  $8$  GHz respectively, and  $1000$  realizations (called  $M$  samples) per SNR of the maximum:

$$M[\hat{\Theta}, X(\hat{\Theta})]$$

of the normalized CCR Eq. 2.21:

$$X(\theta) = \frac{X_{s,r}(\theta)}{\alpha E_s}.$$

Denote by  $N_n$ ,  $n = n_1, n_2$  ( $n_1 < 0$ ,  $n_2 > 0$ ,  $n = 0$  corresponds to the global maximum) the number of  $M$  samples falling around the  $n$ th local maximum of  $R(\theta - \Theta)$  (i.e. between the two local minima adjacent to that maximum). In Table 2.1, we show the CRLB  $c$  Eq. 2.22 of  $\Theta$ , the variance  $\sigma_S^2$  obtained by simulation, the variance to CRLB ratio  $\sigma_S^2/c$ , and the number ( $N_0$  and  $N_1$ ) of  $M$  samples falling around the maxima number  $0$  and  $1$ , with respect to  $f_c$  and  $\rho$ .

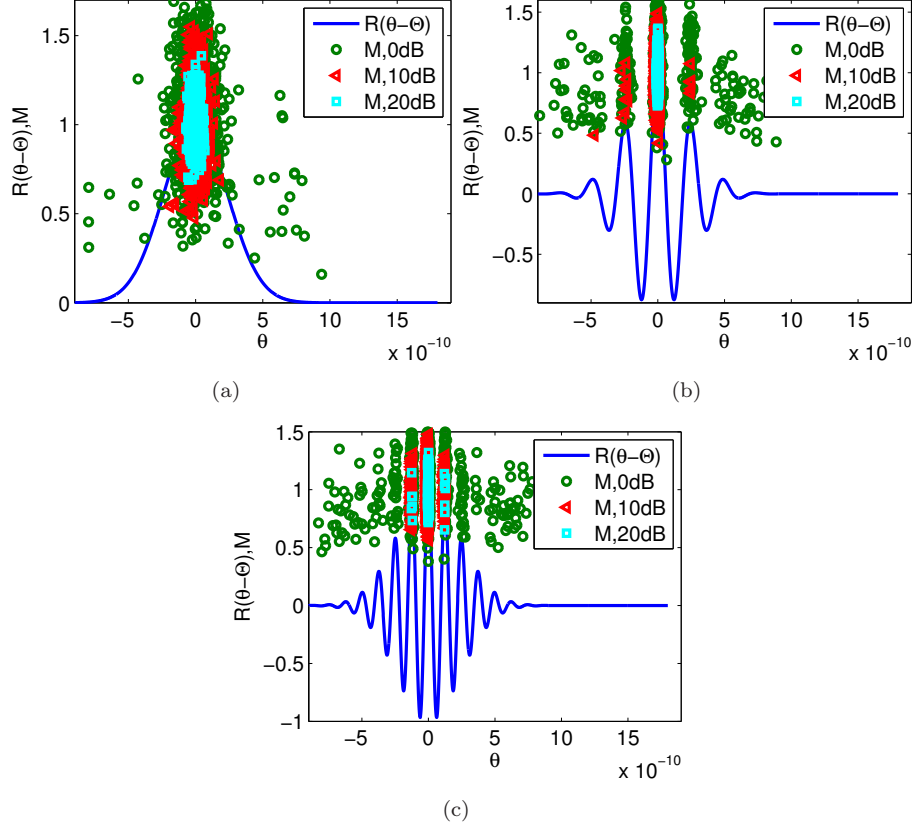


Fig. 2.2.: Normalized ACR  $R(\theta - \Theta)$  and 1000 realizations of  $M[\hat{\Theta}, X(\hat{\Theta})]$  per SNR ( $\rho = 10, 15$  and  $20$  dB); Gaussian pulse modulated by  $f_c$ ,  $\Theta = 0$  ns,  $T_w = 0.6$  ns,  $D_\Theta = [-1.5, 1.5]T_w$  (a)  $f_c = 0$  GHz (b)  $f_c = 4$  GHz (c)  $f_c = 8$  GHz.

Consider first the unmodulated pulse. We can see in Fig. 2.2(a) that the  $M$  samples are very close to the maximum of  $R(\theta - \Theta)$  for  $\rho = 20$  dB, and start to spread progressively along it for  $\rho = 15$  and  $10$  dB. We can see from Table 2.1 that the CRLB is approximately achieved for  $\rho = 20$  and  $15$  dB ( $\sigma_S^2 = 1.03c$  and  $1.1c$  respectively), and not for  $\rho = 10$  dB ( $\sigma_S^2 = 2.6c$ ). From this experience we can describe the threshold phenomenon as follows. For sufficiently high SNR, the maximum of the CCR always falls in the vicinity of the maximum of the ACR so the CRLB is achieved, whereas for moderate and low SNRs it spreads along the ACR so the CRLB is not achieved. We will see in Sec. 2.2 that the CRLB is achieved when the SNR crosses a given threshold which is only function of the shape of the ACR regardless other parameters like the pulse width  $T_w$ .

$f_c$	$\rho$	$c$	$\sigma_S^2$	$\sigma_S^2/c$	$N_0$	$N_1$
0	10	$76^2$	$123^2$	2.6	1000	0
	15	$43^2$	$46^2$	1.2	1000	0
	20	$24^2$	$24^2$	1.03	1000	0
4	10	$12^2$	$196^2$	250	773	59
	15	$7^2$	$31^2$	20	985	8
	20	$4^2$	$4^2$	1.03	1000	0
8	10	$6.3^2$	$198^2$	996	481	199
	15	$3.5^2$	$50^2$	206	838	75
	20	$2^2$	$14^2$	51	987	7

Table 2.1.: CRLB  $c$  (ps<sup>2</sup>), simulated variance  $\sigma_S^2$  (ps<sup>2</sup>), CRLB to variance ratio  $\sigma_S^2/c$ , and the numbers  $N_0$ ,  $N_1$  of the  $M$  samples falling around the maxima number 0 and 1 with respect to  $f_c = 0, 4$  and 8 GHz, and  $\rho = 10, 15$  and 20 dB.

Consider now the waveform with  $f_c = 4$  GHz. We can see from Fig. 2.2(b) and Table 2.1 that for  $\rho = 20$  dB all  $M$  samples ( $N_0 = 1000$ ) fall around the global maximum of  $R(\theta - \Theta)$  and the CRLB is achieved ( $\sigma_S^2 \approx 1.03c$ ), whereas for  $\rho = 15$  and 10 dB they spread along the local maxima of  $R(\theta - \Theta)$  (resp. only  $N_0 = 985$  and 773 samples around the global maximum) and the achieved variance is much larger than the CRLB (resp.  $\sigma_S^2 \approx 20c$  and  $250c$ ). Unlike the case of unmodulated waveform where the  $M$  samples spread in continuous way along the ACR, they spread here in discrete way along its local maxima. From this experience we can describe the ambiguity phenomenon as follows. For sufficiently high SNR (resp. relatively low) the noise  $w(t)$  in the CCR  $X_{s,r}(\theta)$  Eq. 2.21 cannot (resp. can) cross the gap between the global maximum and the local maxima of the ACR  $R(\theta - \Theta)$ . Consequently, for sufficiently high SNR (resp. relatively low) the maximum of the CCR always falls around the global maximum (resp. spreads along the local maxima) of the ACR so the CRLB is (resp. is not) achieved. Obviously, the ambiguity phenomenon affects the threshold phenomenon because the SNR required to achieve the CRLB depends on the gap between the global and the local maxima of the ACR.

Consider now the waveform with  $f_c = 8$  GHz. We can see that the variance achieved with  $\rho = 20$  dB is 51 times larger than the CRLB. In fact, only 987 from 1000  $M$  samples are falling around the global maximum of  $R(\theta - \Theta)$  because the gap between the global and the local maxima is smaller with  $f_c = 8$  GHz so it can be crossed by weaker noise. Consequently, a higher SNR is required to achieve the CRLB. We will see in Sec. 2.2 that the SNR required to achieve the CRLB increases as the inverse fractional bandwidth  $\frac{f_c}{B}$  increases. However, the most unexpected result is that the variance achieved at  $\rho = 20$  dB is 12.25

times smaller with  $f_c = 4$  GHz than with  $f_c = 8$  GHz whereas the CRLB is 4 times smaller with the latter. This result exhibits the significant loss in terms of accuracy if the CRLB is not achieved due to ambiguity. This fact has been discussed in [96] based on experimental results for TOA-based positioning.

### 2.1.3 Approximation of the MLE statistics

In this section we use the method of Wozencraft [89] and the work of McAulay [70] to propose new approximations of the statistics of the MLE.

We have seen in Sec. 2.1.2 that threshold phenomenon is due to the spreading of the maximum likelihood (ML) estimates along the ACR of the signal carrying the information on the unknown parameter  $\Theta$ . To characterize this phenomenon we split the *a priori* domain  $D_\Theta = [\Theta_1, \Theta_2]$  of  $\Theta$  into  $N = n_2 - n_1 + 1$  subdomains  $D_n = [d_n, d_{n+1})$ , ( $n = n_1, \dots, n_2$ ), ( $n_1 \leq 0, n_2 \geq 0$ ) and write the probability density function (PDF), mean and MSE of the MLE  $\hat{\Theta}$  as:

$$\begin{aligned} p(\theta) &= \sum_{n=n_1}^{n_2} P_n p_n(\theta) \\ \mu &= \int_{\Theta_1}^{\Theta_2} \theta p(\theta) d\theta = \sum_{n=n_1}^{n_2} P_n \mu_n \\ e &= \int_{\Theta_1}^{\Theta_2} (\theta - \Theta)^2 p(\theta) d\theta = \sum_{n=n_1}^{n_2} P_n [(\Theta - \mu_n)^2 + \sigma_n^2] \end{aligned} \quad (2.31)$$

where

$$P_n = P\{\hat{\Theta} \in D_n\} = P\{\exists \xi \in D_n; X_{s,r}(\xi) > X_{s,r}(\theta), \forall \theta \in \cup_{n' \neq n} D_{n'}\} \quad (2.32)$$

denotes the subdomain probability (i.e. probability that  $\hat{\Theta}$  falls in  $D_n$ ), and  $p_n(\theta)$ ,  $\mu_n$  and  $\sigma_n^2$  the PDF, mean and variance of the subdomain MLE ( $\hat{\Theta}$  given  $\hat{\Theta} \in D_n$ ):

$$\hat{\Theta}_n = \hat{\Theta} | \hat{\Theta} \in D_n. \quad (2.33)$$

We can approximate  $P_n$  Eq. 2.32 by:

$$\begin{aligned} P_n &= P\{\exists \xi \in D_n; X_{s,r}(\xi) > X_{s,r}(\theta), \forall \theta \in \cup_{n' \neq n} D_{n'}\} \\ &\approx P\{X_n > X_{n'}, \forall n' \neq n\} \\ &= \int_{-\infty}^{+\infty} dx_n \int_{-\infty}^{x_n} dx_{n_1} \cdots \int_{-\infty}^{x_n} dx_{n-1} \int_{-\infty}^{x_n} dx_{n+1} \cdots \int_{-\infty}^{x_n} p_X(x) dx_{n_2} \\ &= \tilde{P}_n \end{aligned} \quad (2.34)$$

where

$$X_n = X_{s,r}(\theta_n) = \alpha R_s(\theta_n, \Theta) + w(\theta_n) = \alpha R_n + w_n$$

denotes the value taken by the CCR  $X_{s,r}(\theta)$  Eq. 2.4 at a testpoint  $\theta_n$  arbitrarily chosen in  $D_n$  and

$$\begin{aligned} p_X(x) &= \frac{1}{(2\pi)^{\frac{N}{2}} |C_X|^{\frac{1}{2}}} e^{-\frac{(x-\mu_X)C_X^{-1}(x-\mu_X)^T}{2}} \\ \mu_X &= \alpha(R_{n_1} \cdots R_{n_2})^T \\ C_X &= \frac{N_0}{2} [R_{n,n'}]_{n,n'=n_1, \dots, n_2} \end{aligned}$$

the joint PDF, mean and covariance matrix of the vector  $X = (X_{n_1} \cdots X_{n_2})^T$  given from Eq. 2.4 and Eq. 2.7 with  $R_n = R_s(\theta_n, \Theta)$  and  $R_{n,n'} = R_s(\theta_n, \theta_{n'})$ . The precision of the approximation in Eq. 2.34 depends on the number of subdomains  $N$ , and the choice of the subdomains and the corresponding testpoints. For oscillating ACR we consider a subdomain around each local maximum (i.e. between the two local minima adjacent to it) and choose the corresponding testpoint as the abscissa of the local maximum, whereas for non-oscillating ACR we split the *a priori* domain into  $N$  equal subdomains and choose the centers of subdomains  $\theta_n = \frac{d_n + d_{n+1}}{2}$  as testpoints. For both oscillating and non-oscillating ACRs the subdomain number zero  $D_0$  contains the global maximum, and the corresponding testpoint  $\theta_0$  is equal to the unknown parameter  $\Theta$ . Wozencraft [89] has considered Cardinal sine waveforms and chosen  $\Theta$  and the roots of the ACR as testpoints, whereas McAulay [70] has considered modulated waveforms and chosen the abscissa of the ACR extrema as testpoints.

Next, we consider in Sec. 2.1.3.1 the approximation of the subdomain probability and in Sec. 2.1.3.2 the approximation of the statistics of the subdomain MLE.

### 2.1.3.1 Computation of the subdomain probability

We consider here the computation of the subdomain probability approximation  $\tilde{P}_n$  Eq. 2.34.

Up to our knowledge, there is no closed form for the integral in Eq. 2.34 for correlated  $X_n$  (non-diagonal  $C_X$ ). However, it can be computed numerically using one of the MATLAB functions QSCMVNV and QSCLATMVNV (written by Genz based on [97–100]) which compute the multivariate normal probability with integration region specified by a set of linear inequalities in the form  $a_1 < B(X - \mu_X) < a_2$ . Using QSCMVNV,  $\tilde{P}_n$  Eq. 2.34 can be approximated by:

$$P_n^{(1)} = \text{QSCMVNV}(N_p, C_X, a_1, B, a_2) \quad (2.35)$$

where  $N_p$  is the number of points used by the algorithm (e.g.  $N_p = 3000$ ),  $a_1 = (-\infty \cdots -\infty)^T$  and  $a_2 = \mu_{X_n} - (\mu_{X_{n_1}} \cdots \mu_{X_{n-1}} \mu_{X_{n+1}} \cdots \mu_{X_{n_2}})^T$  two  $(N-1)$ -column vectors, and  $B = \begin{pmatrix} B_1 & | & B_3 & | & B_4 \\ B_2 & | & B_3 & | & B_5 \end{pmatrix}$  a  $(N-1) \times N$  matrix with  $B_1 = I(n-n_1)$ ,  $B_2 = \text{zeros}(N+n_1-n-1, n-n_1)$ ,  $B_3 = -\text{ones}(N-1, 1)$ ,

$B_4 = 0(N - n_2 + n - 1, n_2 - n)$  and  $B_5 = I(n_2 - n)$  (we denote by  $I(k)$  the identity matrix of rank  $k$ , and  $\text{zeros}(k_1, k_2)$  and  $\text{ones}(k_1, k_2)$  the zero and one matrices of dimension  $k_1 \times k_2$ ).

Denote by  $Q(y) = \frac{1}{\sqrt{2\pi}} \int_y^\infty e^{-\frac{\xi^2}{2}} d\xi$  the Q function and  $R(\theta, \Theta) = \frac{R_s(\theta, \Theta)}{E_s}$  the normalized ACR. As  $P\{A_1 \cap A_2\} \leq P\{A_1\}$ , we can upper bound  $\tilde{P}_n$  Eq. 2.34 by [70]:

$$P_n^{(2)} = \begin{cases} Q(\theta_0, \theta_1) & n = 0 \\ Q(\theta_n, \theta_0) & n \neq 0 \end{cases} \quad (2.36)$$

where

$$Q(\theta, \theta') = P\{X_{s,r}(\theta) > X_{s,r}(\theta')\} = Q\left(\sqrt{\frac{\rho}{2}} \frac{R(\theta', \Theta) - R(\theta, \Theta)}{\sqrt{1 - R(\theta, \theta')}}\right) \quad (2.37)$$

because we can show from Eq. 2.4 and Eq. 2.7 that  $X_{s,r}(\theta) - X_{s,r}(\theta') \sim \mathcal{N}(\alpha[R_s(\theta, \Theta) - R_s(\theta', \Theta)], N_0[E_s - R_s(\theta, \theta')])$ . In [70],  $\tilde{P}_0$  is upper bounded by 1. If  $N$  approaches infinity, then both  $\sum_{n=n_1}^{n_2} P_n^{(2)}$  and the MSE approximation in Eq. 2.31 based on Eq. 2.36 will approach infinity. To solve this problem we propose the following approximation of  $\tilde{P}_n$  Eq. 2.34:

$$P_n^{(3)} = \frac{P_n^{(2)}}{\sum_{n=n_1}^{n_2} P_n^{(2)}}. \quad (2.38)$$

Finally the subdomain probability  $P_n$  Eq. 2.32 can be approximated by  $P_n^{(1)}$  Eq. 2.35 and  $P_n^{(3)}$  Eq. 2.38, and approximately upper bounded by  $P_n^{(2)}$  Eq. 2.36 [70].

To evaluate the subdomain probability approximations  $P_n^{(1)}$  and  $P_n^{(2)}$  given in Eq. 2.35 and Eq. 2.38 respectively, we consider an unmodulated Gaussian pulse Eq. 2.30 with  $T_w = 2$  ns,  $\Theta = 0$  and  $D_\Theta = [-2, 1.5]T_w$  (*a priori* domain), and the same pulse modulated Eq. 2.29 by  $f_c = 6.85$  GHz. We split  $D_\Theta$  to  $N = 9$  equal subdomains with the unmodulated pulse, and we have  $N = 48$  local maxima inside  $D_\Theta$  with the modulated one.

Let us first consider the unmodulated pulse. In Fig. 2.3(a) and Fig. 2.3(b) we show the subdomain probability  $P_n^{(S)}$  obtained by simulation based on 10000 trials, the subdomain probability approximation  $P_n^{(1)}$  Eq. 2.35 based on the Genz's algorithm [97–100], the approximate upper bound  $P_n^{(2)}$  Eq. 2.36 derived by McAulay [70], and the approximation  $P_n^{(3)}$  Eq. 2.38 based on  $P_n^{(2)}$ , all versus the SNR, for the subdomains number 0 (subdomain containing the maximum of the ACR) and 1 respectively. We can observe that:

- The subdomain probability  $P_n^S$  obtained by simulation converges to  $\frac{1}{N}$  at low SNRs  $\forall n$ , and to 1 (resp. 0) at high SNRs for  $n = 0$  (resp.  $n \neq 0$ ). We have  $P_0^S = 0.99$  and  $0.999$  at  $\rho \approx 16$  and  $18$  dB respectively.

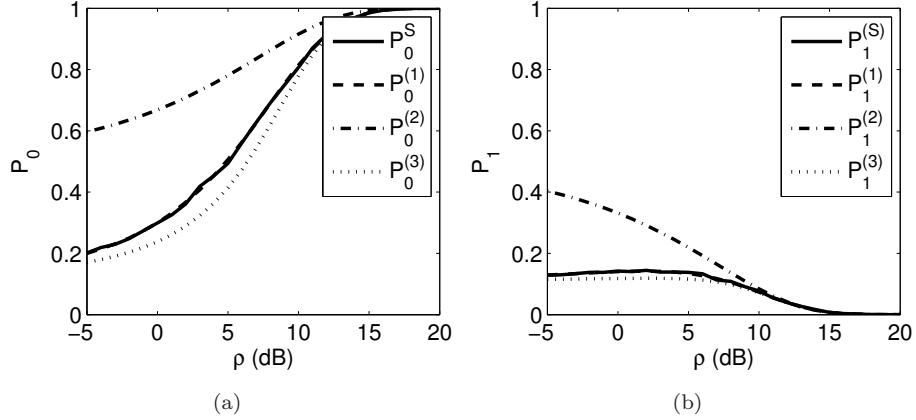


Fig. 2.3.: Subdomain probability obtained by simulation  $P_n^{(S)}$ , approximate subdomain probability upper bound  $P_n^{(2)}$ , and the subdomain probability approximations  $P_n^{(1)}$  and  $P_n^{(3)}$  versus the SNR  $\rho = -5 : 20$  dB (unmodulated Gaussian pulse,  $T_w = 2$  ns,  $\Theta = 0$ ,  $D_\Theta = [-2, 1.5]T_w$ ) (a)  $n = 0$  (b)  $n = 1$ .

- Both  $P_n^{(1)}$  and  $P_n^{(3)}$  are very accurate and closely follow  $P_n^S$ . However,  $P_n^{(1)}$  is more accurate than  $P_n^{(3)}$  because it takes into account the correlation between the testpoints of all subdomains.
- The approximate upper bound  $P_n^{(2)}$  is not tight at low SNRs. It converges to  $0.5 \forall n$  instead of  $\frac{1}{N}$ . This result could be predicted from the expression Eq. 2.36 of  $P_n^{(2)}$ . However, it converges to 1 (resp. 0) for  $n = 0$  (resp.  $n \neq 0$ ) at high SNRs, simultaneously with  $P_n^{(S)}$  so it can be used to accurately approximate the threshold of the asymptotic region as we will see later in Sec. 2.2.

Consider now the modulated pulse. In Fig. 2.4(a) and Fig. 2.4(b) we again show  $P_n^{(S)}$ ,  $P_n^{(1)}$ ,  $P_n^{(2)}$  and  $P_n^{(3)}$  versus the SNR, for the subdomains number 0 and 1 respectively. We can now observe that for  $n = 0$  (subdomain containing the global maximum of the ACR) the subdomain probability  $P_0^{(S)}$  (probability of non-ambiguity) converges to 0.99 and 0.999 at  $\rho \approx 30$  and 32 dB respectively instead of 16 and 18 dB obtained in the case of the unmodulated pulse. In fact, we have now 48 subdomains instead of 9 which makes the ACR gap between the different testpoints smaller so it can be more easily crossed by the noise. We can deduce that the convergence speed depends on the shape of the ACR of the used signal. The convergence is faster for signals with higher fractional bandwidth because the gap between the local maxima of the ACR will be larger.

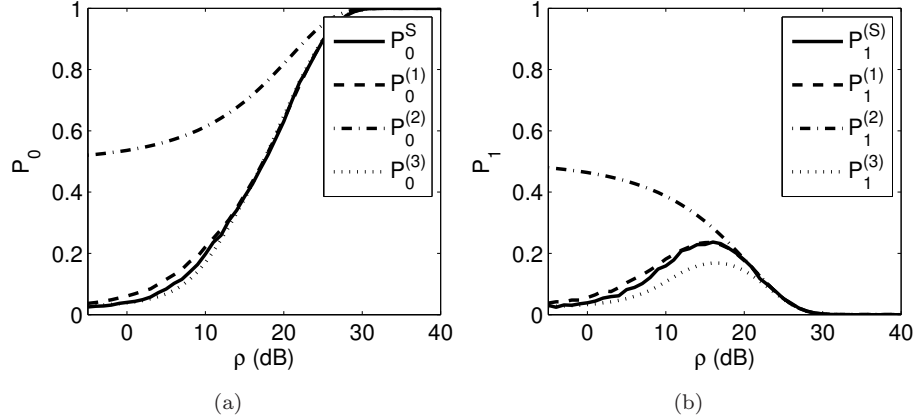


Fig. 2.4.: Subdomain probability obtained by simulation  $P_n^{(S)}$ , approximate subdomain probability upper bound  $P_n^{(2)}$ , and the subdomain probability approximations  $P_n^{(1)}$  and  $P_n^{(3)}$  versus the SNR  $\rho = -5 : 40$  dB (modulated Gaussian pulse,  $T_w = 2$  ns,  $f_c = 6.85$  GHz,  $\Theta = 0$ ,  $D_\Theta = [-2, 1.5]T_w$ ) (a)  $n = 0$  (b)  $n = 1$ .

### 2.1.3.2 Statistics of the subdomain MLE

We approximate here the statistics of the subdomain MLE  $\hat{\Theta}_n = \hat{\Theta} | \hat{\Theta} \in D_n$  Eq. 2.33. We have already mentioned in Sec. 2.1.3 that for an oscillating (resp. non-oscillating) ACR we consider a subdomain around each local maximum (resp. split the *a priori* domain into equal subdomains). The global maximum is always contained in subdomain  $D_0$ . Accordingly, the ACR inside a given subdomain is either increasing then decreasing (i.e. subdomain with local maximum) or monotone (i.e. increasing, decreasing or constant).

As the distribution of  $\hat{\Theta}_n$  should follow the shape of the ACR in the considered subdomain, the subdomain variance is upper bounded by the variance of uniform distribution in  $D_n = [d_n, d_{n+1}]$ . Accordingly, the subdomain mean  $\mu_n$  and variance  $\sigma_n^2$  can be approximated by:

$$\mu_{n,U} = \frac{d_n + d_{n+1}}{2} \quad (2.39)$$

$$\sigma_{n,U}^2 = \frac{(d_{n+1} - d_n)^2}{12}. \quad (2.40)$$

Note that for a subdomain with decreasing then increasing ACR (i.e. subdomain with local minimum, not considered here),  $\sigma_n^2$  is upper bounded by the variance of a Bernoulli distribution with two atoms of equal probability:

$$\sigma_{n,\max}^2 = \frac{(d_{n+1} - d_n)^2}{4} > \sigma_{n,U}^2. \quad (2.41)$$

It has been assumed in [70] that  $\sigma_n^2$  is upper bounded by  $\sigma_{i,U}^2$  Eq. 2.40 for both subdomains with local maximum and minimum. See [94, 95] for further information on maximum variance.

We can approximate the CCR  $X_{s,r}(\theta)$  Eq. 2.4 in  $D_n$  by its Taylor series expansion limited to second order about  $\theta_n$ :

$$\begin{aligned} X_{s,r}(\theta) &= \alpha R_s(\theta, \Theta) + w(\theta) \\ &\approx (\alpha R_n + w_n) + (\alpha \dot{R}_n + \dot{w}_n)(\theta - \theta_n) + (\alpha \ddot{R}_n + \ddot{w}_n) \frac{(\theta - \theta_n)^2}{2} \end{aligned} \quad (2.42)$$

where  $w_n = w(\theta_n)$ ,  $\dot{w}_n = \dot{w}(\theta_n)$ ,  $\ddot{w}_n = \ddot{w}(\theta_n)$ ,  $R_n = R_s(\theta_n, \Theta)$ ,  $\dot{R}_n = \dot{R}_s(\theta_n, \Theta)$  and  $\ddot{R}_n = \ddot{R}_s(\theta_n, \Theta)$ . From Eq. 2.6, we can show that ( $\nu_n$  denotes the coefficient of correlation between  $\dot{w}_n$  and  $\ddot{w}_n$ ):

$$\begin{aligned} \dot{w}_n &\sim \mathcal{N}(0, \sigma_{\dot{w}_n}^2) \\ \ddot{w}_n &\sim \mathcal{N}(0, \sigma_{\ddot{w}_n}^2) \end{aligned} \quad (2.43)$$

with

$$\begin{aligned} \sigma_{\dot{w}_n}^2 &= \frac{N_0}{2} \int_{-\infty}^{+\infty} \dot{s}^2(t; \theta_n) dt = \frac{N_0}{2} E_{\dot{s}}(\theta_n) \\ \sigma_{\ddot{w}_n}^2 &= \frac{N_0}{2} \int_{-\infty}^{+\infty} \ddot{s}^2(t; \theta_n) dt = \frac{N_0}{2} E_{\ddot{s}}(\theta_n) \\ \nu_n &= \frac{\mathcal{E}\{\dot{w}_n \ddot{w}_n\}}{\sigma_{\dot{w}_n} \sigma_{\ddot{w}_n}} = \frac{\int_{-\infty}^{+\infty} \dot{s}(t; \theta_n) \ddot{s}(t; \theta_n) dt}{\sqrt{E_{\dot{s}}(\theta_n) E_{\ddot{s}}(\theta_n)}}. \end{aligned} \quad (2.44)$$

Let us first consider a subdomain with monotone ACR function. By neglecting  $\ddot{w}_n$  and  $\ddot{R}_n$  in Eq. 2.42 (linear approximation), we can approximate the subdomain MLE by:

$$\hat{\Theta}_n = \operatorname{argmax}_{\theta \in D_n} \{X_{s,r}(\theta)\} \approx \begin{cases} d_n & \alpha \dot{R}_n + \dot{w}_n < 0 \\ d_{n+1} & \alpha \dot{R}_n + \dot{w}_n > 0 \\ \frac{d_{n,1} + d_{n,2}}{2} & \alpha \dot{R}_n + \dot{w}_n = 0 \end{cases}. \quad (2.45)$$

As  $P\{\alpha \dot{R}_n + \dot{w}_n = 0\} = 0$ , the latter approximation follows a Bernoulli distribution with two atoms of probabilities, mean and variance given from Eq. 2.15, Eq. 2.43 and Eq. 2.44 by:

$$\begin{aligned} P\{d_n\} &= 1 - P\{d_{n+1}\} = P\{-\dot{w}_n > \alpha \dot{R}_n\} = Q\left(\frac{\alpha \dot{R}_n}{\sigma_{\dot{w}_n}}\right) \\ &= Q\left(\sqrt{\frac{\rho \dot{R}_n^2}{E_s E_{\dot{s}}(\theta_n)}}\right) \\ \mu_{n,B} &= d_n P\{d_n\} + d_{n+1} P\{d_{n+1}\} \\ \sigma_{n,B}^2 &= P\{d_n\} P\{d_{n+1}\} (d_{n+1} - d_n)^2 \end{aligned} \quad (2.46)$$

where  $\sigma_{n,B}^2$  is upper bounded by  $\sigma_{n,\max}^2$  Eq. 2.41 and reaches it for  $P\{d_n\} = 0.5$ . As  $P\{d_n\} = 0.5$  just means that  $\hat{\Theta}_n$  is uniformly distributed in  $D_n$  (because  $\hat{\Theta}_n$  can fall anywhere inside  $D_n$ ),  $\mu_n$  and  $\sigma_n^2$  should be approximated by:

$$\mu_{n,1,c} = \mu_{n,B} \quad (2.47)$$

$$\sigma_{n,1,c}^2 = \min\{\sigma_{n,U}^2, \sigma_{n,B}^2\}. \quad (2.48)$$

By neglecting  $\dot{w}_n$  in Eq. 2.42 and Eq. 2.45 we obtain the following approximation:

$$\mu_{n,2,c} = \begin{cases} d_n & \dot{R}_n < 0 \\ d_{n+1} & \dot{R}_n > 0 \\ \frac{d_n + d_{n+1}}{2} & \dot{R}_n = 0 \end{cases} \quad (2.49)$$

$$\sigma_{n,2,c}^2 = 0. \quad (2.50)$$

Consider now a subdomain with local maximum. By neglecting  $\ddot{w}_n$  in Eq. 2.42, and taking into account that  $\dot{R}_n = 0$  (local maximum),  $\hat{\Theta}_n$  can be approximated by:

$$\hat{\Theta}_n = \operatorname{argmax}_{\theta \in D_n} \{X_{s,r}(\theta)\} \approx \theta_n - \frac{\dot{w}_n}{\alpha \dot{R}_n} \quad (2.51)$$

which follows a normal distribution whose PDF, mean and variance can be obtained from Eq. 2.9, Eq. 2.43, Eq. 2.44 and Eq. 2.51:

$$p_{n,N}(\theta) = \frac{1}{\sqrt{2\pi}\sigma_{n,N}} e^{-\frac{(\theta - \mu_{n,N})^2}{2\sigma_{n,N}^2}} \quad (2.52)$$

$$\mu_{n,N} = \theta_n \quad (2.53)$$

$$\sigma_{n,N}^2 = \frac{\sigma_{\dot{w}_n}^2}{\alpha^2 \dot{R}_n^2} = \frac{\frac{N_0}{2} E_{\dot{s}}(\theta_n)}{\alpha^2 \dot{R}_n^2} = c \frac{-\ddot{R}_0 E_{\dot{s}}(\theta_n)}{\dot{R}_n^2}. \quad (2.54)$$

For  $n = 0$  (around the global maximum),  $\sigma_{n,N}^2$  is equal to the CRLB Eq. 2.9 because  $-\ddot{R}_0 = E_{\dot{s}}(\theta_0)$ . To take into account that subdomain  $D_n$  is finite, we propose from Eq. 2.53 and Eq. 2.54 the following PDF, mean and variance approximation:

$$p_{n,1,o}(\theta) = \frac{p_{n,N}(\theta)}{\int_{d_n}^{d_{n+1}} p_{n,N}(\theta) d\theta}$$

$$\mu_{n,1,o} = \int_{d_n}^{d_{n+1}} \theta p_{n,1,o}(\theta) d\theta \approx \theta_n \quad (2.55)$$

$$\sigma_{n,1,o}^2 = \int_{d_n}^{d_{n+1}} (\theta - \mu_{n,1,o})^2 p_{n,1,o}(\theta) d\theta \approx \min\{\sigma_{n,N}^2, \sigma_{n,U}^2\} \quad (2.56)$$

By neglecting  $w(\theta)$  in Eq. 2.42 and Eq. 2.51, we obtain the following mean and variance approximation:

$$\mu_{n,2,o} = \theta_n \quad (2.57)$$

$$\sigma_{n,2,o}^2 = 0. \quad (2.58)$$

For both oscillating and non-oscillating ACR, subdomain  $D_0$  falls around the global maximum, and the testpoint  $\theta_0$  is equal to  $\Theta$ . To guarantee the convergence of the MSE approximation in Eq. 2.31 to the CRLB  $c$  Eq. 2.9,  $\mu_0$  and  $\sigma_0^2$  should always be approximated using Eq. 2.55 and Eq. 2.56 by:

$$\mu_{0,0} = \Theta \quad (2.59)$$

$$\sigma_{0,0}^2 = \min\{c, \sigma_{0,U}^2\}. \quad (2.60)$$

Finally, the subdomain mean and variance can be approximated by:

- $\mu_{0,0}$  Eq. 2.59 and  $\sigma_{0,0}^2$  Eq. 2.60 for  $n = 0$ .
- $\mu_{n,U}$  Eq. 2.39 and  $\sigma_{n,U}^2$  Eq. 2.40,  $\mu_{n,1,c}$  Eq. 2.47 and  $\sigma_{n,1,c}^2$  Eq. 2.48, or  $\mu_{n,2,c}$  Eq. 2.49 and  $\sigma_{n,2,c}^2$  Eq. 2.50 for subdomain with monotone ACR.
- $\mu_{n,U}$  Eq. 2.39 and  $\sigma_{n,U}^2$  Eq. 2.40,  $\mu_{n,1,o}$  Eq. 2.55 and  $\sigma_{n,1,o}^2$  Eq. 2.56, or  $\mu_{n,2,o}$  Eq. 2.57 and  $\sigma_{n,2,o}^2$  Eq. 2.58 for subdomain with local maximum.

Note that  $\sigma_{n,U}^2$  Eq. 2.40 overestimates  $\sigma_n^2$  whereas  $\sigma_{n,2,c}^2$  Eq. 2.50 and  $\sigma_{n,2,o}^2$  Eq. 2.58 underestimate it. In [70], McAulay approximates  $\mu_n$  and  $\sigma_n^2$  by  $\mu_{n,2}$  Eq. 2.55 and  $\sigma_{n,U}^2$  Eq. 2.40 respectively.

As for TOA estimation,  $E_s(\theta)$  Eq. 2.24 is independent of  $\theta$ , we can then write  $P\{d_n\}$  Eq. 2.46 and  $\sigma_{n,N}^2$  Eq. 2.54 as:

$$P\{d_n\} = Q\left(\sqrt{\frac{\rho \dot{R}_n^2}{E_s E_{\dot{s}}(\theta_n)}}\right) = Q\left(\sqrt{\rho} \frac{\dot{R}_n}{E_s \beta_s}\right)$$

$$\sigma_{n,N}^2 = c \frac{-\ddot{R}_0 E_{\dot{s}}(\theta_n)}{\dot{R}_n^2} = c \frac{\ddot{R}_0^2}{\dot{R}_n^2}.$$

To evaluate the subdomain variance approximations  $\sigma_{n,U}^2$  Eq. 2.40,  $\sigma_{n,1,c}^2$  Eq. 2.48 and  $\sigma_{n,1,o}^2$  Eq. 2.56, we consider an unmodulated Gaussian pulse and a modulated Gaussian pulse with  $T_w = 0.6$  ns,  $f_c = 8$  GHz,  $D_\Theta = [-1.5, 1.5]T_w$  and  $\rho = 10$  dB. For the unmodulated pulse we split  $D_\Theta$  to  $N = 15$  equal subdomains, and for the modulated pulse we have  $N = 15$  local maxima.

Consider first the unmodulated pulse. In Fig. 2.5(a) we show the subdomain variance obtained by simulation  $\sigma_{n,S}^2$  based on 50000 trials, and the subdomain variance approximations  $\sigma_{n,U}^2$  Eq. 2.40 and  $\sigma_{n,1,c}^2$  Eq. 2.48 with respect to the subdomain number  $n = -6, \dots, 6$ . We can see that  $\sigma_{n,S}^2$  is upper bounded by  $\sigma_{n,U}^2$  as expected. We can also see that  $\sigma_{n,S}^2$  is close to  $\sigma_{n,U}^2$  which means that for subdomains with monotone ACR we can approximate the subdomain MLE  $\hat{\Theta}_n$  by a random variable uniformly distributed in  $D_n$  because the ACR is approximately constant in  $D_n$ . The subdomain variance approximation  $\sigma_{n,1,c}^2$  Eq. 2.48 does not follow  $\sigma_{n,S}^2$  closely. For  $n = 2$  (resp. -2), we have  $\sigma_{n,1,c}^2 = 2.7\sigma_{n,S}^2$  (resp.  $2.8\sigma_{n,S}^2$ ). In fact, the subdomain MLE is approximated for  $\sigma_{n,1,c}^2$

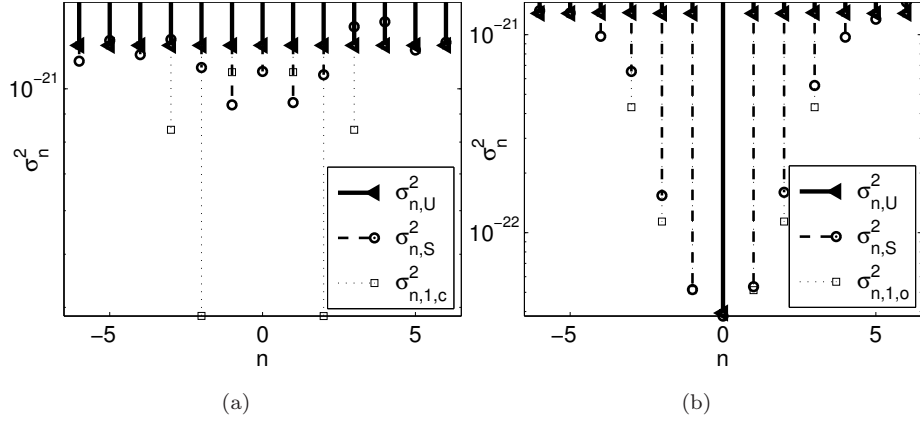


Fig. 2.5.: (a) Subdomain variance obtained by simulation  $\sigma_{n,S}^2$ , and approximate subdomain variances  $\sigma_{n,U}^2$  and  $\sigma_{n,1,c}^2$  with respect to the subdomain number  $n = -6, \dots, 6$  (unmodulated Gaussian pulse,  $T_w = 0.6$  ns,  $N = 15$ ,  $\rho = 10$  dB) (b)  $\sigma_{n,S}^2$ ,  $\sigma_{n,U}^2$  and the approximate subdomain variance  $\sigma_{n,1,o}^2$  with respect to  $n = -6, \dots, 6$  (modulated Gaussian pulse,  $T_w = 0.6$  ns,  $f_c = 8$  GHz,  $\rho = 10$  dB).

by a Bernoulli variable with two atoms while in practice the ML estimate may fall anywhere in  $D_n$ .

Consider now the modulated pulse. In Fig. 2.5(b) we show  $\sigma_{n,S}^2$ ,  $\sigma_{n,U}^2$  and the subdomain variance approximation  $\sigma_{n,1,o}^2$  Eq. 2.56 with respect to  $n = -6, \dots, 6$ . We can see that  $\sigma_{n,S}^2$  is upper bounded by  $\sigma_{n,U}^2$  as expected and that  $\sigma_{n,1,o}^2$  closely follows  $\sigma_{n,S}^2$ . Unlike the case of subdomains with monotone ACR, the subdomain MLE cannot be approximated now by a uniform variable in  $D_n$  because the magnitude of the ACR varies widely in  $D_n$  (between the local maximum and the two local minima). The smallest variance corresponds to  $n = 0$  (subdomain with global maximum) because the curvature of  $R_s(\theta, \Theta)$  reaches its maximum at  $\theta = \Theta$ .

We did not show numerical results for the proposed subdomain mean approximations because they are all very close to the mean obtained by simulation.

#### 2.1.4 Approximate lower bounds based on Ziv and Zakai method

In this section we use the principle of binary detection to derive approximate lower bounds for deterministic estimation. This principle was initiated by Ziv and Zakai [58] to derive exact lower bounds for Bayesian estimation. The lower bound obtained in [58] has been later improved by Bellini and Tartara in [60],

Chazan, Ziv and Zakai in [75], and generalized by Bell, Steinberg, Ephraim and VanTrees in [77].

Before presenting our approximate lower bound that is derived for deterministic estimation problems, we will present the generalized forms of the ZZLB and the Bellini-Tartara lower bound (BTLB) obtained in [77] for Bayesian estimation problems.

Denote by  $p_{\Theta}(\theta)$  the *a priori* distribution of  $\Theta$ ,  $\{\epsilon|\theta\} = \{\hat{\Theta}[r(t)] - \Theta|\Theta = \theta\}$  the local error (error when  $\Theta$  is deterministic and equal to  $\theta$ ) and  $\epsilon = \hat{\Theta}[r(t)] - \Theta$  the global error (error when  $\Theta$  is random). In order to find the global MSE we have to perform the expectation of  $\epsilon^2$  with respect to both  $\Theta$  (because it is random) and the noisy observation  $r(t)$ , while in order to find the local MSE we have to perform the expectation only with respect to  $r(t)$  (because  $\Theta$  is deterministic). According to [101], we can write the global MSE as:

$$\begin{aligned}
 e &= \mathcal{E}_{\Theta, r(t)}\{\epsilon^2\} \\
 &= \int_0^{\Theta_2 - \Theta_1} \xi^2 p_{|\epsilon|}(\xi) d\xi \\
 &= 2 \int_0^{\Theta_2 - \Theta_1} \xi P_{|\epsilon| > \xi} d\xi - \{\xi^2 P_{|\epsilon| > \xi}\}_0^{\Theta_2 - \Theta_1} \\
 &= \frac{1}{2} \int_0^{2(\Theta_2 - \Theta_1)} \xi P_{|\epsilon| > \frac{\xi}{2}} d\xi
 \end{aligned} \tag{2.61}$$

where  $p_{|\epsilon|}(\xi) = \int_{\Theta_1}^{\Theta_2} p_{|\epsilon||\theta}(\xi) p_{\Theta}(\theta) d\theta$  (resp.  $p_{|\epsilon||\theta}(\xi)$ ) is the PDF of the absolute global (resp. local) error, and  $P_{|\epsilon| > \xi} = \int_{\Theta_1}^{\Theta_2} P_{|\hat{\Theta} - \Theta| > \xi|\theta} p_{\Theta}(\theta) d\theta$  (resp.  $P_{|\hat{\Theta} - \Theta| > \xi|\theta}$ ) the probability that the absolute global (resp. local) error is greater than  $\xi$ .

In order to find a lower bound of the global MSE  $e$  Eq. 2.61, we first search for a lower bound of the probability of error  $P_{|\epsilon| > \frac{\xi}{2}}$ :

$$\begin{aligned}
 P_{|\epsilon| > \frac{\xi}{2}} &= \int_{\Theta_1}^{\Theta_2} P_{|\epsilon| > \frac{\xi}{2}|\theta} p_{\Theta}(\theta) d\theta = \int_{\Theta_1}^{\Theta_2} P_{\epsilon > \frac{\xi}{2}|\theta} p_{\Theta}(\theta) d\theta + \int_{\Theta_1}^{\Theta_2} P_{\epsilon < -\frac{\xi}{2}|\theta} p_{\Theta}(\theta) d\theta \\
 &= \int_{\Theta_1}^{\Theta_2} P_{\epsilon > \frac{\xi}{2}|\theta} p_{\Theta}(\theta) d\theta + \int_{\Theta_1 - \xi}^{\Theta_2 - \xi} P_{\epsilon < -\frac{\xi}{2}|\theta + \xi} p_{\Theta}(\theta + \xi) d\theta \\
 &= \int_{\Theta_1}^{\Theta_2 - \xi} [p_{\Theta}(\theta) + p_{\Theta}(\theta + \xi)] P_{\text{near}}(\theta, \theta + \xi) d\theta + \int_{\Theta_2 - \xi}^{\Theta_2} P_{\epsilon > \frac{\xi}{2}|\theta} p_{\Theta}(\theta) d\theta \\
 &\quad + \int_{\Theta_1 - \xi}^{\Theta_1} P_{\epsilon < -\frac{\xi}{2}|\theta + \xi} p_{\Theta}(\theta + \xi) d\theta \\
 &\geq \int_{\Theta_1}^{\Theta_2 - \xi} [p_{\Theta}(\theta) + p_{\Theta}(\theta + \xi)] P_{\text{near}}(\theta, \theta + \xi) d\theta \\
 &\geq \int_{\Theta_1}^{\Theta_2 - \xi} [p_{\Theta}(\theta) + p_{\Theta}(\theta + \xi)] P_{\text{min}}(\theta, \theta + \xi) d\theta
 \end{aligned} \tag{2.62}$$

where

$$P_{\text{near}}(\theta, \theta + \xi) = \frac{p_{\Theta}(\theta)}{p_{\Theta}(\theta) + p_{\Theta}(\theta + \xi)} P_{\epsilon > \frac{\xi}{2} | \theta} + \frac{p_{\Theta}(\theta + \xi)}{p_{\Theta}(\theta) + p_{\Theta}(\theta + \xi)} P_{\epsilon < -\frac{\xi}{2} | \theta + \xi} \quad (2.63)$$

is the probability of error of the nearest decision rule:

$$\hat{H}_{\text{near}} = \begin{cases} H_1 & \text{if } |\hat{\Theta} - \theta| < |\hat{\Theta} - (\theta + \xi)| \\ H_2 & \text{if } |\hat{\Theta} - \theta| > |\hat{\Theta} - (\theta + \xi)| \end{cases}$$

of the decision problem with two hypotheses:

$$H = \begin{cases} H_1 : \Theta = \theta & P_{H_1} = \frac{p_{\Theta}(\theta)}{p_{\Theta}(\theta) + p_{\Theta}(\theta + \xi)} \\ H_2 : \Theta = \theta + \xi & P_{H_2} = \frac{p_{\Theta}(\theta + \xi)}{p_{\Theta}(\theta) + p_{\Theta}(\theta + \xi)} \end{cases} \quad (2.64)$$

and

$$P_{\min}(\theta, \theta + \xi) = P_{H_1} P_{\hat{H}_{\min} = H_2 | H_1} + P_{H_2} P_{\hat{H}_{\min} = H_1 | H_2} \quad (2.65)$$

the minimum probability of error of the same decision problem Eq. 2.64 obtained by the optimum decision rule based on the likelihood ratio test [89, pp. 30]:

$$\hat{H}_{\min} = \begin{cases} H_1 & \text{if } \Lambda(\theta) - \Lambda(\theta + \xi) > \ln \frac{P_{H_2}}{P_{H_1}} \\ H_2 & \text{if } \Lambda(\theta) - \Lambda(\theta + \xi) < \ln \frac{P_{H_2}}{P_{H_1}} \end{cases} \quad (2.66)$$

where  $\Lambda(\theta)$  Eq. 2.2, Eq. 2.3 is the log-likelihood function.

From Eq. 2.61 and Eq. 2.62 we can write the generalized ZZLB  $c_{ZZ}$  as:

$$\begin{aligned} e &= \frac{1}{2} \int_0^{2(\Theta_2 - \Theta_1)} \xi P_{|\epsilon| > \frac{\xi}{2}} d\xi \\ &\geq \frac{1}{2} \int_0^{\Theta_2 - \Theta_1} \xi \int_{\Theta_1}^{\Theta_2 - \xi} [p_{\Theta}(\theta) + p_{\Theta}(\theta + \xi)] P_{\min}(\theta, \theta + \xi) d\theta d\xi \\ &= c_{ZZ} \end{aligned} \quad (2.67)$$

where the upper integration limit is set to  $\Theta_2 - \Theta_1$  instead of  $2(\Theta_2 - \Theta_1)$  because the two-hypothesis decision problem in Eq. 2.62 cannot be formulated if  $|\epsilon| > \Theta_2 - \Theta_1$  because at least one of the two hypotheses ( $\theta$  and  $\theta + \xi$ ) will then fall outside the *a priori* domain  $D_{\Theta}$ .

As  $P_{|\epsilon| > \frac{\xi}{2}}$  Eq. 2.62 is a decreasing function, tighter lower bounds of  $P_{|\epsilon| > \frac{\xi}{2}}$  and  $e$  can be obtained by filling the valleys of the lower bound of  $P_{|\epsilon| > \frac{\xi}{2}}$  in Eq. 2.62 as proposed by Bellini and Tartara in [60] so that the generalized BTLB  $c_{BT}$  can be written as:

$$\begin{aligned} e &\geq \frac{1}{2} \int_0^{\Theta_2 - \Theta_1} \xi V \left\{ \int_{\Theta_1}^{\Theta_2 - \xi} [p_{\Theta}(\theta) + p_{\Theta}(\theta + \xi)] P_{\min}(\theta, \theta + \xi) d\theta \right\} d\xi \\ &= c_{BT} \end{aligned} \quad (2.68)$$

where

$$V\{f(\xi)\} = \begin{cases} \max\{g(\xi' \geq -\xi)\} & \xi < 0 \\ \max\{f(\xi' \geq \xi)\} & \xi > 0 \end{cases}, \quad g(\xi) = f(-\xi)$$

is the valley-filling function.

If  $P_{\min}(\theta, \theta + \xi)$  is independent of  $\theta$  (i.e.  $P_{\min}(\theta, \theta + \xi) = P_{\min}(\xi)$ ,  $\forall \theta$ ) (e.g. time delay estimation), then the bounds in Eq. 2.67 and Eq. 2.68 can be written as:

$$\begin{aligned} c_{ZZ} &= \frac{1}{2} \int_0^{\Theta_2 - \Theta_1} \xi P_{\min}(\xi) \int_{\Theta_1}^{\Theta_2 - \xi} [p_{\Theta}(\theta) + p_{\Theta}(\theta + \xi)] d\theta d\xi \\ c_{BT} &= \frac{1}{2} \int_0^{\Theta_2 - \Theta_1} \xi V\left\{P_{\min}(\xi) \int_{\Theta_1}^{\Theta_2 - \xi} [p_{\Theta}(\theta) + p_{\Theta}(\theta + \xi)] d\theta\right\} d\xi. \end{aligned}$$

In Eq. 2.62 it is possible to find a lower bound of the probability of error  $P_{|\epsilon| > \frac{\epsilon}{2}}$  using the minimum probability of error  $P_{\min}(\theta, \theta + \xi)$  because both  $\theta$  and  $\theta + \xi$  are possible values of the unknown parameter  $\Theta$  thanks to the *a priori* distribution  $p_{\Theta}(\theta)$  of the latter. Accordingly, it is possible to formulate a decision problem with two hypotheses Eq. 2.64 and to find the corresponding nearest-decision-rule probability of error  $P_{\text{near}}(\theta, \theta + \xi)$  Eq. 2.63 and minimum probability of error  $P_{\min}(\theta, \theta + \xi)$  Eq. 2.65. In deterministic estimation problems only one value of the unknown parameter is possible ( $\Theta = \theta_0$  and  $p_{\Theta}(\theta) = \delta(\theta - \theta_0)$ ). Hence, there is no decision problem with two hypotheses that can be formulated in order to find the corresponding nearest-decision-rule probability of error  $P_{\text{near}}(\theta, \theta + \xi)$  and minimum probability of error  $P_{\min}(\theta, \theta + \xi)$ . To overcome this problem we assume that the probabilities  $P_{\epsilon > \frac{\epsilon}{2} | \theta}$  and  $P_{\epsilon < -\frac{\epsilon}{2} | \theta}$  obtained by the estimator achieving the minimum local MSE are independent of  $\theta$  (i.e.  $P_{\epsilon > \frac{\epsilon}{2} | \theta} = P_{\epsilon > \frac{\epsilon}{2} | \theta_0}$ ,  $\forall \theta$  and  $P_{\epsilon < -\frac{\epsilon}{2} | \theta} = P_{\epsilon < -\frac{\epsilon}{2} | \theta_0}$ ,  $\forall \theta$ ). Therefore, we can write:

$$\begin{aligned} e | \theta_0 &= \int_0^{\epsilon_{\max}} \xi^2 p_{|\epsilon| | \theta_0}(\xi) d\xi \\ &= 2 \int_0^{\epsilon_{\max}} \xi P_{|\epsilon| > \xi | \theta_0} d\xi - \{\xi^2 P_{|\epsilon| > \xi | \theta_0}\} \Big|_0^{\epsilon_{\max}} \\ &= \frac{1}{2} \int_0^{2\epsilon_{\max}} \xi P_{|\epsilon| > \frac{\xi}{2} | \theta_0} d\xi \end{aligned} \quad (2.69)$$

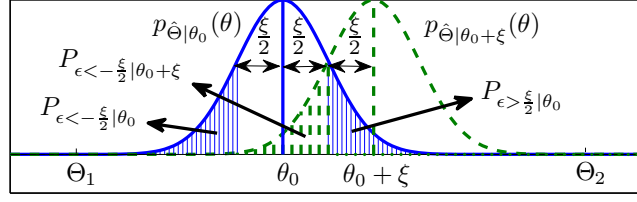


Fig. 2.6.: Decision problem with two equiprobable hypotheses:  $H_1 : \Theta = \theta_0$  and  $H_2 : \Theta = \theta_0 + \xi$ .

where

$$\begin{aligned}
 P_{|\epsilon| > \frac{\xi}{2} | \theta_0} &= 2 \left[ \frac{1}{2} P_{\epsilon > \frac{\xi}{2} | \theta_0} + \frac{1}{2} P_{\epsilon < -\frac{\xi}{2} | \theta_0} \right] \\
 &\approx 2 \begin{cases} P_{\epsilon_0} = \frac{1}{2} P_{\epsilon > \frac{\xi}{2} | \theta_0 - \frac{\xi}{2}} + \frac{1}{2} P_{\epsilon < -\frac{\xi}{2} | \theta_0 + \frac{\xi}{2}} \\ P_{\epsilon_1} = \frac{1}{2} P_{\epsilon > \frac{\xi}{2} | \theta_0 - \xi} + \frac{1}{2} P_{\epsilon < -\frac{\xi}{2} | \theta_0} \\ P_{\epsilon_2} = \frac{1}{2} P_{\epsilon > \frac{\xi}{2} | \theta_0} + \frac{1}{2} P_{\epsilon < -\frac{\xi}{2} | \theta_0 + \xi} \end{cases} \\
 &\geq 2 \begin{cases} P_{\min}(\theta_0 - \frac{\xi}{2}, \theta_0 + \frac{\xi}{2}) \\ P_{\min}(\theta_0 - \xi, \theta_0) \\ P_{\min}(\theta_0, \theta_0 + \xi) \end{cases} \quad (2.70)
 \end{aligned}$$

with  $\epsilon_{\max} = \max\{\Theta_2 - \theta_0, \theta_0 - \Theta_1\}$ . We denote by  $P_{\epsilon_0}$ ,  $P_{\epsilon_1}$  and  $P_{\epsilon_2}$  the probabilities of error of the nearest decision rule of the following two-hypothesis decision problems (decision problem in Eq. 2.72 is illustrated in Fig. 2.6):

$$H = \begin{cases} H_1 : \Theta = \theta_0 - \frac{\xi}{2} & P_{H_1} = \frac{1}{2} \\ H_2 : \Theta = \theta_0 + \frac{\xi}{2} & P_{H_2} = \frac{1}{2} \end{cases} \quad (2.71)$$

$$H = \begin{cases} H_1 : \Theta = \theta_0 - \xi & P_{H_1} = \frac{1}{2} \\ H_2 : \Theta = \theta_0 & P_{H_2} = \frac{1}{2} \end{cases} \quad (2.72)$$

and by  $P_{\min}(\theta_0 - \frac{\xi}{2}, \theta_0 + \frac{\xi}{2})$ ,  $P_{\min}(\theta_0 - \xi, \theta_0)$  and  $P_{\min}(\theta_0, \theta_0 + \xi)$  the corresponding minimum probabilities of error obtained by the optimum decision rule based on the likelihood ratio test.

From Eq. 2.69 and Eq. 2.70 we obtain the following approximate lower bounds:

$$z_0 = \int_0^{\epsilon_0} \xi P_{\min}(\theta_0 - \frac{\xi}{2}, \theta_0 + \frac{\xi}{2}) d\xi \quad (2.73)$$

$$z_1 = \int_0^{\epsilon_1} \xi P_{\min}(\theta_0 - \xi, \theta_0) d\xi \quad (2.74)$$

$$z_0 = \int_0^{\epsilon_2} \xi P_{\min}(\theta_0, \theta_0 + \xi) d\xi \quad (2.75)$$

where  $\epsilon_0 = \min\{2(\theta_0 - \Theta_1), 2(\Theta_2 - \theta_0)\}$ ,  $\epsilon_1 = \min\{\theta_0 - \Theta_1, \epsilon_0\}$  and  $\epsilon_2 = \min\{\Theta_2 - \theta_0, \epsilon_0\}$ . The integration limits are set to  $\epsilon_0$ ,  $\epsilon_1$  and  $\epsilon_2$  because at least  $P_{\epsilon > \frac{\xi}{2} | \theta_0}$  or  $P_{\epsilon < -\frac{\xi}{2} | \theta_0}$  Eq. 2.70 is equal to zero for  $\xi \geq \epsilon_0$ , and because  $\theta_0 - \xi$  Eq. 2.71 and  $\theta_0 + \xi$  Eq. 2.72 fall outside  $D_\Theta$  for  $\xi \geq (\theta_0 - \Theta_1)$  and  $\xi \geq (\Theta_2 - \theta_0)$  respectively.

Similarly to the BTLB for Bayesian estimation, tighter bounds can be obtained by filling the valleys of  $P_{\min}(\theta_0 - \frac{\xi}{2}, \theta_0 + \frac{\xi}{2})$ ,  $P_{\min}(\theta_0 - \xi, \theta_0)$  and  $P_{\min}(\theta_0, \theta_0 + \xi)$ :

$$b_0 = \int_0^{\epsilon_0} \xi V\{P_{\min}(\theta_0 - \frac{\xi}{2}, \theta_0 + \frac{\xi}{2})\} d\xi \quad (2.76)$$

$$b_1 = \int_0^{\epsilon_1} \xi V\{P_{\min}(\theta_0 - \xi, \theta_0)\} d\xi \quad (2.77)$$

$$b_2 = \int_0^{\epsilon_2} \xi V\{P_{\min}(\theta_0, \theta_0 + \xi)\} d\xi. \quad (2.78)$$

When  $P_{\min}(\theta, \theta')$  is a function of  $\theta' - \theta$  (e.g. TOA estimation) we can write the bounds in Eq. 2.73, Eq. 2.74, Eq. 2.75, Eq. 2.76, Eq. 2.77 and Eq. 2.78 as ( $i = 0, 1, 2$ ):

$$z_i = \int_0^{\epsilon_i} \xi P_{\min}(\xi) d\xi \quad (2.79)$$

$$b_i = \int_0^{\epsilon_i} \xi V\{P_{\min}(\xi)\} d\xi \quad (2.80)$$

where  $z_0$  and  $b_0$  are the tightest given that  $\epsilon_0 \geq \epsilon_1, \epsilon_2$ .

As the probability of error of an arbitrary detector  $\hat{H}$  is given by:

$$P_e = P_{H_1} P_{\hat{H}=H_2|H_1} + P_{H_2} P_{\hat{H}=H_1|H_2}. \quad (2.81)$$

we can write the minimum probability of error from Eq. 2.3, Eq. 2.37, Eq. 2.66 and Eq. 2.81 as:

$$\begin{aligned} P_{\min}(\theta, \theta') &= \frac{1}{2} [P_{\Lambda(\theta') > \Lambda(\theta) | \Theta = \theta} + P_{\Lambda(\theta) > \Lambda(\theta') | \Theta = \theta'}] \\ &= \frac{1}{2} [Q(\theta', \theta) |_{\Theta = \theta} + Q(\theta, \theta') |_{\Theta = \theta'}] \\ &= Q\left(\sqrt{\frac{\rho}{2} [1 - R(\theta, \theta')]}\right) \end{aligned} \quad (2.82)$$

where it has been taken into account that  $R_s(\theta, \theta') = R_s(\theta', \theta)$  Eq. 2.5.

### 2.1.5 Alternate MSE approximations and approximate bounds

In this section we derive two approximate upper bounds and two approximations of the statistics of the MLE based on the subdomain probability approximation  $P_n^{(3)}$  Eq. 2.38, as well as an approximate lower bound based on the Taylor series expansion of the CCR to second order Eq. 2.42.

As  $P_n^{(3)}$  Eq. 2.38 is an approximation of  $P_n = P\{\hat{\Theta} \in D_n\}$  Eq. 2.32 (probability that the MLE  $\hat{\Theta}$  falls in subdomain  $D_n$ ), we can approximate the PDF  $\hat{\Theta}$  by the limit of  $P_n^{(3)}$  as  $N$  approaches infinity (so that the width of  $D_n$  approaches zero). As such, we can write the approximate PDF, mean and MSE as:

$$p_M(\theta) = \lim_{N \rightarrow \infty} P_n^{(3)} = \frac{Q(\theta, \Theta)}{\int_{\Theta_1}^{\Theta_2} Q(\theta, \Theta) d\theta} \quad (2.83)$$

$$\mu_M = \int_{\Theta_1}^{\Theta_2} \theta p_M(\theta) d\theta \quad (2.84)$$

$$e_M = \int_{\Theta_1}^{\Theta_2} (\theta - \Theta)^2 p_M(\theta) d\theta. \quad (2.85)$$

We will see from the numerical results in Sec. 2.1.6 that  $e_M$  acts as an upper bound and converges to a multiple of the CRLB at high SNR. In fact,  $p_M(\theta)$  overestimates the true PDF of  $\hat{\Theta}$  in the vicinity of  $\Theta$ . To force  $e_M$  to converge to the CRLB, we approximate the PDF of  $\hat{\Theta}$  by a mixture of  $p_M(\theta)$  and the normal distribution  $p_{0,N}(\theta)$  Eq. 2.52 (of mean equal to  $\Theta$  and variance equal to the CRLB):

$$p_{MC}(\theta) = (1 - 2P_M)p_{0,N}(\theta) + 2P_M p_M(\theta) \quad (2.86)$$

$$\mu_{MC} = (1 - 2P_M)\Theta + 2P_M \mu_M \quad (2.87)$$

$$e_{MC} = (1 - 2P_M)c(\Theta) + 2P_M e_M \quad (2.88)$$

where  $2P_M$  is the probability that  $\hat{\Theta}$  does not fall in the vicinity of  $\Theta$  (i.e. probability of threshold effect). To compute  $P_M$  we choose a testpoint  $\theta_M$ , the closest to  $\Theta$  but not in its vicinity, and compute  $P_M$  as  $P_M = V\{Q_0(\theta_M)\}$ . The factor 2 is due to the symmetry of the ACR around  $\Theta$ . With oscillating ACR,  $\theta_M$  should not be farther than the first local maximum (whose abscissa  $\theta_1$  is the best testpoint) after the global one. We use the valley-filling function  $V\{\cdot\}$  to force  $P_M$  to give a good indication on the threshold effect if  $\theta_M$  falls in the valley between the global and the first local maximum. By doing so,  $P_M$  becomes the same at  $\theta_M$  and  $\theta_1$ . We intuitively assume that the vicinity of  $\Theta$  corresponds to half the positive mainlobe of  $R_s(\theta, \Theta)$  so we can set  $\theta_M$  at  $\theta_M = \Theta + \frac{\pi}{4\beta_s(\Theta)}$ . In fact, as can be seen in Fig. 2.2(b) the half positive mainlobe width can be approximated by  $\frac{1}{4\phi_c(\Theta)}$  that can be approximated in turn from Eq. 2.18 by  $\frac{\pi}{2\beta_s(\Theta)}$ .

As with oscillating ACR,  $\hat{\Theta}$  only falls around the local maxima, more approximations can be obtained using the valley-filling function:

$$p_V(\theta) = \frac{V\{Q(\theta, \Theta)\}}{\int_{\Theta_1}^{\Theta_2} V\{Q(\theta, \Theta)\}d\theta} \quad (2.89)$$

$$\mu_V = \int_{\Theta_1}^{\Theta_2} \theta p_V(\theta) d\theta \quad (2.90)$$

$$e_V = \int_{\Theta_1}^{\Theta_2} (\theta - \Theta)^2 p_V(\theta) d\theta \quad (2.91)$$

$$p_{VN}(\theta) = (1 - 2P_M)p_{0,N}(\theta) + 2P_M p_V(\theta) \quad (2.92)$$

$$\mu_{VN} = (1 - 2P_M)\Theta + 2P_M \mu_V \quad (2.93)$$

$$e_{VN} = (1 - 2P_M)c(\Theta) + 2P_M e_V. \quad (2.94)$$

Consider now the approximation of the statistics of  $\hat{\Theta}$  Eq. 2.8 using the Taylor series in Eq. 2.42 about  $\theta_0 = \Theta$  (global maximum). As  $\dot{R}_0 = 0$ , we can write:

$$\hat{\Theta} = \underset{\theta}{\operatorname{argmax}} \{X_{s,r}(\theta)\} \approx \hat{\Theta}_C = \Theta - \frac{\dot{w}_0}{\alpha \ddot{R}_0 + \ddot{w}_0} \quad (2.95)$$

where  $\frac{\dot{w}_0}{\alpha \ddot{R}_0 + \ddot{w}_0}$  is a ratio of two normal variables. Statistics of normal variable ratio are studied in [102–104]. We can show from [103] that  $\hat{\Theta}_C$  is distributed as:

$$\hat{\Theta}_C \sim \Theta + a_1 + \frac{\chi}{a_2} \quad (2.96)$$

with  $a_1 = \nu_0 \frac{\sigma \dot{w}_0}{\sigma \ddot{w}_0}$ ,  $a_2 = \frac{\sigma \ddot{w}_0}{h}$ ,  $h = \operatorname{sign}(\nu_0) \sigma \dot{w}_0 \sqrt{1 - \nu_0^2}$ ,  $\operatorname{sign}(\xi) = 1$  (resp.  $-1$ ) for  $\xi \geq 0$  (resp.  $\xi < 0$ ), and:

$$p_\chi(\xi) = \frac{e^{-\frac{1}{2}(a_3^2 + a_4^2)}}{\pi(1 + \xi^2)} \left\{ 1 + \sqrt{2\pi} q e^{\frac{q^2}{2}} \left[ \frac{1}{2} - Q(q) \right] \right\} \quad (2.97)$$

where  $p_\chi(\xi)$  is the PDF of  $\chi$ ,  $q = \frac{a_3 \xi + a_4}{\sqrt{1 + \xi^2}}$ ,  $a_3 = \alpha \ddot{R}_0 \frac{a_1}{h}$  and  $a_4 = \frac{-\alpha \ddot{R}_0}{\sigma \ddot{w}_0} = \sqrt{\rho} \frac{\beta^2(\Theta)}{\delta^2(\Theta)}$  with  $\delta^4(\theta) = \frac{E_{\ddot{s}}(\theta)}{E_s}$ . From Eq. 2.97 we can approximate the PDF, mean, variance and MSE of  $\hat{\Theta}_C$  by:

$$p_C(\theta) = \operatorname{sign}(\nu_0) a_2 p_\chi[a_2(\theta - \Theta - a_1)] \quad (2.98)$$

$$\mu_C = \int_{\Theta_1}^{\Theta_2} \theta p_C(\theta) d\theta \quad (2.99)$$

$$\sigma_C^2 = \int_{\Theta_1}^{\Theta_2} (\theta - \mu_C)^2 p_C(\theta) d\theta \quad (2.100)$$

$$e_C = (\mu_C - \tau)^2 + \sigma_C^2. \quad (2.101)$$

Note that the moments  $\int_{-\infty}^{\infty} \xi^i p_X(\xi) d\xi$ ,  $i = 1, 2, \dots$  (infinite domain) are infinite like with Cauchy distribution [103]. We will see in Sec. 2.1.6 that  $e_C$  Eq. 2.101 behaves as a lower bound of the MSE of the MLE. This result could be proved using the Taylor series expansion in Eq. 2.42. As we do not provide here an explicit proof, we will consider  $e_C$  as an approximate lower bound.

### 2.1.6 Numerical results and discussion

In this section we show and discuss some numerical results of the derived MSE approximations and approximate upper and lower bounds for TOA estimation using UWB waveforms.

We consider an unmodulated Gaussian pulse with  $T_w = 2$  ns,  $\Theta = 0$  and  $D_\Theta = [-2, 1.5]T_w$ , and the same pulse modulated by  $f_c = 6.85$  GHz. With the former we consider  $N = 9$  equal subdomains and with the latter a subdomain around each local maximum ( $N = 48$ ).

Denote by:

$$e_{i,j,x} = \sum_{n=n_1}^{n_2} P_n^{(i)} [(\Theta - \mu_{n,j,x})^2 + \sigma_{n,j,x}^2] \quad (2.102)$$

the MSE approximation based on Eq. 2.31 and using the subdomain probability approximation  $P_n^{(i)}$  ( $i \in \{1, 2, 3\}$ , see Eq. 2.35, Eq. 2.36, Eq. 2.38) and subdomain mean and variance approximations  $\mu_{n,x,y}$  and  $\sigma_{n,x,y}^2$  ( $(j, x) = U$  in Eq. 2.39, Eq. 2.40, and  $(j, x) \in \{1, 2\} \times \{c, o\}$  in Eq. 2.47–Eq. 2.50, Eq. 2.55–Eq. 2.58). The approximate upper bound derived in [70] corresponds to  $e_{2,U}$ .

The results about the unmodulated pulse are shown and discussed in Sec. 2.1.6.1 and those about the modulated pulse in Sec. 2.1.6.2

#### 2.1.6.1 Unmodulated Gaussian pulse

Here we show and discuss the numerical results obtained for the unmodulated pulse.

In Fig. 2.7(a) we show the MSE  $e_S$  obtained by simulation based on 10000 trials, five MSE approximations:  $e_{1,U}$ ,  $e_{1,1,c}$ ,  $e_{1,2,c}$ ,  $e_{3,1,c}$  Eq. 2.102 and  $e_{MN}$  Eq. 2.88 (equal to  $e_{MN}$  Eq. 2.94 because of the non-oscillating ACR), the CRLB  $c$  Eq. 2.22 (equal to the ECRLB  $c_e$  Eq. 2.23 because unmodulated pulse) and the maximum MSE  $e_U$  Eq. 2.20, versus the SNR.

In Fig. 2.7(b) we show  $e_S$ ,  $c$ ,  $e_U$  and two approximate upper bounds  $e_{2,U}$  Eq. 2.102 and  $e_M$  Eq. 2.85 (equal to  $e_V$  Eq. 2.91 because of the non-oscillating ACR).

In Fig. 2.7(c) we show  $e_S$ ,  $c$ , the BLB  $c_B$  Eq. 2.19, two approximate lower bounds:  $e_C$  Eq. 2.101 and  $z_0$  Eq. 2.79 (equal to  $b_0$  Eq. 2.80 because non-oscillating ACR), and  $e_U$ .

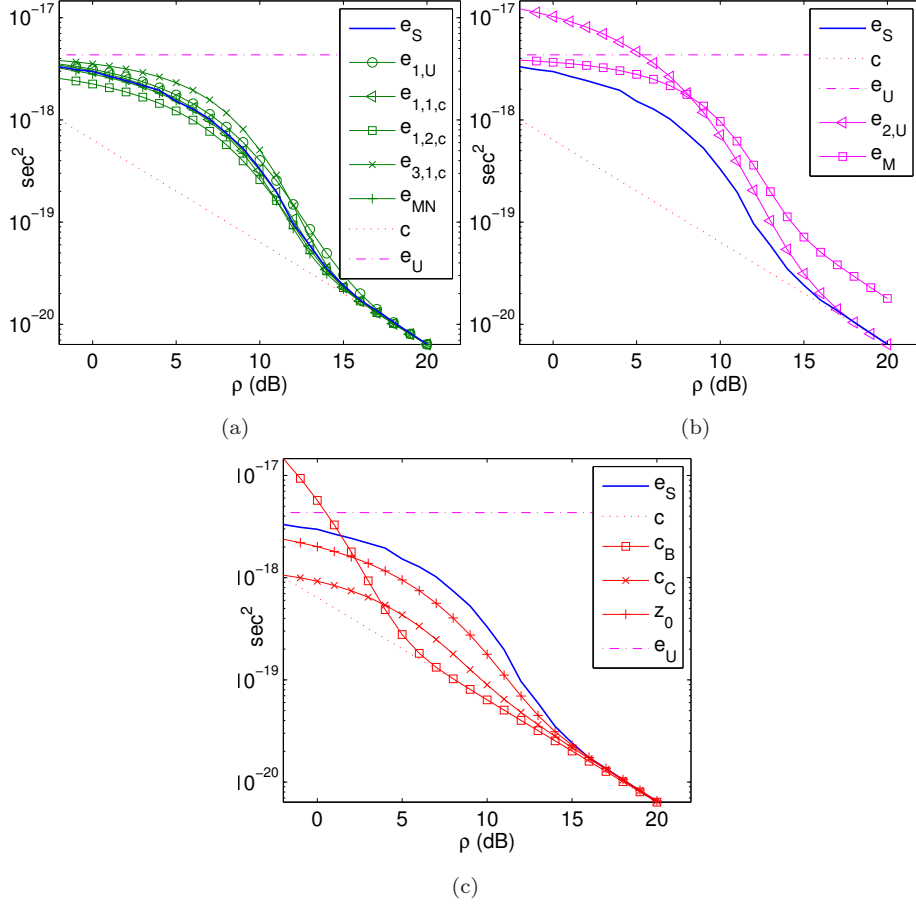


Fig. 2.7.: MSE approximations and approximate upper and lower bounds obtained with the unmodulated Gaussian pulse with respect to the SNR  $\rho$  ( $T_w = 2$  ns,  $\Theta = 0$ ,  $D_\Theta = [-2, 1.5]T_w$ ) (a) Simulated MSE  $e_S$ , MSE approximations  $e_{1,U}$ ,  $e_{1,1,c}$ ,  $e_{1,2,c}$ ,  $e_{3,1,c}$  and  $e_{MN}$ , CRLB  $c$ , maximum MSE  $e_U$  (b)  $e_S$ ,  $c$ ,  $e_U$ , approximate upper bounds  $e_{2,U}$  and  $e_M$  (c)  $e_S$ ,  $c$ , BLB  $c_B$ , approximate lower bounds  $c_C$  and  $z_0$ ,  $e_U$ .

We can see from  $e_S$  that, as mentioned in the introduction of Sec. 2.1, the SNR axis can be divided into three regions:

1. *A priori* region: where the maximum MSE  $e_U$  is achieved (estimator uniformly distributed in the *a priori* domain).
2. Threshold region: the region of transition between the *a priori* and asymptotic regions.

3. Asymptotic region: where the CRLB is achieved.

Denote by:

$$\rho_{pr} = \rho; e(\rho) = 0.5e_U \quad (2.103)$$

$$\rho_{as} = \rho; e(\rho) = 1.1c \quad (2.104)$$

the *a priori* and asymptotic thresholds delimiting the *a priori*, threshold and asymptotic regions (see Fig. 2.1(a)). From  $e_S$ , we have  $\rho_{pr} = 4$  dB and  $\rho_{as} = 16$  dB.

The MSE approximations  $e_{1,U}$ ,  $e_{1,1,c}$ ,  $e_{1,2,c}$ ,  $e_{3,1,c}$  derived in Sec. 2.1.3 using the subdomain method are very accurate and closely follow  $e_S$ ;  $e_{1,1,c}$  is more accurate than  $e_{3,1,c}$  which slightly overestimates  $e_S$ , because  $e_{1,1,c}$  uses the subdomain probability approximation  $P_n^{(1)}$  Eq. 2.35 which considers all testpoints during the computation of the probability, whereas  $e_{3,1,c}$  uses the approximation  $P_n^{(3)}$  Eq. 2.38 based on the approximate upper bound  $P_n^{(2)}$  Eq. 2.36 which only consider the 0th and the  $n$ th testpoints;  $e_{1,1,c}$  is more accurate than  $e_{1,U}$  which slightly overestimates  $e_S$ , and than  $e_{1,2,c}$  which slightly underestimates  $e_S$ , because  $e_{1,1,c}$  uses the subdomain mean and variance approximations  $\mu_{n,1,c}$  Eq. 2.47 and  $\sigma_{n,1,c}^2$  Eq. 2.48 obtained from the Taylor approximation of the noise  $w(\theta)$  in Eq. 2.4 to first order, whereas  $e_{1,U}$  uses  $\mu_{n,U}$  Eq. 2.39 and  $\sigma_{n,U}^2$  Eq. 2.40 assuming the subdomain MLE uniformly distributed in the subdomain  $D_n$  (overestimation of the noise), and  $e_{1,2,c}$  uses  $\mu_{n,2,c}$  Eq. 2.49 and  $\sigma_{n,2,c}^2$  Eq. 2.50 neglecting the noise.

The MSE approximation  $e_{MN}$  derived in Sec. 2.1.5 based on the mixture of two distributions is very accurate as well.

The approximate upper bound  $e_{2,U}$  derived by McAulay [70] converges to the CRLB simultaneously with  $e_S$  so it can be used to accurately compute the asymptotic threshold. However, it is less tight in the *a priori* and *a priori*-asymptotic transition regions because it uses the approximate subdomain probability upper bound  $P_n^{(2)}$  Eq. 2.36 which is not tight in these regions as already shown and discussed in Fig. 2.3(a) and Fig. 2.3(b). Moreover, it approaches infinity when  $N \rightarrow \infty$  as already mentioned in Sec. 2.1.3.1.

The approximate upper bound  $e_M$  derived in Sec. 2.1.5 is quite tight. It converges to a multiple of the CRLB (2.68c) at high SNR. In fact, it is obtained from the PDF approximation  $p_M(\theta)$  Eq. 2.83 which is more flat in the vicinity of  $\Theta$  than the true PDF since it is obtained from the approximate upper bound  $P_n^{(2)}$  Eq. 2.36. Nevertheless, it can be used to accurately calculate the asymptotic threshold because it converges to its asymptotic regime simultaneously with  $e_S$ . This fact will be more apparent in Fig. 2.8(b) with the modulated pulse.

Both the BLB  $c_B$  and the approximate lower bound  $e_C$  derived in Sec. 2.1.5 outperform the CRLB. Unlike the case of modulated pulse considered later,  $e_C$  is much better than  $c_B$  which converges much earlier to the CRLB.

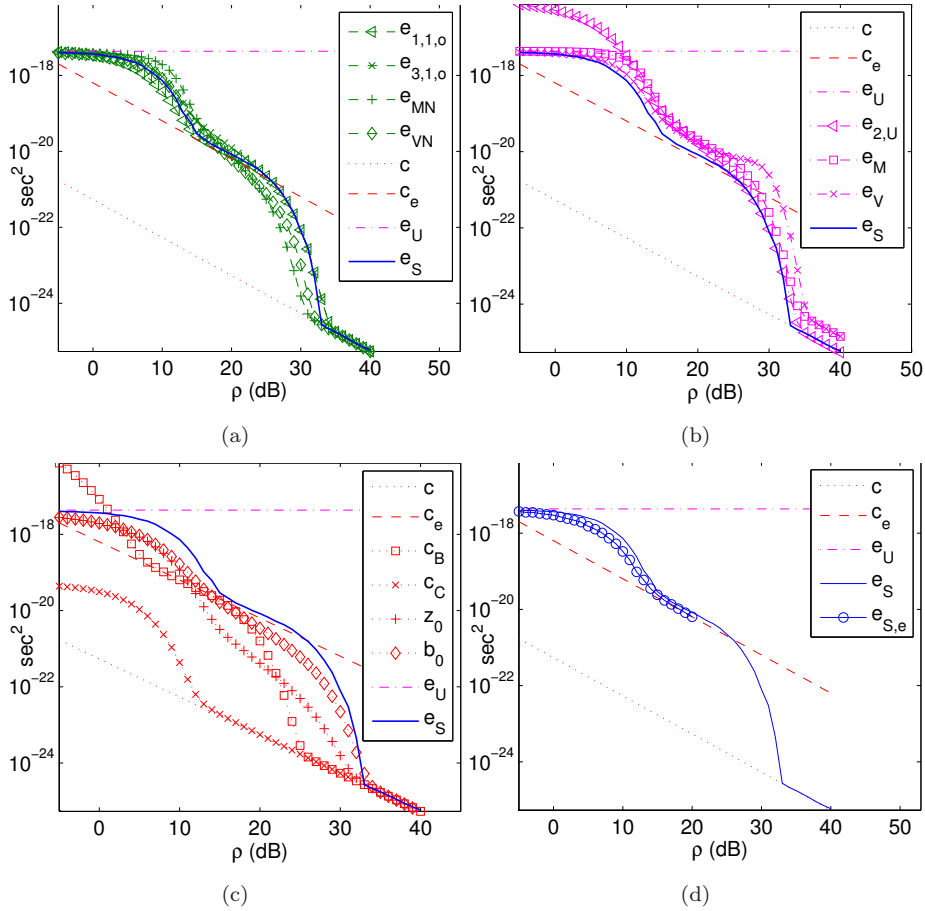


Fig. 2.8.: MSE approximations and approximate upper and lower bounds obtained with the modulated Gaussian pulse with respect to the SNR  $\rho$  ( $T_w = 2$  ns,  $f_c = 6.85$  GHz,  $\Theta = 0$ ,  $D_\Theta = [-2, 1.5]T_w$ ) (a) MSE obtained by simulation  $e_S$ , four MSE approximations  $e_{1,1,0}$ ,  $e_{3,1,0}$ ,  $e_{MN}$  and  $e_{VN}$ , CRLB  $c$ , ECRLB  $c_e$ , maximum MSE  $e_U$  (b)  $e_S$ ,  $c$ ,  $c_e$ ,  $e_U$ , approximate upper bounds  $e_{2,U}$ ,  $e_M$  and  $e_V$  (c)  $e_S$ ,  $c$ ,  $c_e$ , BLB  $c_B$ , approximate lower bounds  $c_C$ ,  $z_0$  and  $b_0$ ,  $e_U$  (d)  $e_S$ ,  $e_{S,e}$  ( $e_{S,e}$  is the MSE obtained by simulation with the unmodulated pulse considered in Sec. 2.1.6.2),  $c$ ,  $c_e$ , and  $e_U$ .

The approximate lower bound  $z_0$  derived in Sec. 2.1.4 is sufficiently tight and converges to the CRLB simultaneously with  $e_S$ .

### 2.1.6.2 Modulated Gaussian pulse

Here we show and discuss the numerical results obtained for the modulated pulse.

In Fig. 2.8(a) we show the MSE obtained by simulation  $e_S$ , four MSE approximations:  $e_{1,1,o}$ ,  $e_{3,1,o}$  Eq. 2.102,  $e_{MN}$  Eq. 2.88 and  $e_{MN}$  Eq. 2.94, the CRLB  $c$  Eq. 2.22, the ECRLB  $c_e$  Eq. 2.23 (equal to CRLB of the unmodulated pulse) and the maximum MSE  $e_U$  Eq. 2.20, versus the SNR.

In Fig. 2.8(b) we show  $e_S$ ,  $c$ ,  $c_e$ ,  $e_U$  and three approximate upper bounds  $e_{2,U}$  Eq. 2.102,  $e_M$  Eq. 2.85 and  $e_V$  Eq. 2.91.

In Fig. 2.8(c) we show  $e_S$ ,  $c$ ,  $c_e$ , the BLB  $c_B$  Eq. 2.19, three approximate lower bounds:  $e_C$  Eq. 2.101,  $z_0$  Eq. 2.79 and  $b_0$  Eq. 2.80, and  $e_U$ .

In Fig. 2.8(d) we show the MSE obtained by simulation for the modulated pulse  $e_S$  ( $\rho = -5, \dots, 40$  dB) and that for the unmodulated pulse  $e_{S,e}$  ( $\rho = -5, \dots, 20$  dB) ( $e_{S,e}$  is equal to  $e_S$  shown in Sec. 2.1.6.1),  $c$ , and  $e_U$ , versus the SNR.

From  $e_S$  we can see that the SNR axis can be divided into five regions as already mentioned in the introduction of Sec. 2.1:

1. *A priori* region.
2. *A priori*-ambiguity transition region.
3. Ambiguity region: where the ECRLB is achieved.
4. Ambiguity-asymptotic transition region.
5. Asymptotic region.

As shown in Fig. 2.1(b), these regions are delimited by the *a priori*  $\rho_{pr}$  and asymptotic  $\rho_{as}$  thresholds defined in Eq. 2.103 and Eq. 2.104 and the begin-ambiguity and end-ambiguity thresholds defined as:

$$\rho_{am1} = \rho; e(\rho) = 2c_e \quad (2.105)$$

$$\rho_{am2} = \rho; e(\rho) = 0.5c_e. \quad (2.106)$$

From  $e_S$  we have  $\rho_{pr} = 7$  dB,  $\rho_{am1} = 15$  dB,  $\rho_{am2} = 28$  dB and  $\rho_{as} = 33$  dB.

The MSE approximations  $e_{1,1,o}$  and  $e_{3,1,o}$  obtained using the subdomain method are very accurate and closely follow  $e_S$ .

The MSE approximations  $e_{MN}$  and  $e_{VN}$  Eq. 2.94 (version of  $e_{MN}$  using the valley-filling function) are very accurate too but less accurate than  $e_{1,1,o}$  and  $e_{3,1,o}$ . They converge to the CRLB a bit earlier than  $e_S$ ;  $e_{MN}$  is more accurate than  $e_{MN}$  thanks to the valley-filling function.

The approximate upper bound  $e_{2,U}$  [70] is very tight above the *a priori* region.

The approximate upper bounds  $e_M$  and  $e_V$  are sufficiently tight (tighter than  $z_0$  based on the binary detection method);  $e_M$  (resp.  $e_V$ ) is tighter than  $e_V$  (resp.  $e_M$ ) at high (resp. low) SNR. They both converge to a multiple of the CRLB

(1.75c) in the asymptotic region. This is due to the overestimation of the PDF of the MLE in the vicinity of the global maximum. This problem is solved in Sec. 2.1.5 by approximating the PDF of the MLE by a mixture of two PDF which leads to the MSE approximations  $e_{MN}$  and  $e_{VN}$  already examined. The main advantage of  $e_M$ ,  $e_V$ ,  $e_{MN}$  and  $e_{VN}$  is that they are very easy to compute (no need of testpoints).

The BLB  $c_B$  clearly indicates the presence of the ambiguity and asymptotic regions. However, it detects them very early so it cannot be used correctly calculate the begin-ambiguity, end-ambiguity and asymptotic thresholds ( $\rho_{am1} = 5$  dB,  $\rho_{am2} = 20$  dB and  $\rho_{as} = 26$  dB instead of 15, 28 and 33 dB). Furthermore, it does not describe correctly the behavior of the MSE in the *a priori* region.

The approximate lower bound  $e_C$  outperforms the CRLB, but is outperformed by the BLB  $c_B$  (unlike the case of unmodulated pulse). It is very optimistic and does not indicate the presence of the ambiguity region.

The approximate lower bound  $z_0$  is sufficiently tight, but  $b_0$  Eq. 2.80 is much tighter thanks to the valley-filling function. They both can be used to accurately calculate the asymptotic threshold and to roughly detect the *a priori* and ambiguity regions.

Let us now compare the MSE  $e_S$  achieved by the modulated pulse with  $e_{S,e}$  achieved by the unmodulated one. Both pulses approximately achieve the same MSE below the end-ambiguity threshold of the modulated pulse ( $\rho_{am2} = 28$  dB) and achieve the ECRLB between the begin-ambiguity and end-ambiguity thresholds. The MSE achieved with the unmodulated pulse is slightly smaller than that achieved with the modulated one because with the former the ML estimates spread in continuous manner along the ACR whereas with the latter they just spread around the local maxima. The asymptotic threshold of the unmodulated pulse (16 dB) is approximately equal to the begin-ambiguity threshold of the modulated pulse (15 dB). Above the end-ambiguity threshold, the MSE of the modulated pulse rapidly converges to the CRLB while that of the unmodulated one remains equal to the ECRLB.

To summarize we can say that, for a given nonlinear estimation problem with oscillating ACR, the MSE achieved by the ACR is the same as that achieved by its envelope below the end-ambiguity threshold. They both achieve the ECRLB between the begin-ambiguity and end-ambiguity thresholds. Above the latter threshold, the MSE achieved by the ACR converges to the CRLB whereas that achieved by its envelope remains equal to the ECRLB.

In the next section we will consider the problem of TOA estimation based on UWB signals and compute the thresholds of the different SNR regions with respect to some features of the transmitted signal. We will then exploit the obtained results to design, according to the available SNR, the spectrum of the transmitted signal that minimizes the achievable MSE.

## 2.2 THRESHOLD COMPUTATION

In Sec. 2.1, we have studied the threshold and ambiguity phenomena. We have seen that due to the threshold phenomenon, the SNR axis can be in general split into three regions (see Fig. 2.1(a)): 1) the *a priori* region where the estimator becomes uniformly distributed in the *a priori* domain, 2) the threshold region where an intermediate accuracy is achieved, and 3) the asymptotic region where the CRLB is achieved. In the special case of oscillating ACRs, the SNR axis can be split into five regions (see Fig. 2.1(b)): 1) the *a priori* region, 2) the *a priori*-ambiguity transition region, 3) the ambiguity region where an intermediate accuracy (the ECRLB) determined by the curvature of the envelope of the ACR is achieved, 4) the ambiguity-asymptotic transition region, and finally 5) the asymptotic region. As depicted in Fig. 2.1(a) and Fig. 2.1(b), we have denoted by  $\rho_{pr}$ ,  $\rho_{am1}$ ,  $\rho_{am2}$  and  $\rho_{as}$  the *a priori*, begin-ambiguity, end-ambiguity and asymptotic thresholds delimiting the different regions.

We have derived some approximations of the MSE of the MLE by splitting the *a priori* domain of the unknown parameter into subdomains and then computing the probability of each subdomain and the statistics of the MLE in each subdomain. As already mentioned in Sec. 2.1, this method has been firstly proposed by Wozencraft [89] and improved by McAulay [70] in order to derive an approximate upper bound for TOA estimation. As shown in Sec. 2.1, the proposed approximations of the MSE are highly accurate and closely follow the truly achieved MSE in practice.

We have also derived some approximate lower bounds for deterministic estimation using the principle of binary detection, which has been firstly used by Ziv and Zakai [58] to derive exact lower bounds for Bayesian estimation. The derived approximate bounds are very tight.

In order to better understand the threshold and ambiguity phenomena, we consider in this section the problem of TOA estimation based on UWB signals. We compute the thresholds of the SNR regions mentioned above with respect to some features of the transmitted signal. The thresholds are computed using the MSE approximations and approximate lower bounds derived in Sec. 2.1, and Analytic expressions of the thresholds have been obtained based on the approximate upper bound derived by McAulay [70]. Both modulated and unmodulated waveforms have been considered. The features of the transmitted signal that we have considered are *a priori* time bandwidth product (ATBW) and the inverse fractional bandwidth (IFBW).

We will show that the *a priori* threshold depends on both the *a priori* domain and the shape of the envelope of the ACR of the transmitted signal. Regarding the begin-ambiguity threshold (beginning of the ambiguity region), it only depends on the shape of the envelope of the ACR. However, the end-ambiguity (end of the ambiguity region) and asymptotic (beginning of the asymptotic region) thresholds only depend on the shape of the ACR, or equivalently on any set of

parameters determining this shape, like the shape of the envelope with the IFBW feature, regardless the values taken by other parameters like the bandwidth and the carrier.

In Sec. 2.2.1 we recall the system model for TOA estimation based on UWB signals, the MSE approximations, the lower bounds and the approximate lower bounds what we will use in this section. In Sec. 2.2.2 we compute the thresholds of the SNR regions with respect to the features of the transmitted signal for both modulated and unmodulated UWB signals. In Sec. 2.2.3 we show and discuss some numerical results about the thresholds for both modulated and unmodulated Gaussian pulses.

### 2.2.1 System model, MSE approximations, and approximate lower bounds

As mentioned before, we recall here the system model, the MSE approximations, the lower bounds and the approximate lower bounds that will be used in Sec. 2.2.

#### 2.2.1.1 System model

We can write the received signal as:

$$r(t) = \alpha s(t - \Theta) + \tilde{w}(t) \quad (2.107)$$

where  $s(t)$  denotes the transmitted signal,  $\alpha$  and  $\Theta$  the gain and the time delay introduced by the channel, and  $\tilde{w}(t)$  the AWGN of two-sided power spectral density (PSD) of  $\frac{N_0}{2}$ . The deterministic unknown parameter to estimate is  $\Theta$ , and  $D_\Theta = [\Theta_1, \Theta_2]$  denotes its *a priori* domain.

We can write the MLE  $\hat{\Theta}$  of  $\Theta$  as:

$$\hat{\Theta} = \operatorname{argmax} \{X_{r,s}(\theta)\} \quad (2.108)$$

$$X_{r,s}(\theta) = \alpha R_s^\theta(\theta - \Theta) + w(\theta) = \alpha E_s R(\theta - \Theta) + w(\theta) \quad (2.109)$$

$$R(\theta) = \frac{R_s(\theta)}{E_s} \quad (2.110)$$

where  $X_{r,s}(\theta)$  is the CCR  $r(t)$  of  $s(t)$ ,  $R_s(\theta)$  the ACR of  $s(t)$ ,  $R(\theta)$  the normalized ACR, and  $w(\theta) = X_{\tilde{w},s}(\theta)$  (CCR  $\tilde{w}(t)$  of  $s(t)$ ) a colored zero-mean Gaussian noise of covariance  $C_w(\theta) = \frac{N_0}{2} E_s R(\theta)$ .

We can write the CRLB, ECRLB (envelope CRLB) and maximum MSE of  $\Theta$  as:

$$c = \frac{N_0/2}{\alpha^2 E_s} = \frac{-N_0/2}{\alpha^2 \ddot{R}_s(0)} = \frac{1}{\rho \beta_s^2} \quad (2.111)$$

$$c_e = -\frac{N_0/2}{\alpha^2 \Re\{\ddot{e}_{R_s}(0)\}} = \frac{1}{\rho \beta_e^2} \quad (2.112)$$

$$e_U = \frac{(\Theta_2 - \Theta_1)^2}{12} + \left[ \Theta - \frac{\Theta_1 + \Theta_2}{2} \right]^2 \quad (2.113)$$

where

$$\rho = \frac{\alpha^2 E_s}{N_0/2} \quad (2.114)$$

$$\beta_s^2 = \frac{E_{\dot{s}}}{E_s} = -\frac{\ddot{R}_s(0)}{E_s} = \frac{\int_{-\infty}^{+\infty} 4\pi^2 f^2 |\mathcal{F}_s(f)|^2 df}{\int_{-\infty}^{+\infty} |\mathcal{F}_s(f)|^2 df} \quad (2.115)$$

$$\beta_e^2 = \frac{\int_{-\infty}^{+\infty} 4\pi^2 f^2 |\mathcal{F}_{e_s}(f)|^2 df}{\int_{-\infty}^{+\infty} |\mathcal{F}_{e_s}(f)|^2 df} \quad (2.116)$$

denote the SNR, the MQBW of  $s(t)$  and the envelope EMQBW (equal to the MQBW of the envelope), with

$$\beta_s^2 = \beta_e^2 + 4\pi^2 f_c^2 \approx 4\pi^2 f_c^2. \quad (2.117)$$

We have already mentioned in Sec. 2.1 that the CRLB  $c$  Eq. 2.111 is much smaller than the ECRLB  $c_e$  Eq. 2.112 because the MQBW  $\beta_s^2$  Eq. 2.117 is much larger than the EMQBW  $\beta_e^2$  Eq. 2.116 so the estimation seriously deteriorates if the ECRLB is achieved instead of the CRLB due to ambiguity. We recall that to benefit from this super accuracy at sufficiently high SNR, the sufficient condition to satisfy is that the phase of the transmitted signal should not be modified across the communication channel (e.g. due to fading), regardless whether the signal is pure impulse-radio UWB (carrier-less), carrier-modulated with known phase (e.g. in monostatic radar), or carrier-modulated with unknown phase (e.g. in most communication systems).

### 2.2.1.2 MSE approximations obtained from the subdomain method

We have seen in Sec. 2.1 that by splitting the *a priori* domain  $D_\Theta = [\Theta_1, \Theta_2]$  of  $\Theta$  into  $N = n_2 - n_1 + 1$  subdomains  $D_n = [d_n, d_{n+1})$ , ( $n = n_1, \dots, n_2$ ), ( $n_1 \leq 0$ ,  $n_2 \geq 0$ ), we can write the MSE of  $\hat{\Theta}$  as:

$$e = \sum_{n=n_1}^{n_2} P_n [(\Theta - \mu_n)^2 + \sigma_n^2] \quad (2.118)$$

where  $P_n = P\{\hat{\Theta} \in D_n\}$  denotes the subdomain probability (i.e. probability that  $\hat{\Theta}$  falls in  $D_n$ ),  $\mu_n$  and  $\sigma_n^2$  the mean and variance of the subdomain MLE  $\hat{\Theta}_n = \hat{\Theta} | \hat{\Theta} \in D_n$ .

According to Sec. 2.1, the subdomain probability  $P_n$  in Eq. 2.118 can be approximately upper bounded by  $P_n^{(2)}$  [70] and approximated by  $P_n^{(3)}$ :

$$P_n^{(2)} = \begin{cases} Q(\theta_0, \theta_1) \text{ or } 1 & n = 0 \\ Q(\theta_n, \theta_0) & n \neq 0 \end{cases} \quad (2.119)$$

$$P_n^{(3)} = \frac{P_n^{(2)}}{\sum_{n=n_1}^{n_2} P_n^{(2)}} \quad (2.120)$$

where  $\theta_{n_1}, \dots, \theta_{n_2}$  denote  $N$  testpoints chosen in the subdomains  $D_{n_1}, \dots, D_{n_2}$  respectively, and

$$Q(\theta, \theta') = P\{X_{r,s}(\theta) > X_{r,s}(\theta')\} = Q\left(\sqrt{\frac{\rho}{2}} \frac{R(\theta' - \Theta) - R(\theta - \Theta)}{\sqrt{1 - R(\theta - \theta')}}\right) \quad (2.121)$$

with  $Q(y) = \frac{1}{\sqrt{2\pi}} \int_y^\infty e^{-\frac{\xi^2}{2}} d\xi$  being the Q function.

We have seen in Sec. 2.1 that for oscillating ACR  $R_s(\theta)$ . we consider a subdomain around each local maximum (i.e. between the two local minima adjacent to it) and choose the corresponding testpoint as the abscissa of the local maximum. Whereas for non-oscillating ACR, we split the *a priori* domain of  $\Theta$  into  $N$  equal subdomains and choose the centers of subdomains  $\theta_n = \frac{d_n + d_{n+1}}{2}$  as testpoints. For both oscillating and non-oscillating ACR the subdomain  $D_0$  contains the global maximum, and the corresponding testpoint  $\theta_0$  is equal to the unknown parameter  $\Theta$ . As such, the ACR inside a given subdomain is either increasing then decreasing (i.e. subdomain with local maximum) or purely monotone (i.e. increasing, decreasing or constant).

As shown in Sec. 2.1, we can approximate the subdomain mean  $\mu_n$  and variance  $\sigma_n^2$  in Eq. 2.118 by:

- $\mu_{0,0}$  and  $\sigma_{0,0}^2$  for  $n = 0$ .
- $\mu_{n,U}$  and  $\sigma_{n,U}^2$ ,  $\mu_{n,1,c}$  and  $\sigma_{n,1,c}^2$ , or  $\mu_{n,2,c}$  and  $\sigma_{n,2,c}^2$  for subdomain with monotone ACR.
- $\mu_{n,U}$  and  $\sigma_{n,U}^2$ ,  $\mu_{n,1,o}$  and  $\sigma_{n,1,o}^2$ , or  $\mu_{n,2,o}$  and  $\sigma_{n,2,o}^2$  for subdomain with local maximum.

where

$$\mu_{n,U} = \frac{d_n + d_{n+1}}{2} ; \sigma_{n,U}^2 = \frac{(d_{n+1} - d_n)^2}{12} \quad (2.122)$$

$$\mu_{n,1,c} = \mu_{n,B} ; \sigma_{n,1,c}^2 = \min\{\sigma_{n,U}^2, \sigma_{n,B}^2\} \quad (2.123)$$

$$\mu_{n,2,c} = \begin{cases} d_n & \dot{R}_n < 0 \\ d_{n+1} & \dot{R}_n > 0 \\ \frac{d_n + d_{n+1}}{2} & \dot{R}_n = 0 \end{cases} ; \sigma_{n,2,c}^2 = 0 \quad (2.124)$$

$$\mu_{n,1,o} = \theta_n ; \sigma_{n,1,o}^2 = \min\{\sigma_{n,N}^2, \sigma_{n,U}^2\} \quad (2.125)$$

$$\mu_{n,2,o} = \theta_n ; \sigma_{n,2,o}^2 = 0 \quad (2.126)$$

$$\mu_{0,0} = \theta_0 = \Theta ; \sigma_{0,0}^2 = \min\{c, \sigma_{0,U}^2\} \quad (2.127)$$

with  $R_n = R_s(\theta_n - \Theta)$  and

$$\mu_{n,B} = d_n P\{d_n\} + d_{n+1} P\{d_{n+1}\} \quad (2.128)$$

$$\sigma_{n,B}^2 = P\{d_n\} P\{d_{n+1}\} (d_{n+1} - d_n)^2 \quad (2.129)$$

$$P\{d_n\} = 1 - P\{d_{n+1}\} = Q\left(\sqrt{\rho} \frac{\dot{R}_n}{E_s \beta_s}\right) \quad (2.130)$$

$$\sigma_{n,N}^2 = c \frac{-\ddot{R}_0 E_s(\theta_n)}{\ddot{R}_n^2} = c \frac{\ddot{R}_0^2}{\ddot{R}_n^2}. \quad (2.131)$$

Finally we can write the MSE approximation based on Eq. 2.118 as:

$$e_{i,j,x} = \sum_{n=n_1}^{n_2} P_n^{(i)} [(\Theta - \mu_{n,j,x})^2 + \sigma_{n,j,x}^2] \quad (2.132)$$

where  $i = 2$  or  $3$  (see Eq. 2.119 and Eq. 2.120), and  $(j, x) = U$  (see Eq. 2.122) or  $(j, x) \in \{1, 2\} \times \{c, o\}$  (see Eq. 2.123, Eq. 2.124, Eq. 2.125, Eq. 2.126).

We have seen in Sec. 2.1 that all combinations of  $e_{i,j,x}$  are highly accurate and closely follow the truly achieved MSE in practice except for  $i = 2$  which gives a very tight upper bound at medium and high SNRs.

### 2.2.1.3 approximate lower bounds based on the Ziv and Zakai method

Using the binary detection principle proposed by Ziv and Zakai [58] we have derived in Sec. 2.1 the following approximate lower bounds:

$$z_0 = \int_0^{\epsilon_0} \xi P_{\min}(\xi) d\xi \quad (2.133)$$

$$b_0 = \int_0^{\epsilon_0} \xi V\{P_{\min}(\xi)\} d\xi \quad (2.134)$$

where  $\epsilon_0 = \min\{2(\theta_0 - \Theta_1), 2(\Theta_2 - \theta_0)\}$ ,  $V\{f(\xi)\}$  denotes the valley-filling function, and

$$P_{\min}(\xi) = Q\left(\sqrt{\frac{\rho}{2}[1 - R(\xi)]}\right). \quad (2.135)$$

We have seen in Sec. 2.1 that both  $z_0$  and  $b_0$  are sufficiently tight, but  $b_0$  is much tighter than  $z_0$  with oscillating ACR.

## 2.2.2 Threshold computation

In order to better understand the threshold and ambiguity phenomena, we compute in this section the thresholds separating the different SNR regions with respect to some features of the transmitted signal. The obtained results will be later used in Sec. 2.3 in the design of the transmitted signal.

The *a priori*, begin-ambiguity, end-ambiguity and asymptotic thresholds can be defined as:

$$\rho_{pr} = \rho ; e(\rho) = \alpha_{pr} e_U \quad (2.136)$$

$$\rho_{am1} = \rho ; e(\rho) = \alpha_{am1} c_e \quad (2.137)$$

$$\rho_{am2} = \rho ; e(\rho) = \alpha_{am2} c_e \quad (2.138)$$

$$\rho_{as} = \rho ; e(\rho) = \alpha_{as} c \quad (2.139)$$

where we take, like in Sec. 2.1,  $\alpha_{pr} = 0.5$ ,  $\alpha_{am1} = 2$ ,  $\alpha_{am2} = 0.5$  and  $\alpha_{as} = 1.1$ .

The aim is to compute these thresholds with respect to the *a priori* time bandwidth product (ATBW), and inverse fractional bandwidth (IFBW) of the transmitted signal, defined as:

$$\gamma = TB \quad (2.140)$$

$$\lambda = \frac{f_c}{B} \quad (2.141)$$

where  $T = \Theta_2 - \Theta_1$  (*a priori* time) denotes the width of the *a priori* domain of  $\Theta$  and  $B$  the bandwidth of the transmitted signal. To realize this aim, we vary  $\gamma$  (resp.  $\lambda$ ) by either fixing  $T$  (resp.  $f_c$ ) and varying  $B$ , or vice versa, and compute the thresholds for each considered value, using one of the MSE approximations or approximate upper and lower bounds presented in Sec. 2.2.1.

### 2.2.2.1 Expressions of the begin-ambiguity, end-ambiguity and asymptotic thresholds

We have just seen that the threshold computation should be performed numerically based on a given MSE approximation or an approximate upper or lower bound. Here we present a simpler method to derive the expressions of the begin-ambiguity, end-ambiguity and asymptotic thresholds based on the MSE approximation in Eq. 2.132 with  $i = 2$ ,  $P_0^{(2)} = 1$  (see Eq. 2.119),  $j = 2$ ,  $x = c$  for non-oscillating ACR, and  $x = o$  for oscillating ACR. The resulting expressions are highly accurate.

Assume that the CRLB is achieved for a given SNR. Then, this SNR falls in the asymptotic region and all the ML estimates of the unknown parameter fall in the vicinity of the maximum (resp. global maximum) of the non-oscillating (resp. oscillating) ACR. In the course of decreasing the SNR, the threshold region (resp. ambiguity region) of the non-oscillating (resp. oscillating) ACR begins when the ML estimates start to spread along the ACR (resp. the local maxima of the ACR) instead of falling only in the vicinity of the maximum (resp. global maximum). Therefore, the ML estimates only fall, at the beginning (if we start from high SNRs) of the threshold (resp. ambiguity) region, in the subdomain  $D_0$  containing the maximum (resp. global maximum) and the subdomains  $D_{-1}$  and  $D_1$  at the left and the right of  $D_0$  respectively. It follows that, the MSE can be

approximated from Eq. 2.132 and Eq. 2.127 by taking  $i = 2$ ,  $P_0^{(2)} = 1$ ,  $j = 2$ ,  $x = c$  for non-oscillating ACR, and  $x = o$  for oscillating ACR by:

$$\begin{aligned}
e_{2,2,x} &= \sum_{n=-1}^1 P_n^{(2)} [(\Theta - \mu_{n,2,x})^2 + \sigma_{n,2,x}^2] \\
&= P_0^{(2)} \sigma_{0,0}^2 + \sum_{n=-1,1} P_n^{(2)} [(\Theta - \mu_{n,2,x})^2] \\
&= c + 2(\Theta - \theta_1)^2 Q(\theta_1, \Theta) \\
&= c + 2b_x^2 Q\left(\sqrt{\frac{\rho}{2}[1 - R(b_x)]}\right); b_x = \theta_1 - \Theta \quad (2.142)
\end{aligned}$$

where we have assumed for non-oscillating ACR ( $x = c$ ) that  $D_{-1}$  and  $D_1$  are sufficiently narrow so that  $\mu_{-1,c} \approx \theta_{-1}$  and  $\mu_{1,c} \approx \theta_1$  (see Eq. 2.124).

For non-oscillating ACR we take  $\theta_{-1} = \Theta - \frac{\pi}{4\beta_s}$  and  $\theta_1 = \Theta + \frac{\pi}{4\beta_s}$ . Note that the latter  $\theta_1$  is equal to the testpoint  $\theta_M$  considered in Eq. 2.88 and Eq. 2.94 in Sec. 2.1 and assumed there as the closest point to the maximum of the non-oscillating ACR, not in its vicinity. Hence, we get:

$$b_c = \theta_1 - \Theta = \frac{\pi}{4\beta_s}. \quad (2.143)$$

For oscillating ACR ( $x = o$ ) we have  $\theta_{-1} \approx \Theta - \frac{1}{f_c}$ ,  $\theta_1 \approx \Theta + \frac{1}{f_c}$  (abscissa of the two local maxima around the global one) so:

$$b_o = \theta_1 - \Theta \approx \frac{1}{f_c} \approx \frac{2\pi}{\beta_s} \quad (2.144)$$

where the approximation  $\frac{2\pi}{\beta_s}$  is obtained using Eq. 2.117.

Consider first the case of non-oscillating ACR. From Eq. 2.111, Eq. 2.139, Eq. 2.142 and Eq. 2.143 we can write the constraint of the asymptotic threshold (right side equality in Eq. 2.139) as:

$$G(\rho, b_c) = \frac{\alpha_{as} - 1}{2b_c^2 \beta_s^2} = \frac{8(\alpha_{as} - 1)}{\pi^2} = G_{as,c} \quad (2.145)$$

where

$$G(\rho, \theta) = \rho Q\left(\sqrt{\frac{\rho}{2}[1 - R(\theta)]}\right). \quad (2.146)$$

Consider now the case of oscillating ACR. From Eq. 2.111, Eq. 2.112, Eq. 2.138, Eq. 2.139, Eq. 2.142 and Eq. 2.144 we can write the constraints of the end-ambiguity and asymptotic thresholds (right side equalities in Eq. 2.138 and Eq. 2.139) as:

$$G(\rho, b_o) = \frac{1}{2b_o^2} \left( \frac{\alpha_{am2}}{\beta_e^2} - \frac{1}{\beta_s^2} \right) \approx \frac{\alpha_{am2} f_c^2}{2\beta_e^2} \approx \frac{\alpha_{am2} \beta_s^2}{8\pi^2 \beta_e^2} = G_{am2,o} \quad (2.147)$$

$$G(\rho, b_o) = \frac{\alpha_{as} - 1}{2b_o^2 \beta_s^2} \approx \frac{\alpha_{as} - 1}{8\pi^2} = G_{as,o}. \quad (2.148)$$

To compute the begin-ambiguity threshold for oscillating ACR using Eq. 2.142 we cannot take  $\theta_1 \approx \Theta + \frac{1}{f_c}$  because the ML estimates fall now, not only around the local maxima numbers  $-1, 0$  and  $1$ , but around all local maxima in the vicinity of the maximum of the envelope of the ACR. Accordingly, we choose similarly to the case of non-oscillating ACR  $\theta_1 \approx \Theta + \frac{\pi}{4\beta_e}$  ( $\beta_e$  Eq. 2.116 instead of  $\beta_s$  Eq. 2.115, Eq. 2.117) so:

$$b_{am1,o} = \theta_1 - \Theta = \frac{\pi}{4\beta_e} \quad (2.149)$$

and use the normalized ACR envelope:

$$e_R(\theta) = \frac{\Re\{e_{R_s}(\theta)\}}{E_{e_{R_s}}} \quad (2.150)$$

in the computation of the Q function in Eq. 2.142. We can then write the constraint of the begin-ambiguity threshold (right side equality in Eq. 2.137) from Eq. 2.137, Eq. 2.142, Eq. 2.149 and Eq. 2.150 as:

$$G_e(\rho, b_{am1,o}) = \frac{1}{2b_{am1,o}^2} \left( \frac{\alpha_{am1}}{\beta_e^2} - \frac{1}{\beta_s^2} \right) \approx \frac{8\alpha_{am1}}{\pi^2} = G_{am1,o} \quad (2.151)$$

where

$$G_e(\rho, \theta) = \rho Q \left( \sqrt{\frac{\rho}{2} [1 - e_R(\theta)]} \right). \quad (2.152)$$

Note that  $G_e(\rho, \theta)$  Eq. 2.152 can be used instead of  $G(\rho, \theta)$  Eq. 2.146 in both Eq. 2.147 and Eq. 2.148 to compute the end-ambiguity and asymptotic thresholds since:

$$\begin{aligned} R(\theta_{\max}) \text{ local maximum of } R(\theta) \\ \Downarrow \\ R(\theta_{\max}) \approx e_R(\theta_{\max}) \end{aligned} \quad (2.153)$$

which extremely simplifies the threshold computation. In fact, if we want to compute the end-ambiguity and asymptotic thresholds of a modulated pulse with respect to the IFBW  $\lambda$  Eq. 2.141, then instead of computing the normalized ACR  $R(\theta)$  for each value of  $\lambda$  we just compute the normalized ACR  $R_e(\theta)$  of the unmodulated pulse (independent of  $\lambda$ ) and vary the value of  $b_o$  Eq. 2.144 with respect to  $\lambda$ . Note also that it is much easier to compute the begin-ambiguity, end-ambiguity and asymptotic thresholds from Eq. 2.145, Eq. 2.147, Eq. 2.148 and Eq. 2.151 than from using one of the MSE approximations and approximate upper and lower bounds presented in Sec. 2.2.1 because  $G(\rho, \theta)$  Eq. 2.146 and  $G_e(\rho, \theta)$  Eq. 2.152 are much easier to evaluate.

Now, in order to derive analytic expressions of the begin-ambiguity, end-ambiguity and asymptotic thresholds we consider the following approximation of the Q function [89, pp. 83]:

$$\begin{aligned} \left( \frac{1}{\xi} - \frac{1}{\xi^3} \right) \frac{1}{\sqrt{2\pi}} e^{-\frac{\xi^2}{2}} < Q(\xi) < \frac{1}{\xi} \frac{1}{\sqrt{2\pi}} e^{-\frac{\xi^2}{2}}, \xi > 0 \\ \Downarrow \\ Q(\xi) \approx \frac{1}{\xi} \frac{1}{\sqrt{2\pi}} e^{-\frac{\xi^2}{2}}, \xi \gg 1 \end{aligned} \quad (2.154)$$

where the downside of Eq. 2.154 is due to the fact that  $\frac{1}{\xi} - \frac{1}{\xi^3} \approx \frac{1}{\xi}$  for  $\xi \gg 1$ . Using Eq. 2.154 we can after some manipulations write Eq. 2.145, Eq. 2.151, Eq. 2.147 and Eq. 2.148 as:

$$H(\rho, b_c)e^{H(\rho, b_c)} = -\frac{\pi G_{as,c}^2[1 - R(b_c)]}{2} = H_{as,c} \quad (2.155)$$

$$H_e(\rho, b_{am1,o})e^{H_e(\rho, b_{am1,o})} = -\frac{\pi G_{am1,o}^2[1 - e_R(b_{am1,o})]}{2} = H_{am1,o} \quad (2.156)$$

$$H(\rho, b_o)e^{H(\rho, b_o)} = -\frac{\pi G_{am2,o}^2[1 - R(b_o)]}{2} = H_{am2,o} \quad (2.157)$$

$$H(\rho, b_o)e^{H(\rho, b_o)} = -\frac{\pi G_{as,o}^2[1 - R(b_o)]}{2} = H_{as,o} \quad (2.158)$$

where

$$H(\rho, \theta) = -\frac{\rho[1 - R(\theta)]}{2} \quad (2.159)$$

$$H_e(\rho, \theta) = -\frac{\rho[1 - e_R(\theta)]}{2} \quad (2.160)$$

so the asymptotic threshold for non-oscillating ACR and the begin-ambiguity, end-ambiguity and asymptotic thresholds for oscillating ACR can be approximated from Eq. 2.155, Eq. 2.156, Eq. 2.157 and Eq. 2.158 as:

$$\rho_{as,c} = -2\frac{W_{-1}(H_{as,c})}{1 - R(b_c)} \quad (2.161)$$

$$\rho_{am1,o} = -2\frac{W_{-1}(H_{am1,o})}{1 - e_R(b_{am1,o})} \quad (2.162)$$

$$\rho_{am2,o} = -2\frac{W_{-1}(H_{am2,o})}{1 - R(b_o)} \quad (2.163)$$

$$\rho_{as,o} = -2\frac{W_{-1}(H_{as,o})}{1 - R(b_o)} \quad (2.164)$$

where  $W_{-1}(\xi)$  denotes the branch “-1” (because  $H_{as,c}$ ,  $H_{am1,o}$ ,  $H_{am2,o}$  and  $H_{as,o}$  are negative) of the Lambert W function that gives the solution of the equation:  $W_{-1}(\xi)e^{W_{-1}(\xi)} = \xi$ . This function, like other non-elementary functions (e.g. Q function, error function, etc), has Taylor series expansion and recursive formula to compute it, and is implemented in MATLAB so the corresponding solution can be considered as an analytic solution as it can directly be obtained.

Now we consider both modulated and unmodulated waveforms and prove that for waveforms that can be written as (e.g. Gaussian, cardinal sine, raised cosine, etc.):

$$w_B(t) = w(t'), \quad t' = Bt \quad (2.165)$$

where  $B$  denotes the bandwidth, the asymptotic threshold only depends on the shape  $w(t')$  (i.e. independent of  $B$ , constant for Gaussian and cardinal sine, and

function of the roll-off for raised cosine), and that for the modulated waveforms:

$$w_{B,f_c}(t) = w_B(t) \cos(2\pi f_c t) = w(t') \cos(2\pi \lambda t'), \quad t' = Bt \quad (2.166)$$

where  $f_c$  denotes the carrier, the begin-ambiguity threshold only depends on the shape  $w(t')$  of the envelope  $w_B(t)$  of  $w_{B,f_c}(t)$ , whereas the end-ambiguity and asymptotic thresholds are functions of the shape  $w(t')$  and the IFBW  $\lambda$  (i.e. independent of the values taken by  $B$  and  $f_c$  separately). This is equivalent to say that the begin-ambiguity threshold is only function of the shape of the envelope of the signal, whereas the end-ambiguity and asymptotic thresholds are only functions of the shape of the signal itself, regardless any other parameters like the bandwidth and the carrier.

Let us first prove that the asymptotic threshold Eq. 2.145 of the unmodulated waveform  $w_B(t)$  is independent of  $B$ . From Eq. 2.165 we can write the normalized ACR of  $w_B(t)$  as  $R(\theta) = R_{w_B}(\theta) = \frac{\int_{-\infty}^{+\infty} w_B(t)w_B(t-\theta)dt}{\int_{-\infty}^{+\infty} w_B^2(t)dt} = \frac{\int_{-\infty}^{+\infty} w(t')w(t'-\theta')dt'}{\int_{-\infty}^{+\infty} w^2(t')dt'} = R_w(\theta')$ ,  $\theta' = B\theta$ , and the MQBW Eq. 2.115 as  $\beta_s^2 = -\frac{\ddot{R}_s(0)}{E_s} = -\ddot{R}(0) = -\frac{d^2 R_{w_B}(\theta)}{d\theta^2}|_{\theta=0} = -B^2 \frac{d^2 R_w(\theta')}{d\theta'^2}|_{\theta'=0} = -B^2 \ddot{R}_w(0)$ , so Eq. 2.145 becomes independent of  $B$  because  $G_{as,c} = \frac{8(\alpha_{as}-1)}{\pi^2}$  is independent of  $B$  and  $G(\rho, b_c) = \rho Q(\sqrt{\frac{\rho}{2}[1-R(b_c)]}) = \rho Q(\sqrt{\frac{\rho}{2}[1-R_w(b'_c)]})$  with  $b'_c = Bb_c = B\frac{\pi}{4\beta_s} = \frac{\pi}{4\sqrt{-\ddot{R}_w(0)}}$  is independent of  $B$ .

Let us now prove that the begin-ambiguity threshold Eq. 2.151 of the modulated waveform  $w_{B,f_c}(t)$  is independent of  $B$  and  $f_c$ . The normalized ACR envelope  $e_R(\theta)$  and the EMQBW  $\beta_e^2$  of  $w_{B,f_c}(t)$  can be written from Eq. 2.166 as the normalized ACR and the MQBW of the envelope  $w_B(t)$  of  $w_{B,f_c}(t)$  derived above:  $e_R(\theta) = R_{w_B}(\theta) = R_w(\theta')$ ,  $\theta' = B\theta$ ,  $\beta_e^2 = -B^2 \ddot{R}_w(0)$ , so Eq. 2.151 becomes independent of  $B$  and  $f_c$  because  $G_{am1,o} = \frac{8\alpha_{am1}}{\pi^2}$  is independent of  $B$  and  $f_c$ , and  $G_e(\rho, b_{am1,o}) = \rho Q(\sqrt{\frac{\rho}{2}[1-e_R(b_{am1,o})]}) = \rho Q(\sqrt{\frac{\rho}{2}[1-R_w(b'_{am1,o})]})$  with  $b'_{am1,o} = Bb_{am1,o} = B\frac{\pi}{4\beta_e} = \frac{\pi}{4\sqrt{-\ddot{R}_w(0)}}$  is independent of  $B$  and  $f_c$ .

Let us prove that the end-ambiguity Eq. 2.147 and asymptotic Eq. 2.148 thresholds of the modulated waveform  $w_{B,f_c}(t)$  are only function of the IFBW  $\lambda$  Eq. 2.141. Using Eq. 2.153 we can write  $G(\rho, b_o)$  in Eq. 2.147 and Eq. 2.148 as  $G(\rho, b_o) \approx \rho Q(\sqrt{\frac{\rho}{2}[1-e_R(b_o)]}) = \rho Q(\sqrt{\frac{\rho}{2}[1-R_w(b'_o)]})$  with  $b'_o = Bb_o = \frac{B}{f_c} = \frac{1}{\lambda}$  (only function of  $\lambda$ ). On the other hand we have  $G_{am2,o} = \frac{\alpha_{am2} f_c^2}{2\beta_e^2} = -\frac{\alpha_{am2} f_c^2}{2B^2 \ddot{R}_w(0)} = -\frac{\alpha_{am2} \lambda^2}{2\ddot{R}_w(0)}$  (only function of  $\lambda$ ) and  $G_{as,o} = \frac{\alpha_{as}-1}{8\pi^2}$  (independent of  $B$  and  $f_c$ ). Whence, Eq. 2.147 and Eq. 2.148 are only functions of  $\lambda$ .

Note that thanks to the latter proved properties we can express the end-ambiguity and asymptotic thresholds with respect to the IFBW  $\lambda$  but we omit it as we have provided many details.

In Sec. 2.2.3 we show and discuss some numerical results about the thresholds for both modulated and unmodulated Gaussian pulses.

### 2.2.3 Numerical results on thresholds

In this subsection we show and discuss some numerical results about the thresholds for both modulated  $s(t)$  and unmodulated  $e_s(t)$  Gaussian pulses. We can write  $s(t)$  and  $e_s(t)$  as:

$$s(t) = e_s(t) \cos(2\pi f_c t) \quad (2.167)$$

$$e_s(t) \propto e^{-2\pi \frac{t^2}{T_w^2}} \quad (2.168)$$

where  $e_s(t)$  is the envelope of  $s(t)$  with respect to  $f_c$ . The bandwidth  $B$  at -10 dB and the EMQBW  $\beta_e^2$  Eq. 2.115 [22] are given by:

$$B = 2\sqrt{\frac{\ln 10}{\pi}} \frac{1}{T_w} \quad (2.169)$$

$$\beta_e^2 = 2\pi \frac{1}{T_w^2} \quad (2.170)$$

The results about the unmodulated pulses are given in Sec. 2.2.3.1 and those about the modulated ones in Sec. 2.2.3.2.

#### 2.2.3.1 *A priori and asymptotic thresholds of unmodulated waveforms with respect to the ATBW*

In this paragraph we consider an unmodulated Gaussian pulse  $s(t) = e_s(t)$  Eq. 2.168 with variable pulse width  $T_w$  and fixed *a priori* domain  $D_\Theta = [-2, 2]$  ns, and compute the *a priori* and asymptotic thresholds with respect to the ATBW  $\gamma$  Eq. 2.140 feature.

In Fig. 2.9(a), we show the CRLB  $c$  Eq. 2.111, the maximum MSE  $e_U$  Eq. 2.113, and the MSE approximation  $e_{1,1,c}$  Eq. 2.132 with respect to the SNR  $\rho$  and the pulse width  $T_w$ . We can see that  $e_{1,1,c}$  converges from  $e_U$  to  $c$  smoothly for large  $T_w$  and promptly for small  $T_w$ .

In Fig. 2.9(b), we show the *a priori* threshold  $\rho_{pr,1,1,c}$  (obtained from Eq. 2.136 using  $e_{1,1,c}$ ), the asymptotic thresholds  $\rho_{as,1,1,c}$ ,  $\rho_{as,3,1,c}$  and  $\rho_{as,z}$  (obtained from Eq. 2.139 using  $e_{1,1,c}$ ,  $e_{3,1,c}$  Eq. 2.132 and  $z_0$  Eq. 2.133 respectively), and the asymptotic threshold  $\rho_{as,c}$  (obtained from the analytic expression in Eq. 2.161) with respect to the ATBW  $\gamma$  Eq. 2.140.

We can see that  $\rho_{as,1,1,c}$ ,  $\rho_{as,3,1,c}$ ,  $\rho_{as,z}$  and  $\rho_{as,c}$  are all almost constant ( $\rho_{as,1,1,c} \approx \rho_{as,3,1,c} = 17$  dB,  $\rho_{as,z} \approx 16.5$  dB and  $\rho_{as,c} = 18.5$  dB). We have already proved in Sec. 2.2.2 that the asymptotic threshold is independent of the bandwidth  $B$  for an unmodulated pulse (inversely proportional to the pulse width  $T_w$ , see Eq. 2.169) if the type (e.g. Gaussian, cardinal sine, raised cosine with constant roll-off, etc.) of the used pulse does not change. In this special case of non-oscillating ACR, we can see that the asymptotic threshold obtained from the approximate ZZLB Eq. 2.133 is the closest to the asymptotic threshold obtained by simulation (equal to 16 dB, see Fig. 2.7(a) in Sec. 2.1.6.1).

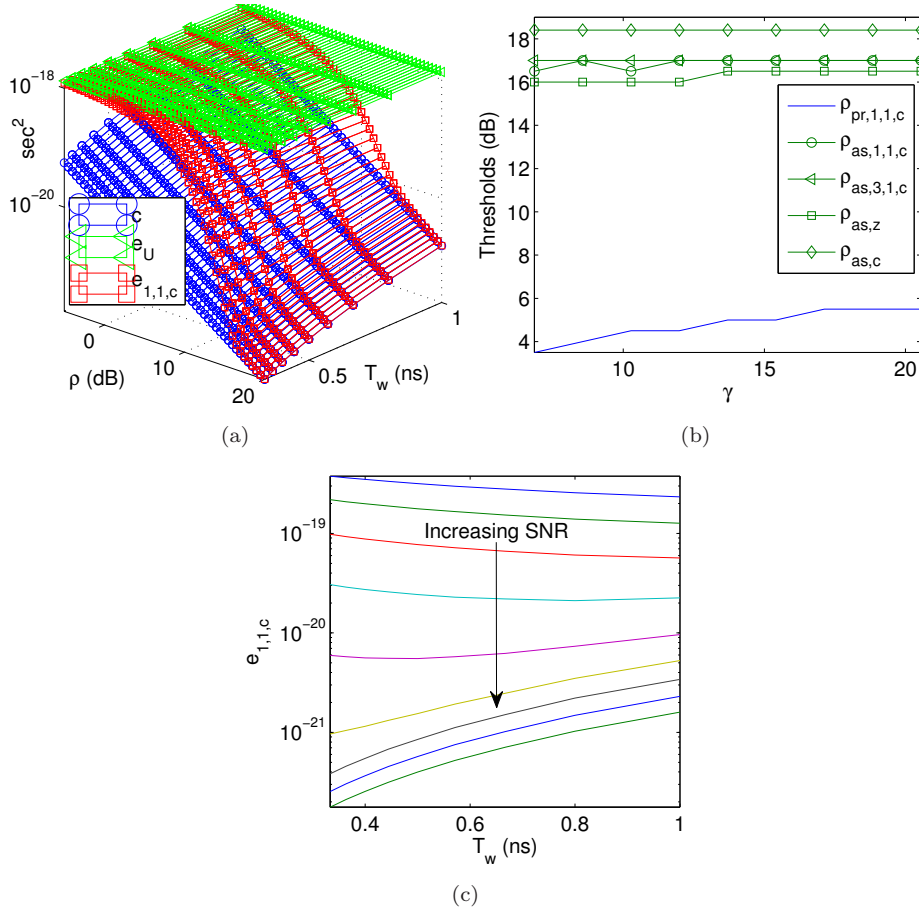


Fig. 2.9.: (a) CRLB  $c$ , maximum MSE  $e_U$  and MSE approximation  $e_{1,1,c}$  with respect to the SNR  $\rho$  and the pulse width  $T_w$  (b) *A priori* and asymptotic thresholds with respect to the ATBW  $\gamma$  (c)  $e_{1,1,c}$  with respect to  $T_w$  for  $\rho = 8 : 1.5 : 20$  dB (unmodulated Gaussian pulse with variable  $T_w$  and fixed  $D_\Theta$ ).

In Fig. 2.9(c), we show  $e_{1,1,c}$  with respect to the pulse width  $T_w$  for different values of the SNR ( $\rho = 8 : 1.5 : 20$  dB). We can see that for relatively low SNR ( $\rho \leq 14$  dB) the achieved MSE is approximately constant, whereas for relatively high SNR ( $\rho \geq 15.5$  dB) it decreases as the pulse width  $T_w$  decreases (resp. the bandwidth  $B$  increases). It becomes proportional to  $T_w^2$  (resp. inversely proportional to  $B^2$ ) when the CRLB  $c$  is achieved (i.e. above the asymptotic threshold) because  $c$  Eq. 2.111 is inversely proportional to  $\beta_s^2$  which is in turn inversely proportional to  $T_w^2$  for unmodulated pulses (see Eq. 2.170). It follows that with unmodulated pulses, we cannot (resp. can) improve the estimation

performance by changing the parameters (resp. increasing the bandwidth) of the used pulse if the available SNR is below (resp. above) the asymptotic threshold.

Note that the achievable MSE and the thresholds of the SNR regions effectively depend on the parameters of the ACR. They depend on those of the transmitted signal via the parameters of the ACR (e.g. dependency on the pulse width  $T_w$  via the bandwidth  $B$ ). In fact, it is possible to design signals with different widths and shapes but with approximately the same spectral content (e.g. chirp with constant amplitude and increasing/decreasing frequency compared to a cardinal sine) so their ACRs become almost identical and approximately achieve the same MSE. This fact can be clearly observed from the derived MSE approximations and approximate upper and lower bounds based all on the ACR of the transmitted signal.

### 2.2.3.2 *A priori, begin-ambiguity, end-ambiguity and asymptotic thresholds of modulated waveforms width respect to the IFBW*

In this paragraph we consider a modulated Gaussian pulse with variable pulse width  $T_w$  and fixed  $f_c = 6.85$  GHz and  $D_\Theta = [-2, 1.5]T_w$ , and compute the *a priori*, begin-ambiguity, end-ambiguity and asymptotic thresholds with respect to the IFBW  $\lambda$  Eq. 2.141 feature. The number of the local maxima of the ACR increases, and the gap between neighboring maxima decreases, as the IFBW increases.

In Fig. 2.10(a), we show the CRLB  $c$  Eq. 2.111, the ECRLB  $c_e$  Eq. 2.112, the maximum MSE  $e_U$  Eq. 2.113, and the MSE approximation  $e_{1,1,o}$  Eq. 2.132 with respect to the SNR  $\rho$  and the pulse width  $T_w$ . We can observe that:

- The maximum MSE increases with  $T_w$  since the width of the *a priori* domain  $D_\Theta = [-2, 1.5]T_w$  is proportional to  $T_w$ .
- The ECRLB increases with  $T_w$  as it is inversely proportional to the EMQBW  $\beta_e^2$  Eq. 2.170 which is inversely proportional to  $T_w^2$ .
- The CRLB is approximately constant with respect to  $T_w$  because it is inversely proportional to the MQBW  $\beta_s^2$  Eq. 2.117 that is approximately equal to  $4\pi^2 f_c^2$  ( $f_c$  is constant in this experience).
- The ambiguity region is not observable for small  $T_w$  since  $e_{1,1,o}$  converges from  $e_U$  to  $c$  without staying long equal to  $c_e$  due to the weak oscillations in the ACR. This explains why the begin-ambiguity and end-ambiguity thresholds are very close to each other for small IFBW as can be seen in Fig. 2.10(b).
- For high  $T_w$ , the ambiguity region is easily observable. It has a triangular shape due to the gap between the begin-ambiguity and end-ambiguity thresholds that increases as the IFBW  $\lambda$  increases as can be seen in Fig. 2.10(b).

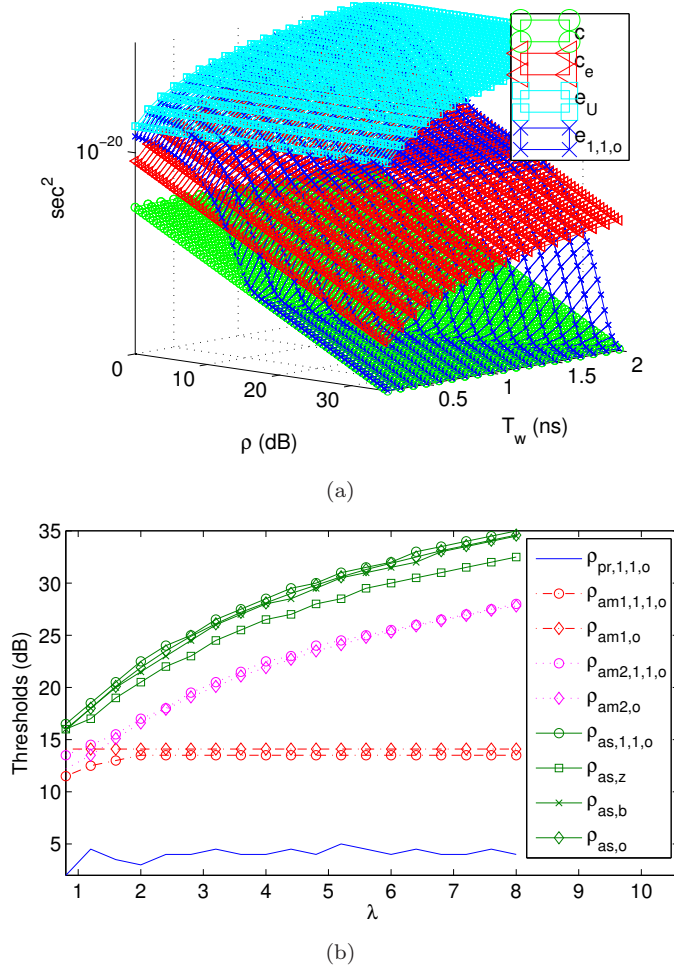


Fig. 2.10.: (a) CRLB  $c$ , ECRLB  $c_e$ , maximum MSE  $e_U$ , and MSE approximation  $e_{1,4}$  with respect to the SNR  $\rho$  and the pulse width  $T_w$  (b) *A priori*, begin-ambiguity, end-ambiguity, and asymptotic thresholds with respect to the IFBW  $\lambda$  (Gaussian pulse with variable  $T_w$  and  $D_\Theta$ , and fixed  $f_c$ ).

In Fig. 2.10(b), we show the *a priori* threshold  $\rho_{pr,1,1,o}$  (obtained from Eq. 2.136 using  $e_{1,1,o}$ ), the begin-ambiguity threshold  $\rho_{am1,1,1,o}$  (obtained from Eq. 2.137 using  $e_{1,1,o}$ ), the begin-ambiguity threshold  $\rho_{am1,o}$  (obtained from the analytic expression in Eq. 2.162), the end-ambiguity threshold  $\rho_{am2,1,1,o}$  (obtained from Eq. 2.138 using  $e_{1,1,o}$ ), the end-ambiguity threshold  $\rho_{am2,o}$  (obtained from the analytic expression in Eq. 2.163), the asymptotic thresholds  $\rho_{as,1,1,o} = \rho_{as,3,1,o}$ ,  $\rho_{as,z}$  and  $\rho_{as,b}$  (obtained from Eq. 2.139 using  $e_{1,1,o}$ ,  $z_0$

Eq. 2.133 and  $b_0$  Eq. 2.134 respectively), and the asymptotic threshold  $\rho_{as,o}$  (obtained from the analytic expression in Eq. 2.164) with respect to the IFBW  $\lambda$  Eq. 2.141. We can observe that:

- Both the *a priori* and begin-ambiguity thresholds are approximately constant. In fact, we have already seen in Sec. 2.1 that a modulated signal achieves below its end-ambiguity threshold the same MSE as its envelope. Therefore, the *a priori* and begin-ambiguity thresholds of the modulated signal are approximately equal to the *a priori* and asymptotic threshold of its envelope. Furthermore, the *a priori* threshold of an unmodulated Gaussian pulse (envelope of the modulated pulse under study) is function of the ATBW Eq. 2.140 (which is now constant), and its asymptotic threshold is constant as proved in Sec. 2.2.2 and observed in Sec. 2.2.3.1. This explains why the *a priori* and begin-ambiguity thresholds should be constant here.
- Both the end-ambiguity and asymptotic thresholds increase as the IFBW increases. In fact, by increasing the IFBW we reduce the gap between the global and the local maxima of the ACR so it can be crossed by a relatively low noise. Therefore, a higher SNR is required to guarantee that all ML estimates will only fall around the global maximum.
- The gap between the end-ambiguity and asymptotic thresholds increases as the IFBW increases. This might be due to the gap between the CRLB and ECRLB that increases with the IFBW.
- The begin-ambiguity, end-ambiguity and asymptotic thresholds  $\rho_{am1,o}$ ,  $\rho_{am2,o}$  and  $\rho_{as,o}$  obtained from the analytic expressions in Eq. 2.162, Eq. 2.163 and Eq. 2.164 are very close to the corresponding thresholds  $\rho_{am1,1,1,o}$ ,  $\rho_{am2,1,1,o}$  and  $\rho_{as,1,1,o}$  obtained from Eq. 2.137, Eq. 2.138 and Eq. 2.139 using  $e_{1,1,o}$  Eq. 2.132. The thresholds  $\rho_{am1,1,1,o}$ ,  $\rho_{am2,1,1,o}$  and  $\rho_{as,1,1,o}$  are computed with respect to the IFBW by fixing the carrier  $f_c$  and varying the pulse width  $T_w$ , whereas  $\rho_{am1,o}$  is directly obtained from its expression by considering an unmodulated Gaussian pulse with an arbitrary value of  $T_w$ , and  $\rho_{am2,o}$  and  $\rho_{as,o}$  are directly from their expressions as well by considering the same unmodulated pulse used for  $\rho_{am1,o}$  and by varying the value of  $f_c$  (in the expressions of the thresholds) according to the value of the IFBW  $\lambda$ . The obtained results validate the obtained expressions of the thresholds, as well as the proved fact, that the begin-ambiguity threshold is constant for a constant envelope shape, and that the end-ambiguity and asymptotic thresholds are functions of the IFBW.
- The asymptotic threshold  $\rho_{as,1,1,o}$  is very close to that obtained from the approximate BTLB  $b_0$  Eq. 2.134, and a bit far from that obtained from the approximate ZZLB  $z_0$  Eq. 2.133. We did not compute the begin-ambiguity and end-ambiguity thresholds using the approximate ZZLB and BTLB because we have seen in Sec. 2.1 that they roughly detect the ambiguity

region, unlike the asymptotic region that they can accurately detect (see Fig. 2.8(c)).

Thanks to Fig. 2.10(b), we can predict the value of the achievable MSE based on the values of the available SNR and IFBW  $(\rho, \lambda)$ . It is approximately equal to the maximum MSE if  $(\rho, \lambda)$  falls in the *a priori* region (below the *a priori* threshold curve), between the maximum MSE and the ECRLB if  $(\rho, \lambda)$  falls in the *a priori* ambiguity transition region (between the *a priori* and begin-ambiguity threshold curves), approximately equal to the ECRLB if  $(\rho, \lambda)$  falls in the ambiguity region (between the begin-ambiguity and end-ambiguity threshold curves), between the ECRLB and the CRLB if  $(\rho, \lambda)$  falls in the ambiguity asymptotic transition region (between the end-ambiguity and asymptotic threshold curves), and approximately equal to CRLB if  $(\rho, \lambda)$  falls in the asymptotic region (above the asymptotic threshold curve).

To summarize we can say that:

- The *a priori* threshold depends on both the shape of the envelope of the ACR and the *a priori* domain.
- The begin-ambiguity threshold only depends on the shape of the envelope of the ACR function regardless any other parameter like the bandwidth. This shape is sometimes described by a parameter like the roll-off for raised cosine waveforms.
- The end-ambiguity and asymptotic thresholds only depend on the shape of the ACR function, or on any set of parameters describing this shape like the shape of the envelope and the IFBW together. They do not depend on any other parameter like the bandwidth and the mean frequency separately.

### 2.3 SIGNAL DESIGN FOR MINIMUM MSE ON TOA ESTIMATION

We have seen in Sec. 2.2.2 and Sec. 2.2.3 that the achievable MSE depends on the available SNR and some parameters of the transmitted signal. It has been shown that according to the IFBW of the transmitted waveform, the MSE achieved by a given SNR can be equal to the CRLB, the ECRLB, the maximum MSE, or an in-between value. In this section we investigate the design of the transmitted signal with respect to the available SNR in order to minimize the achievable MSE.

We assume that the transmitted signal is a modulated Gaussian pulse Eq. 2.167. Our goal is to find the optimal values  $T_{w,0}$  and  $f_{c,0}$  of the pulse width  $T_w$  and the carrier  $f_c$  that minimize the achievable MSE given that the available SNR  $\rho$  is equal to  $\rho_0$ .

We consider two constraints about the spectrum of the transmitted pulse. The first constraint says that the spectrum of the transmitted pulse should fall in a

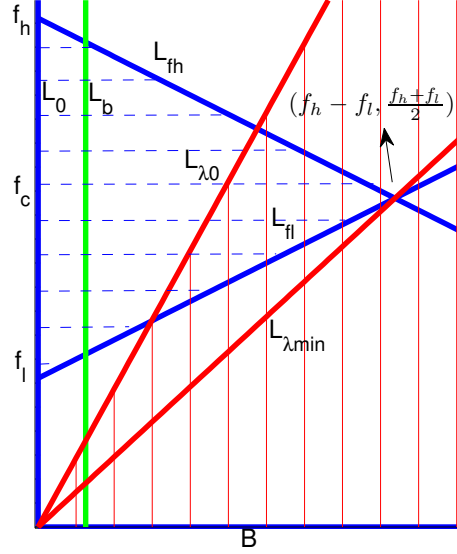


Fig. 2.11.: Feasible regions corresponding to the constraints  $C_1$  Eq. 2.171 (region with horizontal dashed bars) and  $C_2$  Eq. 2.183 (region with vertical solid bars).

given available frequency band, whereas the second one says that the spectrum should fall in the available band, and it should also have a given bandwidth. The optimization problem with respect to the first constraint is considered in Sec. 2.3.1 and the problem with respect to the second constraint in Sec. 2.3.2.

### 2.3.1 Waveform with spectrum falling in a given frequency band

In this subsection we consider the constraint that the spectrum of the transmitted pulse should fall into the frequency band  $[f_l, f_h]$ . This constraint can be written as:

$$C_1 : \begin{cases} f_c, B > 0 \\ f_c - \frac{B}{2} \geq f_l \\ f_c + \frac{B}{2} \leq f_h. \end{cases} \quad (2.171)$$

In our numerical examples we consider the FCC [1] UWB band  $[f_l, f_h] = [3.1, 10.6]$  GHz. We can formulate our optimization problem as:

$$(B_0, f_{c,0}) = \underset{(B, f_c)}{\operatorname{argmin}} \{e\} \text{ s.t. } \rho = \rho_0, C_1 \quad (2.172)$$

where  $e$  is the achievable MSE. The optimal pulse width  $T_{w,0}$  can be obtained from the optimal bandwidth  $B_0$  using Eq. 2.169. As we can see in Fig. 2.11, the feasible region corresponding to constraint  $C_1$  Eq. 2.171 is a triangular region (region with horizontal dashed bars) in the space of  $(B, f_c)$  limited by the three

lines:

$$L_0 : B = 0 \quad (2.173)$$

$$L_{f_l} : f_c = f_l + \frac{B}{2} \quad (2.174)$$

$$L_{f_h} : f_c = f_h - \frac{B}{2}. \quad (2.175)$$

Obviously, the maximum available bandwidth is:

$$B_{\max} = f_h - f_l \quad (2.176)$$

where  $B_{\max} = 7.5$  GHz for the FCC UWB band.

For a given bandwidth  $B = b$ , the minimal IFBW is given by:

$$\lambda_{b,\min} = \frac{f_l}{b} + \frac{1}{2} \quad (2.177)$$

and corresponds to the point of intersection

$$L_b \cap L_{f_l} = (b, f_l + \frac{b}{2}) \quad (2.178)$$

of the lines  $L_{f_l}$  Eq. 2.174 and

$$L_b : B = b. \quad (2.179)$$

It follows that, the minimal IFBW in the feasible region of  $C_1$  Eq. 2.171 is equal to:

$$\lambda_{\min} = \frac{f_l}{f_h - f_l} + \frac{1}{2} \quad (2.180)$$

and corresponds to the point  $(f_h - f_l, \frac{f_l + f_h}{2})$ . We have  $\lambda_{\min} = 0.913$  for the FCC UWB band.

Let us now consider the minimization of the achievable MSE. According to the value of the available SNR  $\rho_0$ , four cases can be distinguished:

1.  $\rho_0$  is lower than or equal to the *a priori* threshold.
2.  $\rho_0$  is between the *a priori* and the begin-ambiguity thresholds.
3.  $\rho_0$  is close to the begin-ambiguity threshold
4.  $\rho_0$  is larger than the begin-ambiguity threshold.

Consider first the case  $\rho_0 \leq \rho_{pr}$  where the available SNR is lower than or equal to the *a priori* threshold. Obviously, the maximum MSE is achieved in this case and nothing can be done to improve the estimation which is useless.

Consider now the second case where the available SNR is between the *a priori* and begin-ambiguity thresholds ( $\rho_{pr} < \rho_0 < \rho_{am1}$ ). We have already seen

that both the modulated signal and its envelope approximately achieve the same MSE below the begin-ambiguity threshold of the modulated signal (approximately equal to the asymptotic threshold of the envelope), and we have seen in Fig. 2.9(c) that below the asymptotic threshold of the envelope the achieved MSE is approximately constant and independent of the pulse width and the bandwidth. In result, nothing can be done to reduce the MSE when  $\rho_{pr} < \rho_0 < \rho_{am1}$ .

Consider the third case where the available SNR is close to the begin-ambiguity threshold ( $\rho_0 \approx \rho_{am1}$ ). As the ECRLB  $c_e$  Eq. 2.112 is approximately achieved in this case, we can minimize the achievable MSE by maximizing the bandwidth  $B$  (i.e. minimizing the pulse width  $T_w$ , see Eq. 2.169) so the EMQBW  $\beta_e^2$  Eq. 2.112 is maximized and  $c_e$  (inversely proportional to  $\beta_e^2$ ) is minimized. We have already seen in Fig. 2.9(c) that the achieved MSE becomes proportional to the squared pulse width  $T_w^2$  when the SNR is approximately equal to the begin-ambiguity threshold. Accordingly, the optimal solution when  $\rho_0 \approx \rho_{am1}$  and the corresponding achievable MSE are given by:

$$(B_0, f_{c,0}) = (f_h - f_l, \frac{f_l + f_h}{2}) \quad (2.181)$$

$$e_0 \approx \frac{1}{\rho_0 \beta_{e,0}^2} = \frac{T_{w,0}^2}{2\pi \rho_0} = \frac{2 \ln 10}{\pi^2 B_0^2 \rho_0} \quad (2.182)$$

where Eq. 2.182 is obtained using Eq. 2.169 and Eq. 2.170. Note that  $f_h - f_l$  is equal to the maximum bandwidth  $B_{\max}$  Eq. 2.176. As  $\rho_{am1} \approx 14$  dB as can be seen in Fig. 2.10(b), we have  $e_0 \approx 330.24$  ps<sup>2</sup> for the FCC band ( $B_0 = 7.5$  GHz).

Consider now the last case where the available SNR is larger than the begin-ambiguity threshold ( $\rho_0 > \rho_{am1}$ ). As we can see in Fig. 2.10(b), the point  $(\rho_0, \lambda)$  will fall, according to the value of the IFBW  $\lambda$ , in the ambiguity region, the ambiguity-asymptotic transition region, or the asymptotic region. Therefore, the achievable MSE is equal to the ECRLB  $c_e$ , between the ECRLB and the CRLB  $c$ , or equal to the CRLB. Now, in order to find the optimal bandwidth  $B_0$  and carrier  $f_{c,0}$  we proceed as follows:

1. We pick from Fig. 2.10(b) the value  $\lambda_0$  of the IFBW  $\lambda$  for which the available SNR  $\rho_0$  belongs to the asymptotic threshold curve. Note that it is possible to express  $\lambda_0$  with respect to  $\rho_0$ , but this is omitted for the sake of conciseness.
2. In order to guarantee that the CRLB is achieved, we consider the constraint that  $\lambda$  is lower than or equal to the picked  $\lambda_0$ . If this constraint cannot be satisfied because  $\rho_0$  is lower than the minimal IFBW  $\lambda_{\min}$  Eq. 2.180 in the feasible region of constraint  $C_1$  Eq. 2.171, then the CRLB cannot be achieved. In order to make the achievable MSE the closest possible to the CRLB, we set  $\lambda$  at the minimal IFBW  $\lambda_{\min}$ . This constraint can be expressed as:

$$C_2 : \begin{cases} \lambda = \frac{f_c}{B} = \lambda_{\min} & \text{if } \lambda_0 < \lambda_{\min} \\ \lambda = \frac{f_c}{B} \leq \lambda_0 & \text{if } \lambda_0 \geq \lambda_{\min} \end{cases} \quad (2.183)$$

3. Now, given that the estimator achieves the CRLB or a MSE that is the closest possible to the CRLB thanks to the previous step, we minimize the achievable MSE by minimizing the CRLB itself.

Following the last step, we can write from Eq. 2.171 and Eq. 2.183 the minimization problem in Eq. 2.172 as:

$$(B_0, f_{c,0}) = \underset{(B, f_c)}{\operatorname{argmin}} \{c\} \text{ s.t. } C_1, C_2. \quad (2.184)$$

As  $c$  can be approximated from Eq. 2.111 and Eq. 2.117 by:

$$c = \frac{1}{\rho\beta_s^2} = \frac{1}{\rho(\beta_e^2 + 4\pi^2 f_c^2)} \approx \frac{1}{\rho 4\pi^2 f_c^2} \quad (2.185)$$

we can rewrite the minimization problem in Eq. 2.184 as:

$$(B_0, f_{c,0}) = \underset{(B, f_c)}{\operatorname{argmax}} \{f_c\} \text{ s.t. } C_1, C_2. \quad (2.186)$$

As shown in Fig. 2.11, the feasible region of constraint  $C_2$  Eq. 2.183 is the half-space (region with vertical solid bars) below the line:

$$L_{\lambda_0} : f_c = \lambda_0 B. \quad (2.187)$$

We have already seen that the feasible region of constraint  $C_1$  Eq. 2.171 is the triangle limited by the lines  $L_0$ ,  $L_{f_l}$  and  $L_{f_h}$ . Therefore, the feasible region of  $C_1$  and  $C_2$  together is the triangular region limited by  $L_{f_l}$ ,  $L_{f_h}$  and  $L_{\lambda_0}$  (region with both vertical and horizontal bars). Consequently, the solution of the maximization problem in Eq. 2.186 corresponds to the point of intersection  $(\frac{2}{2\lambda_0+1}f_h, \frac{2\lambda_0}{2\lambda_0+1}f_h)$  of the lines  $L_{f_h}$  and  $L_{\lambda_0}$  as can easily be seen from Fig. 2.11. In the special case where  $\lambda_0 < \lambda_{\min}$ , the feasible region of  $C_2$  reduces to the line  $L_{\lambda_{\min}} : f_c = \lambda_{\min}B$  so the feasible region of  $C_1$  and  $C_2$  reduces to the point  $(f_h - f_l, \frac{f_l+f_h}{2})$  which is consequently the solution of Eq. 2.186.

Finally, the solution for  $\rho_0 > \rho_{am1}$  and the corresponding achievable MSE are given by:

$$\begin{cases} (B_0, f_{c,0}) = (f_h - f_l, \frac{f_l+f_h}{2}) \\ e_0 \in (\frac{2\ln 10}{\pi^2 B_0^2 \rho_0}, e_{0,1}); e_{0,1} < \frac{1}{4\pi^2 f_{c,0}^2 \rho_0} & \text{if } \lambda_0 < \lambda_{\min} \\ (B_0, f_{c,0}) = (\frac{2}{2\lambda_0+1}f_h, \frac{2\lambda_0}{2\lambda_0+1}f_h) \\ e_0 = \frac{1}{4\pi^2 f_{c,0}^2 \rho_0} & \text{if } \lambda_0 \geq \lambda_{\min} \end{cases} \quad (2.188)$$

where the term  $\frac{2\ln 10}{\pi^2 B_0^2 \rho_0}$  is the achievable MSE Eq. 2.182 when  $\rho_0 \approx \rho_{am1}$ .

The solution given in Eq. 2.188 for  $\lambda_0 \geq \lambda_{\min}$  is suboptimal. As a matter of fact:

- The minimum MSE is not reached in the asymptotic region but at the end of the end-ambiguity asymptotic transition region but slightly below the asymptotic region.

- The asymptotic threshold is defined as the SNR when the MSE becomes equal to  $\alpha_{as} = 1.1$  times the CRLB.
- The asymptotic threshold is obtained from a MSE approximation or approximate bound.
- We have neglected the term  $\beta_e^2$  in the expression of the CRLB in Eq. 2.185 used to formulate Eq. 2.186.

Even though, the obtained solution is approximately equal to the optimal one as we will see below in Fig. 2.12(a), Fig. 2.12(b) and Fig. 2.12(c). The main two advantages of the proposed method is that it is highly accurate and very easy to compute. It can directly be found from the curve of the asymptotic threshold with respect to the IFBW. To find the optimal solution we should perform an exhaustive search in the feasible region using the true achievable MSE. The latter method is however much more complicated than our proposal. Furthermore, as we do not know the expression of the true MSE, the exhaustive search should be performed using a MSE approximation or an approximate bound.

Denote by  $(B_1, f_{c,1})$  the point minimizing the MSE approximation  $e_{1,1,o}$  in the feasible region of  $C_1$  Eq. 2.171,  $e_1$  the minimal  $e_{1,1,o}$ , and  $\lambda_1$  the corresponding IFBW. The feasible region is swept using an increment of 0.2 GHz for the bandwidth  $B$  and 0.1 GHz for the carrier  $f_c$ .

In Fig. 2.12(a) we show  $\lambda_0$  (obtained from the suboptimal method) and  $\lambda_1$  with respect to the available SNR  $\rho_0$ . We can see that  $\lambda_1$  is a bit smaller than  $\lambda_0$ . This is due to the factor  $\alpha_{as} = 1.1$  in the definition of the asymptotic threshold in Eq. 2.139.

In Fig. 2.12(b) we show  $B_0$  and  $f_{c,0}$  (bandwidth and carrier obtained from the suboptimal method), and  $B_1$  and  $f_{c,1}$  (obtained from the exhaustive search) with respect to  $\rho_0$ . We can see that  $B_0$  is very close to  $B_1$ , and  $f_{c,0}$  to  $f_{c,1}$  which validates that the suboptimal solution  $(B_0, f_{c,0})$  is very close to the optimal one. We can also see that  $B_1$  (resp.  $f_{c,1}$ ) is a bit larger (resp. lower) than  $B_0$  (resp.  $f_{c,0}$ ). In fact,  $\rho_1 \lesssim \rho_0$  as already seen from Fig. 2.12(a).

In Fig. 2.12(c) we show  $e_0$  (minimum MSE obtained by the suboptimal method) and  $e_1$  (obtained from the exhaustive search) with respect to  $\rho_0$ . We can see that  $e_0$  and  $e_1$  are very close to each other. For  $\rho_0 = 22$  dB, we have  $\lambda_0 = 1.9$  and  $\lambda_1 = 1.8$ ,  $(B_0, f_{c,0}) = (4.42, 8.39)$  GHz and  $(B_1, f_{c,1}) = (4.6, 8.3)$  GHz, and  $e_0 = 2.27$  ps<sup>2</sup> and  $e_1 = 2.32$  ps<sup>2</sup>.

To summarize, we can say that:

- For an available SNR lower than the begin-ambiguity threshold ( $\rho_0 < \rho_{am1}$ ), nothing can be done to improve the estimation.
- For an available SNR approximately equal to the begin-ambiguity threshold ( $\rho_0 \approx \rho_{am1}$ ) the optimal solution given in Eq. 2.181 consists on using the

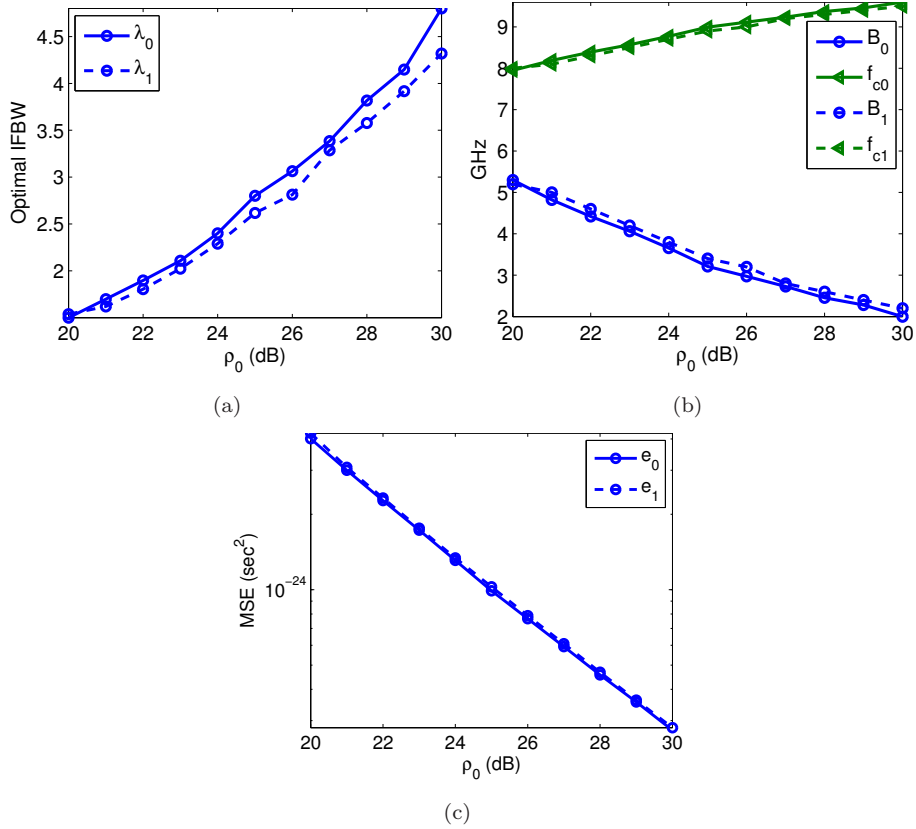


Fig. 2.12.: (a) Suboptimal  $\lambda_0$  and optimal  $\lambda_1$  IFBW with respect to the available SNR  $\rho_0$  (b) Suboptimal ( $B_0, f_{c,0}$ ) and optimal ( $B_1, f_{c,1}$ ) bandwidth and carrier frequency with respect to  $\rho_0$  (c) Suboptimal  $e_0$  and optimal  $e_1$  MSE with respect to  $\rho_0$ .

total available band. The achievable MSE in this case is approximately equal to the ECRLB Eq. 2.182.

- For an available SNR greater than the begin-ambiguity threshold ( $\rho_0 > \rho_{am1}$ ) with  $\lambda_0 \geq \lambda_{\min}$ , the suboptimal solution given in Eq. 2.188 varies with  $\rho_0$ . The achievable MSE in this case is approximately equal to the CRLB.
- For an available SNR greater than the begin-ambiguity threshold ( $\rho_0 > \rho_{am1}$ ) with  $\lambda_0 < \lambda_{\min}$ , the optimal solution given in Eq. 2.188 consists on using the total available band. The achievable MSE in this case lies

between the ECRLB Eq. 2.182 achievable for  $\rho_0 \approx \rho_{am1}$ , and the CRLB achievable for  $\rho_0 > \rho_{am1}$  and  $\lambda_0 \geq \lambda_{\min}$ .

In practice, we do not need to compute the suboptimal bandwidth  $B_0$  and carrier  $f_{c,0}$  in real time. It suffices to compute them once for all possible values of the available SNR, then during the communication we measure the SNR, pick the corresponding  $B_0$  and  $f_{c,0}$ , and tune the spectrum of the transmitted signal to meet the suboptimal band.

### 2.3.2 Waveform with spectrum falling in a given frequency band and having a given bandwidth

In this subsection we consider the constraint that the spectrum of the transmitted pulse has a given bandwidth  $B = b$ , and falls in the frequency band  $[f_l, f_h]$ .

The feasible region corresponding to the constraints  $C_1$  Eq. 2.171 and:

$$C_3 : B = b \quad (2.189)$$

is the segment of the line  $L_b$  Eq. 2.179 limited by the lines  $L_{f_l}$  Eq. 2.174 and  $L_{f_h}$  Eq. 2.175. We can see from Fig. 2.11 that in this feasible region, the IFBW  $\lambda$  belongs to the interval  $[\lambda_{b,\min}, \lambda_{b,\max}]$  where  $\lambda_{b,\min}$  is given in Eq. 2.177 and corresponds to the intersection  $L_b \cap L_{f_l}$  Eq. 2.178 of the lines  $L_b$  and  $L_{f_l}$ , and  $\lambda_{b,\max}$  is given by:

$$\lambda_{b,\max} = \frac{f_h}{b} - \frac{1}{2} \quad (2.190)$$

and corresponds to the intersection

$$L_b \cap L_{f_h} = (b, f_h - \frac{b}{2}) \quad (2.191)$$

of the lines  $L_b$  and  $L_{f_h}$ .

As the available SNR should fall in the asymptotic region in order to minimize the MSE, we can write the following constraint similarly to  $C_2$  Eq. 2.183:

$$C_4 : \begin{cases} \lambda = \frac{f_c}{B} = \lambda_{b,\min} & \text{if } \lambda_0 < \lambda_{b,\min} \\ \lambda = \frac{f_c}{B} \leq \lambda_0 & \text{if } \lambda_{b,\min} \leq \lambda_0 \leq \lambda_{b,\max} \\ \lambda = \frac{f_c}{B} = \lambda_{b,\max} & \text{if } \lambda_0 > \lambda_{b,\max}. \end{cases} \quad (2.192)$$

Similarly to Eq. 2.186 we formulate our optimization problem as:

$$(B_0, f_{c,0}) = \underset{(B, f_c)}{\operatorname{argmax}} \{f_c\} \text{ s.t. } C_1, C_3, C_4. \quad (2.193)$$

Obviously, the solution of Eq. 2.193 is  $L_b \cap L_{f_l}$  Eq. 2.178 for  $\lambda_0 < \lambda_{b,\min}$ ,  $L_b \cap L_{f_h}$  Eq. 2.191 for  $\lambda_0 > \lambda_{b,\max}$ , and the intersection:

$$L_b \cap L_{\lambda_0} = (b, \lambda_0 b) \quad (2.194)$$

of the lines  $L_b$  and  $L_{\lambda_0}$ .

Finally, we can write the solution of our optimization problem and the corresponding achievable MSE as:

$$\left\{ \begin{array}{l} (B_0, f_{c,0}) = (b, f_l + \frac{b}{2}) \\ e_0 > \frac{1}{4\pi^2 f_{c,0}^2 \rho_0} \end{array} \right. \quad \text{if } \lambda_0 < \lambda_{b,\min}$$

$$\left\{ \begin{array}{l} (B_0, f_{c,0}) = (b, \lambda_0 b) \\ e_0 = \frac{1}{4\pi^2 f_{c,0}^2 \rho_0} \end{array} \right. \quad \text{if } \lambda_{b,\min} \leq \lambda_0 \leq \lambda_{b,\max} \quad (2.195)$$

$$\left\{ \begin{array}{l} (B_0, f_{c,0}) = (b, f_h - \frac{b}{2}) \\ e_0 = \frac{1}{4\pi^2 f_{c,0}^2 \rho_0} \end{array} \right. \quad \text{if } \lambda_0 > \lambda_{b,\max}.$$

Note that the results obtained in this section are completely different from the results that we get by minimizing the CRLB. With the latter method, the threshold and ambiguity effects are not taken into account so the optimal solution always consists on filling the available band with the maximum allowed PSD starting from the highest frequency, which is absolutely different from the method described above.

## 2.4 CONCLUSION

In this chapter, we have considered the problem of deterministic nonlinear estimation and studied the threshold and the ambiguity phenomena.

We have approximated the statistics of the MLE by splitting the *a priori* domain of the unknown parameter into subdomains, and computing the subdomain probability and the statistics of the subdomain MLE. The derived MSE approximations are highly accurate and follow closely the truly achieved MSE. We have used the subdomain probability to propose other approximations of the MLE statistics and to derive two approximate upper bounds. The MSE approximations obtained via this method are very accurate as well and the approximate upper bounds are sufficiently tight. We have used the Taylor series expansion of the noise limited to second order to get an approximate lower bound tighter than the CRLB. We have employed the principle of binary detection proposed by Ziv and Zakai to derive some approximate lower bounds for deterministic estimation. Numerical results about the derived MSE approximations and approximate upper and lower bounds are obtained by considering the problem of TOA estimation based on UWB signals.

By making use of the derived MSE approximations and approximate upper and lower bounds, we have computed the thresholds of the *a priori*, ambiguity and asymptotic regions. We have derived analytic expressions for the begin-ambiguity, end-ambiguity and asymptotic thresholds. We have shown that the *a priori* threshold depends on both the shape of the envelope of the ACR and the *a priori* domain, whereas the begin-ambiguity threshold only depends on the

shape of the envelope of the ACR. The end-ambiguity and asymptotic thresholds only depend on the shape of the ACR regardless any other parameter like the bandwidth and the carrier. We have accordingly shown that both the asymptotic threshold of unmodulated waveforms and begin-ambiguity threshold of modulated waveforms are constant for a given waveform shape (e.g. Gaussian, cardinal sine, raised cosine with constant roll-off), and that the end-ambiguity and asymptotic thresholds of modulated waveforms vary with the IFBW regardless the values of the bandwidth and the carrier separately.

We have exploited the results about the begin-ambiguity and asymptotic thresholds to design, according to the available SNR, the spectrum of the signal that achieves the minimum attainable MSE. We have proposed an optimization method that is very simple and very accurate. We have considered the constraint that the spectrum of the transmitted signal falls in a given frequency band, and the constraint that it falls in a given band and has a fixed bandwidth.



## CHAPTER 3

---

# NEW TOA ESTIMATORS: MAXIMUM DELAYING-AND-MULTIPLYING ESTIMATOR AND DFT-BASED ESTIMATORS

---

THANKS to their ultra short pulses, IR-UWB signals can serve to perform highly accurate positioning by employing the TOA technique. However, TOA estimation via IR-UWB signals suffers from the MP aspect of the channel and the effects of the MUI. While the estimation of the TOA is widely investigated in the literature for MP channels, only few works addressed this problem in MU systems (see Sec. 1.1.4 for more details about the state-of-the-art).

As already mentioned in Sec. 1.1.4, the existing TOA estimators are based on either the time-domain or the frequency-domain. Most time-domain estimators make use of the following receivers:

- CR/MF receivers.
- Energy receivers.
- Dirty-template receivers.

In this chapter we propose two new TOA estimators. The first one is considered for MU systems employing TH-IR-UWB signals and is based on the time-domain; it makes use of a new receiver, also proposed in this chapter. The second estimator, or more precisely, class of estimators, is based on the frequency-domain and can be used with any type of UWB signals; the proposed frequency-domain estimators are investigated for single-user in AWGN/MP channels.

In Sec. 3.1, we describe the new receiver that we call “delaying-and-multiplying” (DM) receiver. We derive some statistics and probabilities of error related to both, the new receiver and the CR receiver.

In Sec. 3.2, we introduce the new TOA estimator that we name “maximum delaying-and-multiplying estimator” (MME). We derive some approximations of the local MSE achieved by this estimator, and compute the asymptotic MSE. The MME is compared to the MLE. Note that in the case of single-user, the MLE is equivalent to the so-called “maximum CR estimator” (MCE) that is based on the CR receiver. The MCE consists on maximizing the CCR of the received signal and the waveform corresponding to the user of interest.

In Sec. 3.3, we propose two TOA estimators based on the phase of the DFT of the received signal. The first one relies on the relative phase, whereas the second one relies on the absolute phase. We derive the statistics of the proposed estimators and compare them to the MLE. Both the cases of AWGN and MP channels will be considered.

The main contributions in this chapter are the following:

- We propose a new receiver for TH-IR-UWB signals, compute its statistics and compare it with the CR receiver. The proposed receiver is totally different from the three receivers presented at the beginning of this chapter.
- We propose the MME, compute its local and asymptotic MSE, and compare to the MLE. We show that both estimators approximately have the same performances.
- We propose two TOA estimators for AWGN channels based on the DFT of the received signal. We compute the MSE achieved by both estimators. The first/second estimator asymptotically achieves the baseband/passband CRLB. The passband CRLB is achieved by the MLE faster than ours. Despite the case of time-domain estimators where the sampling period should be smaller than desired accuracy (which increases the number of the treated samples), only few samples (obtained at a sampling rate equal to the signal bandwidth) are required in our approach to perform the estimation. At low SNRs, the proposed estimators outperforms the MLE. We show that many improvements can be introduced to our estimators in order to make them achieving the CRLB faster.
- A two-step TOA estimator for MP channels is proposed by making use of the DFT based estimators mentioned above.
- We compute the exact statistics of the unwrapped phase of the DFT of a signal corrupted by an AWGN.

We recall that the MME is mainly proposed for MU systems; therefore, its main role is to mitigate the MUI. Optimal mitigation can be performed using the joint MLE of the TOAs of all users. As this estimator is very complex to

implement (even by using iterative algorithms like the one proposed in [48]), a simple approach (proposed in [39] for symbol detection, see Sec. 1.1.4) consists on modeling the MUI by an AWGN so the TOA of the user of interest can be estimated using the MCE. The main goal in this thesis regarding the MME, is to compare the potentials of the MME and the MCE in mitigating the MUI. As the MCE is equivalent for single-user to the MLE, we are interested in checking the asymptotic (whether the estimator achieves the CRLB), local (effects of the shape of the used pulse) and global (effects of the shape of the TH-IR-UWB waveform) performances of the MME in the case of single-user as well. Note that the performance degradation related to the shape of a given TH-IR-UWB waveform is due to the collision among the pulses of the same waveform (when an ACR is performed), whereas the degradation related to the MUI is due to the collision among the pulses of the different user waveforms (when a CCR is performed). For this reason, it seems more coherent to study the asymptotic and local performances for single-user in this chapter, and to postpone the study of the global performances for single-user and multiuser to the next chapter.

### 3.1 DELAYING-AND-MULTIPLYING RECEIVER

In this section, we introduce the DM receiver. We compute the local and global statistics and probabilities of error for both the DM and the CR receivers. As we will see later, the DM receiver consists on filtering the received signal, delaying it according to the used TH codeword, then multiplying the delayed branches.

The DM receiver will be used later in this chapter to derive the MME. The local (resp. global) statistics will be employed in this chapter (resp. the next chapter) to study the asymptotic and local (resp. global) performances of both the MME and the MCE.

In Sec. 3.1.1, we describe the considered system model. In Sec. 3.1.2, we present the DM and the CR receivers. In Sec. 3.1.3 and Sec. 3.1.4, we compute the local and global statistics and probabilities of error for both receivers.

#### 3.1.1 System model

We describe here the considered system model. The transmitted signal

$$s(t) = \sqrt{\frac{E}{N_c}} \sum_{i=0}^{N_c-1} p(t - c_i T_h) \quad (3.1)$$

consists of a TH waveform of energy  $E$  and duration  $T$ , containing  $N_c$  pulses located at  $c_i T_h$ , ( $i = 0, \dots, N_c - 1$ ) with  $T_h = \frac{T}{N_h}$  the time-hop (larger than the pulse width) and  $c = (c_i)_{i=0, \dots, N_c-1}$ ,  $c_i \in \{0, \dots, N_h - 1\}$  the considered TH codeword. Obviously, the energy of  $p(t)$  in Eq. 3.1 is normalized to one.

We can write the received signal as:

$$r(t) = \alpha s(t - \Theta) + \tilde{w}(t) \quad (3.2)$$

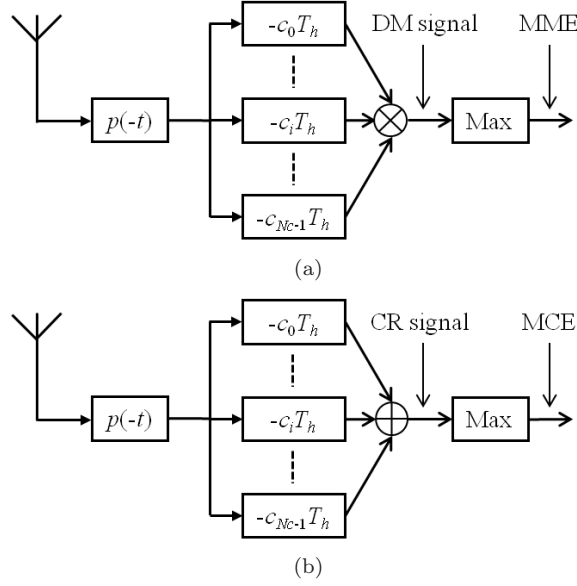


Fig. 3.1.: (a) DM receiver and MME estimator (b) CR receiver and MCE estimator.

where  $\alpha$  and  $\Theta$  denote the gain and the time delay introduced by the channel, and  $\tilde{w}(t)$  the AWGN of two-sided PSD of  $\frac{N_0}{2}$ .

### 3.1.2 CR receiver and delaying-and-multiplying receiver

We present now the DM and the CR receivers. As depicted in Fig. 3.1(a), the DM receiver consists on filtering the received signal with the filter  $p(-t)$  matched to the transmitted pulse  $p(t)$ , delaying the filtered signal by the delays  $-c_i T_h$ , ( $i = 0, \dots, N_c - 1$ ) corresponding to the different pulses of the transmitted signal, then multiplying the  $N_c$  obtained signals. The CR receiver, represented in Fig. 3.1(b) simply consists on adding the delayed signals instead of multiplying them. Denote by  $X_{r,p}(\theta)$  the received signal filtered with  $p(-t)$ , and by  $P_{r,p}(\theta)$  and  $A_{r,p}(\theta)$  the DM and the CR signals obtained at the outputs of the DM and CR receivers respectively.

By splitting the time axis into the intervals

$$I_n = \left[ nT_h + \Theta - \frac{T_h}{2}, nT_h + \Theta + \frac{T_h}{2} \right], \quad n = -\infty, \dots, +\infty \quad (3.3)$$

of equal width  $T_h$ , we can write  $X_{r,p}(\theta)$  from Eq. 3.2 as:

$$\begin{aligned} X_{r,p}(\theta) &= r(\theta) \otimes p(-\theta) = \alpha \sqrt{\frac{E}{N_c}} \sum_{i=0}^{N_c-1} R_p(\theta - \Theta - c_i T_h) + w(\theta) \\ &= \sum_{n=-\infty}^{+\infty} X_n(\theta) \end{aligned} \quad (3.4)$$

$$X_n(\theta) = R_n(\theta) + w_n(\theta) \quad (3.5)$$

$$R_n(\theta) = \begin{cases} \alpha \sqrt{\frac{E}{N_c}} R_p(\theta - \Theta - n T_h) & n \in \{c_0, \dots, c_{N_c-1}\} \\ 0 & n \notin \{c_0, \dots, c_{N_c-1}\} \end{cases} \quad (3.6)$$

$$w_n(\theta) = \begin{cases} w_n(\theta) & \theta \in I_n \\ 0 & \theta \notin I_n \end{cases} \quad (3.7)$$

where  $R_p(\theta)$  denotes the ACR of  $p(t)$ ,  $w(\theta)$  the filtered Gaussian noise of covariance

$$C_w(\theta) = \frac{N_0}{2} R_p(\theta), \quad (3.8)$$

and  $X_n(\theta)$ ,  $R_n(\theta)$  and  $w_n(\theta)$  the filtered received signal, filtered useful signal, and filtered noise in the interval  $I_n$  respectively. Obviously, each  $I_n$  contains either the sum of a pulse ACR component  $\alpha \sqrt{\frac{E}{N_c}} R_p(\theta - \Theta - n T_h)$  and a noise component  $w_n(\theta)$  (when  $n \in \{c_0, \dots, c_{N_c-1}\}$ , see Eq. 3.6), or only a noise component (when  $n \notin \{c_0, \dots, c_{N_c-1}\}$ , see Eq. 3.6). Given that  $T_h$  (equal to the width of  $I_n$ ) is larger than the width of  $p(t)$ , we can deduce from Eq. 3.8 that the noise components  $w_n(\theta)$  corresponding to different intervals are uncorrelated.

As both the DM and CR signals are obtained from  $N_c$  delayed versions of the filtered received signal  $X_{r,p}(\theta)$  containing  $N_c$  pulse ACR components  $\alpha \sqrt{\frac{E}{N_c}} R_p(\theta - \Theta - n T_h)$  corrupted by noise, the signal at the output of the DM receiver (resp. CR receiver) will contain in each interval  $I_n$  the product (resp. the sum) of  $N_n \in \{0, \dots, N_c\}$  pulse ACR components corrupted by uncorrelated noise components, and of  $N_c - N_n$  pure uncorrelated noise components. Accordingly, the DM and CR signals  $P_{r,p}(t)$  and  $A_{r,p}(t)$  can be written as:

$$P_{r,p}(\theta) = \prod_{i=0}^{N_c-1} X_{r,p}(\theta + c_i T_h) = \sum_{n=-\infty}^{+\infty} P_n(\theta) \quad (3.9)$$

$$A_{r,p}(\theta) = \sum_{i=0}^{N_c-1} X_{r,p}(\theta + c_i T_h) = \sum_{n=-\infty}^{+\infty} A_n(\theta) \quad (3.10)$$

$$P_n(\theta) = \prod_{i=0}^{N_n-1} \left\{ \alpha \sqrt{\frac{E}{N_c}} R_p(\theta - \Theta - n T_h) + w_{n,i}(\theta) \right\} \prod_{i=N_n}^{N_c-1} w_{n,i}(\theta) \quad (3.11)$$

$$A_n(\theta) = \sum_{i=0}^{N_n-1} \left\{ \alpha \sqrt{\frac{E}{N_c}} R_p(\theta - \Theta - n T_h) + w_{n,i}(\theta) \right\} \sum_{i=N_n}^{N_c-1} w_{n,i}(\theta) \quad (3.12)$$

where  $w_{n,0}(\theta), \dots, w_{n,N_c-1}(\theta)$  correspond to a permutation of the  $N_c$  uncorrelated noise components  $w_{n+c_0}(\theta + c_0T_h), \dots, w_{n+c_{N_c-1}}(\theta + c_{N_c-1}T_h)$ . Note that  $A_{r,p}(\theta)$  is also equal to the received signal filtered by the filter  $s(-t)$  matched to the transmitted signal  $s(t)$ . For  $n = 0$ , we have  $N_0 = N_c$ , and the interval  $I_0 = [\Theta - \frac{T_h}{2}, \Theta + \frac{T_h}{2}]$  is located around  $\Theta$  (the unknown time delay to estimate) and contains the global maxima of the useful components of both  $P_{r,p}(\theta)$  and  $A_{r,p}(\theta)$ . Therefore, we can write:

$$P_0(\theta) = \prod_{i=0}^{N_c-1} \left\{ \alpha \sqrt{\frac{E}{N_c}} R_p(\theta - \Theta) + w_{0,i}(\theta) \right\} \quad (3.13)$$

$$A_0(\theta) = \sum_{i=0}^{N_c-1} \left\{ \alpha \sqrt{\frac{E}{N_c}} R_p(\theta - \Theta) + w_{0,i}(\theta) \right\} \quad (3.14)$$

### 3.1.3 Local statistics and probabilities of error

In this subsection, we compute the local statistics and probabilities of error relative to the DM and the CR receivers. By local statistics and probabilities of error, we mean those in the interval  $I_0$ . The goal of computing these statistics is to study the impact of the ambiguity due to the pulse shape on the DM receiver.

Let us consider the interval  $I_0$  containing the useful component carrying the information on  $\Theta$ . We rewrite  $P_0(\theta)$  and  $A_0(\theta)$  from Eq. 3.13 and Eq. 3.14 as:

$$P_0(\theta) = \Pi_0(\theta) + V_0(\theta) \quad (3.15)$$

$$A_0(\theta) = S_0(\theta) + U_0(\theta) \quad (3.16)$$

where

$$\Pi_0(\theta) = \left[ \alpha \sqrt{\frac{E}{N_c}} R_p(\theta - \Theta) \right]^{N_c} \quad (3.17)$$

$$S_0(\theta) = \alpha \sqrt{N_c E} R_p(\theta - \Theta) \quad (3.18)$$

$$V_0(\theta) = \sum_{i=1}^{N_c} \left[ \alpha \sqrt{\frac{E}{N_c}} R_p(\theta - \Theta) \right]^{N_c-i} W_{0,i}(\theta) \quad (3.19)$$

$$W_{0,i}(\theta) = \sum_{j_1 \neq \dots \neq j_i} w_{0,j_1}(\theta) \cdots w_{0,j_i}(\theta), \quad (j_1, \dots, j_i = 0, \dots, N_c - 1) \quad (3.20)$$

$$U_0(\theta) = W_{0,1}(\theta) = \sum_{j=0}^{N_c-1} w_{0,j}(\theta) \quad (3.21)$$

with  $W_{0,i}(\theta)$  equal to the sum of the product of the possible combinations  $w_{0,j_1}(\theta), \dots, w_{0,j_i}(\theta)$  of  $i$  elements among the  $N_c$  noise components  $w_{0,0}(\theta), \dots, w_{0,N_c-1}(\theta)$ . The number of terms in  $W_{0,i}(\theta)$  is equal to  $C_i^{N_c}$  (the combination of  $i$  in  $N_c$ ). We can see  $\Pi_0(\theta)$  and  $S_0(\theta)$  as the useful DM and CR

observations respectively. To illustrate this, we write  $\Pi_0(\theta)$  in the case of  $N_c = 3$ :

$$\begin{aligned}
 P_0(\theta) &= \left[ \alpha \sqrt{\frac{E}{N_c}} R_p(\theta - \Theta) \right]^3 \\
 &+ \left[ \alpha \sqrt{\frac{E}{N_c}} R_p(\theta - \Theta) \right]^2 \left[ w_{0,0}(\theta) + w_{0,1}(\theta) + w_{0,2}(\theta) \right] \\
 &+ \alpha \sqrt{\frac{E}{N_c}} R_p(\theta - \Theta) \left[ w_{0,0}(\theta)w_{0,1}(\theta) + w_{0,0}(\theta)w_{0,2}(\theta) + w_{0,1}(\theta)w_{0,2}(\theta) \right] \\
 &+ w_{0,0}(\theta)w_{0,1}(\theta)w_{0,2}(\theta).
 \end{aligned}$$

As the noise components  $w_{0,i}(\theta)$ , ( $i = 0, \dots, N_c - 1$ ) are all zero-mean and uncorrelated, we can easily show that  $\mathcal{E}\{w_{0,j_1}(\theta) \cdots w_{0,j_i}(\theta)\} = 0$  if  $j_1 \neq \dots \neq j_i$ ,  $\mathcal{E}\{w_{0,j_1}(\theta) \cdots w_{0,j_i}(\theta)w_{0,j'_1}(\theta') \cdots w_{0,j'_i}(\theta')\} = 0$  if  $i \neq i'$  (because we have at least one noise component that appears only one time inside the expectation),  $\mathcal{E}\{W_{0,i}(\theta)W_{0,i'}(\theta')\} = 0$  if  $i \neq i'$  (thanks to the previous equation),  $\mathcal{E}\{w_{0,j_1}(\theta) \cdots w_{0,j_i}(\theta)w_{0,j'_1}(\theta') \cdots w_{0,j'_i}(\theta')\} = 0$  if  $(j_1, \dots, j_i) \neq (j'_1, \dots, j'_i)$  (because we have at least two noise components that appear only one time inside the expectation), and  $\mathcal{E}\{W_{0,i}(\theta)W_{0,i}(\theta')\} = \sum_{j_1 \neq \dots \neq j_i} \mathcal{E}\{w_{0,j_1}(\theta) \cdots w_{0,j_i}(\theta)w_{0,j_1}(\theta') \cdots w_{0,j_i}(\theta')\} = C_i^{N_c} C_w^i(\theta - \theta') = C_i^{N_c} \left[ \frac{N_0}{2} R_p(\theta - \theta') \right]^i$  (thanks to the previous equation,  $C_i^{N_c}$  denotes the combination and  $C_w(\theta)$  the covariance in Eq. 3.8) so the mean, the covariance and the variance of  $P_0(\theta)$  Eq. 3.15 can be expressed as:

$$m_{P_0}(\theta) = \Pi_0(\theta) \quad (3.22)$$

$$\begin{aligned}
 C_{P_0}(\theta, \theta') &= \left[ \frac{\alpha^2 E_s}{N_c} \right]^{N_c} \left[ R_p(\theta - \Theta) R_p(\theta' - \Theta) \right]^{N_c} \left\{ \left[ 1 \right. \right. \\
 &+ \left. \left. \frac{N_c}{\rho} \frac{R_p(\theta - \theta')}{R_p(\theta - \Theta) R_p(\theta' - \Theta)} \right]^{N_c} - 1 \right\} \quad (3.23)
 \end{aligned}$$

$$\begin{aligned}
 &\approx \frac{N_c^2}{\rho} \left[ \frac{\alpha^2 E_s}{N_c} \right]^{N_c} R_p(\theta - \theta') \left[ R_p(\theta - \Theta) R_p(\theta' - \Theta) \right]^{N_c - 1} \\
 &= C_{P_0, G}(\theta, \theta') \quad (3.24)
 \end{aligned}$$

$$\begin{aligned}
 \sigma_{P_0}^2(\theta) &= C_{V_0}(\theta, \theta) = \left[ \frac{\alpha^2 E_s}{N_c} \right]^{N_c} R_p^{2N_c}(\theta - \Theta) \left\{ \left[ 1 \right. \right. \\
 &+ \left. \left. \frac{N_c}{\rho} \frac{1}{R_p^2(\theta - \Theta)} \right]^{N_c} - 1 \right\} \quad (3.25)
 \end{aligned}$$

$$\approx \frac{N_c^2}{\rho} \left[ \frac{\alpha^2 E_s}{N_c} \right]^{N_c} R_p^{2(N_c - 1)}(\theta - \Theta) = \sigma_{P_0, G}^2(\theta) \quad (3.26)$$

and those of  $A_0(\theta)$  Eq. 3.16 as:

$$m_{A_0}(\theta) = S_0(\theta) \quad (3.27)$$

$$C_{A_0}(\theta, \theta') = N_c \frac{N_0}{2} R_p(\theta - \theta') \quad (3.28)$$

$$\sigma_{A_0}^2(\theta) = C_{A_0}(\theta, \theta) = N_c \frac{N_0}{2}. \quad (3.29)$$

We can see from Eq. 3.23 and Eq. 3.24 that  $P_0(\theta)$  is not a weak-stationary process because  $C_{P_0}(\theta, \theta')$  cannot be written as a function of  $\theta - \theta'$ . We can also see that  $C_{P_0}(\theta, \theta') = C_{P_0}(\theta', \theta)$ . In Eq. 3.24 and Eq. 3.26,  $C_{P_{0,G}}(\theta, \theta')$  and  $\sigma_{P_{0,G}}^2(\theta)$  denote the covariance and the variance of the process  $P_{0,G}(\theta)$  defined below in Eq. 3.31. For  $\theta = \Theta$ , the variance of  $P_0(\theta)$  is given by:

$$\sigma_{P_0}^2(\Theta) = \left[ \frac{\alpha^2 E_s}{N_c} \right]^{N_c} \left\{ \left[ 1 + \frac{N_c}{\rho} \right]^{N_c} - 1 \right\} \approx \frac{N_c^2}{\rho} \left[ \frac{\alpha^2 E_s}{N_c} \right]^{N_c}. \quad (3.30)$$

Note that the approximated Covariance and variance in Eq. 3.24 and Eq. 3.26 can directly be obtained by approximating  $P_0(\theta)$  from Eq. 3.15 and Eq. 3.19 by:

$$P_{0,G}(\theta) = \left[ \alpha \sqrt{\frac{E}{N_c}} R_p(\theta - \Theta) \right]^{N_c-1} \left[ \alpha \sqrt{\frac{E}{N_c}} R_p(\theta - \Theta) + U_0(\theta) \right] \quad (3.31)$$

where the process  $P_{0,G}(\theta)$  is Gaussian due to the distribution of  $U_0(\theta)$  Eq. 3.21. Note that although  $P_{0,G}(\theta)$  is Gaussian, it is not weak-stationary. The approximation in Eq. 3.31 is only valid at sufficiently high SNRs where the sum in Eq. 3.19 can be limited to the first term (i.e.  $i = 1$ ).

As the approximate upper bounds, as well as the approximate ZZLB and BTLB lower bounds, all derived in Chap. 2, are based on the probability that the observation at a given testpoint is larger than the observation at the testpoint  $\theta = \Theta$ , it makes sense to define the local probabilities of error relative to the DM and CR receivers as follows:

$$Q_{P_0}(\theta, \Theta) = \mathcal{P}\{P_0(\theta) > P_0(\Theta)\} \quad (3.32)$$

$$Q_{A_0}(\theta, \Theta) = \mathcal{P}\{A_0(\theta) > A_0(\Theta)\} \quad (3.33)$$

and to express from Eq. 3.23 and Eq. 3.24 the covariance of the DM observation  $P_0(\theta)$  for  $\theta' = \Theta$  as:

$$C_{P_0}(\theta, \Theta) = \left[ \frac{\alpha^2 E_s}{N_c} \right]^{N_c} R_p^{N_c}(\theta - \Theta) \left\{ \left[ 1 + \frac{N_c}{\rho} \right]^{N_c} - 1 \right\} \quad (3.34)$$

$$\approx \frac{N_c^2}{\rho} \left[ \frac{\alpha^2 E_s}{N_c} \right]^{N_c} R_p^{N_c}(\theta - \Theta) = C_{P_{0,G}}(\theta, \Theta). \quad (3.35)$$

To compute the probability of error relative to the DM receiver we have to know the bivariate cumulative distribution function relative to the distribution

of  $P_0(\theta)$  Eq. 3.15, which does not seem easy to compute analytically. To overcome this problem we assume that the SNR is sufficiently high so  $P_0(\theta)$  can be approximated by the Gaussian process  $P_{0,G}(\theta)$  in Eq. 3.31. Accordingly, we can approximate  $Q_{P_0}(\theta, \Theta)$  Eq. 3.32 and write  $Q_{A_0}(\theta, \Theta)$  Eq. 3.33 as:

$$\begin{aligned} Q_{P_{0,G}}(\theta, \Theta) &= \mathcal{P}\left\{P_{0,G}(\theta) - P_{0,G}(\Theta) > 0\right\} \\ &= Q\left[\frac{\sqrt{\rho}}{N_c} \frac{1 - R_p^{N_c}(\theta - \Theta)}{\sqrt{1 + R_p^{2(N_c-1)}(\theta - \Theta) - 2R_p^{N_c}(\theta - \Theta)}}\right] \end{aligned} \quad (3.36)$$

$$Q_{A_0}(\theta, \Theta) = Q\left[\sqrt{\frac{\rho}{2}}[1 - R_p(\theta - \Theta)]\right] \quad (3.37)$$

where denotes the Q function already introduced in Chap. 2. The statistics of  $P_{0,G}(\theta) - P_{0,G}(\Theta)$  are given from Eq. 3.31, Eq. 3.26 and Eq. 3.35 by:

$$P_{0,G}(\theta) - P_{0,G}(\Theta) \sim \mathcal{N}\left(m_{\Delta P_{0,G}}(\theta), \sigma_{\Delta P_{0,G}}^2(\theta)\right) \quad (3.38)$$

where

$$\begin{aligned} m_{\Delta P_{0,G}}(\theta) &= \left[\alpha\sqrt{\frac{E}{N_c}}\right]^{N_c} \left[R_p^{N_c}(\theta - \Theta) - 1\right] \\ \sigma_{\Delta P_{0,G}}^2(\theta) &= \frac{N_c^2}{\rho} \left[\frac{\alpha^2 E_s}{N_c}\right]^{N_c} \left[1 + R_p^{2(N_c-1)}(\theta - \Theta) - 2R_p^{N_c}(\theta - \Theta)\right] \end{aligned} \quad (3.39)$$

We can see from Eq. 3.36 and Eq. 3.37 that the approximated probability of error of the DM receiver is equal to the probability of error of the CR receiver for  $N_c = 1$ .

As the distribution involving the product of independent Gaussian variables has, unlike the Gaussian distribution, a very sharp shape in the vicinity of zero, we expect that the approximation of the joint distribution of  $P_0(\theta)$  and  $P_0(\Theta)$  by a joint Gaussian distribution (based on Eq. 3.31) leads to a considerable overestimation of the probability of error  $Q_{P_0}(\theta, \Theta)$  Eq. 3.32. To solve this problem, we evaluate  $Q_{P_0}(\theta, \Theta)$  by simulation. To do so we proceed as follows. From Eq. 3.13, we can easily show that  $Q_{P_0}(\theta, \Theta)$  can be written as:

$$\begin{aligned} C_{P_0}(\theta, \Theta) &= \mathcal{P}\left\{\zeta - \xi > 0\right\} \quad (3.40) \\ \xi &= \prod_{i=1}^{N_c} \left\{1 + \left[\frac{N_c}{\rho}\right]^{\frac{1}{2}} \gamma_i\right\} \\ \zeta &= \prod_{i=1}^{N_c} \left\{R_p(\theta - \Theta) + \left[\frac{N_c}{\rho}\right]^{\frac{1}{2}} \left[R_p(\theta - \Theta)\gamma_i + \sqrt{1 - R_p^2(\theta - \Theta)}\nu_i\right]\right\} \end{aligned}$$

where  $\gamma_1, \dots, \gamma_{N_c}, \nu_1, \dots, \nu_{N_c} \sim \mathcal{N}(0, 1)$  and are statistically independent. Then, by randomly generating according to  $\mathcal{N}(0, 1)$ , once, a  $2N_c \times N_{rnd}$  matrix of independent elements, with  $N_{rnd}$  being the size of the population, we can compute  $C_{P_0}(\theta, \Theta)$  along the  $\theta$  axis.

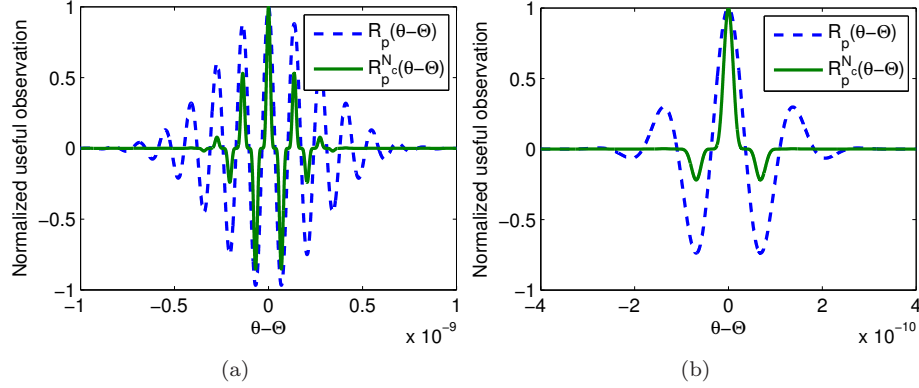


Fig. 3.2.:  $R_p(\theta - \Theta)$  and  $R_p^{N_c}(\theta - \Theta)$  ( $N_c = 5$ ,  $\Theta = 0$ ) (a)  $T_w = 0.685$  ns,  $B = 2.5$  GHz,  $f_c = 7.25$  GHz (b)  $T_w = 0.228$  ns,  $B = 7.5$  GHz,  $f_c = 6.85$  GHz.

In Fig. 3.2(a) we show  $R_p(\theta - \Theta)$  (useful CR observation  $S_0(\theta)$  Eq. 3.18 normalized with respect to  $\alpha\sqrt{N_c E}$ ) and  $R_p^{N_c}(\theta - \Theta)$  (useful DM observation  $\Pi_0(\theta)$  Eq. 3.17 normalized with respect to  $[\frac{\alpha^2 E}{N_c}]^{\frac{N_c}{2}}$ ) with respect to  $\theta - \Theta$ . We consider a Gaussian pulse of  $T_w = 0.685$  ns of width (bandwidth at -10 dB equal to  $B = 2.5$  GHz) modulated with  $f_c = 7.25$  GHz (pulse filling the total EC UWB spectrum [2, 3]). We take  $N_c = 5$  and  $\Theta = 0$ . We can see that  $R_p^{N_c}(\theta - \Theta)$  is much shorter than  $R_p(\theta - \Theta)$  and that the gap between the global and the local maxima is much larger with  $R_p^{N_c}(\theta - \Theta)$  than with  $R_p(\theta - \Theta)$ .

In Fig. 3.2(b) we show  $R_p(\theta - \Theta)$  and  $R_p^{N_c}(\theta - \Theta)$  for  $T_w = 0.228$  ns ( $B = 7.5$  GHz) and  $f_c = 6.85$  GHz (pulse filling the total FCC UWB spectrum [1]). Now,  $R_p^{N_c}(\theta - \Theta)$  has only one positive maximum.

We can expect from the shape of  $R_p^{N_c}(\theta - \Theta)$  (i.e. the relatively high gap between the global and the local maxima), that the DM receivers can serve to mitigate the ambiguity effects due to the local maxima in  $R_p(\theta - \Theta)$ . However, we will see later that, unfortunately this is not true because the noise is amplified due to the multiplication with  $R_p(\theta - \Theta)$  in the expression of  $P_0(\theta)$  (see Eq. 3.15 and Eq. 3.19).

In Fig. 3.3(a) we show  $\tilde{C}_{P_0}(\theta, \Theta)$  and  $\tilde{C}_{P_{0,G}}(\theta, \Theta)$  (exact  $C_{P_0}(\theta, \Theta)$  Eq. 3.34 and approximated  $C_{P_{0,G}}(\theta, \Theta)$  Eq. 3.35 variances of the DM observation, normalized with respect to  $[\frac{\alpha^2 E_s}{N_c}]^{N_c}$ ) with respect to  $\theta - \Theta$ , for the EC pulse (i.e.  $T_w = 0.685$  ns and  $f_c = 7.25$  GHz) with  $N_c = 5$ ,  $\Theta = 0$  and  $\rho = 15$  dB (SNR), and in Fig. 3.3(b)  $\tilde{\sigma}_{P_0}^2(\theta)$  and  $\tilde{\sigma}_{P_{0,G}}^2(\theta)$  (exact  $\sigma_{P_0}^2(\theta)$  Eq. 3.25 and approximated  $\sigma_{P_{0,G}}^2(\theta)$  Eq. 3.26 variances of the DM observation, normalized with respect to  $[\frac{\alpha^2 E_s}{N_c}]^{N_c}$ ). We can see that for the considered SNR ( $\rho = 15$  dB), the exact covariance is slightly larger than the approximated one, and this holds similarly for

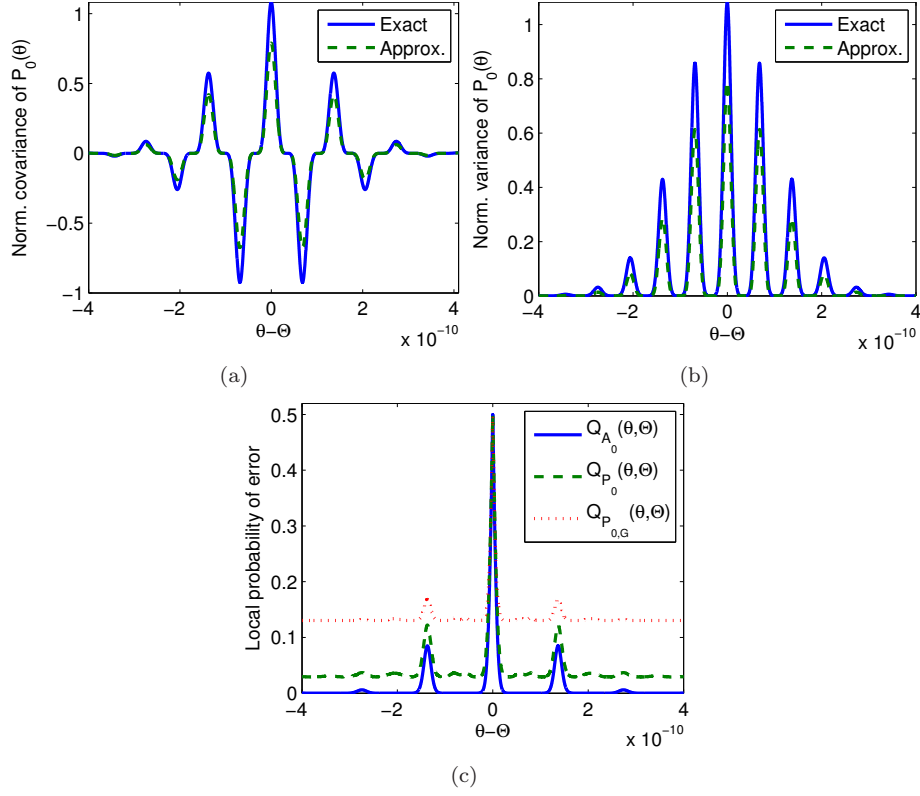


Fig. 3.3.: (a) Exact  $\tilde{C}_{P_0}(\theta, \Theta)$  and approximated  $\tilde{C}_{P_{0,G}}(\theta, \Theta)$  normalized covariances of the DM observation  $P_0(\theta)$  (b) Exact  $\tilde{\sigma}_{P_0}^2(\theta)$  and approximated  $\tilde{\sigma}_{P_{0,G}}^2(\theta)$  normalized variances of  $P_0(\theta)$  (c) Local probability of error  $Q_{A_0}(\theta, \Theta)$  of the CR receiver, and simulated  $Q_{P_0}(\theta, \Theta)$  and approximated  $Q_{P_{0,G}}(\theta, \Theta)$  local probabilities of error of the DM receiver (Gaussian pulse,  $T_w = 0.685$  ns,  $f_c = 7.25$  GHz,  $N_c = 5$ ,  $\Theta = 0$ ,  $\rho = 15$  dB).

the exact and approximated variances. This means that a higher SNR is required to ensure the convergence of the DM observation  $P_0(\theta)$  to the Gaussian process  $P_{0,G}(\theta)$  in Eq. 3.31.

In Fig. 3.3(c) we show for the same setup as in Fig. 3.3(a) and Fig. 3.3(b), the local probability of error  $Q_{A_0}(\theta, \Theta)$  Eq. 3.37 of the CR receiver, and simulated  $Q_{P_0}(\theta, \Theta)$  Eq. 3.40 and approximated  $Q_{P_{0,G}}(\theta, \Theta)$  Eq. 3.36 local probabilities of error of the DM receiver. We can see that the CR probability of error is smaller than the DM probability of error. Note that the gap between  $Q_{A_0}(\theta, \Theta)$  and  $Q_{P_0}(\theta, \Theta)$  increases as  $N_c$  increases. We can expect from this that TOA estimation based on the CR receiver will outperform that based on the DM

receiver. We can also see that the probability of error  $Q_{P_{0,G}}(\theta, \Theta)$  obtained from the Gaussian estimation of the DM observation highly overestimates the one  $Q_{P_0}(\theta, \Theta)$  obtained by simulation. This validates the fact, already mentioned above, that the DM observation  $P_0(\theta)$  cannot be rigorously approximated by a Gaussian process except for sufficiently high SNRs.

We show neither the variance of the CR observation since it is constant, nor its covariance because it has the same shape as  $R_p(\theta - \Theta)$  (see Fig. 3.2(a) and Fig. 3.2(b)).

### 3.1.4 Global statistics and probabilities of error

We compute here the global statistics and probabilities of error relative to the DM and the CR receivers. By global statistics, we mean those inside an interval  $I_n$ ,  $n \neq 0$ , and by global probability of error, the probability that the observed signal is stronger in  $I_n$ ,  $n \neq 0$ , than in  $I_0$ . The goal of this study is to evaluate the effects of the ambiguity due to the collision between the different pulses of the TH transmitted waveform on the TOA estimators based on the DM and the CR receivers. Unlike the case of Sec. 3.1.3, the results of this subsection will not be used in this chapter but in Chap. 4 dedicated to TOA estimation in MU systems.

From Eq. 3.11 and Eq. 3.12, we can write the DM and CR observations in the interval  $I_n$  as:

$$P_n(\theta) = P_{n,N_n}(\theta)V_{n,N_n}(\theta) \quad (3.41)$$

$$A_n(\theta) = A_{n,N_n}(\theta) + U_{n,N_n}(\theta) \quad (3.42)$$

where

$$P_{n,N_n}(\theta) = \prod_{i=0}^{N_n-1} \left\{ \alpha \sqrt{\frac{E}{N_c}} R_p(\theta - \Theta - nT_h) + w_{n,i}(\theta) \right\} \quad (3.43)$$

$$V_{n,N_n}(\theta) = \prod_{i=N_n}^{N_c-1} w_{n,i}(\theta) \quad (3.44)$$

$$A_{n,N_n}(\theta) = \sum_{i=0}^{N_n-1} \left\{ \alpha \sqrt{\frac{E}{N_c}} R_p(\theta - \Theta - nT_h) + w_{n,i}(\theta) \right\} \quad (3.45)$$

$$U_{n,N_n}(\theta) = \sum_{i=N_n}^{N_c-1} w_{n,i}(\theta) \quad (3.46)$$

Note that  $P_{n,N_n}(\theta)$  and  $A_{n,N_n}(\theta)$  correspond to the product and the sum of the  $N_n$  pulse ACR components corrupted by noise, colliding in  $I_n$ , respectively.

Let us consider the computation of the global probabilities of error  $Q_{P_0}(\theta, \Theta)$  and  $Q_{A_0}(\theta, \Theta)$  corresponding to the DM and CR receivers respectively. We define

the global probability of error relative to a given observation, as the probability that the observation at the testpoint (middle of  $I_n$ )

$$\theta_n = \Theta + nT_h \quad (3.47)$$

is stronger than the observation at  $\Theta$  (abscissa of the global maximum of the useful observation, middle of  $I_0$ ). We can write from Eq. 3.9, Eq. 3.10, Eq. 3.11 and Eq. 3.12:

$$Q_{P_n}(\theta_n, \Theta) = \mathcal{P}\{P_{r,p}(\theta_n) > P_{r,p}(\Theta)\} = \mathcal{P}\{P_n(\theta_n) > P_0(\Theta)\} \quad (3.48)$$

$$Q_{A_n}(\theta_n, \Theta) = \mathcal{P}\{A_{r,p}(\theta_n) > A_{r,p}(\Theta)\} = \mathcal{P}\{A_n(\theta_n) > A_0(\Theta)\}. \quad (3.49)$$

As the transmitted signal contains only  $N_c$  pulses, and as the interval  $I_0$  contains  $N_c$  pulse ACR components (after delaying the filtered received signal with respect to the TH delays corresponding to the different pulses), the DM component  $P_{n,N_n}(\theta)$  Eq. 3.43 of  $P_n(\theta)$  Eq. 3.41 is totally contained in  $P_0(\theta)$  Eq. 3.13 (interval  $I_0$ ), and the CR component  $A_{n,N_n}(\theta)$  Eq. 3.45 of  $A_n(\theta)$  Eq. 3.42 is totally contained in  $A_0(\theta)$  Eq. 3.14. It follows from Eq. 3.13 and Eq. 3.14 that:

$$P_0(\theta) = P_{n,N_n}(\theta + nT_h)P_{0,N_c-N_n}(\theta) \quad (3.50)$$

$$A_0(\theta) = A_{n,N_n}(\theta + nT_h) + A_{0,N_c-N_n}(\theta) \quad (3.51)$$

where the noise components in  $P_{0,N_c-N_n}(\theta)$  and  $A_{0,N_c-N_n}(\theta)$  are different (so uncorrelated) from those in  $P_{n,N_n}(\theta + nT_h)$  and  $A_{n,N_n}(\theta + nT_h)$ .

Using Eq. 3.41, Eq. 3.42, Eq. 3.50 and Eq. 3.51, we can write the probabilities of error  $Q_{P_0}(\theta, \Theta)$  Eq. 3.48 and  $Q_{A_0}(\theta, \Theta)$  Eq. 3.49 as:

$$\begin{aligned} Q_{P_n}(\theta_n, \Theta) &= \mathcal{P}\{P_{n,N_n}(\theta_n)V_{n,N_n}(\theta_n) > P_{n,N_n}(\theta_n)P_{0,N_c-N_n}(\Theta)\} \\ &= Q_{P_n,1}Q_{P_n,2} + (1 - Q_{P_n,1})(1 - Q_{P_n,2}) \\ &= 1 + 2Q_{P_n,1}Q_{P_n,2} - (Q_{P_n,1} + Q_{P_n,2}) \end{aligned} \quad (3.52)$$

$$\begin{aligned} Q_{A_n}(\theta_n, \Theta) &= \mathcal{P}\{A_{n,N_n}(\theta_n) + U_{n,N_n}(\theta_n) > A_{n,N_n}(\theta_n) + A_{0,N_c-N_n}(\Theta)\} \\ &= \mathcal{P}\{U_{n,N_n}(\theta_n) > A_{0,N_c-N_n}(\Theta)\} \end{aligned} \quad (3.53)$$

where

$$Q_{P_n,1} = \mathcal{P}\{P_{n,N_n}(\theta_n) > 0\} \quad (3.54)$$

$$Q_{P_n,2} = \mathcal{P}\{V_{n,N_n}(\theta_n) > P_{0,N_c-N_n}(\Theta)\}. \quad (3.55)$$

Let us now compute the means and the covariances of the signals  $P_{n,N_n}(\theta)$ ,  $V_{n,N_n}(\theta)$ ,  $A_{n,N_n}(\theta)$  and  $U_{n,N_n}(\theta)$  present in Eq. 3.52 and Eq. 3.53. Similarly to

the methodology followed in Sec. 3.1.3 we can write:

$$m_{P_{n,N_n}}(\theta) = \Pi_{n,N_n}(\theta) \quad (3.56)$$

$$C_{P_{n,N_n}}(\theta, \theta') = \left[ \frac{\alpha^2 E_s}{N_c} \right]^{N_n} \left[ R_p(\theta - \theta_n) R_p(\theta' - \theta_n) \right]^{N_n} \left\{ \left[ 1 + \frac{N_c}{\rho} \frac{R_p(\theta - \theta')}{R_p(\theta - \theta_n) R_p(\theta' - \theta_n)} \right]^{N_n} - 1 \right\} \quad (3.57)$$

$$\approx \frac{N_n N_c}{\rho} \left[ \frac{\alpha^2 E_s}{N_c} \right]^{N_n} R_p(\theta - \theta') \left[ R_p(\theta - \theta_n) R_p(\theta' - \theta_n) \right]^{N_n - 1} \\ = C_{P_{n,N_n,G}}(\theta, \theta') \quad (3.58)$$

$$m_{V_{n,N_n}}(\theta) = 0 \quad (3.59)$$

$$C_{V_{n,N_n}}(\theta, \theta') = \left[ \frac{N_0}{2} \right]^{N_c - N_n} R_p^{N_c - N_n}(\theta - \theta') \quad (3.60)$$

$$m_{A_{n,N_n}}(\theta) = S_{n,N_n}(\theta) \quad (3.61)$$

$$C_{A_{n,N_n}}(\theta, \theta') = N_n \frac{N_0}{2} R_p(\theta - \theta'). \quad (3.62)$$

$$m_{U_{n,N_n}}(\theta) = 0 \quad (3.63)$$

$$C_{U_{n,N_n}}(\theta, \theta') = (N_c - N_n) \frac{N_0}{2} R_p(\theta - \theta'). \quad (3.64)$$

where

$$\Pi_{n,N_n}(\theta) = \left[ \alpha \sqrt{\frac{E}{N_c}} R_p(\theta - \theta_n) \right]^{N_n} \quad (3.65)$$

$$S_{n,N_n}(\theta) = \alpha N_n \sqrt{\frac{E}{N_c}} R_p(\theta - \theta_n). \quad (3.66)$$

Note that both  $P_{n,N_n}(\theta)$  and  $V_{n,N_n}(\theta)$  are not weak-stationary, and that  $P_{n,N_n}(\theta)$  can be approximated by a Gaussian process at sufficiently high SNRs which is not the case of  $V_{n,N_n}(\theta)$  (product of pure zero-mean Gaussian processes). However, both  $A_{n,N_n}(\theta)$  and  $U_{n,N_n}(\theta)$  are weak-stationary and Gaussian.

From Eq. 3.61, Eq. 3.62, Eq. 3.63 and Eq. 3.64 we can write the CR global probability of error  $Q_{A_n}(\theta_n, \Theta)$  Eq. 3.53 as:

$$Q_{A_n}(\theta_n, \Theta) = \mathcal{P} \left\{ \mathcal{N} \left[ - (N_c - N_n) \left[ \frac{\alpha^2 E}{N_c} \right]^{\frac{1}{2}}, 2(N_c - N_n) \frac{N_0}{2} \right] > 0 \right\} \\ = Q \left( \sqrt{\frac{\rho}{2} \left[ 1 - \frac{N_n}{N_c} \right]} \right). \quad (3.67)$$

By assuming both  $P_{n,N_n}(\theta)$  and  $V_{n,N_n}(\theta)$  Gaussian, we can approximate  $Q_{P_n}(\theta_n, \Theta)$  Eq. 3.52 from  $Q_{P_{n,1}}$  Eq. 3.54,  $Q_{P_{n,2}}$  Eq. 3.55, Eq. 3.56, Eq. 3.58, Eq. 3.59 and Eq. 3.60 by:

$$Q_{P_{n,G}}(\theta_n, \Theta) = 1 + 2Q_{P_{n,G,1}}Q_{P_{n,G,2}} - (Q_{P_{n,G,1}} + Q_{P_{n,G,2}}) \quad (3.68)$$

where

$$\begin{aligned} Q_{P_{n,G},1} &= \mathcal{P}\left\{\mathcal{N}\left(\left[\frac{\alpha^2 E}{N_c}\right]^{\frac{N_n}{2}}, \frac{N_n N_c}{\rho} \left[\frac{\alpha^2 E_s}{N_c}\right]^{N_n}\right) > 0\right\} \\ &= Q\left(-\sqrt{\frac{\rho}{N_n N_c}}\right) \end{aligned} \quad (3.69)$$

$$\begin{aligned} Q_{P_{n,G},2} &= \mathcal{P}\left\{\mathcal{N}\left(-\left[\frac{\alpha^2 E}{N_c}\right]^{\frac{N_c-N_n}{2}}, \left[\frac{N_0}{2}\right]^{N_c-N_n} + \frac{(N_c-N_n)N_c}{\rho}\right.\right. \\ &\quad \left.\left.\times \left[\frac{\alpha^2 E_s}{N_c}\right]^{N_c-N_n}\right) > 0\right\} \\ &= Q\left(\left[\frac{(N_c-N_n)N_c}{\rho} + \left[\frac{N_c}{\rho}\right]^{N_c-N_n}\right]^{-\frac{1}{2}}\right). \end{aligned} \quad (3.70)$$

Like the local DM probability of error (see Sec. 3.1.3), the global DM probability of error  $Q_{P_n}(\theta_n, \Theta)$  can be computed from Eq. 3.52 via simulation by noticing that:

$$Q_{P_{n,1}} = \mathcal{P}\{\kappa > 0\} \quad (3.71)$$

$$Q_{P_{n,2}} = \mathcal{P}\{\zeta - \xi > 0\} \quad (3.72)$$

$$\begin{aligned} \kappa &= \prod_{i=1}^{N_n} \left\{1 + \left[\frac{N_c}{\rho}\right]^{\frac{1}{2}} \nu_i\right\} \\ \xi &= \prod_{i=1}^{N_c-N_n} \left\{1 + \left[\frac{N_c}{\rho}\right]^{\frac{1}{2}} \gamma_i\right\} \\ \zeta &= \left[\frac{N_c}{\rho}\right]^{\frac{N_c-N_n}{2}} \prod_{i=1}^{N_c-N_n} \nu_i \end{aligned}$$

where  $\nu_1, \dots, \nu_{N_n}, \gamma_1, \dots, \gamma_{N_c-N_n}, \nu_1, \dots, \nu_{N_c-N_n} \sim \mathcal{N}(0,1)$  and are statistically independent. Accordingly, by randomly generating following  $\mathcal{N}(0,1)$ , a  $2N_c \times N_{rnd}$  matrix of independent elements, with  $N_{rnd}$  being the size of the population, we can compute  $Q_{P_{n,1}}$  and  $Q_{P_{n,2}}$  for all possible values of  $\rho$  and  $N_n$ . Note that for a given  $N_n$ , a  $[N_n + 2(N_c - N_n)] \times N_{rnd}$  matrix is required.

In Fig. 3.4(a) we show with respect to the SNR  $\rho$  for  $N_n = 0, \dots, N_c - 1$  with  $N_c = 5$ , the global probabilities of error of the CR observation  $Q_{A_n}(\theta_n, \Theta)$  Eq. 3.67, and the global probability of error of the CR observation obtained by the Gaussian approximation  $Q_{P_{n,G}}(\theta_n, \Theta)$  Eq. 3.68 and by simulation (from a population of million elements)  $Q_{P_n}(\theta_n, \Theta)$  based on Eq. 3.52, Eq. 3.71 and Eq. 3.72. We can observe that:

- The probabilities of error corresponding to both, the CR and the DM observations converge to zero at high SNRs for all the values of  $N_n$ .
- The probability of error is much smaller (at low SNRs) and convergences (to zero) much faster with the CR receiver than with the DM receiver.

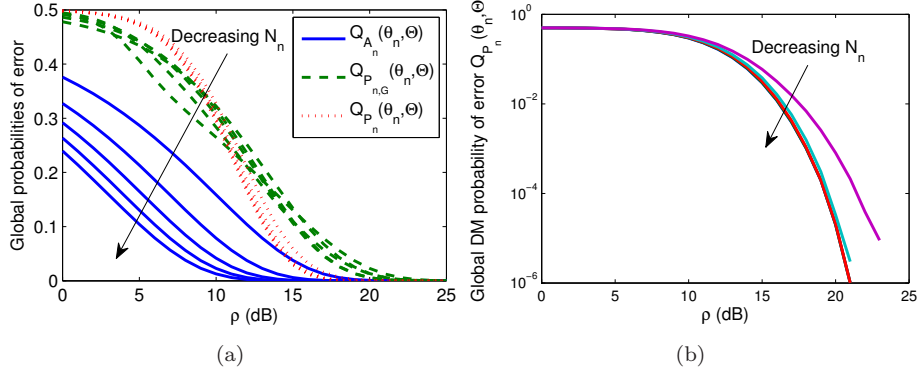


Fig. 3.4.: (a) Global probability of error of the CR receiver  $Q_{A_n}(\theta_n, \Theta)$ , and global probabilities of error of the CR receiver obtained by the Gaussian approximation  $Q_{P_{n,G}}(\theta_n, \Theta)$  and by simulation  $Q_{P_n}(\theta_n, \Theta)$  (from a population of million elements) with respect to the SNR  $\rho$  for  $N_n = 0, \dots, N_c - 1$  with  $N_c = 5$  (b)  $Q_{P_n}(\theta_n, \Theta)$  in logarithmic scale.

- The probability of error increases as the number  $N_n$  of the colliding pulses in the interval  $I_n$  increases.
- The gap between the values of the probability of error obtained at the different values of  $N_n$  is more significant with the CR receiver than with the DM receiver. This is due to the addition of the elementary observations (i.e. the delayed versions of the filtered received signal) with the former and to their multiplication with the latter.
- The Gaussian approximation of the probability of error relative to the DM receiver significantly underestimates (resp. overestimates) at low (resp. relatively high) SNRs the probability obtained by simulation.

In Fig. 3.4(b) we show the global probability of error of the DM observation obtained by simulation  $Q_{P_n}(\theta_n, \Theta)$  in the logarithmic scale. We can see that  $Q_{P_n}(\theta_n, \Theta)$  is not evaluated above  $\rho = 21$  dB for  $N_n = 0, 1$  and  $2$  because it becomes lower than  $10^{-6}$  while we have considered a population of million elements.

### 3.2 MAXIMUM DELAYING-AND-MULTIPLYING ESTIMATOR

In this section, we compute the asymptotic and local performances of the MME (maximum delaying-and-multiplying estimator); as mentioned above, we postpone the global performances to the next chapter.

In Sec. 3.2.1, we define the new estimator. In Sec. 3.2.2, we compute its asymptotic performances. In Sec. 3.2.3, we derive some approximations of its

achieved MSE. In Sec. 3.2.4, we present and discuss some numerical results about the proposed estimator in comparison with the MLE.

### 3.2.1 The estimator

Denote by  $\hat{\Theta}_{dm}$  the MME obtained by maximizing the DM observation (see Fig. 3.1(a)). We have:

$$\hat{\Theta}_{dm} = \underset{\theta \in D_{\Theta}}{\operatorname{argmax}} P_{r,p}(\theta) \quad (3.73)$$

where  $P_{r,p}(\theta)$  is the DM observation given in Eq. 3.9 and  $D_{\Theta} = [\Theta_1, \Theta_2]$  the *a priori* domain of  $\Theta$ .

In this chapter, we are only interested in the local performances of the proposed estimator. The goal is to study how it is influenced by the ambiguity due to the shape of the transmitted pulse. The ambiguity due to the shape of transmitted TH waveform will be considered in Chap. 4. Accordingly, we can limit our study to the interval  $I_0 = [\Theta + \frac{T_h}{2}, \Theta - \frac{T_h}{2}]$  Eq. 3.3. Using Eq. 3.9, we can write  $\hat{\Theta}_{dm}$  as:

$$\hat{\Theta}_{dm} = \underset{\theta \in I_0}{\operatorname{argmax}} P_0(\theta) \quad (3.74)$$

where  $P_0(\theta)$  Eq. 3.15 is the DM observation inside the interval  $I_0$ .

### 3.2.2 Asymptotic performances

In this subsection, we study the asymptotic (i.e. at high SNRs) performances of the MME  $\hat{\Theta}_{dm}$ .

To do so, we consider the Taylor series expansion of the DM observation  $P_0(\theta)$  about  $\Theta$ . For convenience, we recall the expressions of  $P_0(\theta)$  Eq. 3.15, the useful DM observation  $\Pi_0(\theta)$  Eq. 3.17, and the Gaussian approximation of the covariance  $C_{P_0}(\theta, \Theta)$  Eq. 3.35 of  $P_0(\theta)$ :

$$P_0(\theta) = \Pi_0(\theta) + V_0(\theta) \quad (3.75)$$

$$\Pi_0(\theta) = \left[ \alpha \sqrt{\frac{E}{N_c}} R_p(\theta - \Theta) \right]^{N_c} \quad (3.76)$$

$$C_{P_0}(\theta, \Theta) \approx \frac{N_c^2}{\rho} \left[ \frac{\alpha^2 E_s}{N_c} \right]^{N_c} R_p^{N_c}(\theta - \Theta). \quad (3.77)$$

By limiting the expansion of the useful observation  $\Pi_0(\theta)$  to second order and that of the DM noise  $V_0(\theta)$  to first order, and taking into account that  $\dot{\Pi}_0(\Theta) = 0$  (because  $\Theta$  is the abscissa of the global maximum of  $\Pi_0(\theta)$ , see Eq. 3.17), we can approximate  $P_0(\theta)$  Eq. 3.75 by:

$$P_0(\theta) \approx \Pi_0(\Theta) + \frac{1}{2} \ddot{\Pi}_0(\Theta)(\theta - \Theta)^2 + V_0(\Theta) + \dot{V}_0(\Theta)(\theta - \Theta)$$

so that  $\hat{\Theta}_{dm}$  Eq. 3.74 can be approximated by:

$$\hat{\Theta}_{dm} = \{\theta; \dot{P}_0(\theta) = 0\} \approx \Theta - \frac{\dot{V}_0(\Theta)}{\ddot{\Pi}_0(\Theta)}. \quad (3.78)$$

The second derivative of  $\Pi_0(\theta)$  follows from Eq. 3.76:

$$\begin{aligned} \ddot{\Pi}_0(\theta) &= N_c \left[ \alpha \sqrt{\frac{E}{N_c}} \right]^{N_c} \left[ (N_c - 1) R_p^{N_c - 2}(\theta - \Theta) \dot{R}_p^2(\theta - \Theta) \right. \\ &\quad \left. + R_p^{N_c - 1}(\theta - \Theta) \ddot{R}_p(\theta - \Theta) \right]. \end{aligned} \quad (3.79)$$

Using the Wiener-Khintchine theorem, we can write the mean and the covariance of the derivative  $\dot{V}_0(\theta)$  of the DM noise  $V_0(\theta)$ , from Eq. 3.19 and Eq. 3.77 as:

$$\begin{aligned} m_{\dot{V}_0}(\theta) &= \mathcal{E}\{\dot{V}_0(\theta)\} = 0 \quad (3.80) \\ C_{\dot{V}_0}(\theta, \Theta) &= \mathcal{F}^{-1} \left\{ 4\pi^2 f^2 \mathcal{F}\{C_{P_0}(\theta, \Theta)\} \right\} \\ &= \frac{N_c^2}{\rho} \left[ \frac{\alpha^2 E_s}{N_c} \right]^{N_c} \mathcal{F}^{-1} \left\{ 4\pi^2 f^2 \left[ \otimes^{N_c} \mathcal{F}\{R_p(\theta - \Theta)\} \right] \right\} \\ &= \frac{N_c^2}{\rho} \left[ \frac{\alpha^2 E_s}{N_c} \right]^{N_c} \mathcal{F}^{-1} \left\{ \left[ \otimes^{N_c - 1} \mathcal{F}\{R_p(\theta - \Theta)\} \right] \otimes 4\pi^2 f^2 \mathcal{F}\{R_p(\theta \right. \right. \\ &\quad \left. \left. - \Theta)\} \right\} = -\frac{N_c^2}{\rho} \left[ \frac{\alpha^2 E_s}{N_c} \right]^{N_c} R_p^{N_c - 1}(\theta - \Theta) \ddot{R}_p(\theta - \Theta) \end{aligned} \quad (3.81)$$

where  $\mathcal{F}\{\cdot\}$  denotes the Fourier transform operator and  $f$  the frequency variable. It has been taken into account in Eq. 3.81 that  $j2\pi f$  and  $-4\pi^2 f^2$  are the frequency responses of the first and second derivative filters, respectively. By taking  $\theta = \Theta$  we get from Eq. 3.79 and Eq. 3.81:

$$\ddot{\Pi}_0(\Theta) = N_c \left[ \alpha \sqrt{\frac{E}{N_c}} \right]^{N_c} \ddot{R}_p(0) \quad (3.82)$$

$$m_{\dot{V}_0}(\Theta) = 0 \quad (3.83)$$

$$\sigma_{\dot{V}_0}^2(\Theta) = -\frac{N_c^2}{\rho} \left[ \frac{\alpha^2 E_s}{N_c} \right]^{N_c} \ddot{R}_p(0) \quad (3.84)$$

From Eq. 3.78, Eq. 3.82, Eq. 3.83 and Eq. 3.84, we can write the asymptotic mean and variance of the MME  $\hat{\Theta}_{dm}$  as:

$$\mu_\infty = \Theta \quad (3.85)$$

$$\sigma_\infty^2 = \frac{\sigma_{\dot{V}_0}^2(\Theta)}{\ddot{\Pi}_0^2(\Theta)} = -\frac{1}{\rho \ddot{R}_p(0)} = \frac{1}{\rho \beta^2} = c \quad (3.86)$$

where

$$\beta^2 = -\ddot{R}_p(0) = \int_{-\infty}^{+\infty} 4\pi^2 f^2 |\mathcal{F}\{p(t)\}|^2 df \quad (3.87)$$

$$c = \frac{1}{\rho \beta^2} \quad (3.88)$$

denote the MQBW of  $p(t)$  and the CRLB of  $\Theta$ , respectively (the energy of  $p(t)$  in the expression of  $\beta^2$  is equal to one).

Finally, we can deduce that the MME is asymptotically unbiased and achieves asymptotically the CRLB.

### 3.2.3 Approximation of the local MSE

We have shown in the last subsection that the MME achieves asymptotically the CRLB. In this subsection, we consider the performances of the MME at medium and low SNRs. We use the subdomain method proposed in Chap. 2 to approximate the MSE of the MME, and the approximate lower bounds derived therein to propose two alternate approximations of the MSE.

We have seen in Chap. 2 that by splitting the *a priori* domain  $D_\Theta = [\Theta_1, \Theta_2]$  of  $\Theta$  into  $N = n_2 - n_1 + 1$ , ( $n_1 \leq 0$ ,  $n_2 \geq 0$ ) subdomains  $D_n$  ( $\Theta$  should be contained in  $D_0$ ), we can write the MSE of the MME  $\hat{\Theta}_{dm}$  as:

$$e = \sum_{n=n_1}^{n_2} \mathcal{P}_n [(\Theta - \mu_n)^2 + \sigma_n^2] \quad (3.89)$$

where  $\mathcal{P}_n$  denotes the probability that  $\hat{\Theta}_{dm}$  falls in the subdomain  $D_n$ , and  $\mu_n$  and  $\sigma_n^2$  its mean and variance in that subdomain. As pointed out above, the *a priori* domain  $D_\Theta$  is equal in our case to  $I_0 = [\Theta + \frac{T_b}{2}, \Theta - \frac{T_b}{2}]$  (see Eq. 3.3) because we are interested here in the local performances of  $\hat{\Theta}_{dm}$ .

Let us choose a testpoint  $t_n$  in each subdomain  $D_n$ , assume that  $\mu_0 \approx \Theta$  and  $\sigma_0^2 \approx c$  ( $c$  is the CRLB) in  $D_0$  (around  $\Theta$ ) thanks to the asymptotic performances of the MME (see Sec. 3.2.2), approximate  $\mu_n$  by  $t_n$  (width of  $D_n$  much smaller than  $|t_n - \Theta|$ ,  $\forall t_n \in D_n$ ), neglecting  $\sigma_n^2$  for  $n \neq 0$  ( $\sigma_n^2$  much smaller than  $(\Theta - \mu_n)^2$ ), and approximate, as in Sec. 2.1.3.1,  $\mathcal{P}_n$  by:

$$\mathcal{P}_n^{(3)} = \frac{\mathcal{P}_n^{(2)}}{\sum_{n=n_1}^{n_2} \mathcal{P}_n^{(2)}}$$

where

$$\mathcal{P}_n^{(2)} = \begin{cases} 1 & n = 0 \\ \mathcal{P}\{P_0(t_n) > P_0(\Theta)\} = Q_{P_0}(t_n, \Theta) & n \neq 0 \end{cases}$$

with  $Q_{P_0}(\theta, \Theta)$  being the local probability of error of the DM receiver computed in Sec. 3.1.3. We recall that  $Q_{P_0}(\theta, \Theta)$  can either be computed from Eq. 3.36 by assuming Gaussian processes or from Eq. 3.40 by simulation. We also recall that for signals with oscillating ACR, the testpoints  $t_n$  should be chosen as the abscissa of the local maxima of the ACR. Let us further approximating  $\mathcal{P}_0$  by 1 (because  $\sigma_0^2 \approx c \ll \mu_n^2 \approx t_n^2$ ,  $n \neq 0$ ). We can now approximate the MSE of the

MME by:

$$e_{dm} = c + \sum_{n \neq 0} \mathcal{P}_n^{(3)} (t_n - \Theta)^2. \quad (3.90)$$

From the approximated ZZLB and BTLB lower bounds derived in Chap. 2, we propose the following two approximations of the MSE of the MME:

$$z_{dm} = \int_0^{\epsilon_0} \theta Q_{P_0}(\theta, \Theta) d\theta \quad (3.91)$$

$$b_{dm} = \int_0^{\epsilon_0} \theta V\{Q_{P_0}(\theta, \Theta)\} d\theta \quad (3.92)$$

where  $V\{f(\xi)\} = \max\{f(\xi') \geq \xi\}$ ,  $\xi > 0$ , is the valley-filling function, and  $\epsilon_0 = 2\sqrt{e_U}$ , with

$$e_U = \sigma_U^2 + (\Theta - \mu_U)^2 \quad (3.93)$$

the maximum MSE given in Chap. 2 (see Eq. 2.20). We have considered  $z_{dm}$  and  $b_{dm}$  as approximations and not as approximate lower bounds. Indeed, to derive the approximate lower bounds we have to find the likelihood function of the DM observation, then compute properly the minimum probability of error relative to the optimal decision rule based on the likelihood ratio (see Sec. 2.1.4). We have set  $\epsilon_0$  at  $2\sqrt{e_U}$  to force  $z_{dm}$  and  $b_{dm}$  to converge to  $e_U$  at low SNRs. In fact,  $Q_{P_0}(\theta, \Theta)$  approaches  $\frac{1}{2}$  at low SNRs, so both  $z_{dm}$  and  $b_{dm}$  approach  $\frac{1}{2} \int_0^{\epsilon_0} \theta d\theta = \frac{\epsilon_0^2}{4}$ .

### 3.2.4 Numerical results and discussion

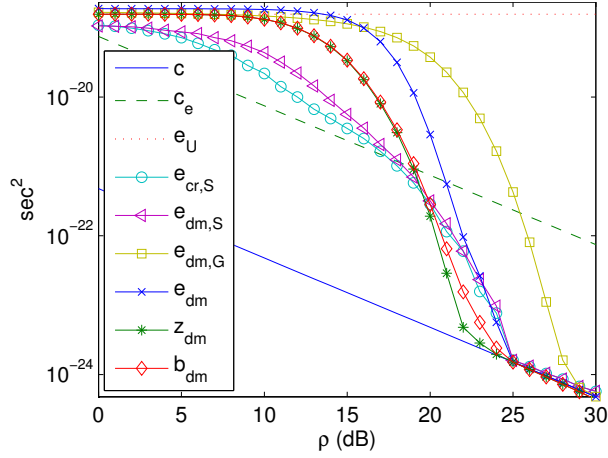
Here, we discuss some numerical results about the MME and compare it with the MLE. We consider the EC (i.e.  $T_w = 0.685$  ns and  $f_c = 7.25$  GHz) and FCC (i.e.  $T_w = 0.228$  ns and  $f_c = 6.85$  GHz) pulses already used in Sec. 3.1.3 (see Fig. 3.2(a) and Fig. 3.2(a)). We take  $\Theta = 0$  and  $T_h = 2T_w$ .

As mentioned in the beginning of this chapter, the MLE is equivalent for single-user to the MCE (maximum correlation estimator)  $\hat{\Theta}_{cr}$  obtained by maximizing the CR observation (see Fig. 3.1(b)). We have:

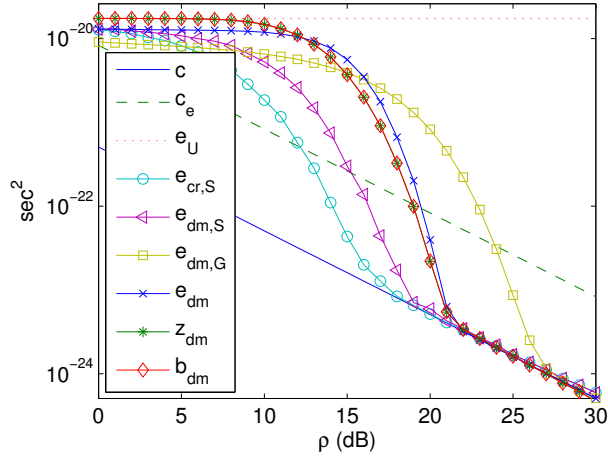
$$\hat{\Theta}_{cr} = \operatorname{argmax}_{\theta \in I_0} A_0(\theta) \quad (3.94)$$

where  $A_0(\theta)$  is the CR observation in  $I_0$  (see Eq. 3.14, Eq. 3.16).

In Fig. 3.5(a) and Fig. 3.5(b) we show for the EC and FCC pulses, respectively, the CRLB  $c$  Eq. 3.88, the ECRLB  $c_e$  (derived in Chap. 2, see Eq. 2.23), the maximum MSE  $e_U$  Eq. 3.93, the MSE  $e_{cr,S}$  of the MLE obtained by simulation (10000 trials), the MSE  $e_{dm,S}$  of the MME obtained by simulation, and four MSE approximations  $e_{dm,G}$ ,  $e_{dm}$ ,  $z_{dm}$  and  $b_{dm}$  of the MME, all versus the SNR  $\rho$ . Note that both  $e_{dm,G}$  and  $e_{dm}$  are obtained from the subdomain formula Eq. 3.90,



(a)



(b)

Fig. 3.5.: CRLB  $c$ , ECRLB  $c_e$ , maximum MSE  $e_U$ , MSE  $e_{cr,S}$  of the MLE obtained by simulation, MSE  $e_{dm,S}$  of the MME obtained by simulation, and four MSE approximations  $e_{dm,G}$ ,  $e_{dm}$ ,  $z_{dm}$  and  $b_{dm}$  of the MME, all versus the SNR  $\rho$  (a) EC pulse (b) FCC pulse.

whereas  $z_{dm}$  and  $b_{dm}$  follow from Eq. 3.91 and Eq. 3.91 respectively. However,  $e_{dm,G}$  uses the Gaussian approximation (in Eq. 3.36) of the local probability of error  $Q_{P_0}(t_n, \Theta)$ , whereas  $e_{dm}$ ,  $z_{dm}$  and  $b_{dm}$  all use the local probability of error computed by simulation according to Eq. 3.40.

We can observe that:

- The CRLB is approximately achieved by both the MLE and the MME at the same SNR.
- In the ambiguity region of the EC pulse, the MLE slightly outperforms the MME. We can deduce that the ambiguity phenomenon has approximately the same impact on both estimators.
- In the threshold region of the FCC pulse, the MLE outperforms significantly the MME. We can deduce that the impact of the threshold phenomenon is stronger on the MME.
- The MSE approximation  $e_{dm,G}$  of the MME based on the subdomain method and the Gaussian approximation of the local probability of error overestimates appreciably the MSE truly achieved in both ambiguity/threshold and asymptotic regions. In fact, the Gaussian probability approximation overestimates widely the true probability as already observed and discussed in Fig. 3.3(c).
- The MSE approximation  $e_{dm}$  of the MME based on the subdomain method and the simulated local probability of error converges to the CRLB at approximately the same SNR (especially for the EC pulse) as the simulated MSE  $e_{dm,S}$ . However, it overestimates  $e_{dm,S}$  in the ambiguity/threshold region. This can be interpreted by the fact that the local probability of error does not take into account the correlation between all testpoints, but just between the actual testpoint and the testpoint  $\Theta$ .
- Both MSE approximations  $z_{dm}$  and  $b_{dm}$ , based on the approximated ZZLB and BTLB respectively, seem to be more accurate below the asymptotic/threshold region than the MSE approximation  $e_{dm}$ ;  $b_{dm}$  is slightly more accurate than  $z_{dm}$  thanks to the valley-filling function (especially for the EC pulse where the local maxima are stronger).

Let us now discuss why the MLE outperforms the MME at medium SNRs. Due to the TH coding, the total available energy is split among the pulses of the TH waveform, so the SNR relative to each pulse is  $N_c$  times lower than the total SNR. This makes the ambiguity and threshold effects stronger if we consider the pulses separately. With the CR receiver, the effect of the SNR splitting is completely canceled thanks to the addition operation (because the noise components are independent). However, with the delaying-and-multiplying receiver, this effect cannot be completely canceled, due to the multiplication operation.

Finally, we can say that the local performances of the MLE and the proposed maximum delaying-and-multiplying estimator are very similar.

### 3.3 DFT-BASED ESTIMATORS

In this section, we propose two TOA estimators based on the phase of the DFT of the received signal. The first one relies on the relative phase, whereas the second

one on the absolute phase. For both estimators, we compute the local estimates corresponding to the different frequency components, and then combine them to get the global estimates.

The main contributions of this work have been stated in the beginning of this chapter. We have already mentioned in Sec. 1.1.4 that some estimators investigated in the literature employ the DFT. However, there are many differences between this work and the previous proposals. The TOA estimation in [51, 52] is not built on the phase of the DFT. In [53, 54], the authors bypass the problem of phase ambiguity by assuming that the maximum time delay is smaller than the period of the highest frequency component. Although the problem of phase ambiguity is well investigated in [49, 50, 55], it is however solved by the Chinese remainder theorem in [49, 50], and by a recursive correction of the TOA estimate in [55]. In contrast, the problem is solved in our approach by unwrapping the phase.

From the advantages of our estimators is that they require a sampling frequency equal to the bandwidth of the transmitted signal and generate directly their TOA estimates from few samples with no need of further interpolations. They can be used for IR-UWB signals as well as for MC-UWB signals. However, they do perform better with IR-UWB signals. The main goal of this work is to show that we can estimate the TOA by using the phase of the DFT of the received signal in such a way to obtain interesting performances. Many improvements can be introduced to the proposed estimators in order to make them achieving the CRLB at lower SNRs.

In Sec. 3.3.1, we describe our system model. In Sec. 3.3.2, we consider the MLE of the local (i.e. at a given frequency component) phase and compute the statistics of the unwrapped phase. In Sec. 3.3.3, we derive the local phase-slope-based and the local absolute-phase-based TOA estimators, and in Sec. 3.3.4 the corresponding global ones. In Sec. 3.3.5, we show how one can apply our proposed estimators in UWB MP channels.

### 3.3.1 System model

We describe here our system model. We assume that the transmitter and the receiver communicate through an AWGN channel.

Denote by  $s(t)$ ,  $r(t)$  and  $n(t)$  the complex envelopes (i.e. baseband signals) of the transmitted signal, the received signal and the AWGN, all band-pass filtered in the band  $[f_c - \frac{B}{2}, f_c + \frac{B}{2}]$  ( $f_c$  is the central frequency and  $B$  the bandwidth). We can write  $r(t)$  as:

$$\begin{aligned} r(t) &= \alpha e^{-j2\pi f_c \tau} s(t - \tau) + n(t) \\ &= \alpha e^{-j2\pi f_c \tau} s_\tau(t) + n(t) \end{aligned}$$

where  $\alpha$  and  $\tau$  are the gain and the time delay introduced by the channel, and  $s_\tau(t) = s(t - \tau)$ .

After sampling at the rate  $B$ , we get:

$$r[m] = \alpha e^{-j2\pi f_c \tau} s_\tau[m] + n[m]$$

where  $z[m]$  denotes the sample of the signal  $z(t)$  at  $t = mT_s$  ( $T_s = \frac{1}{B}$  is the sampling period). The sequence  $n[m]$  is a white (i.e., the samples  $n[m]$  are independent and identically distributed) Gaussian sequence because the sampling rate is equal to band-pass filter width. The variance of  $n[m]$  is given by  $\sigma_n^2 = 2N_0B$  where  $2N_0$  is the one-sided power spectral density of the AWGN.

Denote by  $R[k]$ , ( $k = -\frac{M}{2}, \dots, \frac{M}{2} - 1$  assuming  $M$  to be even) the DFT of  $r[m]$ . Then:

$$R[k] = \sum_{m=0}^{M-1} r[m] e^{-j2\pi \frac{mk}{M}} = \alpha e^{-j2\pi f_c \tau} S_\tau[k] + N[k] \quad (3.95)$$

where  $S_\tau[k]$  and  $N[k]$  are the DFTs of  $s_\tau[m]$  and  $n[m]$ , respectively. As  $n[m]$  is a white Gaussian sequence,  $N[k]$  is also white Gaussian with a variance given by  $\sigma_N^2 = M\sigma_n^2 = 2MN_0B$  [78]. By assuming that the Shannon sampling theorem is respected, and that both  $s(t)$  and  $s_\tau(t)$  are falling in the period of observation, we can write:

$$S_\tau[k] = \frac{S_\tau(f_k)}{T_s} = \frac{e^{-j2\pi f_k \tau} S(f_k)}{T_s} = e^{-j2\pi f_k \tau} S[k] \quad (3.96)$$

where  $S_\tau(f)$  and  $S(f)$  denote the FTs of  $s_\tau(t)$  and  $s(t)$ , respectively,  $S[k]$  the DFT of  $s[m]$ , and:

$$f_k = \frac{k}{MT_s} = k\Delta f. \quad (3.97)$$

To simplify the discussion, we denote from now on  $S[k]$ ,  $R[k]$  and  $N[k]$  by  $S_k$ ,  $R_k$  and  $N_k$ , respectively. From Eq. 3.95 and Eq. 3.96, we can write  $R_k$  as follows:

$$R_k = \alpha e^{-j2\pi(f_c + f_k)\tau} S_k + N_k = U_k + N_k \quad (3.98)$$

where  $U_k = \alpha e^{-j2\pi(f_c + f_k)\tau} S_k$  is the DFT of the useful part of the received signal. Denote by  $\rho_Z, \theta_Z, x_Z$  and  $y_Z$  the modulus, phase, real part and imaginary part of the complex number  $Z$ . From Eq. 3.98, we can define  $\varphi_k$  as:

$$\varphi_k = \theta_{S_k} - \theta_{U_k} = 2\pi(f_c + f_k)\tau. \quad (3.99)$$

Given that  $N_k$  is Gaussian, we can write the PDF of  $R_k$  as:

$$\begin{aligned} T_{R_k}(x_{R_k}, y_{R_k}) &= \frac{1}{2\pi\sigma^2} e^{-\frac{(x_{R_k} - x_{U_k})^2 + (y_{R_k} - y_{U_k})^2}{2\sigma^2}} \\ T_{R_k}(\rho_{R_k}, \theta_{R_k}) &= \frac{\rho_{R_k}}{2\pi\sigma^2} e^{-\frac{\rho_{R_k}^2 + \rho_{U_k}^2 - 2\rho_{R_k}\rho_{U_k}\cos(\theta_{R_k} - \theta_{U_k})}{2\sigma^2}} \end{aligned} \quad (3.100)$$

where  $\sigma^2 = \frac{\sigma_N^2}{2} = MN_0B$  denotes the variance of both  $x_{N_k}$  and  $y_{N_k}$ .

### 3.3.2 Statistics of the unwrapped phase

In this subsection, we consider the MLE of the phase and compute the statistics of its unwrapped version.

The joint log-likelihood function of  $\rho_{U_k}$  and  $\varphi_k$  can be written from Eq. 3.99 and Eq. 3.100 as:

$$\Lambda^{\rho_{U_k}, \varphi_k} = -\frac{\rho_{R_k}^2 + \rho_{U_k}^2 - 2\rho_{R_k}\rho_{U_k}\cos(\theta_{R_k} - \theta_{S_k} + \varphi_k)}{2\sigma^2}. \quad (3.101)$$

From Eq. 3.101, we can easily write the CRLB of  $\varphi_k$  as:

$$c^{\varphi_k} = \frac{\sigma^2}{\rho_{U_k}^2} = \frac{1}{\nu_k} \quad (3.102)$$

where

$$\nu_k = \frac{\rho_{U_k}^2}{\sigma^2} = \alpha^2 \frac{\rho_{S_k}^2}{\sigma^2} \quad (3.103)$$

is the SNR obtained at the frequency  $f_k$ . We call  $\nu_k$  the local (or instantaneous) SNR (i.e. the SNR corresponding to the local frequency  $f_k$ ). The global SNR is defined as:

$$\nu = \sum_{k=-\frac{N}{2}}^{\frac{N}{2}-1} \nu_k. \quad (3.104)$$

Obviously, the time delay can be estimated from an estimate of  $\varphi_k$  Eq. 3.99 as:

- The phase  $\varphi_k$  to angular frequency  $2\pi(f_c + f_k)$  ratio.
- The slope of the phase with respect to the angular frequency.

For both approaches, the phase estimate should be continuous (i.e. not limited to an interval of width  $2\pi$ ). With the former the phase estimate should also be around its true absolute value, whereas with the latter a constant offset along the frequency axis is acceptable. As in practice the phase is computed modulo  $2\pi$  (i.e. the wrapped phase), an unwrapped version of it is needed in order to rebuild the continuous phase.

In practice, the unwrapped phase can be obtained recursively by adding a multiple of  $2\pi$  to the wrapped one until the absolute difference between the neighboring unwrapped phases becomes less than or equal to  $\pi$ . Denote by  $\hat{\varphi}_k$  the wrapped MLE of the phase and by  $\tilde{\varphi}_k$  the unwrapped version of  $\hat{\varphi}_k$ . We can write the unwrapping criterion as follows:

$$|\tilde{\varphi}_k - \tilde{\varphi}_{k-1}| \leq \pi \quad (3.105)$$

where the non-ambiguity condition  $2\pi\Delta f\tau < \pi$  should be respected. The unwrapping procedure can be performed using the “unwrap” MATLAB function.

As the true value of the phase is unknown in practice, we can start the unwrapping procedure from an arbitrary  $k_0$  by taking  $\tilde{\varphi}_{k_0} = \hat{\varphi}_{k_0}$ , then running the unwrapping procedure for  $k_0 + 1, \dots, \frac{M}{2} - 1$  and  $k_0 - 1, \dots, -\frac{M}{2}$ . Obviously, the unwrapped phase may have an offset (almost the same for all frequency components) with respect to the true phase. This offset depends on the offset  $2\pi(f_{k_0} + f_c)\tau - \hat{\varphi}_{k_0}$  present at the starting unwrapping point.

Let us now consider the wrapped MLE  $\hat{\varphi}_k$  (called in the sequel the “wrapped phase”). By equating to zero the partial derivative of  $\Lambda^{\rho_{R_k}, \varphi_k}$  Eq. 3.101 with respect to  $\varphi_k$ , we can write  $\hat{\varphi}_k$  as:

$$\hat{\varphi}_k = \theta_{S_k} - \theta_{R_k} = \theta_{S_k R_k^*} \quad (3.106)$$

where  $\{\cdot\}^*$  denotes the complex conjugate. Given that  $N_k$  Eq. 3.98 is a white sequence, the estimates  $\hat{\varphi}_k$  obtained at the different frequencies  $k$  are independent. By integrating the joint PDF  $T_{R_k}(\rho_{R_k}, \theta_{R_k})$  Eq. 3.100 of  $\rho_{R_k}$  and  $\theta_{R_k}$  over  $\rho_{R_k}$  (in order to obtain the marginal PDF of  $\theta_{R_k}$  [105]), we can write the PDF of  $\hat{\varphi}_k$  using Eq. 3.106 as:

$$\begin{aligned} T_{\hat{\varphi}_k}^{wr}(\hat{\varphi}_k) &= \frac{e^{-\frac{\nu_k}{2}}}{2\pi} + \sqrt{\frac{\nu_k}{2\pi}} \cos(\hat{\varphi}_k - \varphi_k) e^{-\frac{\nu_k}{2} \sin^2(\hat{\varphi}_k - \varphi_k)} \\ &\times Q[\sqrt{\nu_k} \cos(\hat{\varphi}_k - \varphi_k)] \end{aligned} \quad (3.107)$$

where  $Q(\cdot)$  denotes the Q function, and the superscript  $^{wr}$  the wrapped phase. Obviously,  $T_{\hat{\varphi}_k}^{wr}(\hat{\varphi}_k)$  is  $2\pi$ -periodic and can be defined in any interval  $I_{c_k} = [c_k - \pi, c_k + \pi]$  of width  $2\pi$  ( $\int_{I_{c_k}} T_{\hat{\varphi}_k}^{wr}(\hat{\varphi}_k) d\hat{\varphi}_k = 1, \forall c_k$ ). It has been shown in [106] that the distribution of the wrapped phase can be approximated by a normal distribution if the local SNR  $\nu_k$  is sufficiently high, and a uniform distribution along  $I_{c_k}$  if  $\nu_k$  is very low.

Let us now compute the PDF of the unwrapped version  $\tilde{\varphi}_k$  (called from now on the “unwrapped phase”) of the wrapped phase  $\hat{\varphi}_k$ . We assume that we start the unwrapping procedure from  $k = 0$  (i.e.  $\tilde{\varphi}_0 = \hat{\varphi}_0$ ). Let  $T_{\tilde{\varphi}_k}(\tilde{\varphi}_k)$  be the marginal PDF of  $\tilde{\varphi}_k$ . We will show below that  $T_{\tilde{\varphi}_k}(\tilde{\varphi}_k)$  can be computed recursively for  $k = 1, \dots, \frac{M}{2} - 1$  and  $k = -1, \dots, -\frac{M}{2}$  starting from  $\tilde{\varphi}_0$ .

From the unwrapping criterion in Eq. 3.105 we can write the domain of  $\tilde{\varphi}_k$  given  $\tilde{\varphi}_{k-1}$  as:

$$D_k | \tilde{\varphi}_{k-1} = I_{\tilde{\varphi}_{k-1}} = [\tilde{\varphi}_{k-1} - \pi, \tilde{\varphi}_{k-1} + \pi]. \quad (3.108)$$

As for  $k = 0$  the marginal domain of  $\tilde{\varphi}_k$  is given by  $D_0 = [-\pi, \pi]$  (because  $\tilde{\varphi}_0 = \hat{\varphi}_0$ ), we can write from Eq. 3.108 the marginal domain of  $\tilde{\varphi}_k$  as:

$$D_k = \left[ -|k+1|\pi, |k+1|\pi \right], \quad (k = -\frac{N}{2}, \dots, \frac{N}{2} - 1). \quad (3.109)$$

Given that  $\tilde{\varphi}_k$  is unwrapped with respect to  $\tilde{\varphi}_{k-1}$ ,  $T_{\tilde{\varphi}_k}^{wr}(\tilde{\varphi}_k)$  Eq. 3.107 is  $2\pi$ -periodic, and  $|\tilde{\varphi}_k - \tilde{\varphi}_{k-1}| = 2l\pi$  (with  $l$  integer due to the unwrapping), we can write the PDF of  $\tilde{\varphi}_k$  given  $\tilde{\varphi}_{k-1}$  as:

$$T_{\tilde{\varphi}_k|\tilde{\varphi}_{k-1}}(\tilde{\varphi}_k) = T_{\tilde{\varphi}_k}^{wr}(\tilde{\varphi}_k)$$

where the domain of  $T_{\tilde{\varphi}_k|\tilde{\varphi}_{k-1}}(\tilde{\varphi}_k)$  is  $I_{\tilde{\varphi}_{k-1}}$  Eq. 3.108.

Now, in order to express the marginal PDF  $T_{\tilde{\varphi}_k}(\tilde{\varphi}_k)$  of  $\tilde{\varphi}_k$  with respect to that of  $\tilde{\varphi}_{k-1}$ , we first compute the joint PDF  $T_{\tilde{\varphi}_k, \tilde{\varphi}_{k-1}}(\tilde{\varphi}_k, \tilde{\varphi}_{k-1})$  of  $\tilde{\varphi}_k$  and  $\tilde{\varphi}_{k-1}$ , and then integrate with respect to  $\tilde{\varphi}_{k-1}$  taking into account that  $\tilde{\varphi}_{k-1}|\tilde{\varphi}_k \in [\tilde{\varphi}_k - \pi, \tilde{\varphi}_k + \pi]$  (due to the unwrapping criterion in Eq. 3.105). Accordingly we can write:

$$\begin{aligned} T_{\tilde{\varphi}_k, \tilde{\varphi}_{k-1}}(\tilde{\varphi}_k, \tilde{\varphi}_{k-1}) &= T_{\tilde{\varphi}_k|\tilde{\varphi}_{k-1}}(\tilde{\varphi}_k)T_{\tilde{\varphi}_{k-1}}(\tilde{\varphi}_{k-1}) = T_{\tilde{\varphi}_k}^{wr}(\tilde{\varphi}_k)T_{\tilde{\varphi}_{k-1}}(\tilde{\varphi}_{k-1}) \\ T_{\tilde{\varphi}_k}(\tilde{\varphi}_k) &= \int_{\tilde{\varphi}_k - \pi}^{\tilde{\varphi}_k + \pi} T_{\tilde{\varphi}_k, \tilde{\varphi}_{k-1}}(\tilde{\varphi}_k, \tilde{\varphi}_{k-1})d\tilde{\varphi}_{k-1} \\ &= T_{\tilde{\varphi}_k}^{wr}(\tilde{\varphi}_k) \int_{\tilde{\varphi}_k - \pi}^{\tilde{\varphi}_k + \pi} T_{\tilde{\varphi}_{k-1}}(\tilde{\varphi}_{k-1})d\tilde{\varphi}_{k-1} \end{aligned} \quad (3.110)$$

where the domain of  $T_{\tilde{\varphi}_k}(\tilde{\varphi}_k)$  is  $D_k$  Eq. 3.109. So,  $T_{\tilde{\varphi}_k}(\tilde{\varphi}_k)$  can now be computed recursively from Eq. 3.110 for  $k = 1, \dots, \frac{M}{2} - 1$  and  $k = -1, \dots, -\frac{M}{2}$  taking into account that:

$$T_{\tilde{\varphi}_0}(\tilde{\varphi}_0) = T_{\tilde{\varphi}_k}^{wr}(\tilde{\varphi}_0)$$

Using Eq. 3.109 we can write the mean and the variance of  $\tilde{\varphi}_k$  as:

$$\mu_{\tilde{\varphi}_k} = \int_{-|k+1|\pi}^{|k+1|\pi} \tilde{\varphi}_k T_{\tilde{\varphi}_k}(\tilde{\varphi}_k)d\tilde{\varphi}_k \quad (3.111)$$

$$\sigma_{\tilde{\varphi}_k}^2 = \int_{-|k+1|\pi}^{|k+1|\pi} (\tilde{\varphi}_k - \mu_{\tilde{\varphi}_k})^2 T_{\tilde{\varphi}_k}(\tilde{\varphi}_k)d\tilde{\varphi}_k. \quad (3.112)$$

In Fig. 3.6(a), we show the true phase  $\varphi_k$  Eq. 3.99, a realization of the wrapped phase  $\hat{\varphi}_k$  ( $\hat{\varphi}_k \in [-\pi, \pi]$ ), and the corresponding unwrapped phase  $\tilde{\varphi}_k$ , all versus the frequency  $f_k + f_c$ . The transmitted signal consists on a cardinal sine of a bandwidth of  $B = 2$  GHz modulated by the carrier  $f_c = 2$  GHz. We consider a time delay of  $\tau = 2$  ns, a global SNR Eq. 3.104 of  $\nu = 17$  dB, and  $M = 16$  samples ( $k = -8, \dots, 7$ ). The unwrapping procedure is started here from  $k = -8$ . We can see that  $\tilde{\varphi}_k$  is almost continuous with a phase offset almost constant with respect to the true phase.

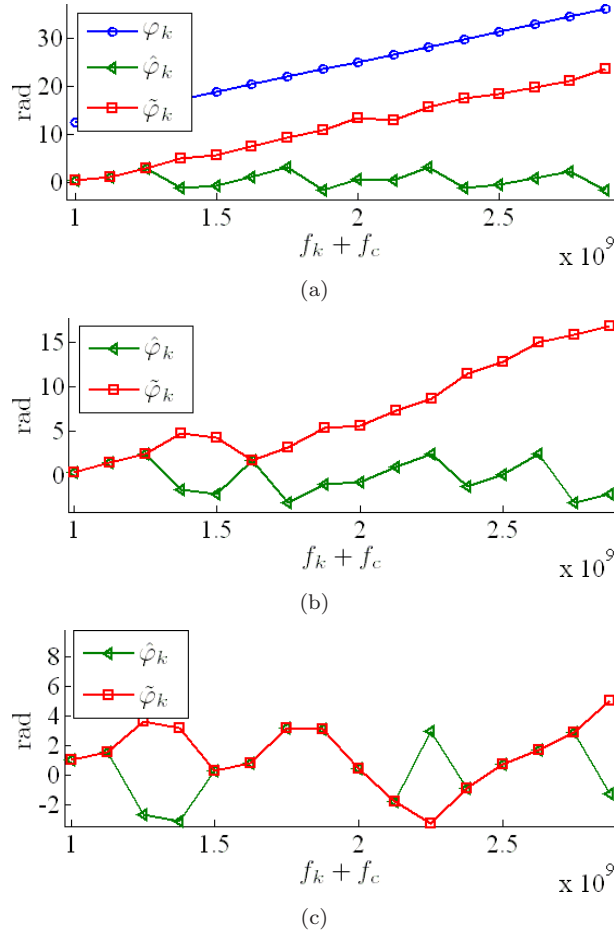


Fig. 3.6.: (a) True phase  $\varphi_k$  versus  $f_k + f_c$  (a) (b) (c) one realization of the wrapped phase  $\hat{\varphi}_k$  and the corresponding unwrapped one  $\tilde{\varphi}_k$  (cardinal sine wave-form modulated by  $f_c = 2$  GHz,  $k = -8, \dots, 7$ ).

In Fig. 3.6(b) and Fig. 3.6(c) we show two more realizations of the wrapped  $\hat{\varphi}_k$  and unwrapped  $\tilde{\varphi}_k$  phases. We can see that some errors multiple of  $-2\pi$  have been introduced to  $\tilde{\varphi}_k$  during the unwrapping procedure. This happens when the unwrapping procedure should add a multiple of  $2\pi$  to the next phase (for instance at  $k = -3$  in Fig. 3.6(b)), but does not add it because the absolute difference between the neighboring wrapped phases is less than  $\pi$  (i.e.  $|\hat{\varphi}_{-3} - \hat{\varphi}_{-4}| \leq \pi$ ) due to the noise. Each time this phenomenon happens, an further error of  $-2\pi$  will be introduced.

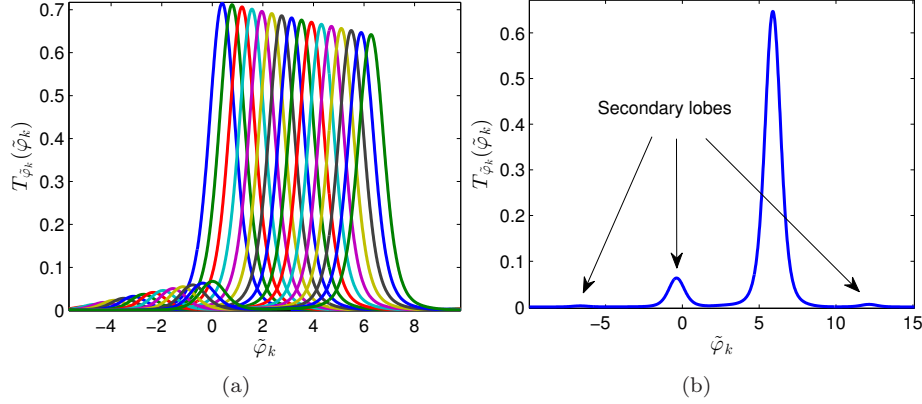


Fig. 3.7.: Marginal PDF  $T_{\tilde{\varphi}_k}(\tilde{\varphi}_k)$  of the unwrapped phase  $\tilde{\varphi}_k$  (a)  $k = 1, \dots, 15$  (b)  $k = 15$ .

Note that errors multiple of  $2\pi$  can also be introduced. This happens when the unwrapping procedure should not add a multiple of  $2\pi$  to the next phase, but adds it because the absolute difference between the neighboring wrapped phases is greater than  $\pi$  due to the noise. Such errors rarely occur if the phase  $\varphi_k$  Eq. 3.99 is increasing with the frequency (i.e. positive slope).

In Fig. 3.7(a) and Fig. 3.7(b) we show the marginal PDF  $T_{\tilde{\varphi}_k}(\tilde{\varphi}_k)$  Eq. 3.110 of the unwrapped phase  $\tilde{\varphi}_k$  for  $k = 1, \dots, 15$  and  $k = 15$ , respectively. We take  $B = 2$  GHz,  $f_c = 0$  GHz,  $\tau = 1$  ns,  $M = 32$ , and a local SNR Eq. 3.103 of  $\nu_k = 5$  dB,  $\forall k$ . In this experience, we have started the unwrapping procedure from  $k = 0$ . We can see in Fig. 3.7(b) that for  $k = 15$  (the phase corrected at the end of the unwrapping procedure), the PDF has three secondary lobes located at  $-4\pi$ ,  $-2\pi$ , and  $2\pi$  from the main lobe. The strongest secondary lobe is the one located at  $-2\pi$  from the main lobe.

As already mentioned above, the presence of these secondary lobes is due to errors multiple of  $\pm 2\pi$  introduced by the unwrapping procedure. The main lobe becomes weaker and the secondary lobes stronger as the frequency increases. This means that we have more chance that such errors (i.e. the errors multiple of  $\pm 2\pi$ ) occur. In fact, the  $\pm 2\pi$  errors accumulate over the course of the unwrapping procedure as the frequency increases because the unwrapping is performed recursively (see Fig. 3.6(b) and Fig. 3.6(c)). If we decrease the local SNR Eq. 3.103 by either increasing the number of samples or decreasing the global SNR Eq. 3.104, then the secondary lobes (which are located at  $\dots, -4\pi, -2\pi, 2\pi, 4\pi, \dots$  from the main lobe) become stronger. Errors multiple of  $-2\pi$  (resp.  $2\pi$ ) are more frequent if the slope of the true phase is positive (resp. negative). We can see from the PDF of  $\tilde{\varphi}_k$  that the unwrapped phase is biased. As the secondary lobes

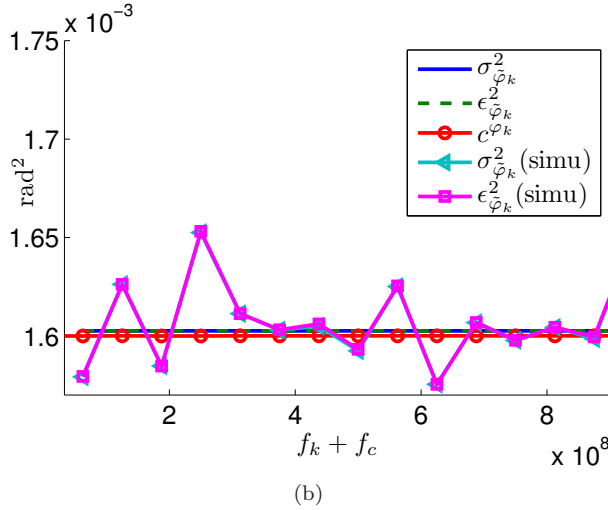
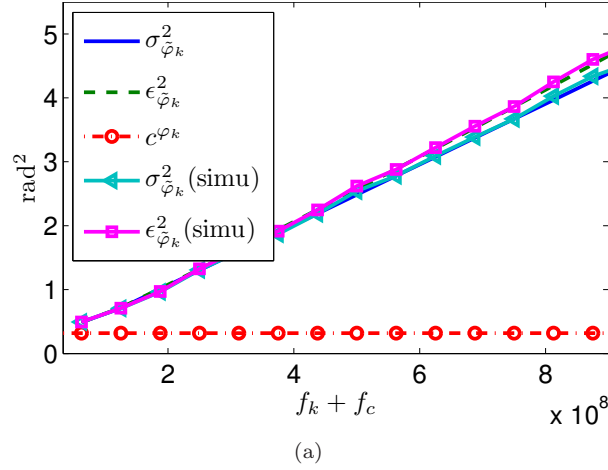


Fig. 3.8.: Theoretical and simulated (simu) variance  $\sigma_{\tilde{\varphi}_k}^2$  and MSE  $\epsilon_{\tilde{\varphi}_k}^2$ , and the CRLB  $c^{\varphi_k}$  of  $\varphi_k$  versus  $f_k + f_c$  (a)  $\nu_k = 5$  dB,  $\forall k$  (b)  $\nu_k = 28$  dB,  $\forall k$ .

become stronger when the frequency increases, we can expect that both the bias and the variance of  $\tilde{\varphi}_k$  will increase with the frequency.

In Fig. 3.8(a) and Fig. 3.8(b), we show for the same setup considered in Fig. 3.7(a) and Fig. 3.7(b) the theoretical variance  $\sigma_{\tilde{\varphi}_k}^2$  and MSE  $\epsilon_{\tilde{\varphi}_k}^2 = \sigma_{\tilde{\varphi}_k}^2 + (\mu_{\tilde{\varphi}_k} - \varphi_k)^2$  of the unwrapped phase  $\tilde{\varphi}_k$  ( $\mu_{\tilde{\varphi}_k}$  and  $\sigma_{\tilde{\varphi}_k}^2$  are computed from Eq. 3.111 and Eq. 3.112 respectively), the CRLB  $c^{\varphi_k}$  Eq. 3.102 of  $\varphi_k$ , and the variance and MSE of obtained by simulation (based on 10000 trials), all versus the frequency, for a local SNR of  $\nu_k = 5$  and 28 dB,  $\forall k$ , respectively.

In Fig. 3.8(a) (where a relatively low local SNR of  $\nu_k = 5$  dB is considered), we can see that the simulated variance and MSE follow closely the theoretical ones, which validates our theoretical approach. However, the variance and the MSE do not follow the CRLB, and they both increase with the frequency. This fact, which has been expected in our comments to the PDF of  $\tilde{\varphi}_k$  in Fig. 3.7(b), is due to the errors multiple of  $\pm 2\pi$  introduced by the unwrapping procedure.

In Fig. 3.8(b) (where a sufficiently high local SNR of  $\nu_k = 28$  dB is considered), we can see that the theoretical and simulated variance and MSE are all very close to the CRLB. In fact, the wrapped phase  $\hat{\varphi}_k$  is correctly unwrapped, and there are no  $\pm 2\pi$  errors that have been introduced by the unwrapping procedure, because the considered local SNR is very high.

### 3.3.3 Phase-slope-based and absolute-phase-based local TOA estimators

In the previous subsection, we have studied the wrapped  $\hat{\varphi}_k$  and unwrapped  $\tilde{\varphi}_k$  phases. Here, we propose two local TOA estimators based on the unwrapped phase  $\tilde{\varphi}_k$ .

In order to overcome the defect of the phase offset between the true phase  $\varphi_k$  and the unwrapped phase  $\tilde{\varphi}_k$  recognized in Fig. 3.6(a), we can define from Eq. 3.99 the first local TOA estimator based on the slope of  $\tilde{\varphi}_k$  as:

$$\tilde{\tau}_k^{bb} = \frac{\tilde{\varphi}_k - \tilde{\varphi}_0}{2\pi f_k}, k \neq 0 \quad (3.113)$$

where  $\tilde{\tau}_k^{bb}$  is referred to as the “local baseband TOA estimator” because the information on the time delay  $\tau$  is only carried by the frequency components  $f_k$  of the envelope (we have get rid of the information carried by  $f_c$ , see Eq. 3.99). By assuming (for simplicity of the exposition) that the samples of  $\tilde{\varphi}_k$  obtained at the different frequency tones are independent (not true due to the unwrapping procedure), the covariance of  $\tilde{\tau}_k^{bb}$  can be written as:

$$\Gamma(\tilde{\tau}_k^{bb}, \tilde{\tau}_{k'}^{bb}) = \begin{cases} \frac{\sigma_{\tilde{\varphi}_0}^2}{4\pi^2 f_k f_{k'}} & k \neq k' \\ \frac{\sigma_{\tilde{\varphi}_k}^2 + \sigma_{\tilde{\varphi}_0}^2}{4\pi^2 f_k^2} = \sigma_{\tilde{\tau}_k^{bb}}^2 & k = k' \end{cases} \quad (3.114)$$

where  $\sigma_{\tilde{\tau}_k^{bb}}^2$  denotes the variance of  $\tilde{\tau}_k^{bb}$ .

As the offset between  $\tilde{\varphi}_k$  and  $\varphi_k$  is multiple of  $2\pi$ , it can be estimated by:

$$\tilde{\Delta}\varphi = 2\pi \text{round} \left\{ \frac{2\pi f_c \tilde{\tau}^{bb} - \tilde{\varphi}_0}{2\pi} \right\} \quad (3.115)$$

where “round” denotes the “round to nearest integer” function, and  $\tilde{\tau}^{bb}$  the global slope-based estimator (i.e. the estimator involving the samples of the local estimator obtained at all frequency tones). The expression of  $\tilde{\tau}^{bb}$  is given in Sec. 3.3.4 as a linear combination of  $\tilde{\tau}_k^{bb}$  Eq. 3.113.

In order to benefit from the information carried on  $\tau$  by the passband frequency components, we can now define from Eq. 3.99 and Eq. 3.115 the second local TOA estimator, based on the absolute phase as:

$$\tilde{\tau}_k^{pb} = \frac{\tilde{\varphi}_k + \tilde{\Delta}\varphi}{2\pi(f_k + f_c)} \quad (3.116)$$

where  $\tilde{\tau}_k^{pb}$  is named “the local passband TOA estimator” because the information on  $\tau$  is carried now by the frequency components  $f_c + f_k$  of the real passband transmitted signal (see Eq. 3.99). By assuming  $\tilde{\Delta}\varphi$  equal to the true offset (true for sufficiently high SNRs), and by assuming that the samples of  $\tilde{\varphi}_k$  are independent, the covariance of  $\tilde{\tau}_k^{pb}$  can be written as:

$$\Gamma(\tilde{\tau}_k^{pb}, \tilde{\tau}_{k'}^{pb}) = \begin{cases} 0 & k \neq k' \\ \frac{\sigma_{\tilde{\varphi}_k}^2}{4\pi^2(f_k + f_c)^2} = \sigma_{\tilde{\tau}_k^{pb}}^2 & k = k' \end{cases} \quad (3.117)$$

where  $\sigma_{\tilde{\tau}_k^{pb}}^2$  denotes the variance of  $\tilde{\tau}_k^{pb}$ .

The local passband CRLB of  $\tau$  can be written from Eq. 3.99 and Eq. 3.102 as:

$$c_k^{pb} = \frac{1}{4\pi^2\nu_k(f_c + f_k)^2}. \quad (3.118)$$

By getting rid of the information carried on  $\tau$  by the central frequency  $f_c$  we can define the local baseband CRLB (equivalent to the envelope CRLB defined in Chap. 2) from Eq. 3.118 as:

$$c_k^{bb} = \frac{1}{4\pi^2\nu_k f_k^2}. \quad (3.119)$$

As for sufficiently high SNRs, the unwrapped phase becomes unbiased and its variance converges to its CRLB  $c^{\varphi_k}$  Eq. 3.102, we can deduce from Eq. 3.117 and Eq. 3.118 that the local passband TOA estimator becomes unbiased and achieves its local passband CRLB too. From Eq. 3.102, Eq. 3.114 and Eq. 3.119 we can see that the local baseband TOA estimator achieves asymptotically the sum  $c_0^{bb} + c_k^{bb}$ .

In Fig. 3.9, we show the local baseband and passband CRLBs ( $c_k^{bb}$  and  $c_k^{pb}$ ), and the MSEs of the local baseband and passband TOA estimators ( $\epsilon_{\tilde{\tau}_k^{bb}}^2$  and  $\epsilon_{\tilde{\tau}_k^{pb}}^2$ ) obtained by simulation based on 1000 trials, versus  $f_k + f_c$ . The transmitted signal is a Gaussian pulse of width  $T_w$  modulated by a carrier:

$$s(t) \propto e^{-2\pi\frac{t^2}{T_w^2}} \cos(2\pi f_c t).$$

We take  $T_w = 0.5$  ns,  $T_s = \frac{T_w}{4}$  (sampling period),  $f_c = 4$  GHz,  $\tau = 1$  ns,  $M = 32$  (number of samples) and  $\nu = 25$  dB (global SNR). We can see that  $\tilde{\tau}_k^{pb}$  achieves

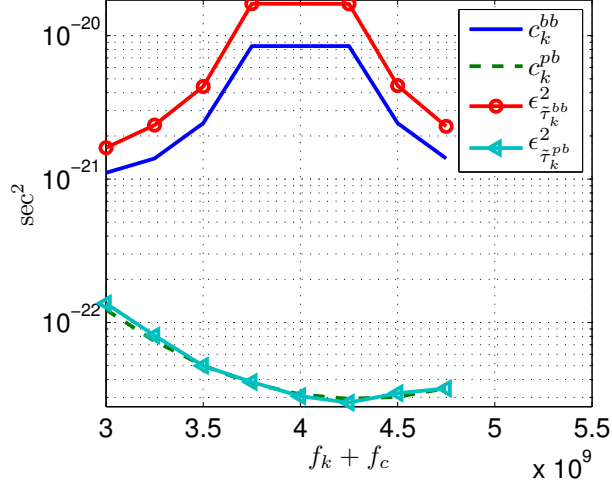


Fig. 3.9.: Local baseband and passband CRLBs ( $c_k^{bb}$ ,  $c_k^{pb}$ ), and MSEs of the local baseband and passband TOA estimators ( $\epsilon_{\tilde{\tau}_k^{bb}}^2$  and  $\epsilon_{\tilde{\tau}_k^{pb}}^2$ ) obtained by simulation, versus  $f_k + f_c$ .

the passband CRLB because the SNR is sufficiently high, whereas  $\tilde{\tau}_k^{bb}$  does not achieve the baseband CRLB. In fact, The gap between  $\epsilon_{\tilde{\tau}_k^{bb}}^2$  and  $c_k^{bb}$  is equal to the baseband CRLB  $c_0^{bb}$  at  $k = 0$  and corresponds to the term  $\frac{\sigma_{\tilde{z}_0}^2}{4\pi^2 f_k^2}$  in the expression of  $\sigma_{\tilde{\tau}_k^{bb}}^2$  in Eq. 3.114.

### 3.3.4 Phase-slope-based and absolute-phase-based global TOA estimators

In this subsection, we derive the global TOA estimators based on the local TOA estimators considered in Sec. 3.3.3.

The global baseband (resp. passband) TOA estimator  $\tilde{\tau}^{bb}$  (resp.  $\tilde{\tau}^{pb}$ ) is defined as the minimum-variance unbiased linear combination of the local estimators  $\tilde{\tau}_k^{bb}$ , ( $k = -\frac{M}{2}, \dots, \frac{M}{2} - 1$ ) (resp.  $\tilde{\tau}_k^{pb}$ ).

Consider  $M$  unbiased estimators  $\tilde{\zeta}_k$  of the same parameter  $\zeta$ . The minimum-variance unbiased linear combination of ( $\tilde{\zeta}_k$ ) is given by:

$$\tilde{\zeta} = \underline{\tilde{a}}_{\tilde{\zeta}}^T \underline{\tilde{\zeta}}; \begin{cases} \underline{\tilde{a}}_{\tilde{\zeta}} = \underset{\underline{a}}{\operatorname{argmin}} \{ \sigma_{\underline{a}^T \underline{\tilde{\zeta}}}^2 \} \\ \text{s. t. } \sum \underline{a} = 1 \end{cases} \Rightarrow \underline{\tilde{a}}_{\tilde{\zeta}} = \frac{\underline{\Gamma}_{\tilde{\zeta}}^{-1} \underline{\mathbf{1}}}{\sum (\underline{\Gamma}_{\tilde{\zeta}}^{-1} \underline{\mathbf{1}})} \quad (3.120)$$

where  $\{\cdot\}^T$  denotes the transpose operator,  $\underline{z}$  the vector  $(z_1 \cdots z_M)^T$ ,  $\sigma_{\underline{a}^T \underline{\tilde{\zeta}}}^2 = \mathcal{E}\{(\underline{a}^T (\underline{\tilde{\zeta}} - \zeta \underline{\mathbf{1}}))^2\}$  ( $\mathcal{E}\{\cdot\}$  denotes the expectation operator),  $\sum \underline{a}$  the sum of the

elements of  $\underline{a}$ ,  $\underline{1} = (1 \cdots 1)^T$ , and  $\underline{\Gamma}_{\underline{\zeta}}$  the covariance matrix of  $\underline{\zeta}$ . The variance of  $\tilde{\zeta}$  is given by:

$$\underline{\tilde{a}}^T \underline{\Gamma}_{\underline{\zeta}} \underline{\tilde{a}}.$$

From Eq. 3.114 and Eq. 3.120, we can write the global baseband estimator and its variance as:

$$\tilde{\tau}^{bb} = \frac{(\underline{\Gamma}_{\tilde{\tau}^{bb}}^{-1} \underline{1})^T}{\sum (\underline{\Gamma}_{\tilde{\tau}^{bb}}^{-1} \underline{1})} \tilde{\tau}^{bb} \quad (3.121)$$

$$\sigma_{\tilde{\tau}^{bb}}^2 = \underline{\tilde{a}}_{\tilde{\tau}^{bb}}^T \underline{C}_{\tilde{\tau}^{bb}} \underline{\tilde{a}}_{\tilde{\tau}^{bb}}. \quad (3.122)$$

Given that the covariance matrix of  $\tilde{\tau}^{pb}$  is diagonal (see Eq. 3.117), we can write the global passband estimator and its variance as:

$$\tilde{\tau}^{pb} = \frac{\sum_{k=0}^{N-1} \frac{\tilde{\tau}_k^{pb}}{\sigma_{\tilde{\tau}_k^{pb}}^2}}{\sum_{k=0}^{N-1} \frac{1}{\sigma_{\tilde{\tau}_k^{pb}}^2}} \quad (3.123)$$

$$\sigma_{\tilde{\tau}^{pb}}^2 = \frac{1}{\sum_{k=0}^{N-1} \frac{1}{\sigma_{\tilde{\tau}_k^{pb}}^2}}. \quad (3.124)$$

We can see from Eq. 3.121 and Eq. 3.123 that in order to compute the global baseband and passband TOA estimators, we need to know the covariances of the corresponding local estimators. These covariances can be computed from Eq. 3.114 and Eq. 3.117 based on the variance  $\sigma_{\tilde{\varphi}_k}^2$  Eq. 3.112 of  $\tilde{\varphi}_k$ . If we assume that  $\tilde{\varphi}_k$  achieves its CRLB  $c^{\varphi_k}$  Eq. 3.102, we can replace  $\sigma_{\tilde{\varphi}_k}^2$  in Eq. 3.121 and Eq. 3.123 by  $\frac{1}{\rho_{S_k}^2}$  (because  $c^{\varphi_k}$  is inversely proportional to  $\rho_{S_k}^2$ , see Eq. 3.102 and Eq. 3.103). If  $c^{\varphi_k}$  is not achieved by  $\tilde{\varphi}_k$  (due to the threshold phenomenon studied in Chap. 2), then the latter approach (i.e. replacing  $\sigma_{\tilde{\varphi}_k}^2$  by  $\frac{1}{\rho_{S_k}^2}$ ) will not be anymore optimal and the performances of the global estimators deteriorate with respect to what can be achieved by considering the true variance  $\sigma_{\tilde{\varphi}_k}^2$ . We have already seen in Fig. 3.8(a) that for relatively low local SNRs,  $\sigma_{\tilde{\varphi}_k}^2$  becomes much larger than the CRLB  $c^{\varphi_k}$ , and increases with the frequency.

Given that  $N_k$  in Eq. 3.98 is a white sequence (which makes the global log-likelihood function equal to the sum over  $k$  of the local log-likelihood functions in Eq. 3.101), the global passband and baseband CRLBs of  $\tau$  can be written from the corresponding local CRLBs in Eq. 3.118 and Eq. 3.119 as:

$$c^{pb} = \frac{1}{\sum_k \frac{1}{c_k^{pb}}} = \frac{1}{\sum_k 4\pi^2 \nu_k (f_c + f_k)^2} = \frac{1}{\nu(4\pi^2 f_c^2 + \beta_s^2)}$$

$$c^{bb} = \frac{1}{\sum_k \frac{1}{c_k^{bb}}} = \frac{1}{\sum_k 4\pi^2 \nu_k f_k^2} = \frac{1}{\nu \beta_s^2}$$

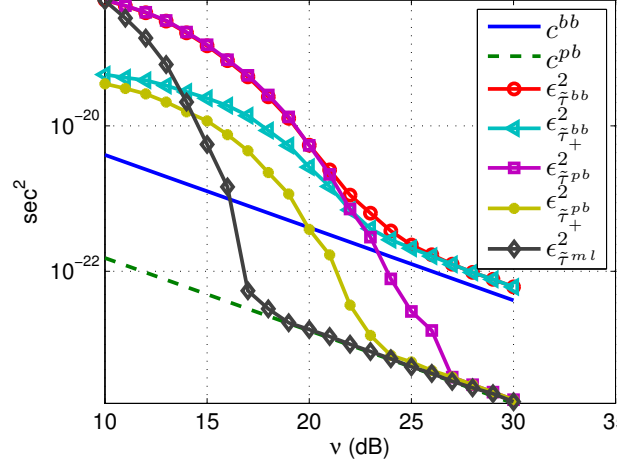


Fig. 3.10.: Global baseband  $c^{bb}$  and passband  $c^{pb}$  CRLBs, MSEs  $\epsilon_{\tilde{\tau}^{bb}}^2$ ,  $\epsilon_{\tilde{\tau}_+^{bb}}^2$ ,  $\epsilon_{\tilde{\tau}^{pb}}^2$  and  $\epsilon_{\tilde{\tau}_+^{pb}}^2$  (obtained by simulation) of the first  $\tilde{\tau}^{bb}$  and the second  $\tilde{\tau}_+^{bb}$  global baseband TOA estimators, and the first  $\tilde{\tau}^{pb}$  and the second  $\tilde{\tau}_+^{pb}$  global passband TOA estimators, and the MSE  $\epsilon_{\tilde{\tau}^{ml}}^2$  (obtained by simulation) of the time-domain MLE, all versus the SNR  $\nu$ .

where  $\nu$  is the global SNR defined in Eq. 3.104 and  $\beta_s^2 = \frac{\sum_k 4\pi^2 \rho_{s_k}^2 f_k^2}{\sum_k \rho_{s_k}^2}$  the discrete mean quadratic bandwidth of  $s[k]$ . Note that when the assumptions of Eq. 3.96 are satisfied, then the global SNR and the discrete mean quadratic bandwidth become equal to the SNR and the mean quadratic bandwidth of the continuous signal  $s(t)$ , respectively.

Denote by  $s_{pb}(t)$  and  $r_{pb}(t)$  the real passband transmitted and received signals respectively. We can write the time-domain MLE of  $\tau$  as:

$$\tilde{\tau}^{ml} = \underset{\zeta}{\operatorname{argmax}} \{r_{pb}(\zeta) \otimes s_{pb}(-\zeta)\}$$

where  $\otimes$  denotes the convolution operator.

In Fig. 3.10, we show the baseband and passband CRLBs ( $c^{bb}$  and  $c^{pb}$ ) of  $\tau$ , the MSEs ( $\epsilon_{\tilde{\tau}^{bb}}^2$  and  $\epsilon_{\tilde{\tau}^{pb}}^2$ ) obtained by simulation based on 10000 trials of the global baseband and passband TOA estimators ( $\tilde{\tau}^{bb}$  Eq. 3.121 and  $\tilde{\tau}^{pb}$  Eq. 3.123), and the MSE  $\epsilon_{\tilde{\tau}^{ml}}^2$  of the time-domain MLE  $\tilde{\tau}^{ml}$  obtained by simulation, all versus the global SNR  $\nu$ . We consider a modulated Gaussian pulse with  $T_w = 0.5$  ns,  $f_c = 4$  GHz,  $T_s = \frac{T_w}{4}$  (sampling period),  $\tau = 1$  ns, and  $M = 32$  (number of samples). For the MLE, the sampling period must be smaller than the expected accuracy ( $T_s^{ml} \leq \sqrt{c^{pb}}$ ). For instance we have taken  $T_s^{ml} = 1$  ps (125 times smaller than the DFT-based sampling period  $T_s$ ). The global TOA estimators

$\tilde{\tau}^{bb}$  and  $\tilde{\tau}^{pb}$  are computed from Eq. 3.121 and Eq. 3.123 respectively by assuming that  $\tilde{\varphi}_k$  achieves the CRLB  $c^{\varphi_k}$  of  $\varphi_k$ .

We can see that the global baseband estimator  $\tilde{\tau}^{bb}$  achieves asymptotically a multiple of the the baseband CRLB  $c^{bb}$  ( $\epsilon_{\tilde{\tau}^{bb}}^2 \approx 1.5c^{bb}$  at  $\nu = 28$  dB). This factor of 1.5 is due to the term  $\sigma_{\tilde{\varphi}_0}^2$  in the expression of the variance of the local baseband estimator  $\tilde{\tau}_k^{bb}$  and to the CR between the different samples of  $\tilde{\tau}_k^{bb}$  (see the covariance of  $\tilde{\tau}_k^{bb}$  in Eq. 3.114). Both the time-domain MLE  $\tilde{\tau}^{ml}$  and the global passband estimator  $\tilde{\tau}^{pb}$  achieve asymptotically the passband CRLB  $c^{pb}$ . However,  $\tilde{\tau}^{ml}$  achieves  $c^{pb}$  much faster than  $\tilde{\tau}^{pb}$  (8 dB of difference between the corresponding asymptotic SNR thresholds). We have already mentioned that many improvements can be introduced to our estimators for they achieve the baseband and passband CRLBs faster (e.g. considering the true variance  $\sigma_{\tilde{\varphi}_k}^2$  of  $\tilde{\varphi}_k$  instead of approximating it by the CRLB  $c^{\varphi_k}$ ).

We have to emphasize the fact that with time-domain-based estimators the sampling period should be smaller than the expected accuracy (i.e. the square root of the CRLB), or interpolation should be performed to find precisely the location of the global maximum. However, with the proposed DFT-based estimators, the required sampling frequency is equal to the bandwidth of the transmitted signal, and the TOA estimates are directly generated from a very small number of samples, and without any interpolation.

Below, we will briefly describe one more improved baseband estimator and another improved passband estimator. We have already seen that the unwrapping procedure introduces errors multiple of  $-2\pi$  to the unwrapped phase. These errors seriously deteriorate our estimators. In order to overcome this vexing defect, we first consider the following phase-slope-based TOA estimator:

$$\tilde{\tau}_k^{sp} = \frac{\tilde{\varphi}_k - \tilde{\varphi}_{k-1}}{2\pi\Delta f} \quad (3.125)$$

where  $\Delta f = \frac{1}{MT_s}$  (already defined in Eq. 3.97). Its covariance can be written as:

$$\Gamma(\tilde{\tau}_k^{sp}, \tilde{\tau}_{k'}^{sp}) = \begin{cases} 0 & |k - k'| > 1 \\ -\frac{\sigma_{\tilde{\varphi}_k}^2}{4\pi^2\Delta f^2} & k' = k + 1 \\ \frac{\sigma_{\tilde{\varphi}_k}^2 + \sigma_{\tilde{\varphi}_{k-1}}^2}{4\pi^2\Delta f^2} = \sigma_{\tilde{\tau}_k^{sp}}^2 & k' = k \end{cases} \quad (3.126)$$

where  $\sigma_{\tilde{\tau}_k^{sp}}^2$  denotes the variance of  $\tilde{\tau}_k^{sp}$ . In order to mitigate the  $-2\pi$  errors introduced by the unwrapping procedure, we force the time delay to be positive by putting the reference pulse at the beginning of the observation period, then compute  $\tilde{\tau}_k^{sp}$  Eq. 3.125 and only keep the positive samples. Denote by  $\tilde{\tau}_+^{sp}$  the vector containing the positive samples of  $\tilde{\tau}_k^{sp}$  and by  $\Gamma_{\tilde{\tau}_+^{sp}}$  the corresponding covariance matrix. A new global phase-slope-based TOA estimator can be obtained from

Eq. 3.120 and Eq. 3.126 as:

$$\tilde{\tau}_+^{sp} = \frac{(\underline{\Gamma}_{\tilde{\tau}_+^{sp}}^{-1} \underline{1})^T}{\sum (\underline{\Gamma}_{\tilde{\tau}_+^{sp}}^{-1} \underline{1})} \tilde{\tau}_+^{sp}. \quad (3.127)$$

Now, we want to find again the baseband and passband local and global TOA estimators using  $\tilde{\tau}_+^{sp}$  Eq. 3.127. To do so we generate from the wrapped phase  $\hat{\varphi}_k$  a new unwrapped phase  $\tilde{\varphi}_k^{sp}$ , which is not unwrapped recursively like  $\hat{\varphi}_k$ , but for each  $k$  we unwrap  $\hat{\varphi}_k$  with respect to  $2\pi(f_k + f_c)\tilde{\tau}_+^{sp}$  to obtain  $\tilde{\varphi}_k^{sp}$ . Accordingly,  $\tilde{\varphi}_k^{sp}$  falls now around the true phase  $\varphi_k$  and there is no phase offset (i.e. the phase offset is equal to zero for good SNRs) to be estimated like in Eq. 3.115. Denote by  $\tilde{\tau}_{k,+}^{bb}$  and  $\tilde{\tau}_+^{bb}$  the new local and global baseband TOA estimators respectively, and by  $\tilde{\tau}_{k,+}^{pb}$  and  $\tilde{\tau}_+^{pb}$  the new local and global passband estimators. Finally,  $\tilde{\tau}_{k,+}^{bb}$  is obtained from Eq. 3.113 after replacing  $\tilde{\varphi}_k$  by  $\tilde{\varphi}_k^{sp}$ ,  $\tilde{\tau}_+^{bb}$  from Eq. 3.121 using  $\tilde{\tau}_{k,+}^{bb}$  instead of  $\tilde{\tau}_k^{bb}$ ,  $\tilde{\tau}_{k,+}^{pb}$  from Eq. 3.116 after replacing  $\tilde{\varphi}_k + \tilde{\Delta}\varphi$  by  $\tilde{\varphi}_k^{sp}$ , and  $\tilde{\tau}_+^{pb}$  from Eq. 3.123 using  $\tilde{\tau}_{k,+}^{pb}$  instead of  $\tilde{\tau}_k^{pb}$ ,

The MSEs  $\epsilon_{\tilde{\tau}_+^{bb}}^2$  and  $\epsilon_{\tilde{\tau}_+^{pb}}^2$  (obtained by simulation) of  $\tilde{\tau}_+^{bb}$  and  $\tilde{\tau}_+^{pb}$  respectively, are shown in Fig. 3.10. We can see that the new global baseband estimator  $\tilde{\tau}_+^{bb}$  achieves the global baseband CRLB  $c^{bb}$  faster than the initial estimator  $\tilde{\tau}_+^{bb}$ , and the new global passband estimator  $\tilde{\tau}_+^{pb}$  achieves the global passband CRLB  $c^{pb}$  faster than the initial estimator  $\tilde{\tau}_+^{pb}$ . Still, the time-domain MLE achieves the global passband CRLB  $c^{pb}$  much faster than both the initial and the new global passband estimators. However, both the new global baseband and passband estimators outperform the time-domain MLE at low SNRs ( $\nu < 14$  dB).

### 3.3.5 DFT-based estimation in multipath channels

Consider now a multipath UWB channel with IR-UWB signals. The baseband channel impulse response can be written as:

$$h(t) = 2 \sum_{l=1}^L \alpha^{(l)} e^{-j2\pi f_c \tau^{(l)}} \delta(t - \tau^{(l)})$$

where  $\alpha^{(l)}$  and  $\tau^{(l)}$  denote the gain and the time delay introduced by the  $l$ th MPC. We assume that the relative delay between two neighboring MPCs is greater than the width of the transmitted pulses so the MPCs can be assumed resolvable. The corresponding baseband received signal can be written as:

$$r_{MP}(t) = s(t) \otimes h(t).$$

Denote by:

$$\Gamma_{r_{MP},s}(t) = |r_{MP}(t) \otimes s(-t)|$$

the modulus of the CCR of the baseband transmitted and received signals. We assume that the baseband received signal is sampled at a rate equal to the bandwidth  $B$  of  $s(t)$ .

The proposed estimator consists of two steps:

1. Coarse estimation: we estimate the time delays of the different MPCs as the locations of the peaks of  $\Gamma_{r_{MP},s}(t)$  crossing a given threshold.
2. Fine estimation: we consider a window around each MPC slightly wider than the pulse width and we apply our DFT-based estimators to each MPC separately.

The performances of the proposed multipath estimator are expected to be the same as those of the DFT-based estimators presented in the previous subsections.

### 3.4 CONCLUSION

In this chapter we have introduced a new receiver (the DM receiver) for TH-IR-UWB signals. We have computed for both the DM and the CR receivers, the local and global statistics and probabilities of error. We have seen that the CR receiver always outperforms the DM receiver.

We have proposed a new TOA estimator (the MME) based on the DM receiver. We have computed its asymptotic performances and derived some approximations of its local MSE. We have compared it with the MLE. The MME and the MLE approximately achieve the CRLB at the same SNR. However, the MLE slightly outperforms the MME in the ambiguity and the threshold regions.

We have proposed two TOA estimators (the global baseband estimator and the global passband estimator) based on the relative and the absolute unwrapped phase of the DFT of the received signal. We have derived the local estimators and combined them to get the corresponding global estimators. We have shown that the global baseband (resp. passband) estimator achieves asymptotically the global baseband (resp. passband) CRLB. We have seen that the time-domain MLE achieves the global passband CRLB faster than the global passband estimator which outperforms the MLE at low SNRs. Unlike the case of time-domain estimators where the sampling period should be in the same order of the expected accuracy, the proposed DFT-based estimators require a sampling frequency equal to the bandwidth of the transmitted signal, and estimate the TOA directly from few samples without performing any interpolation. We have calculated the statistics of the unwrapped phase. We have shown that our estimators can be improved for they achieve the CRLB faster. We have also described how the proposed estimators can be employed in MP channels.

## CHAPTER 4

---

# TOA ESTIMATION IN MULTIUSER SYSTEMS USING TH-IR-UWB SIGNALS: MAXIMUM-DELAYING-AND-MULTIPLYING AND MAXIMUM-CORRELATION ESTIMATORS

---

MULTIUSER interference is one of the major challenges in the realization of low-complexity TOA estimators. It has been already mentioned in Sec. 1.1.4 that few publications addressed this field in the literature.

In this chapter, we investigate the MME (maximum delaying-and-multiplying estimator) and the MCE (maximum correlation estimator) introduced in the previous chapter. We consider the case of single-user, then the case of multiuser. We evaluate the global performances of both estimators. We derive some approximations of the MSE and some approximate lower bounds. The MUI effects are studied by assuming both deterministic MUI and random MUI. Given that the effects of the MUI closely depend on the properties of the ACR and the CCR of the used waveforms, we propose some algorithms to generate THMA codes with minimum sidelobe ACR and minimum CCR.

The main contributions in this chapter are as follows:

- We derive some approximations of the MSE achieved by both estimators and some approximate lower bounds for the case of single-user, by employing the subdomain and the Ziv and Zakai methods introduced in Chap. 2. The obtained results allow us to examine the properties of the candidate TH-IR-UWB waveform before using it.

- We consider some particular setups with deterministic MUI, and analyzed for each case the potential of each estimator in mitigating the MUI.
- We derive an approximation of the MSE achieved by each estimator when the MUI is random. We have modeled the MUI as an AWGN. We have compared the derived approximations with the MSEs obtained by simulation and discussed the obtained results.

In Sec. 4.1, we introduce our system model. In Sec. 4.2, we consider the MCE and the MME and derive some MSE approximations and some approximate lower bounds. We handle the case of single-user in Sec. 4.3 and study the MUI effects in Sec. 4.4. In Sec. 4.5, we consider the generation of THMA codes with optimal properties.

## 4.1 MULTIUSER SYSTEM MODEL AND JOINT MLE AND CRLBS

In this section we describe the considered MU system model and derive the expressions of the joint MU gain and TOA MLE and the CRLBs for the joint MU gain and TOA estimation.

In Sec. 4.1.1 we describe the structure of the considered TH waveforms, and in Sec. 4.1.2 we consider the joint MLE and CRLBs.

### 4.1.1 Time-hopping waveforms

Denote by:

$$w_k(t) = \sqrt{\frac{E}{N_c}} \sum_{n=0}^{N_c-1} p(t - t_n^{(k)}) \quad (4.1)$$

the TH waveform of energy  $E$  and duration  $T$  transmitted by the  $k$ th user ( $k = 1, \dots, K$ ) ( $E$  and  $T$  are assumed to be equal for all users), where  $p(t)$  denotes the used pulse, and  $t_n^{(k)} \in [0, T[$ , ( $n = 0, \dots, N_c - 1$ ) the time delays introduced by the TH code to the  $N_c$  pulses of  $w_k(t)$  (called Waveform  $k$ ). The energy of  $p(t)$  is normalized to one.

We consider two types of TH waveforms:

- Waveforms with chip separation: the time delay corresponding to the  $n$ th pulse is given by:

$$t_n^{(k)} = nT_c + c_n^{(k)}T_h = (nN_h + c_n^{(k)})T_h \quad (4.2)$$

where  $T_c = \frac{T}{N_c}$  denotes the chip period (average pulse repetition period) (we have  $N_c$  chips per waveform),  $T_h = \frac{T_c}{N_h}$  the time-hop ( $N_h$  is the number of time-hops per chip), and

$$c^{(k)} = (c_n^{(k)})_{n=0, \dots, N_c-1}, \quad c_n^{(k)} \in \{0, \dots, N_h - 1\} \quad (4.3)$$

the TH codeword associated with the  $k$ th user (called User  $k$ ). In this case we have:

$$N_s = \frac{T}{T_h} = N_c N_h \quad (4.4)$$

time-hops per waveform.

- Waveforms without chip separation: in order to make the waveforms shorter, we directly split the waveform duration  $T$  into

$$N_s = N_h = \frac{T}{T_h} \quad (4.5)$$

time-hops so that the time delay corresponding to the  $n$ th pulse can be written as:

$$t_n^{(k)} = c_n^{(k)} T_h \quad (4.6)$$

where  $c_n^{(k)}$  is given in Eq. 4.3.

For both codes, the time-hop  $T_h$  should be larger than the pulse width  $T_w$ . Obviously, the waveform  $w_k(t)$  is totally contained in the interval:

$$I_T = \left[-\frac{T_h}{2}, T - \frac{T_h}{2}\right]. \quad (4.7)$$

Denote by:

$$\begin{aligned} X_{x,y}(\theta) &= \int_{-\infty}^{+\infty} x(t+\theta)y(t)dt \\ R_x(\theta) &= X_{x,x}(\theta) \\ E_x &= R_x(0) \end{aligned}$$

the CCR of the two generic signals  $x(t)$  and  $y(t)$ , the ACR and the energy of  $x(t)$ , respectively. From Eq. 4.1 we can write the CCR  $X_{w_k, w_{k'}}(\theta)$  of Waveforms  $k$  and  $k'$  and the ACR  $R_{w_k}(\theta)$  of Waveform  $k$  as:

$$X_{w_k, w_{k'}}(\theta) = \frac{E}{N_c} \sum_{n=0}^{N_c-1} \sum_{n'=0}^{N_c-1} R_p(\theta - [t_n^{(k)} - t_{n'}^{(k')}]) \quad (4.8)$$

$$R_{w_k}(\theta) = \frac{E}{N_c} \sum_{n=0}^{N_c-1} \sum_{n'=0}^{N_c-1} R_p(\theta - [t_n^{(k)} - t_{n'}^{(k)}]) \quad (4.9)$$

where  $R_p(\theta)$  is the ACR of  $p(t)$  ( $R_p(0) = E_p = 1$ ). As  $T_h > T_w$ , we can write  $R_p(\theta) \approx 0$  for  $\tau \notin [-\frac{T_h}{2}, \frac{T_h}{2}]$ .

Let us call  $\xi R_p(\theta - \zeta)$  ‘‘pulse ACR component’’ ( $\xi$  and  $\zeta$  denote two constants). We can see from Eq. 4.8 and Eq. 4.9 that  $X_{w_k, w_{k'}}(\theta)$  contains up to  $N_c^2$  pulse ACR components corresponding to the  $N_c^2$  possible couples  $(t_n^{(k)}, t_{n'}^{(k')})$ ,

$(n = 0, \dots, N_c - 1)$ ,  $(n' = 0, \dots, N_c - 1)$ . If, for  $M_j^{(k,k')}$  different couples  $(t_n^{(k)}, t_{n'}^{(k')})$  the relative delays  $t_n^{(k)} - t_{n'}^{(k')}$  are all equal to the same value  $t_j^{(k,k')}$ , then  $X_{w_k, w_{k'}}(\theta)$  will contain the pulse ACR component  $M_j^{(k,k')} \frac{E}{N_c} R_p(\theta - t_j^{(k,k')})$  (of amplitude  $M_j^{(k,k')} \frac{E}{N_c}$ , and located at  $t_j^{(k,k')}$ ). As for  $R_{w_k}(\theta)$ , the  $N_c$  different couples  $(t_n^{(k)}, t_n^{(k)})$ ,  $(n = 0, \dots, N_c - 1)$  have all the same relative delay  $t_n^{(k)} - t_n^{(k)} = 0$ ,  $R_{w_k}(\theta)$  contains up to  $N_c^2 - (N_c - 1) = N_c(N_c - 1) + 1$  pulse ACR components (for this reason, we will have  $N_0^{(k)} = N_c$ , below in Eq. 4.16). Let:

$$T^{(k,k')} = \{t_n^{(k)} - t_{n'}^{(k')} \mid_{n, n'=0, \dots, N_c-1}\} \quad (4.10)$$

$$T^{(k)} = \{t_n^{(k)} - t_{n'}^{(k)} \mid_{n, n'=0, \dots, N_c-1}\}. \quad (4.11)$$

Given that  $t_n^{(k)}$  is a multiple of  $T_h$ , we can write  $X_{w_k, w_{k'}}(\theta)$  and  $R_{w_k}(\theta)$  in the interval

$$I_{2T} = ] - T, T[ \quad (4.12)$$

as:

$$X_{w_k, w_{k'}}(\theta) = \frac{E}{N_c} \sum_{j=1}^{j^{(k,k')}} M_j^{(k,k')} R_p(\theta - t_j^{(k,k')}) \quad (4.13)$$

$$= \frac{E}{N_c} \sum_{i=-(N_s-1)}^{N_s-1} N_i^{(k,k')} R_p(\theta - iT_h) \quad (4.14)$$

$$R_{w_k}(\theta) = \frac{E}{N_c} \sum_{j=1}^{j^{(k)}} M_j^{(k)} R_p(\theta - t_j^{(k)}) \quad (4.15)$$

$$= \frac{E}{N_c} \sum_{i=-(N_s-1)}^{N_s-1} N_i^{(k)} R_p(\theta - iT_h) \quad (4.16)$$

where  $N_s$  is given in Eq. 4.4, Eq. 4.5,  $j^{(k,k')} \leq N_c^2$ ,  $M_j^{(k,k')} \in \{0, \dots, N_c\}$ ,  $j^{(k)} \leq N_c(N_c - 1) + 1$ ,  $M_j^{(k)} \in \{0, \dots, N_c\}$ ,  $\sum_{j=1}^{j^{(k,k')}} M_j^{(k,k')} = \sum_{i=-\infty}^{+\infty} N_i^{(k,k')} = \sum_{i=-\infty}^{+\infty} N_i^{(k)} = \sum_{j=1}^{j^{(k)}} M_j^{(k)} = N_c^2$ ,  $t_j^{(k,k')} \in T^{(k,k')}$ ,  $t_j^{(k)} \in T^{(k)}$ , and

$$N_i^{(k,k')} = \begin{cases} 0 & iT_h \notin T^{(k,k')} \\ M_j^{(k,k')} & iT_h = t_j^{(k,k')} \end{cases} \quad (4.17)$$

$$N_i^{(k)} = \begin{cases} N_c & i = 0 \\ 0 & iT_h \notin T^{(k)} \\ M_j^{(k)} & iT_h = t_j^{(k)}. \end{cases} \quad (4.18)$$

Note that both  $X_{w_k, w_{k'}}(\theta)$  and  $R_{w_k}(\theta)$  are null outside  $I_{2T}$  Eq. 4.12 because  $t_n^{(k)} \in [0, T[$ , ( $n = 0, \dots, N_c - 1$ ). From now on, we call  $M_j^{(k, k')}$ ,  $N_i^{(k, k')}$ ,  $M_j^{(k)}$  and  $N_i^{(k)}$  “normalized amplitudes”.

We can deduce that if

$$t_n^{(k)} - t_{n'}^{(k')} \neq t_m^{(k)} - t_{m'}^{(k')}, \quad \forall (n, n') \neq (m, m') \quad (4.19)$$

$$t_n^{(k)} - t_{n'}^{(k)} \neq t_m^{(k)} - t_{m'}^{(k)}, \quad \forall (n, n') \neq (m, m'), n \neq n', \quad (4.20)$$

then Waveforms  $k$  and  $k'$  will have minimum CCR, and Waveform  $k$  will have minimum sidelobe ACR, respectively. We mean by minimum CCR that  $X_{w_k, w_{k'}}(\theta)$  contains  $N_c^2$  different pulse ACR components of normalized amplitudes equal to one (i.e.  $M_j^{(k, k')} = 1, \forall j, N_i^{(k, k')} = 0$  or  $1, \forall i$ , in Eq. 4.13, Eq. 4.14), and by minimum sidelobe ACR that  $R_{w_k}(\theta)$  contains one pulse ACR component of normalized amplitude equal to  $N_c$ , and  $N_c(N_c - 1)$  other pulse ACR components of amplitude equal to one (i.e.  $M_j^{(k)} = N_c$  for  $t_j^{(k)} = 0, M_j^{(k)} = 1, \forall t_j^{(k)} \neq 0, N_0^{(k)} = N_c$  and  $N_i^{(k)} = 0$  or  $1, \forall i \neq 0$ , in Eq. 4.15, Eq. 4.16).

#### 4.1.2 Joint MLE and CRLBs for the multiuser gain and TOA

In this subsection we describe the considered MU system model and derive the expressions of the joint MU gain and TOA MLE and the CRLBs for the joint MU gain and TOA estimation. We consider in Sec. 4.1.2.1 the case where only one waveform is transmitted by each user, then in Sec. 4.1.2.2 the case where periodic signals are transmitted.

##### 4.1.2.1 One transmitted waveform per user

Let us assume here that every user only transmits one waveform. We can write the signal received through an AWGN channel as:

$$r(t) = \sum_{k=1}^K \alpha_k w_k(t - \Theta_k) + \tilde{v}_G(t) \quad (4.21)$$

where  $\alpha_k$  and  $\Theta_k$  denote, respectively the gain and the time delay introduced by the channel between User  $k$  and the receiver, and  $\tilde{v}_G(t)$  stands for the AWGN of two-sided power spectral density (PSD) of  $\frac{N_0}{2}$ .

Throughout this chapter, we consider User  $k$  as the user of interest, and the other as interfering users. We assume that the delay  $\Theta_k$  corresponding to User  $k$  has a deterministic unknown value in the *a priori* domain assumed equal to be equal to  $I_T$ :

$$D_\Theta = I_T = \left[-\frac{T_h}{2}, T - \frac{T_h}{2}\right]. \quad (4.22)$$

We also assume that the delays corresponding to the interfering users are uniformly distributed in  $D_\Theta$ . Accordingly, the maximum MSE (obtained when the

estimator becomes uniformly distributed in  $D_\Theta$ ) is given by:

$$e_U = \left( \Theta_k - \frac{T - T_h}{2} \right)^2 + \frac{T^2}{12}. \quad (4.23)$$

From Eq. 4.21, we can write the log-likelihood function for the joint estimation of all users parameters  $\underline{\alpha} = (\alpha_1 \cdots \alpha_K)^T$  and  $\underline{\Theta} = (\Theta_1 \cdots \Theta_K)^T$  as [78]:

$$\begin{aligned} \Lambda(\underline{\alpha}', \underline{\theta}) &= -\frac{1}{N_0} \int_{-\infty}^{+\infty} \left\{ r(t) - \sum_{k=1}^K \alpha'_k w_k(t - \theta_k) \right\}^2 dt \\ &= -\frac{1}{N_0} \left\{ E_r + \sum_{k=1}^K \sum_{k'=1}^K \alpha'_k \alpha'_{k'} X_{w_k, w_{k'}}(\theta_{k'} - \theta_k) - 2 \sum_{k=1}^K \alpha'_k X_{r, w_k}(\theta_k) \right\} \end{aligned} \quad (4.24)$$

$$(4.25)$$

where  $\underline{\alpha}' = (\alpha'_1 \cdots \alpha'_K)^T$  and  $\underline{\theta} = (\theta_1 \cdots \theta_K)^T$  denote the vectors of the users candidate gains and delays, respectively. From Eq. 4.21 we can write the CCR  $X_{r, w_k}(\theta)$ , in Eq. 4.25, of the received signal  $r(t)$  and Waveform  $k$  as:

$$\begin{aligned} X_{r, w_k}(\theta) &= \alpha_k R_{w_k}(\theta - \Theta_k) + \sum_{k'=1, k' \neq k}^K \alpha_{k'} X_{w_{k'}, w_k}(\theta - \Theta_{k'}) + v_k(\theta) \\ &= \alpha_k R_{w_k}(\theta - \Theta_k) + v_{MU}^{(k)}(\theta) + v_{G, k}(\theta) \end{aligned} \quad (4.26)$$

where  $v_{G, k}(\theta) = X_{\bar{v}_{G, w_k}}(\theta)$  is a zero-mean colored Gaussian noise of covariance given by:

$$C_{v_{G, k}}(\theta) = \mathcal{E} \{ v_{G, k}(t) v_{G, k}(t - \theta) \} = \frac{N_0}{2} R_{w_k}(\theta) \quad (4.27)$$

and

$$v_{MU}^{(k)}(\theta) = \sum_{k'=1, k' \neq k}^K \alpha_{k'} X_{w_{k'}, w_k}(\theta - \Theta_{k'}) \quad (4.28)$$

is the MUI component corrupting, beside the noise component  $v_{G, k}(\theta)$ , the useful correlation component  $\alpha_k R_{w_k}(\theta - \Theta_k)$ . Note that we can regard  $X_{r, w_k}(\theta)$  as the observation relative to User  $k$ . Note also that  $X_{r, w_k}(\theta)$  can be written as  $[\frac{E}{N_c}]^{\frac{1}{2}}$  times the correlation observation at the output of the correlation receiver presented in Chap. 3.

By assuming that the waveforms associated with different users are uncorrelated:

$$X_{w_k, w_{k'}}(\theta) = 0, \quad \forall \theta, \quad \forall k \neq k' \quad (4.29)$$

we can write the log-likelihood function in Eq. 4.25 as:

$$\Lambda(\underline{\alpha}', \underline{\theta}) = -\frac{1}{N_0} \left\{ E_r + E_w \sum_{k=1}^K (\alpha'_k)^2 - 2 \sum_{k=1}^K \alpha'_k X_{r, w_k}(\theta_k) \right\}. \quad (4.30)$$

As the energy  $E_r$  of the received signal is independent of the candidate gains  $\underline{\alpha}'$  and delays  $\underline{\theta}$ , we can easily show from Eq. 4.30, by equating to zero the partial derivatives of  $\Lambda(\underline{\alpha}', \underline{\theta})$  with respect to the elements of the vectors  $\underline{\alpha}'$  and  $\underline{\theta}$ , that the joint MLE of the gains  $\alpha_k$  and delays  $\Theta_k$  of all users ( $k = 1, \dots, K$ ) is given by:

$$\hat{\alpha}_k = \frac{X_{r,w_k}(\hat{\Theta}_k)}{E}, \quad (4.31)$$

$$\hat{\Theta}_k = \operatorname{argmax}_{\theta \in D_\Theta} \{X_{r,w_k}(\theta)\}. \quad (4.32)$$

We can see from the expression of the observation  $X_{r,w_k}(\theta)$  in Eq. 4.26 that, when the assumption of uncorrelated waveforms in Eq. 4.29 is not satisfied, then the estimator in Eq. 4.32 no longer corresponds to the MLE of  $\Theta_k$  due to the MUI component  $v_{MU}^{(k)}(\theta)$  in Eq. 4.28 corrupting  $X_{r,w_k}(\theta)$ . Note that  $\hat{\Theta}_k$  corresponds to the maximum correlation estimator already considered in Chap. 3.

Let us now compute the CRLBs for the joint estimation of  $\underline{\alpha}$  and  $\underline{\Theta}$ . The CRLBs of the elements of  $\underline{\alpha}$  and  $\underline{\Theta}$  are the diagonal elements of the inverse of the Fisher information matrix (FIM) given by [78]:

$$F(\underline{\alpha}, \underline{\Theta}) = (f_{\Phi_l, \Phi_{l'}})_{l, l'=1, \dots, 2K}, \quad \Phi_l \in (\underline{\alpha} | \underline{\Theta}) \quad (4.33)$$

$$f_{\Phi_l, \Phi_{l'}} = -\mathcal{E} \left\{ \frac{\partial^2 \Lambda(\underline{\alpha}', \underline{\theta})}{\partial \phi_l \partial \phi_{l'}} \Big|_{\phi_l = \Phi_l, \phi_{l'} = \Phi_{l'}} \right\}, \quad \phi_l \in (\underline{\alpha}' | \underline{\theta}).$$

Always under the assumption of uncorrelated waveforms, we can show from the expression of the log-likelihood function in Eq. 4.30 that the elements of the FIM in Eq. 4.33 can be written as:

$$f_{\alpha_k, \alpha_{k'}} = \frac{E}{N_0/2} \delta_{k, k'} \quad (4.34)$$

$$f_{\Theta_k, \Theta_{k'}} = \frac{\alpha_k^2 X_{w_k, \ddot{w}_k}(0)}{N_0/2} \delta_{k, k'} = \frac{\alpha_k^2 \ddot{R}_{w_k}(0)}{N_0/2} \delta_{k, k'} \quad (4.35)$$

$$f_{\Theta_k, \alpha_{k'}} = \frac{\alpha_k w_k(t) \Big|_{-\infty}^{+\infty}}{N_0/2} \delta_{k, k'} = 0 \quad (4.36)$$

where  $\delta_{k, k'} = \begin{cases} 1, & k=k' \\ 0, & k \neq k' \end{cases}$ . We have assumed in Eq. 4.36 that  $w_k(t) \rightarrow 0$  as  $t \rightarrow \pm\infty$ . We can see from Eq. 4.34, Eq. 4.35 and Eq. 4.36 that the FIM  $F(\underline{\alpha}, \underline{\Theta})$  is diagonal, so we can write the CRLBs of  $\alpha_k$  and  $\Theta_k$  as:

$$c_{\alpha_k} = \frac{1}{f_{\alpha_k, \alpha_k}} = \frac{1}{\rho_t} \quad (4.37)$$

$$c_{\Theta_k} = \frac{1}{f_{\Theta_k, \Theta_k}} = \frac{1}{\rho_k \beta_w^2} \quad (4.38)$$

where

$$\rho = \frac{\alpha^2 E_w}{N_0/2} \quad (4.39)$$

$$\begin{aligned} \beta_w^2 &= -\frac{\ddot{R}_{w_k}(0)}{E} = \frac{E_{\dot{w}_k}}{E} = \frac{\int_{-\infty}^{+\infty} 4\pi^2 f^2 |\mathcal{F}_{w_k}(f)|^2 df}{\int_{-\infty}^{+\infty} |\mathcal{F}_{w_k}(f)|^2 df} \\ &\approx \int_{-\infty}^{+\infty} 4\pi^2 f^2 |\mathcal{F}_p(f)|^2 df = \beta_p^2 \end{aligned} \quad (4.40)$$

denote, respectively the SNR and the MQBW of  $w_k(t)$ . We assume that  $\beta_w^2$  is the same for all users, and is equal to the MQBW of the used pulse  $p(t)$ . In Eq. 4.40 we denote by  $\mathcal{F}_{w_k}(f)$  and  $\mathcal{F}_p(f)$  the Fourier Transforms of  $w_k(t)$  and  $p(t)$ , respectively.

We recall that the expressions of the MLEs and the CRLBs of  $\alpha_k$  and  $\Theta_k$  in Eq. 4.31, Eq. 4.32, Eq. 4.37 and Eq. 4.37 are all obtained under the assumption of uncorrelated waveforms in Eq. 4.29. In practice, this assumption can be satisfied only if the multiple-access codes are orthogonal and the users are synchronized. As we consider in this work the localization in asynchronous systems, the uncorrelated waveforms assumption is not satisfied, so the estimators in Eq. 4.31 and Eq. 4.32 no longer correspond to the MLEs and the CRLBs in Eq. 4.37 and Eq. 4.37 can no longer be necessarily achieved. To obtain the true joint MLE corresponding to this case, we have to maximize the log-likelihood function in Eq. 4.24 and Eq. 4.25, which is obviously much more complicated to perform.

Nevertheless, in the sake of designing low complexity receivers, we will employ the estimators in Eq. 4.31 and Eq. 4.32. Therefore, it is interesting to reduce as much as possible the effects of the MUI component  $v_{MU}^{(k)}(\theta)$  in  $X_{r,w_k}(\theta)$  Eq. 4.26. From the expressions of  $v_{MU}^{(k)}(\theta)$  Eq. 4.28 and the CCR  $X_{w_k,w_{k'}}(\theta)$  Eq. 4.13 of Waveforms  $k$  and  $k'$ , one may intuitively says that it is possible to reduce the effects of  $v_{MU}^{(k)}(\theta)$  by considering waveforms with minimum CCR components  $N_i^{(k,k')} R_p(\theta - iT_h)$  (i.e.  $N_i^{(k,k')} = 0$  or  $1, \forall i$ ).

We have also seen in Chap. 2 that the performances of any nonlinear estimation problem fully depend on the shape of the ACR, and that they drastically deteriorate at low and medium SNRs due to the presence of strong local maxima in the ACR. Therefore, it seems to be interesting to consider waveforms with minimum sidelobe ACR components  $N_i^{(k)} R_p(\theta - iT_h)$  (i.e.  $N_i^k = 0$  or  $1, \forall i \neq 0$ , see Eq. 4.15). The design of waveforms with both minimum sidelobe ACR and minimum CCR is investigated below in Sec. 4.5.

#### 4.1.2.2 Periodic transmitted signals

Assume now that the waveforms of the different users are periodically transmitted. This assumption matches to the reality more than the last assumption

of only one transmitted waveform does. In this case, we can write the signal transmitted by User  $k$  and the signal received from all users as:

$$s_k(t) = \sum_{i=-\infty}^{+\infty} w_k(t - iT) \quad (4.41)$$

$$r(t) = \sum_{k=1}^K \alpha_k s_k(t - \Theta_k) + \tilde{v}_G(t). \quad (4.42)$$

As the signal transmitted by User  $k$  is infinite, we have to correlate at the receiver side by the waveform  $w_k(t)$  instead of the whole transmitted signal. Therefore, all the integrals considered above should now be computed in an interval of duration  $T$ . Obviously, this can be performed using the circular ACR and CCR. Without loss of generality, let us assume that the interval of interest (i.e. period of observation) is  $I_T$  Eq. 4.7. We can then define the circular CCR of the signals  $x(t)$  and  $y(t)$  inside  $I_T$  as:

$$X_{x,y}^C(\theta) = \int_{I_T} x(t) \sum_{i=-\infty}^{+\infty} y(t - iT - \theta) dt. \quad (4.43)$$

It can be easily seen that  $X_{x,y}^C(\theta)$  is  $T$ -periodic. Now all the signals  $X_{w_k, w_{k'}}(\theta)$ ,  $R_{w_k}(\theta)$ ,  $X_{r, w_k}(\theta)$ ,  $v_{G,k}(\theta)$  and  $v_{MU}^{(k)}(\theta)$  should be replaced by their circular versions.

Let us first consider the circular CCR  $X_{w_k, w_{k'}}^C(\theta)$  of Waveforms  $k$  and  $k'$  and the circular ACR  $R_{w_k}^C(\theta)$  of Waveform  $k$ . We can show from the non-circular CCR  $X_{w_k, w_{k'}}(\theta)$  and ACR  $R_{w_k}(\theta)$  in Eq. 4.14 and Eq. 4.16 respectively that we can write  $X_{w_k, w_{k'}}^C(\theta)$  and  $R_{w_k}^C(\theta)$  inside  $I_T$  as:

$$X_{w_k, w_{k'}}^C(\theta) = \frac{E}{N_c} \sum_{i=0}^{N_s-1} N_{i,C}^{(k,k')} R_p(\theta - iT_h) \quad (4.44)$$

$$R_{w_k}^C(\theta) = \frac{E}{N_c} \sum_{i=0}^{N_s-1} N_{i,C}^{(k)} R_p(\theta - iT_h), \quad (4.45)$$

where

$$N_{i,C}^{(k,k')} = \begin{cases} N_0^{(k,k')} & i = 0 \\ N_i^{(k,k')} + N_{i-N_c}^{(k,k')} & i \neq 0 \end{cases}$$

$$N_{i,C}^{(k)} = \begin{cases} N_c & i = 0 \\ N_i^{(k)} + N_{i-N_c}^{(k)} & i \neq 0, \end{cases}$$

with  $N_i^{(k,k')}$  and  $N_i^{(k)}$  being the normalized amplitudes corresponding to the non-circular CCR and ACR, respectively (see Eq. 4.14, Eq. 4.16, Eq. 4.17 and

Eq. 4.18). Note that the main difference between the non-circular CCR and ACR, and the circular ones, is that the latter contain all the pulse ACR components which are contained in the former, but concentrated in the interval  $I_T$  Eq. 4.7 (instead of being spread out in  $I_{2T}$  Eq. 4.12).

Note that the circular CCR expression in Eq. 4.44 can be interpreted as follows: if the circular relative delay  $(\Theta_{k'} - \Theta_k)^C$  (where  $(\Theta_{k'} - \Theta_k)^C = \Theta_{k'} - \Theta_k + \kappa T$ ,  $\Theta_{k'} - \Theta_k + \iota T \in I_T$ ,  $\kappa$  integer) corresponding to the signals  $w_{k'}(t - \Theta_{k'})$  and  $w_k(t - \Theta_k)$  is equal to  $iT_h$ , then we will have  $N_{i,C}^{(k,k')}$  colliding pulses.

Let us now consider the circular versions of the signals  $R_{w_k}(\theta - \Theta_k)$  and  $X_{w_{k'},w_k}(\theta - \Theta_{k'})$  in Eq. 4.26 and Eq. 4.28 respectively. Let:

$$i_k = \text{round}\left(\frac{\Theta_k}{T_h}\right) \quad (4.46)$$

$$\delta_k = \Theta_k - i_k T_h \quad (4.47)$$

$$\theta_i^{(k)} = \delta_k + iT_h \quad (4.48)$$

where round denotes the ‘‘round to nearest integer’’ function (we have  $|\delta_k| \leq \frac{T_h}{2}$ ). From Eq. 4.44 and Eq. 4.45, we can write:

$$R_{w_k}^C(\theta \ominus \Theta_k) = \frac{E}{N_c} \sum_{i=0}^{N_s-1} L_i^{(k)} R_p(\theta - \theta_i^{(k)}) \quad (4.49)$$

$$X_{w_{k'},w_k}^C(\theta \ominus \Theta_{k'}) = \frac{E}{N_c} \sum_{i=0}^{N_s-1} L_i^{(k',k)} R_p(\theta - \theta_i^{(k')}) \quad (4.50)$$

where  $\ominus$  denotes the operator of the circular shifting to the right, with

$$L_i^{(k)} = \begin{cases} N_{i-i_k,C}^{(k)} & i = i_k, \dots, N_s - 1 \\ N_{N_s-i_k+i,C}^{(k)} & i = 0, \dots, i_k - 1 \end{cases} \quad (4.51)$$

$$L_i^{(k',k)} = \begin{cases} N_{i-i_{k'},C}^{(k',k)} & i = i_{k'}, \dots, N_s - 1 \\ N_{N_s-i_{k'}+i,C}^{(k',k)} & i = 0, \dots, i_{k'} - 1. \end{cases} \quad (4.52)$$

In the case of periodic waveforms, two categories of estimators can be considered. In the first category we look at the whole received signal to estimate the TOA, whereas in the second category we only look at the received signal in the interval  $I_T$ . From the first category, we can give the example of the estimator consisting on correlating the whole received signal, using the normal correlation, with the waveform of the user of interest, then looking at the maximum in the *a priori* domain of  $\Theta_k$ . From the second category, we can give the example of the estimator consisting on correlating the received signal inside  $I_T$ , using the circular correlation, with the waveform of the user of interest, then looking at the maximum. We can show that the second estimator outperforms the first one.

In fact, the first estimator introduces noise components from outside  $I_T$ . However, the main drawback of the second estimator is that, for signals modulated with data, we have to consider all the cases possible for two consecutive data symbols, then to correlate for each case, the received signal inside  $I_T$ , with the two consecutive waveforms corresponding to that case.

Note that in this work, we consider the case of periodic transmitted signals, and study some estimators from the second category where we only look at the received signal in the interval  $I_T$ .

#### 4.2 MSE APPROXIMATIONS AND APPROXIMATE LOWER BOUNDS FOR THE MAXIMUM-CORRELATION ESTIMATOR AND THE MAXIMUM-DELAYING-AND-MULTIPLYING ESTIMATOR

In this section we consider the MME and the MCE already introduced in Chap. 3. In Sec. 4.2 we derive for both estimators the general expressions of the MSE approximation based on the subdomain method proposed in Chap. 2, and of the approximate ZZLB and BTLB also proposed in Chap. 2, then we consider the special case of single-user in Sec. 4.3 and the case of multiuser in Sec. 4.4.

In the system model considered now, where the transmitted signals are periodic, the CR (resp. DM) receiver consist on filtering the received signal with the filter matched to the used pulse  $p(t)$ , retaining the piece of the filtered signal falling inside the interval  $I_T$  Eq. 4.7, circularly delaying the retained filtered piece by the delays  $-t_n^{(k)}$ , ( $i = 0, \dots, N_c - 1$ ) corresponding to the different pulses of Waveform  $k$ , then adding (resp. multiplying) the  $N_c$  delayed signals.

Denote by  $X_{r,p}^{(k)}(\theta)$  the filtered signal inside  $I_T$  (i.e. before performing the delaying operation). From Eq. 4.1, Eq. 4.41 and Eq. 4.42, we can write  $X_{r,p}^{(k)}(\theta)$  as:

$$X_{r,p}^{(k)}(\theta) = \alpha_k \sqrt{\frac{E}{N_c}} \sum_{n=0}^{N_c-1} R_p(\theta - t_n^{(k)} \ominus \Theta_k) + u^{(k)}(\theta) \quad (4.53)$$

$$u^{(k)}(\theta) = u_{MU}^{(k)}(\theta) + u_G(\theta) \quad (4.54)$$

$$u_{MU}^{(k)}(\theta) = \sqrt{\frac{E}{N_c}} \sum_{k'=1, k' \neq k}^K \alpha_{k'} \sum_{n=0}^{N_c-1} R_p(\theta - t_n^{(k')} \ominus \Theta_{k'}) \quad (4.55)$$

where  $u^{(k)}(\theta)$  denotes the total noise,  $u_{MU}^{(k)}(\theta)$  the MUI noise, and  $u_G(\theta)$  a zero-mean colored Gaussian noise of covariance given by:

$$C_{u_G}(\theta) = \frac{N_0}{2} R_p(\theta). \quad (4.56)$$

Let us split the *a priori* domain  $D_\Theta$  Eq. 4.22 into the subdomains:

$$D_i^{(k)} = [\theta_i^{(k)} - \frac{T_h}{2}, \theta_i^{(k)} + \frac{T_h}{2}], \quad (i = 0, \dots, N_s - 1). \quad (4.57)$$

Note that if  $\delta_k \neq 0$ , then  $D_0^{(k)} \cup \dots \cup D_{N_s-1}^{(k)}$  corresponds to a slightly translated version of  $D_\Theta$ . Denote by:

$$u_i^{(k)}(\theta) = \begin{cases} u^{(k)}(\theta) & \theta \in D_i^{(k)} \\ 0 & \theta \notin D_i^{(k)} \end{cases} \quad (4.58)$$

$$u_{G,i}^{(k)}(\theta) = \begin{cases} u_G^{(k)}(\theta) & \theta \in D_i^{(k)} \\ 0 & \theta \notin D_i^{(k)} \end{cases} \quad (4.59)$$

$$u_{MU,i}^{(k)}(\theta) = \begin{cases} u_{MU}^{(k)}(\theta) & \theta \in D_i^{(k)} \\ 0 & \theta \notin D_i^{(k)} \end{cases} \quad (4.60)$$

the total, Gaussian and MUI noise components inside the subdomain  $D_i^{(k)}$ , respectively.

Denote by  $P_{r,p}^{(k)}(\theta)$  and  $A_{r,p}^{(k)}(\theta)$  the signals at the outputs of the DM and CR receivers (called like in Chap. 3, DM and CR observations), respectively. From Eq. 4.53 and Eq. 4.49 we can write:

$$P_{r,p}^{(k)}(\theta) = \sum_{i=0}^{N_s-1} P_i^{(k)}(\theta) \quad (4.61)$$

$$A_{r,p}^{(k)}(\theta) = \sum_{i=0}^{N_s-1} A_i^{(k)}(\theta) \quad (4.62)$$

$$P_i^{(k)} = \prod_{l=0}^{L_i^{(k)}-1} \left\{ \alpha \sqrt{\frac{E}{N_c}} R_p(\theta - \theta_i^{(k)}) + u_{i,l}^{(k)}(\theta) \right\} \prod_{l=L_i^{(k)}}^{N_c-1} u_{i,l}^{(k)}(\theta) \quad (4.63)$$

$$A_i^{(k)} = \sum_{l=0}^{L_i^{(k)}-1} \left\{ \alpha \sqrt{\frac{E}{N_c}} R_p(\theta - \theta_i^{(k)}) + u_{i,l}^{(k)}(\theta) \right\} \sum_{l=L_i^{(k)}}^{N_c-1} u_{i,l}^{(k)}(\theta) \quad (4.64)$$

where  $u_{i,0}^{(k)}(\theta), \dots, u_{i,N_c-1}^{(k)}(\theta)$  correspond to a permutation of the  $N_c$  noise components  $w_{n+t_0^{(k)}/T_h}(\theta \oplus t_0^{(k)}), \dots, w_{n+t_{N_c-1}^{(k)}/T_h}(\theta \oplus t_{N_c-1}^{(k)})$  (see Eq. 4.59) (we denote by  $\oplus$  the operator of the circular shifting to the left).

Let us consider the MCE  $\hat{\Theta}_{cr}^{(k)}$  and the MME  $\hat{\Theta}_{dm}^{(k)}$ . These estimators have been already utilized in Chap. 3. They consist on maximizing the outputs of the CR and DM receivers, respectively. Accordingly, we can write:

$$\hat{\Theta}_{cr}^{(k)} = \underset{\theta \in D_\Theta}{\operatorname{argmax}} \{ A_{r,p}^{(k)}(\theta) \} \quad (4.65)$$

$$\hat{\Theta}_{dm}^{(k)} = \underset{\theta \in D_\Theta}{\operatorname{argmax}} \{ P_{r,p}^{(k)}(\theta) \}. \quad (4.66)$$

Denote by  $e_{cr}^{(k)}$  and  $e_{dm}^{(k)}$  the MSEs achieved by the MCE  $\hat{\Theta}_{cr}^{(k)}$  Eq. 4.65 and the MME  $\hat{\Theta}_{dm}^{(k)}$  Eq. 4.66, respectively. For simplicity, we use from now on the

subscript  $x$  to refer to both the CR and the DM receivers (i.e.  $x = cr$  or  $dm$ ) (e.g.  $\hat{\Theta}_x^{(k)}$ ,  $e_x^{(k)}$ ).

Using the subdomain method presented in Chap. 2, we can write the MSE  $e_x^{(k)}$  achieved by the estimator  $\hat{\Theta}_x^{(k)}$  as:

$$e_x^{(k)} = \sum_{i=0}^{N_s-1} \mathcal{P}_{x,i}^{(k)} e_{x,i}^{(k)} = \sum_{i=0}^{N_s-1} \mathcal{P}_{x,i}^{(k)} [(\Theta_k - \mu_{x,i}^{(k)})^2 + (\sigma_{x,i}^{(k)})^2] \quad (4.67)$$

where  $\mathcal{P}_{x,i}^{(k)} = \mathcal{P}\{\hat{\Theta}_x^{(k)} \in D_i^{(k)}\}$  denotes the probability that the estimator  $\hat{\Theta}_x^{(k)}$  falls in the subdomain  $D_i^{(k)}$  (subdomain probability), and  $\mu_{x,i}^{(k)}$ ,  $(\sigma_{x,i}^{(k)})^2$  and  $e_{x,i}^{(k)}$  the mean, the variance and the MSE of the subdomain estimator  $\hat{\Theta}_{x,i}^{(k)}$  defined by  $\hat{\Theta}_{x,i}^{(k)} = \{\hat{\Theta}_x^{(k)} | \hat{\Theta}_x^{(k)} \in D_i^{(k)}\}$  (subdomain mean, variance and MSE).

We have seen in Sec. 2.1.3.1 that  $\mathcal{P}_{x,i}^{(k)}$  can be approximated by:

$$\mathcal{P}_{x,i}^{(k)(3)} = \frac{\mathcal{P}_{x,i}^{(k)(2)}}{\sum_{i=0}^{N_s-1} \mathcal{P}_{x,i}^{(k)(2)}} \quad (4.68)$$

where

$$\mathcal{P}_{x,i}^{(k)(2)} = \begin{cases} 1 & i = i_k \\ \mathcal{P}\{O_{r,p}^{(k)}(\theta_i^{(k)}) > O_{r,p}^{(k)}(\Theta_k)\} & i \neq i_k, \end{cases} \quad (4.69)$$

with  $O_{r,p}^{(k)}(\theta)$  being the observation at the output of the receiver of interest (i.e.  $O = A$  for the CR receiver and  $P$  for the DM receiver). We have already defined  $i_k$  in Eq. 4.46 and  $\theta_i^{(k)}$  in Eq. 4.48.

Note that  $\mathcal{P}_{x,i}^{(k)(2)}$  in Eq. 4.69 corresponds to the global probability of error considered in Sec. 3.1.4 in the case of single-user, and  $e_{x,i_k}^{(k)}$  in Eq. 4.67 to the local MSE considered in Sec. 3.2.3 in the same case of single-user. Remind that  $i_k$  Eq. 4.46 is the index of the subdomain  $D_{i_k}^{(k)}$  containing the global maximum of the useful observation. Accordingly,  $\mathcal{P}_{x,i_k}^{(k)}$  is the probability of the local error (i.e. probability that the estimator  $\hat{\Theta}_x^{(k)}$  falls inside  $D_{i_k}^{(k)}$ ).

By approximating the probability of the local error  $\mathcal{P}_{x,i_k}^{(k)}$  by 1 (because  $e_{x,i_k}^{(k)} \ll e_{x,i}^{(k)}$ ,  $i \neq i_k$ ),  $\mu_{x,i}^{(k)}$  by  $\theta_i^{(k)}$  Eq. 4.48 (because the width  $T_h$  of  $D_i^{(k)}$  is much smaller than  $|\theta_i^{(k)} - \Theta_k|$ ) and neglecting  $(\sigma_{x,i}^{(k)})^2$  for  $i \neq 0$  (because  $(\sigma_{x,i}^{(k)})^2$  is upper bounded by  $\frac{T_h^2}{12}$  which is much smaller than  $(\theta_i^{(k)} - \Theta_k)^2$ ), we can approximate  $e_x^{(k)}$  Eq. 4.67 by:

$$e_{1,x}^{(k)} = e_{x,i_k}^{(k)} + T_h^2 \sum_{i=0, i \neq i_k}^{N_s-1} \mathcal{P}_{x,i}^{(k)} (i - i_k)^2. \quad (4.70)$$

Denote by:

$$\mathcal{P}_{x,g}^{(k)} = \sum_{i=0, i \neq i_k}^{N_s-1} \mathcal{P}_{x,i}^{(k)} = 1 - \mathcal{P}_{x,i_k}^{(k)} \quad (4.71)$$

the probability of the global error (i.e. probability that the estimator  $\hat{\Theta}_x^{(k)}$  falls outside  $D_{i_k}^{(k)}$ ). By assuming  $\mathcal{P}_{x,i_k}^{(k)} = 1$ , that all subdomains, except  $D_{i_k}^{(k)}$ , have equal probabilities (i.e.  $\mathcal{P}_{x,i}^{(k)} = \frac{\mathcal{P}_{x,g}^{(k)}}{N-1}$ ,  $\forall i \neq i_k$ ) and that the subdomain estimator  $\hat{\Theta}_{x,i}^{(k)}$  is uniformly distributed in  $D_i^{(k)}$  (i.e.  $\mu_{x,i}^{(k)} = \theta_i^{(k)}$  and  $(\sigma_{x,i}^{(k)})^2 = \frac{T_h^2}{12}$ ,  $\forall i \neq i_k$ ), we get from Eq. 4.67 the following MSE approximation:

$$\begin{aligned} e_{2,x}^{(k)} &= e_{x,i_k}^{(k)} + \frac{\mathcal{P}_{x,g}^{(k)}}{N-1} T_h^2 \sum_{i=0, i \neq i_k}^{N_s-1} \left[ (i - i_k)^2 + \frac{1}{12} \right] \\ &= e_{x,i_k}^{(k)} + \mathcal{P}_{x,g}^{(k)} \frac{N}{N-1} \left\{ T_h^2 \sum_{i=0}^{N_s-1} \frac{1}{N} \left[ (i - i_k)^2 + \frac{1}{12} \right] - \frac{1}{N} \frac{T_h^2}{12} \right\} \\ &= e_{x,i_k}^{(k)} + \mathcal{P}_{x,g}^{(k)} \frac{N}{N-1} \left\{ e_U - \frac{1}{N} \frac{T_h^2}{12} \right\} \\ &\approx e_{x,i_k}^{(k)} + \mathcal{P}_{x,g}^{(k)} e_U \end{aligned} \quad (4.72)$$

where  $e_U^{(k)}$  is the maximum MSE given in Eq. 4.23. To simplify the discussion, we can approximate  $\mathcal{P}_{x,g}^{(k)}$  by:

$$\mathcal{P}_{x,g,\min}^{(k)} = (N_s - 1) \min_{i \neq i_k} \{ \mathcal{P}_{x,i}^{(k)} \}, \quad (4.73)$$

and so we obtain from Eq. 4.72 an approximation that acts globally (i.e. with respect to the effects of the shape of the considered TH waveform) as an approximate lower bound. However, the behavior of  $e_{2,x}^{(k)}$  depends locally (i.e. with respect to the effects of the shape of the used pulse) on the approximation adopted for the local MSE  $e_{x,i_k}^{(k)}$ . As we will see later, the approximate lower bound obtained from Eq. 4.72 and Eq. 4.73 is very interesting because it is independent of the used codeword.

Let us now consider the derivation of the approximate ZZLB. As shown in Sec. 2.1.4, if the minimum probability of error corresponding to the considered observation can be written as a function of one variable, then we can write the approximate ZZLB as:

$$z_x^{(k)} = \int_0^{\epsilon^{(k)}} \xi P_{\min,x}^{(k)}(\xi) d\xi, \quad (4.74)$$

where  $P_{\min,x}^{(k)}(\xi)$  denotes the minimum probability of error to find, and

$$\epsilon^{(k)} = \max \left\{ \epsilon_1^{(k)}, \epsilon_2^{(k)} \right\} \quad (4.75)$$

with

$$\begin{aligned}\epsilon_1^{(k)} &= \min \left\{ \Theta_k + \frac{T_h}{2}, \epsilon_0^{(k)} \right\} \\ \epsilon_2^{(k)} &= \min \left\{ T - \frac{T_h}{2} - \Theta_k, \epsilon_0^{(k)} \right\} \\ \epsilon_0^{(k)} &= \min \left\{ 2 \left( \Theta_k + \frac{T_h}{2} \right), 2 \left( T - \frac{T_h}{2} - \Theta_k \right) \right\}.\end{aligned}$$

As we will see later, the shape of  $P_{\min,x}^{(k)}(\xi)$  follows that of the circular ACR  $R_{w_k}^C(\theta)$  in Eq. 4.45. Accordingly,  $P_{\min,x}^{(k)}(\xi)$  is even around  $iT_h$  in the interval  $[iT_h - \frac{T_h}{2}, iT_h + \frac{T_h}{2}]$  for  $i \neq 0$  (because the corresponding pulse ACR component is even) so  $\int_{-\frac{T_h}{2}}^{\frac{T_h}{2}} \xi P_{\min,x}^{(k)}(\xi + iT_h) d\xi = 0$ . Taking this fact into account, we can write  $z_x^{(k)}$  from Eq. 4.74 as:

$$\begin{aligned}z_x^{(k)} &= \int_0^{\frac{T_h}{2}} \xi P_{\min,x}^{(k)}(\xi) d\xi + \sum_{i=1}^{i^{(k)}} \int_{iT_h - \frac{T_h}{2}}^{iT_h + \frac{T_h}{2}} \xi P_{\min,x}^{(k)}(\xi) d\xi \\ &= \int_0^{\frac{T_h}{2}} \xi P_{\min,x}^{(k)}(\xi) d\xi + \sum_{i=1}^{i^{(k)}} \int_{-\frac{T_h}{2}}^{\frac{T_h}{2}} (\xi + iT_h) P_{\min,x}^{(k)}(\xi + iT_h) d\xi \\ &= \int_0^{\frac{T_h}{2}} \xi P_{\min,x}^{(k)}(\xi) d\xi + T_h \sum_{i=1}^{i^{(k)}} i \int_{-\frac{T_h}{2}}^{\frac{T_h}{2}} P_{\min,x}^{(k)}(\xi + iT_h) d\xi \\ &= z_{x,0}^{(k)} + T_h^2 \sum_{i=1}^{i^{(k)}} i \bar{z}_{x,i}^{(k)}\end{aligned}\tag{4.76}$$

where

$$z_{x,0}^{(k)} = \int_0^{\frac{T_h}{2}} \xi P_{\min,x}^{(k)}(\xi) d\xi\tag{4.77}$$

denotes the local approximate ZZLB (the one considered in Chap. 2 for the CR receiver and in Chap. 3 for the DM receiver) with

$$\bar{z}_{x,i}^{(k)} = \frac{1}{T_h} \int_{-\frac{T_h}{2}}^{\frac{T_h}{2}} P_{\min,x}^{(k)}(\xi + iT_h) d\xi\tag{4.78}$$

the average of the minimum probability of error in the interval  $[iT_h - \frac{T_h}{2}, iT_h + \frac{T_h}{2}]$  for  $i \neq 0$ , and

$$i^{(k)} = \text{round} \left( \frac{\epsilon^{(k)} - \frac{T_h}{2}}{T_h} \right) - 1.\tag{4.79}$$

Let:

$$\bar{z}_{x,\min}^{(k)} = \min_{i \neq 0} \{ \bar{z}_{x,i}^{(k)} \}.\tag{4.80}$$

From Eq. 4.76 and Eq. 4.80, we obtain the following approximate lower bound:

$$z_{1,x}^{(k)} = z_{x,0}^{(k)} + \bar{z}_{x,\min}^{(k)} T_h^2 \frac{i^{(k)}(i^{(k)} + 1)}{2} \approx z_{x,0}^{(k)} + \bar{z}_{x,\min}^{(k)} \frac{(\epsilon^{(k)})^2}{2} \quad (4.81)$$

where  $\epsilon^{(k)}$  is the upper integration limit in Eq. 4.74. The last approximate ZZLB is very interesting because it is valid for any considered codeword.

Let us now consider the derivation of the approximate BTLB. As shown in Sec. 2.1.4, we can write the approximate BTLB as:

$$b_x^{(k)} = \int_0^{\epsilon^{(k)}} \xi V\{P_{\min,x}^{(k)}(\xi)\} d\xi \quad (4.82)$$

where  $V\{\cdot\}$  denotes the valley-filling function. We have already mentioned that the shape of  $P_{\min,x}^{(k)}(\xi)$  follows that of the circular ACR  $R_{w_k}^C(\theta)$  in Eq. 4.45. Accordingly, the global maximum of  $P_{\min,x}^{(k)}(\xi)$  in each interval  $[iT_h - \frac{T_h}{2}, iT_h + \frac{T_h}{2}]$  is located at  $\xi = iT_h$ . Denote by  $i_1, \dots, i_{N_{b,x}^{(k)}}$  the indexes of the intervals containing the highest normalized amplitudes  $N_{i,C}^{(k)}$  (see Eq. 4.45) in the descending order starting from  $i = 1$ . We look at the intervals with  $i = 1, \dots, i^{(k)}$  ( $i^{(k)}$  is given in Eq. 4.79). We can write:

$$i_1 = \operatorname{argmax}_{i=1, \dots, i^{(k)}} N_{i,C}^{(k)} \quad (4.83)$$

$$i_j = \operatorname{argmax}_{i=i_{j-1}, \dots, i^{(k)}} N_{i,C}^{(k)} \quad (4.84)$$

$$i_{N_{b,x}^{(k)}} = i^{(k)} \quad (4.85)$$

Accordingly,  $b_x^{(k)}$  can be written as:

$$\begin{aligned} b_x^{(k)} &= \int_0^{\frac{T_h}{2}} \xi V\{P_{\min,x}^{(k)}(\xi)\} d\xi + \sum_{i=1}^{i^{(k)}} \int_{iT_h - \frac{T_h}{2}}^{iT_h + \frac{T_h}{2}} \xi V\{P_{\min,x}^{(k)}(\xi)\} d\xi \\ &= \int_0^{\frac{T_h}{2}} \xi V\{P_{\min,x}^{(k)}(\xi)\} d\xi + P_{\min,x}^{(k)}(i_1 T_h) \int_{\frac{T_h}{2}}^{i_1 T_h} \xi d\xi \\ &\quad + \sum_{j=2}^{N_{b,x}^{(k)}} P_{\min,x}^{(k)}(i_j T_h) \int_{i_{j-1} T_h}^{i_j T_h} \xi d\xi \\ &= b_{x,0}^{(k)} + \frac{T_h^2}{2} \left[ P_{\min,x}^{(k)}(i_1 T_h)(i_1^2 - 0.5^2) + \sum_{j=2}^{N_{b,x}^{(k)}} P_{\min,x}^{(k)}(i_j T_h)(i_j^2 - i_{j-1}^2) \right] \quad (4.86) \end{aligned}$$

where

$$b_{x,0}^{(k)} = \int_0^{\frac{T_h}{2}} \xi V\{P_{\min,x}^{(k)}(\xi)\} d\xi \quad (4.87)$$

denotes the local approximate BTLB (the one considered in Chap. 2 for the CR receiver and in Chap. 3 for the DM receiver).

When the used code is with minimum sidelobe ACR, then the maximum normalized amplitude (i.e.  $N_{i,C}^{(k)}$  in Eq. 4.45) is less than or equal to one for  $\forall i \neq 0$ . By assuming that the last pulse MPC ACR component falls in the interval  $[(N_s - 1)T_h - \frac{T_h}{2}, (N_s - 1)T_h + \frac{T_h}{2}]$ , then we can show that  $N_{b,x}^{(k)} = 1$  (see Eq. 4.85) so  $b_x^{(k)}$  becomes from Eq. 4.86:

$$b_{1,x}^{(k)} = b_{x,0}^{(k)} + \frac{T_h^2}{2} P_{\min,x}^{(k)} (i_1 T_h) (i_1^2 - 0.5^2) \approx b_{x,0}^{(k)} + \bar{b}_{x,\min}^{(k)} \frac{(\epsilon^{(k)})^2}{2} \quad (4.88)$$

where

$$\bar{b}_{x,\min}^{(k)} = P_{\min,x}^{(k)} (i T_h); N_{i,C}^{(k)} = 1. \quad (4.89)$$

The bound in Eq. 4.88 is also a bound that fits to any codeword. It is very close globally to that given in Eq. 4.81. However, it depends locally on the used pulse shape (like we have seen in Chap. 2).

Finally, note that if we are only interested in the global performances of the used TH waveforms then we can replace  $e_{x,i_k}^{(k)}$  in Eq. 4.70 and Eq. 4.72,  $z_{x,0}^{(k)}$  in Eq. 4.76 and Eq. 4.81, and  $b_{x,0}^{(k)}$  in Eq. 4.86 and Eq. 4.88 by the CRLB.

### 4.3 TOA ESTIMATION WITH SINGLE-USER

In this section, we consider the case where only one user is transmitting. The goal is to study the impact of the shape of the used TH waveform on the achieved MSE, and then to compare the performances of TH codes with and without minimum sidelobe ACR. Another point to mention is that the case of multiuser with random MUI is very similar to the case of single-user. In fact, the main difference between both cases is how the MUI noise will be modeled. However, the case of single-user is totally different from that of multiuser with deterministic MUI. As the case of single-user is considered, the corrupting noise is only the AWGN.

In this work, we only consider deterministic codes. We mean by deterministic codes that the codewords associated with the different users are known. Considering the case of deterministic codes seems to be more interesting than the case of random codes, because it allows us to examine the performances of the candidate codeword before using it. However, by just studying the average performances of a given random code, we may generate a codeword with very bad performances even the average performances are very good.

In Sec. 4.3.1 we consider the MCE and in Sec. 4.3.2 the MME.

### 4.3.1 Maximum-correlation estimator

We consider here the maximum correlation estimator. The MSE approximations and approximate lower bounds that we will evaluate here are  $e_{1,cr}^{(k)}$  Eq. 4.70,  $e_{2,cr}^{(k)}$  Eq. 4.72,  $z_{cr}^{(k)}$  Eq. 4.76,  $z_{1,cr}^{(k)}$  Eq. 4.81,  $b_{cr}^{(k)}$  Eq. 4.86 and  $b_{1,cr}^{(k)}$  Eq. 4.88.

To compute  $e_{1,cr}^{(k)}$  Eq. 4.70 based on the probability approximation in Eq. 4.68, we need  $\mathcal{P}_{cr,i}^{(k)(2)}$  Eq. 4.69, which corresponds to the global CR probability of error computed in Sec. 3.1.4. From Eq. 3.67 and Eq. 4.49 we can write  $\mathcal{P}_{cr,i}^{(k)(2)}$  as:

$$\mathcal{P}_{cr,i}^{(k)(2)} = Q\left(\sqrt{\frac{\rho}{2}\left[1 - \frac{L_i^{(k)}}{N_c}\right]}\right). \quad (4.90)$$

To compute  $e_{2,cr}^{(k)}$  Eq. 4.72 we need  $\mathcal{P}_{cr,g,\min}^{(k)}$  Eq. 4.73. By noticing that the lowest  $L_i^{(k)}$  is equal to zero, we can easily show from Eq. 4.68, Eq. 4.69, Eq. 4.73 and Eq. 4.90 that:

$$\mathcal{P}_{cr,g,\min}^{(k)} = Q\left(\sqrt{\frac{\rho}{2}}\right). \quad (4.91)$$

Notice that the expression of  $e_{2,cr}^{(k)}$  Eq. 4.72 obtained by means of Eq. 4.91 is very easy to evaluate, especially if we replace  $e_{x,i_k}^{(k)}$  by the CRLB. We recall that  $e_{x,i_k}^{(k)}$  corresponds to the local MSE approximated in Chap. 2.

To compute  $z_{cr}^{(k)}$  Eq. 4.76 we need  $P_{\min,cr}^{(k)}(\xi)$ . We can show from the expression of the CR observation in Eq. 4.62 and Eq. 4.64 and from Eq. 4.45 that  $P_{\min,x}^{(k)}(\xi)$  can be written as:

$$P_{\min,cr}^{(k)}(\xi) = Q\left(\sqrt{\frac{\rho}{2}\left[1 - \sum_{i=0}^{i_{z,b}^{(k)}} \frac{N_{i,C}^{(k)}}{N_c} R_p(\xi - iT_h)\right]}\right) \quad (4.92)$$

where

$$i_{z,b}^{(k)} = \text{round}\left(\frac{\max\left\{\Theta_k + \frac{T_h}{2}, T - \frac{T_h}{2} - \Theta_k\right\}}{T_h}\right) - 1. \quad (4.93)$$

From Eq. 4.92 we can see that  $\bar{z}_{cr,i}^{(k)}$  Eq. 4.78 used in  $z_{cr}^{(k)}$  Eq. 4.76 is given by:

$$\bar{z}_{cr,i}^{(k)} = \frac{1}{T_h} \int_{-\frac{T_h}{2}}^{\frac{T_h}{2}} Q\left(\sqrt{\frac{\rho}{2}\left[1 - \frac{N_{i,C}^{(k)}}{N_c} R_p(\xi)\right]}\right) d\xi. \quad (4.94)$$

To compute  $z_{1,cr}^{(k)}$  Eq. 4.81 we need  $\bar{z}_{cr,\min}^{(k)}$  Eq. 4.80. Now, we can easily see from Eq. 4.94 that  $\bar{z}_{cr,\min}^{(k)}$  is given by:

$$\bar{z}_{cr,\min}^{(k)} = Q\left(\sqrt{\frac{\rho}{2}}\right). \quad (4.95)$$

Again, the expression of  $z_{1,cr}^{(k)}$  Eq. 4.81 becomes very easy to compute by making use of Eq. 4.95.

To compute  $b_{cr}^{(k)}$  Eq. 4.86 and  $b_{1,cr}^{(k)}$  Eq. 4.88 we need  $P_{\min,cr}^{(k)}(i_j T_h)$  and  $\bar{b}_{cr,\min}^{(k)}$  Eq. 4.89 respectively. Now, we can easily see from Eq. 4.92 that:

$$P_{\min,cr}^{(k)}(i_j T_h) = Q\left(\sqrt{\frac{\rho}{2}\left[1 - \frac{N_{i_j,C}^{(k)}}{N_c}\right]}\right) \quad (4.96)$$

$$\bar{b}_{cr,\min}^{(k)} = Q\left(\sqrt{\frac{\rho}{2}\left[1 - \frac{1}{N_c}\right]}\right). \quad (4.97)$$

Let us consider some THMA codewords with and without minimum sidelobe ACR and compute the derived MSE approximation and approximate ZZLB and BTLB, as well as the MSE obtained by simulation.

We consider the following three codewords with  $N_c = 5$  and  $N_s = 25$ :

- $c_1 = (0, 1, 3, 7, 12)$  (with minimum sidelobe ACR);
- $c_2 = (3, 14, 16, 20, 24)$  (randomly generated);
- $c_3 = (0, 1, 2, 3, 4)$  (with equidistant pulses).

We use the FCC pulse used in Chap. 3 (i.e. with pulse width of  $T_w = 0.228$  ns and carrier of  $f_c = 6.85$  GHz). We take  $T_h = 0.5$  ns and  $\Theta_k = 12T_h$ . From Eq. 4.79 and Eq. 4.75, we have  $\epsilon^{(k)} = \frac{T}{2}$  and  $i^{(k)} = 12$  and from Eq. 4.93 we have  $i_{z,b}^{(k)} = 12$ .

In Fig. 4.1(a), Fig. 4.1(b) and Fig. 4.1(c), we show the circular ACR  $R_{w_k}^C(\theta)$  Eq. 4.45 normalized with respect to  $\frac{E}{N_c}$ , corresponding to  $c_1$ ,  $c_2$ , and  $c_3$  respectively. We can see that with  $c_1$  the normalized amplitudes of all sidelobe ACR components are equal to one, whereas with  $c_2$  we have sidelobe components with normalized amplitudes equal to one, two and three, and with  $c_3$  normalized amplitudes equal to one, two, three and four.

In order to make the equations of the approximate ZZLB and BTLB more clear we show in Fig. 4.2(a), Fig. 4.2(b) and Fig. 4.2(c), for the considered codewords, the minimum probability of error  $P_{\min,cr}^{(k)}(\xi)$  Eq. 4.92 and its version after applying the valley-filling function. We take  $\rho = 0$  dB. Now the derivation of Eq. 4.76 can be understood by looking at  $P_{\min,cr}^{(k)}(\xi)$  for any considered code. To understand Eq. 4.86 we look at  $P_{\min,cr}^{(k)}(\xi)$  and  $V\{P_{\min,cr}^{(k)}(\xi)\}$  for the second code; in this case we have  $N_{b,cr}^{(k)} = 3$  Eq. 4.85. To understand Eq. 4.88 we look at  $P_{\min,cr}^{(k)}(\xi)$  and  $V\{P_{\min,cr}^{(k)}(\xi)\}$  for the first code; in this case we have  $N_{b,x}^{(k)} = 1$ . By examining  $P_{\min,cr}^{(k)}(\xi)$  we can see that for oscillating pulse ACR, the average  $\bar{z}_{cr,i}^{(k)}$  Eq. 4.94 can be approximated by  $\bar{z}_{cr,\min}^{(k)}$  Eq. 4.95; this is in fact due to the

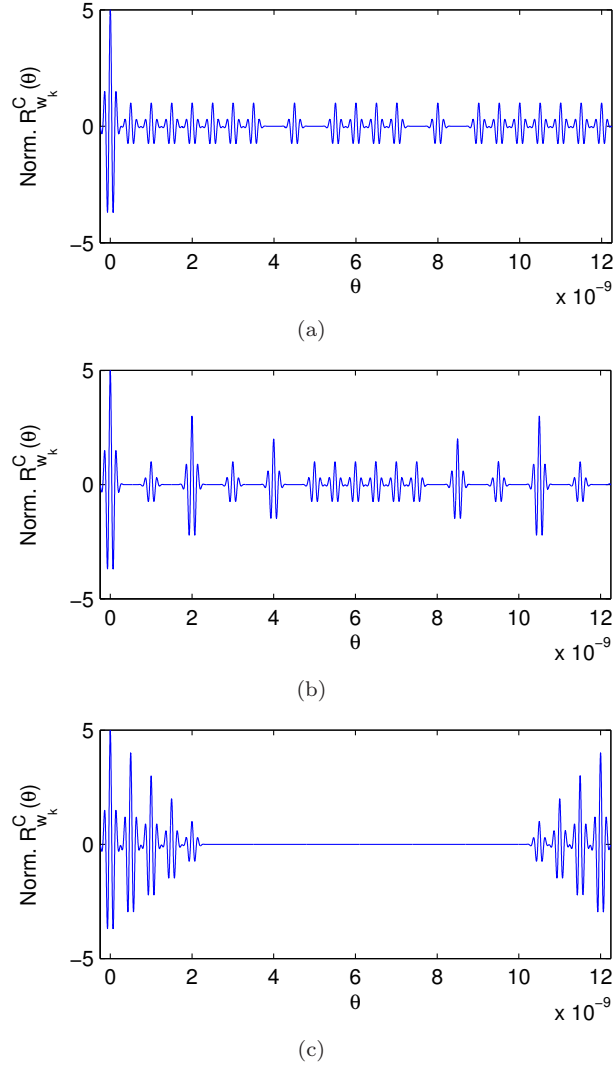
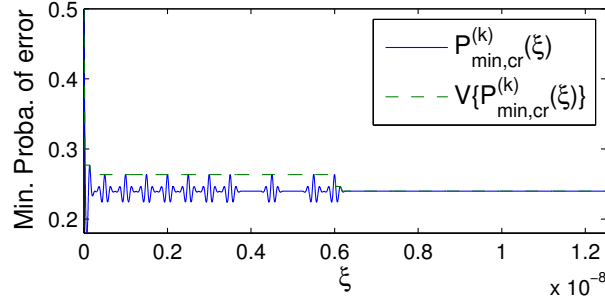


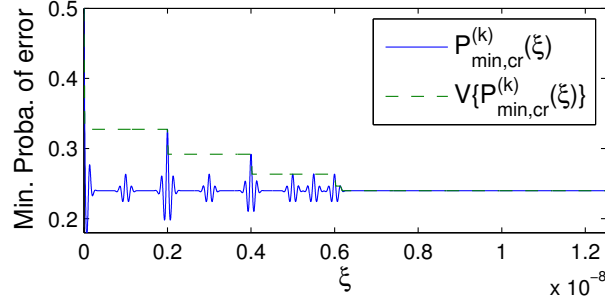
Fig. 4.1.: Normalized circular ACR  $R_{w_k}^C(\theta)$  of the codewords ( $N_c = 5$  and  $N_s = 25$ ): (a)  $c_1 = (0, 1, 3, 7, 12)$  (b)  $c_2 = (3, 14, 16, 20, 24)$  (c)  $c_3 = (0, 1, 2, 3, 4)$ .

average of  $R_p(\xi)$  which is approximately null, and to the approximate linearity of  $P_{\min,cr}^{(k)}(\xi)$  with respect to  $R_p(\xi)$ .

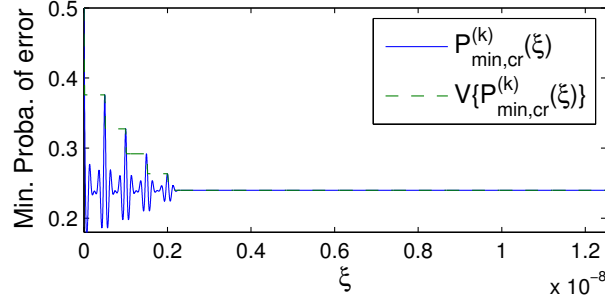
In Fig. 4.3(a), Fig. 4.3(b) and Fig. 4.3(c) we show for  $c_1$ ,  $c_2$ , and  $c_3$  respectively, the maximum MSE  $e_U$  Eq. 4.23, the CRLB  $c_{\Theta_k}$  Eq. 4.38 (we have omitted the subscript  $\Theta_k$ ), the MSE obtained by simulation  $e_{S,cr}$ , the MSE approxima-



(a)



(b)



(c)

Fig. 4.2.: Minimum probability of error  $P_{\min,cr}^{(k)}(\xi)$  before and after filling its valleys, for the codewords ( $N_c = 5$  and  $N_s = 25$ ): (a)  $c_1 = (0, 1, , 3, 7, 12)$  (b)  $c_2 = (3, 14, 16, 20, 24)$  (c)  $c_3 = (0, 1, 2, 3, 4)$ .

tions  $e_{1,cr}$  Eq. 4.70 and  $e_{2,cr}$  (approximate lower bound) Eq. 4.72 (we have omitted the superscript  $(k)$ ), the approximate ZZLBs  $z_{cr}$  Eq. 4.76 and  $z_{1,cr}$  Eq. 4.81, and BTLBs  $b_{cr}$  Eq. 4.86 and  $b_{1,cr}$  Eq. 4.88 (the superscript  $(k)$  is omitted), all with respect to the SNR  $\rho$ . We can observe that:

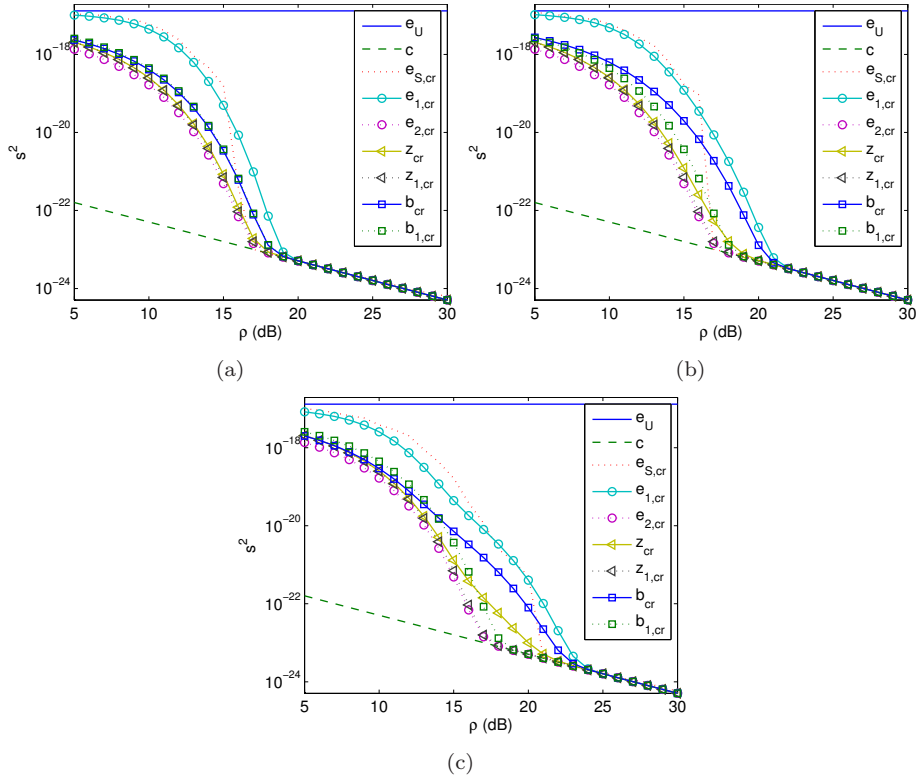


Fig. 4.3.: Maximum correlation estimator (MCE): maximum MSE  $e_U$ , CRLB  $c$ , MSE obtained by simulation  $e_{S,cr}$ , MSE approximations  $e_{1,cr}$  and  $e_{2,cr}$ , approximate ZZLBs  $z_{cr}$  and  $z_{1,cr}$ , and approximate BTLBs  $b_{cr}$  and  $b_{1,cr}$ , with respect to the SNR  $\rho$  in dB (a) codeword  $c_1$  (b) codeword  $c_2$  (c) codeword  $c_3$ .

- The MSE obtained by simulation  $e_{S,cr}$  converges to the CRLB at  $\rho = 17$  dB with both  $c_1$  and  $c_2$ , and at  $\rho = 21$  dB with  $c_3$ . The codeword  $c_1$  with minimum sidelobe ACR slightly outperforms  $c_2$  randomly generated, whereas both  $c_1$  and  $c_2$  highly outperform  $c_3$  due to the strong sidelobes in the ACR of the latter.
- The MSE approximation  $e_{1,cr}$  is very close to  $e_{S,cr}$  below the asymptotic region but converges to the CRLB later than  $e_{S,cr}$ . The same problem is observed with the approximate BTLB  $b_{cr}$  which is only tight below the asymptotic region. We think that this problem is due to some issues related to the simulation (the number of trials should probably be larger than 10000).
- The approximate ZZLB  $z_{cr}$  act very well in all regions.

- The approximate lower bounds  $e_{2,cr}$ ,  $z_{1,cr}$  and  $b_{1,cr}$  (stated to be valid for any codeword) act very well.

### 4.3.2 Maximum-delaying-and-multiplying estimator

We consider here the MME. The MSE approximations and approximate lower bounds that we want to evaluate here are  $e_{1,dm}^{(k)}$  Eq. 4.70,  $e_{2,dm}^{(k)}$  Eq. 4.72,  $z_{1,dm}^{(k)}$  Eq. 4.81,  $b_{dm}^{(k)}$  Eq. 4.86 and  $b_{1,dm}^{(k)}$  Eq. 4.88. We do not compute here  $z_{dm}^{(k)}$  Eq. 4.76 because the continuous minimum probability of error function  $P_{\min,dm}^{(k)}(\xi)$  is not easy to evaluate.

Similarly to the case of the maximum correlation estimator, the required probabilities of error have been already computed in Sec. 3.1.4. However, with the DM receiver we have seen in Sec. 3.1.4 that probabilities are evaluated by simulation, and under the Gaussian approximation.

From Eq. 3.52 we can write  $\mathcal{P}_{dm,i}^{(k)(2)}$  (needed to compute  $e_{1,dm}^{(k)}$ ) as:

$$\mathcal{P}_{dm,i}^{(k)(2)} = 1 + 2\mathcal{P}_{dm,i,1}^{(k)(2)}\mathcal{P}_{dm,i,2}^{(k)(2)} - (\mathcal{P}_{dm,i,1}^{(k)(2)} + \mathcal{P}_{dm,i,2}^{(k)(2)}) \quad (4.98)$$

where  $\mathcal{P}_{dm,i,1}^{(k)(2)}$  and  $\mathcal{P}_{dm,i,2}^{(k)(2)}$  are given under the Gaussian approximation from Eq. 3.69 and Eq. 3.70 by:

$$\mathcal{P}_{dm,i,1}^{(k)(2)} = Q\left(-\sqrt{\frac{\rho}{L_i^{(k)}N_c}}\right) \quad (4.99)$$

$$\mathcal{P}_{dm,i,2}^{(k)(2)} = Q\left(\left[\frac{(N_c - L_i^{(k)})N_c}{\rho} + \left[\frac{N_c}{\rho}\right]^{N_c - L_i^{(k)}}\right]^{-\frac{1}{2}}\right) \quad (4.100)$$

and by simulation from Eq. 3.71 and Eq. 3.72 by:

$$\mathcal{P}_{dm,i,1}^{(k)(2)} = \mathcal{P}\{\kappa > 0\} \quad (4.101)$$

$$\mathcal{P}_{dm,i,2}^{(k)(2)} = \mathcal{P}\{\zeta - \xi > 0\} \quad (4.102)$$

$$\begin{aligned} \kappa &= \prod_{i=1}^{L_i^{(k)}} \left\{1 + \left[\frac{N_c}{\rho}\right]^{\frac{1}{2}} v_i\right\} \\ \xi &= \prod_{i=1}^{N_c - L_i^{(k)}} \left\{1 + \left[\frac{N_c}{\rho}\right]^{\frac{1}{2}} \gamma_i\right\} \\ \zeta &= \left[\frac{N_c}{\rho}\right]^{\frac{N_c - L_i^{(k)}}{2}} \prod_{i=1}^{N_c - L_i^{(k)}} \nu_i \end{aligned}$$

where  $v_1, \dots, v_{L_i^{(k)}}, \gamma_1, \dots, \gamma_{N_c - L_i^{(k)}}, \nu_1, \dots, \nu_{N_c - L_i^{(k)}} \sim \mathcal{N}(0, 1)$  and are statistically independent.

We can write  $\mathcal{P}_{dm,g,\min}^{(k)}$  and  $\bar{z}_{dm,\min}^{(k)}$  needed to compute  $e_{2,dm}^{(k)}$  and  $z_{1,dm}^{(k)}$  respectively, under the Gaussian approximation as:

$$\mathcal{P}_{dm,g,\min}^{(k)} = \bar{z}_{dm,\min}^{(k)} = Q\left(\left[\frac{N_c^2}{\rho} + \left[\frac{N_c}{\rho}\right]^{N_c}\right]^{-\frac{1}{2}}\right) \quad (4.103)$$

and by simulation as:

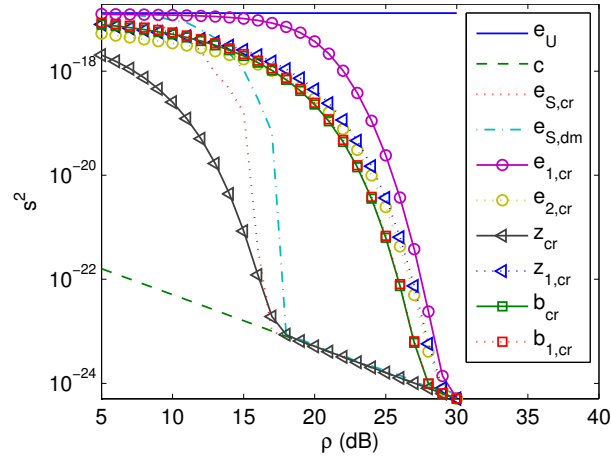
$$\begin{aligned} \mathcal{P}_{dm,g,\min}^{(k)} &= \bar{z}_{dm,\min}^{(k)} = \mathcal{P}\{\zeta - \xi > 0\} \\ \xi &= \prod_{i=1}^{N_c} \left\{1 + \left[\frac{N_c}{\rho}\right]^{\frac{1}{2}} \gamma_i\right\} \\ \zeta &= \left[\frac{N_c}{\rho}\right]^{\frac{N_c}{2}} \prod_{i=1}^{N_c} \nu_i \end{aligned} \quad (4.104)$$

where  $\gamma_1, \dots, \gamma_{N_c}, \nu_1, \dots, \nu_{N_c} \sim \mathcal{N}(0, 1)$  and are statistically independent.

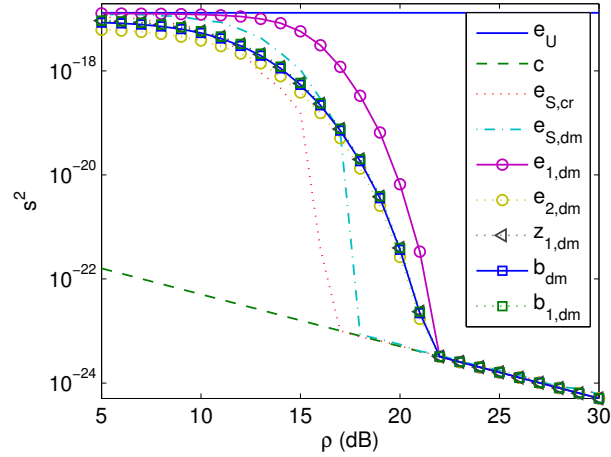
Now,  $P_{\min,dm}^{(k)}(i_j T_h)$  and  $\bar{b}_{dm,\min}^{(k)}$  that are needed to compute  $b_{dm}^{(k)}$  and  $b_{1,dm}^{(k)}$ , respectively, are given from Eq. 4.98 by replacing  $L_i^{(k)}$  by  $N_{i_j,C}^{(k)}$  Eq. 4.45 and 1, respectively.

Now we only treat the codeword with minimum sidelobe ACR  $c_1$  considered above. The probabilities of error are computed using the Gaussian approximation and by simulation. In Fig. 4.4(a) (Probabilities of error obtained by the Gaussian approximation) and Fig. 4.4(b) (Probabilities of error obtained by simulation) we show the maximum MSE  $e_U$ , the CRLB  $c$  (the subscript  $\Theta_k$  is omitted), the MSEs  $e_{S,cr}$  and  $e_{S,dm}$  obtained by simulation for the MCE and the MME, the MSE approximations  $e_{1,dm}$  and  $e_{2,dm}$  (approximate lower bound) (the superscript  $^{(k)}$  is omitted), the approximate ZZLB  $z_{1,dm}$ , and the approximate BTLBs  $b_{dm}$  and  $b_{1,dm}$  (the superscript  $^{(k)}$  is omitted), all with respect to the SNR  $\rho$ . We can observe that:

- The MCE outperforms the MME. However, the MME comports very well. We recall that we do not expect that the MME outperforms the MCE in the case where only an AWGN is corrupting the observation, because the MCE corresponds in this case to the MLE which is the best. We just want that the MME will not be very worse than the MCE.
- All the MSE approximations and approximate lower bounds obtained using the Gaussian approximation highly overestimate the MSE truly achieved. In fact, the Gaussian approximation overestimates the probability of error as we have already seen in Sec. 3.1.4 (see Fig. 3.4(a)).
- The MSE approximations and approximate lower bounds obtained using the probabilities of error computed by simulation, are much better than those obtained via the Gaussian approximation. However, they still overestimate the truly achieved MSE.



(a)



(b)

Fig. 4.4.: Maximum delaying-and-multiplying estimator (MME): maximum MSE  $e_U$ , CRLB  $c$ , MSEs obtained by simulation  $e_{S,cr}$  (MCE) and  $e_{S,dm}$  (MME), MSE approximations  $e_{1,dm}$  and  $e_{2,dm}$ , approximate ZZLB  $z_{1,dm}$ , and approximate BTLBs  $b_{dm}$  and  $b_{1,dm}$ , with respect to the SNR  $\rho$  in dB (codeword  $c_1$ ) (a) Gaussian approximation (b) Probabilities of error obtained by simulation.

### 4.3.3 Summary

Let us summarize what we have seen in this section with single-user. We have applied the subdomain method proposed in Chap. 2 and the approximate lower bounds derived there to derive some MSE approximations and approximate lower

bounds for TOA estimation based on TH-IR-UWB signals. We have considered both the MCE and the MME.

We have also compared the global performances of the MCE and the MME and seen that the MCE slightly outperforms the MME. We have also noticed that this result was expected because the MCE corresponds in the case of single-user to the MLE which is the best. However, the MME comports very well as it approximately achieves the CRLB at the same SNR as the MME.

#### 4.4 TOA ESTIMATION WITH MULTIUSER INTERFERENCE

In this section, we consider both the MCE and the MME in the case of multiuser. We consider the case where the MUI is deterministic in Sec. 4.4.1, and the case where it is random in Sec. 4.4.2.

Before continuing, we recall here that the MME has been mainly proposed as mentioned in Chap. 3 to examine its potential in mitigating the MUI.

##### 4.4.1 Deterministic multiuser interference

We mean here by deterministic interference that we know the values of the delays introduced by the channel to the waveforms of the interfering users.

The first goal of this study is to understand in a rigorous manner the origin of the deterioration of the estimation caused by MUI. The second goal is to verify whether there are some special scenarios where the MME outperforms the MCE. To reach both goals we consider a MU system with three users using codes with minimum circular sidelobe ACR and minimum circular CCR (in Sec. 4.5 we describe some algorithms proposed to generate code with minimum CCR and sidelobe ACR). For the underlying system we consider different realizations of the delays of the interfering users and examine for each realization the achieved MSE by both the MCE and the MME.

Before proceeding, let us explain why we have thought that the MME may outperform the MCE in mitigating the effects of MUI. We have seen that, for both CR and DM receivers, we filter the received signal with the filter matched to the transmitted pulse, then shift the filtered signal with the negatives of the delays corresponding to the different pulses of the TH codeword of the user of interest. Accordingly, we will obtain  $N_c$  branches corresponding to the  $N_c$  pulses of the TH-IR-UWB waveform. With the CR receiver, we add the signals of these branches whereas with the DM receiver, we multiply them.

Assume for instance that the AWGN is null. Then imagine that inside a given subdomain  $D_i^{(k)}$  (of width  $T_h$ , see Eq. 4.57), some branches contain interfering components whereas the remaining branches do not. By adding the different branches the resulting signal will contain an interfering component in the considered subdomain. However, by multiplying the branches, the resulting signal

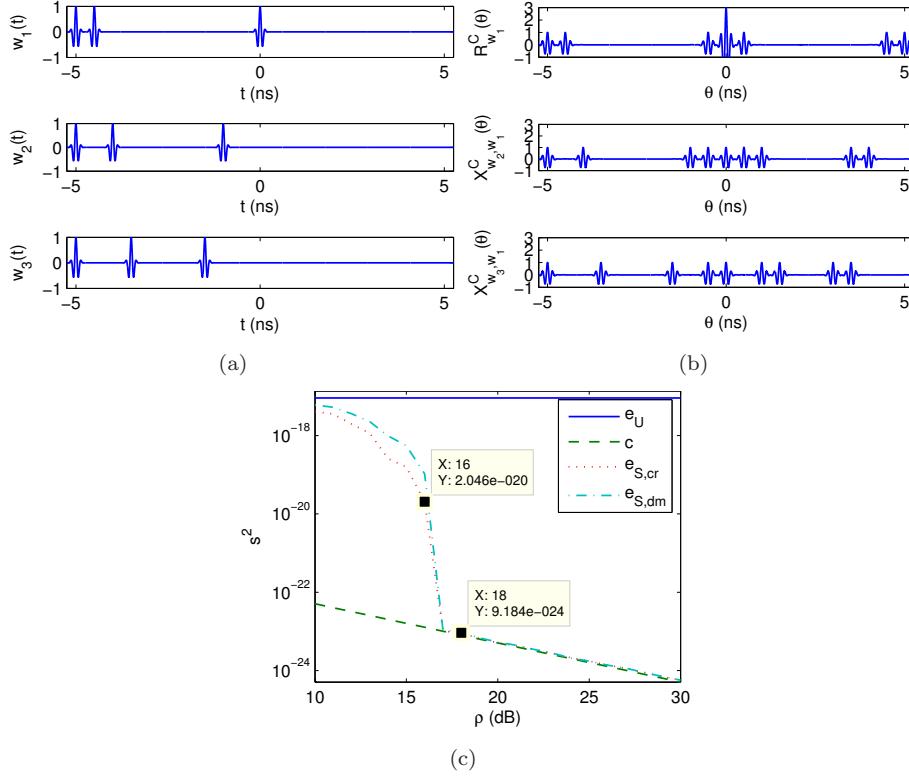


Fig. 4.5.: Reference case: (a) Normalized TH-IR-UWB waveforms  $w_1(t)$ ,  $w_2(t)$  and  $w_3(t)$  (b) Normalized  $R_{w_1}^C(\theta)$ ,  $X_{w_2,w_1}^C(\theta)$  and  $X_{w_3,w_1}^C(\theta)$  (c) Maximum MSE  $e_U$ , CRLB  $c$ , MSEs  $e_{S,cr}$  (MCE) and  $e_{S,dm}$  (MME) obtained by simulation, with respect to the SNR  $\rho$ .

will not contain any interfering component thanks to the multiplying operation if one or more branches do not contain interfering components. Assume now that the AWGN is not null. We can expect that the probability that the observation in the considered subdomain is stronger than that in the subdomain  $D_{i_k}^{(k)}$  (see Eq. 4.46) containing the maximum of the useful observation, is lower with the DM receiver than with the CR receiver.

In our case study we consider the following codewords with  $N_c = 3$  and  $N_s = 21$ :

- $c_1 = (0, 1, 10)$ ;
- $c_2 = (0, 2, 8)$ ;
- $c_3 = (0, 3, 7)$ .

We assume that User 1 is the user of interest. We take  $\alpha_1 = \alpha_2 = \alpha_3 = \alpha$ .

In Fig. 4.5(a) we show the normalized waveforms associated with  $c_1$ ,  $c_2$  and  $c_3$ , and in Fig. 4.5(b) the normalized (with respect to  $\frac{E}{N_c}$ ) ACR  $R_{w_1}^C(\theta)$  Eq. 4.45 of Waveform 1 and the normalized CCRs  $X_{w_k, w_1}^C(\theta)$ ,  $k = 2, 3$  Eq. 4.44 of Waveform 2 and 3 with Waveform 1.

In Fig. 4.5(c) we show, in the case where only  $w_1(t)$  is transmitted, the maximum MSE  $e_U$ , the CRLB  $c$ , and the MSEs  $e_{S,cr}$  and  $e_{S,dm}$  achieved by the MCE and MME respectively (obtained by simulation), with respect to the SNR. This case is considered as the reference case for all the cases considered later. We can see that both the MCE and the MME achieve the CRLB at  $\rho = 17$  dB.

#### 4.4.1.1 Case 1

We consider here the first case. We take  $\Theta_1 = 0$ ,  $\Theta_2 = -4T_h$  and  $\Theta_3 = -4T_h$ .

We show in Fig. 4.6(a) the three normalized branches of the receiver (by assuming null AWGN), and in Fig. 4.6(b) the normalized CR  $A_{r,p}(\theta)$  and DM  $P_{r,p}(\theta)$  observations (i.e. the sum and the product of the branches respectively, we have omitted the superscript  $(k)$ ). In Fig. 4.6(c) we show the maximum MSE  $e_U$ , the CRLB  $c$ , and the MSEs  $e_{S,cr}$  and  $e_{S,dm}$  achieved by the MCE and MME respectively (obtained by simulation), with respect to the SNR.

We can see in Fig. 4.6(a) that we have in the filtered signal a component of normalized amplitude equal to 2. This means that there are two signals (those of Users 2 and 3) colliding at one position. In Fig. 4.6(b), the useful component (around  $\theta = 0$ ) of the CR observation  $A_{r,p}(\theta)$  has an amplitude equal to 3 which is expected because we have three pulses per waveform.  $A_{r,p}(\theta)$  also contains sidelobe components of amplitudes equal to 1 and 2. With the DM receiver, we can only see the useful component of amplitude equal to 1. In fact, the sidelobe components are all killed by the branch with no MU component. Note that in this scenario, Waveform 1 is not colliding with any other waveform because the amplitude of the useful component of  $A_{r,p}(\theta)$  is equal to  $N_c$  and that of  $P_{r,p}(\theta)$  to one.

In Fig. 4.6(c) we can see that MME outperforms the MCE. It achieves the CRLB at  $\rho = 22$  dB instead of  $\rho = 25$  dB with the MCE. This is in fact due to the MUI components killed thanks to the DM receiver.

#### 4.4.1.2 Case 2

We consider here the second case, with  $\Theta_1 = 0$ ,  $\Theta_2 = 0$  and  $\Theta_3 = 0$ .

The results are shown in Fig. 4.7(a), Fig. 4.7(b) and Fig. 4.7(c). We can observe that:

- Waveforms 1, 2 and 3 are all colliding at one pulse. In fact, the filtered signal (see Fig. 4.7(a)) has a component of amplitude equal to 3, and the amplitude of the useful component of  $A_{r,p}(\theta)$  (see Fig. 4.7(b)) is equal to 5.

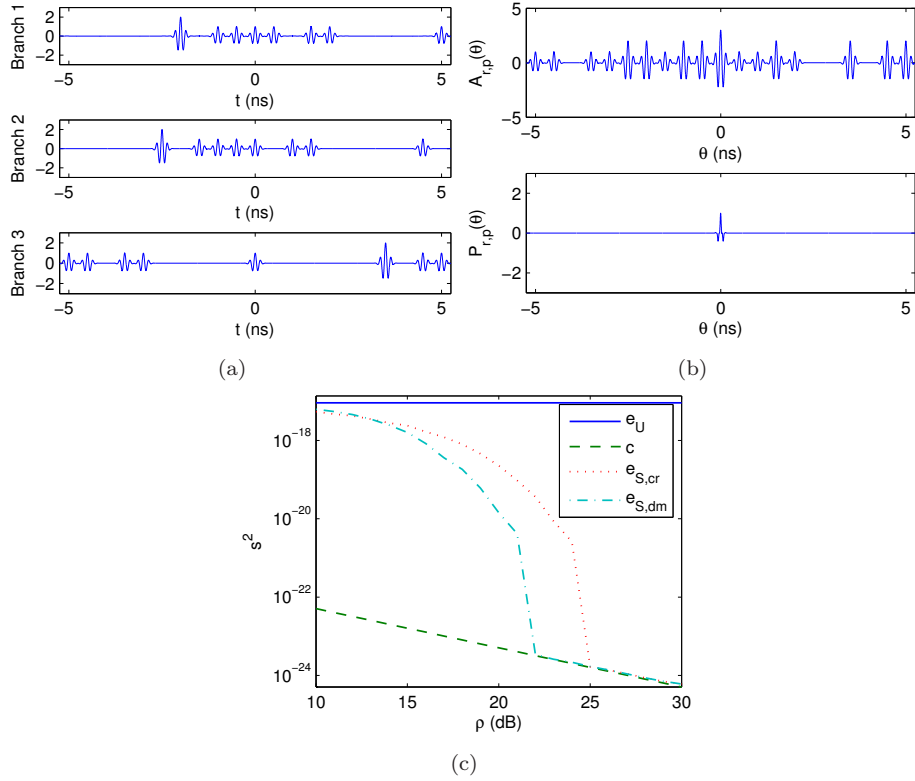


Fig. 4.6.: Case 1: (a) Normalized branches of the CR and DM receivers (b) Normalized CR  $A_{r,p}(\theta)$  and DM  $P_{r,p}(\theta)$  observations (c) Maximum MSE  $e_U$ , CRLB  $c$ , MSEs  $e_{S,cr}$  (MCE) and  $e_{S,dm}$  (MME) obtained by simulation, with respect to the SNR  $\rho$ .

- Both the MCE and the MME achieve a bound lower than the CRLB. This is in fact due to the constructive collision with the user of interest which makes its energy higher.
- Both  $e_{S,cr}$  and  $e_{S,dm}$  converge approximately to their asymptotic regions at the same SNR ( $\rho = 18$  dB). The MME does not outperform the MCE because the gap between the useful and the sidelobe components of  $A_{r,p}(\theta)$  is sufficiently big (equal to 2). In Case 1 (see Fig. 4.6(b)), it was equal to one.

#### 4.4.1.3 Case 3

We consider here the third case, with  $\Theta_1 = 0$ ,  $\Theta_2 = T_h$  and  $\Theta_3 = 2T_h$ .

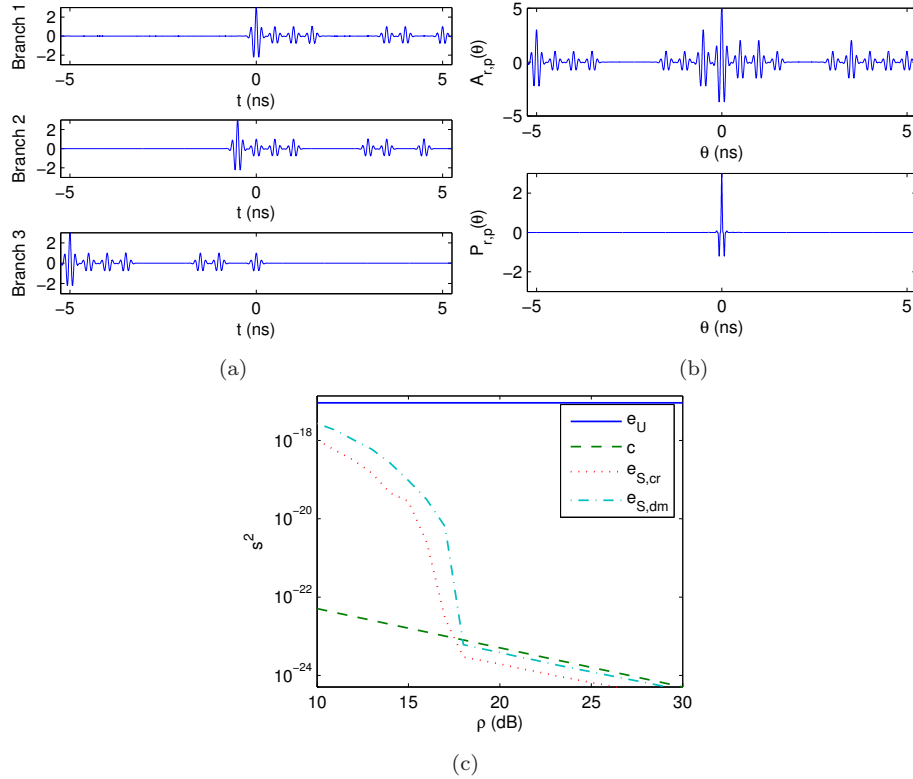


Fig. 4.7.: Case 2: (a) Normalized branches of the CR and DM receivers (b) Normalized CR  $A_{r,p}(\theta)$  and DM  $P_{r,p}(\theta)$  observations (c) Maximum MSE  $e_U$ , CRLB  $c$ , MSEs  $e_{S,cr}$  (MCE) and  $e_{S,dm}$  (MME) obtained by simulation, with respect to the SNR  $\rho$ .

The results are shown in Fig. 4.8(a), Fig. 4.8(b) and Fig. 4.8(c). We can observe that:

- Waveform 1 collides with Waveform 2 or 3 at one pulse, and Waveforms 2 and 3 collide at one pulse. Note that it is impossible that two waveforms collide at more than one pulse thanks to the minimum CCR of the considered code.
- The gap between the useful and the sidelobe components of  $A_{r,p}(\theta)$  is not sufficiently big (equal to 1). We can expect that, like in Case 1 (with gap equal to 1 too, see Fig. 4.6(b)), the MME will outperform the MCE.
- The MME outperforms the MCE; it achieves the CRLB at  $\rho = 21$  dB instead of  $\rho = 24$  dB.

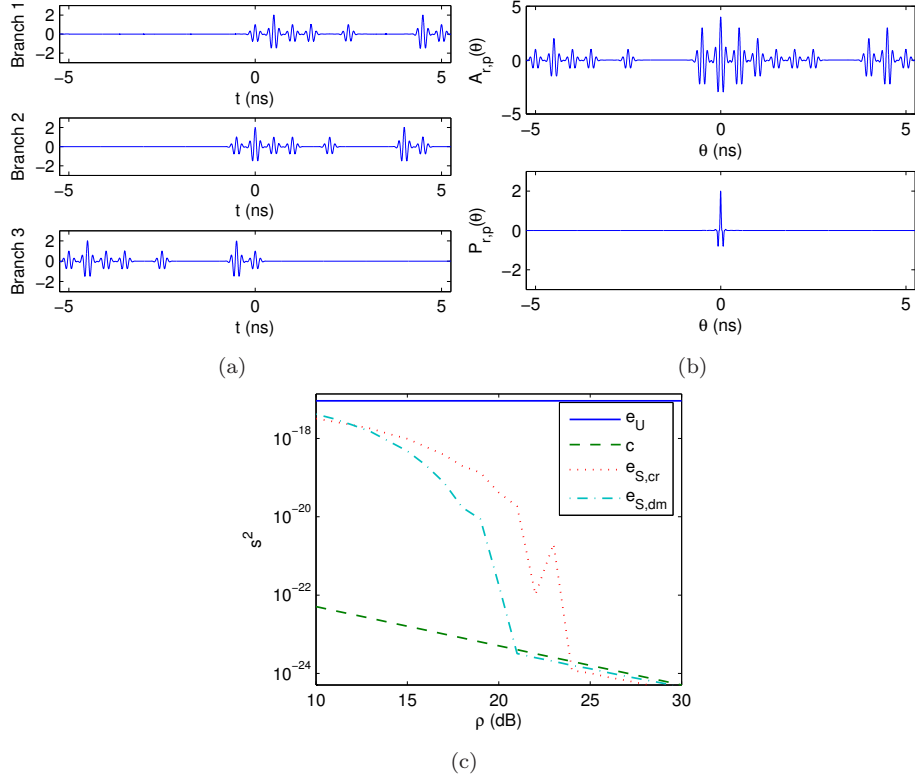


Fig. 4.8.: Case 3: (a) Normalized branches of the CR and DM receivers (b) Normalized CR  $A_{r,p}(\theta)$  and DM  $P_{r,p}(\theta)$  observations (c) Maximum MSE  $e_U$ , CRLB  $c$ , MSEs  $e_{S,cr}$  (MCE) and  $e_{S,dm}$  (MME) obtained by simulation, with respect to the SNR  $\rho$ .

#### 4.4.1.4 Case 4

We consider here the fourth case, with  $\Theta_1 = 0$ ,  $\Theta_2 = 3T_h$  and  $\Theta_3 = 4T_h$ .

The results are shown in Fig. 4.9(a), Fig. 4.9(b) and Fig. 4.9(c). We observe that:

- In  $A_{r,p}(\theta)$ , we have three sidelobe components with amplitudes equal to that of the useful component (i.e. 3). This phenomenon is not observed in  $P_{r,p}(\theta)$ . In fact, by looking at the three branches of the filtered signal, we can see that the sidelobe component at the right of the useful one, is the sum of three components of amplitudes 1, 0 and 2 respectively. In the DM receiver, the component of amplitude 0 kills the two other components.

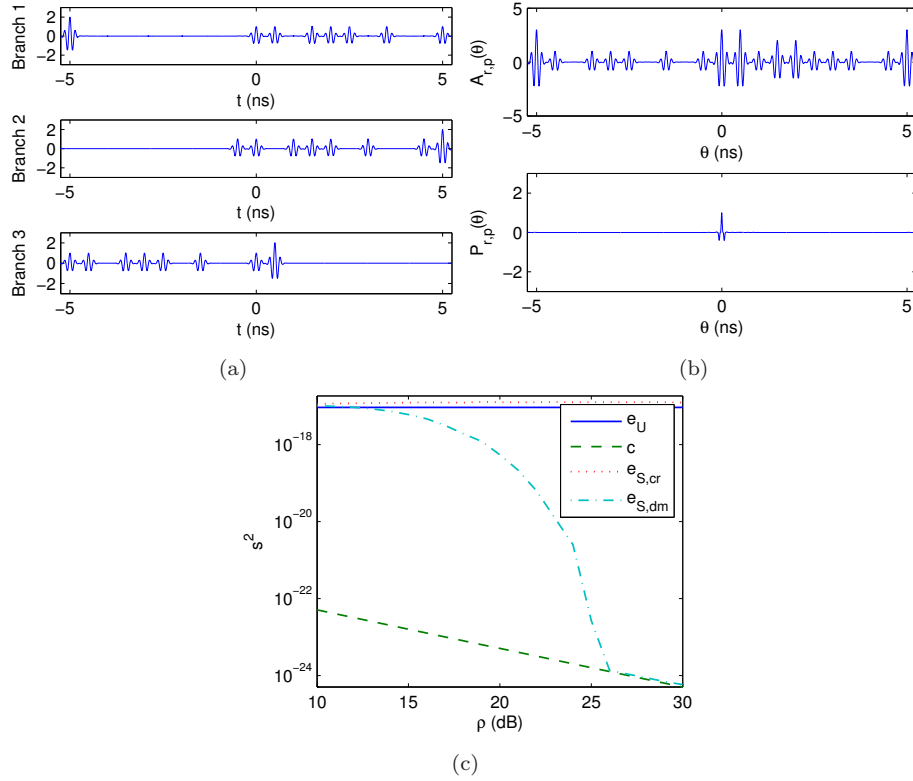


Fig. 4.9.: Case 4: (a) Normalized branches of the CR and DM receivers (b) Normalized CR  $A_{r,p}(\theta)$  and DM  $P_{r,p}(\theta)$  observations (c) Maximum MSE  $e_U$ , CRLB  $c$ , MSEs  $e_{S,cr}$  (MCE) and  $e_{S,dm}$  (MME) obtained by simulation, with respect to the SNR  $\rho$ .

- Due to the phenomenon discussed in the last point, the MCE is approximately uniformly distributed in the *a priori* domain of  $\Theta_1$ ; the MSE achieved by it is slightly larger than the maximum MSE. However, the MME achieves the CRLB at  $\rho = 24$  dB.

#### 4.4.1.5 Case 5

In the last four considered cases, the collisions among the different waveforms were constructive because the relative delays were multiples of the modulating carrier period. As in practice the waveforms can arrive with any relative delays, it seems to be interesting to consider too the case of destructive collisions. To do so we consider the destructive version of the last case (Case 4) which was the worst for the MCE.

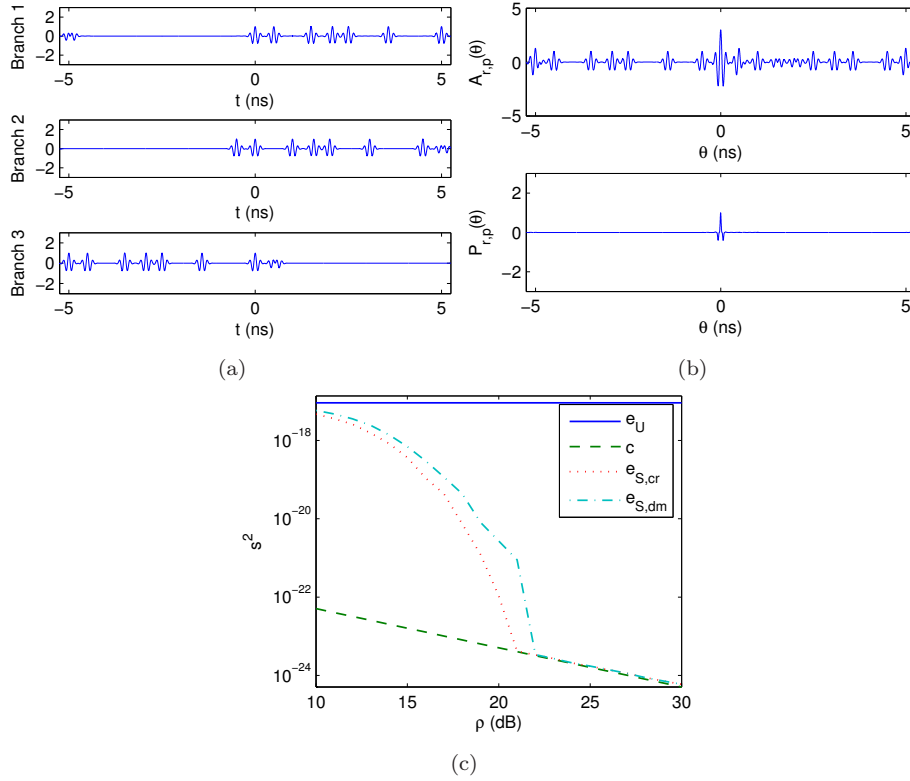


Fig. 4.10.: Case 5: (a) Normalized branches of the CR and DM receivers (b) Normalized CR  $A_{r,p}(\theta)$  and DM  $P_{r,p}(\theta)$  observations (c) Maximum MSE  $e_U$ , CRLB  $c$ , MSEs  $e_{S,cr}$  (MCE) and  $e_{S,dm}$  (MME) obtained by simulation, with respect to the SNR  $\rho$ .

Let  $\Theta_1 = 0$ ,  $\Theta_2 = 3T_h$  and  $\Theta_3 = 4T_h + \frac{1}{2f_c}$  ( $f_c$  is the carrier). The results are shown in Fig. 4.10(a), Fig. 4.10(b) and Fig. 4.10(c).

We can observe that:

- In  $A_{r,p}(\theta)$ , there are no sidelobe components with amplitudes equal to that of the useful component like in Case 4. By contrast,  $A_{r,p}(\theta)$  has now the shape of a CR observation in the case of single-user (sidelobe amplitudes equal to 1) because the colliding pulses of Waveforms 2 and 3 are destructive.
- Both the MCE and the MME comport now much better than in Case 4; they achieve the CRLB at  $\rho = 21$  dB and  $\rho = 22$  dB respectively. Obviously, the MCE outperforms now the MME.

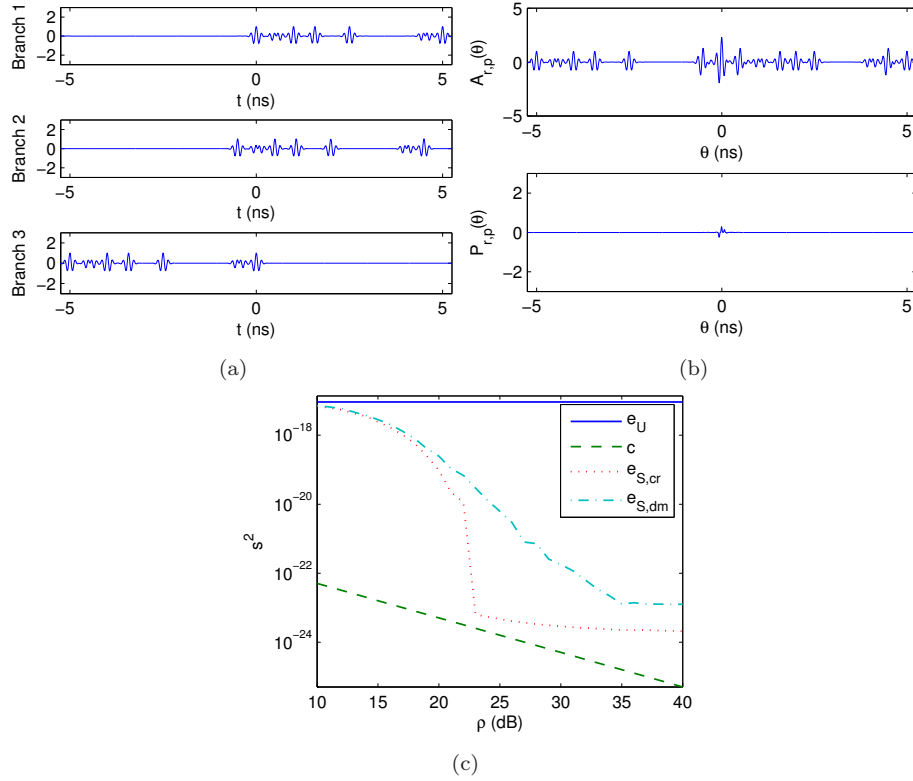


Fig. 4.11.: Case 6: (a) Normalized branches of the CR and DM receivers (b) Normalized CR  $A_{r,p}(\theta)$  and DM  $P_{r,p}(\theta)$  observations (c) Maximum MSE  $e_U$ , CRLB  $c$ , MSEs  $e_{S,cr}$  (MCE) and  $e_{S,dm}$  (MME) obtained by simulation, with respect to the SNR  $\rho$ .

#### 4.4.1.6 Case 6

In Case 5 we have considered interfering users destructing themselves (favorable case). Let us consider here the case of interfering users destructing the user of interest. To do so, we consider the destructive version of Case 3. Note that this case is very important to understand what will happen with random MUI.

Let  $\Theta_1 = 0$ ,  $\Theta_2 = T_h + \frac{1}{2f_c}$  and  $\Theta_3 = 2T_h$ . The results are shown in Fig. 4.11(a), Fig. 4.11(b) and Fig. 4.11(c).

We can observe that:

- The amplitude of  $A_{r,p}(\theta)$  at  $\theta = 0$  is now equal to 2.275 instead of 3 due to the destructive collision.

- The asymptotic MSE does not converge in this case to the CRLB but to a constant value. This means that a bias has been introduced by the destructive collision. The absolute value of this bias will almost be lower than the pulse width  $T_w$  of  $p(t)$ . Accordingly, we can propose the following asymptotic MSE approximation in the case of random MUI:

$$e_{MU,as} = \frac{(2T_w)^2}{12} \quad (4.105)$$

which corresponds to a variable uniformly distributed in  $[-T_w, T_w]$ . We did not propose  $[-T_w, T_w]$  because we will find this value in the case of random MUI but because in both  $A_{r,p}(\theta)$  and  $P_{r,p}(\theta)$ , the present component is the AC of  $p(t)$  and not  $p(t)$  itself.

#### 4.4.2 Random multiuser interference

In this subsection we consider the case of random MUI. We assume that the TOA of the user of interest is deterministic, whereas those of the interfering users are uniformly distributed in the *a priori* domain  $D_\Theta$  Eq. 4.22.

Let us first consider the CR receiver. Instead of using the expression of the CR observation  $A_{r,p}^{(k)}(\theta)$  in Eq. 4.62, we consider the circular version of  $X_{r,w_k}(\theta)$  in Eq. 4.26 (the latter is equal to  $[\frac{E}{N_c}]^{\frac{1}{2}}$  times the former). The circular version of  $X_{r,w_k}(\theta)$  can be written as:

$$\begin{aligned} X_{r,w_k}^C(\theta) &= \alpha_k R_{w_k}^C(\theta \ominus \Theta_k) + v_{MU}^C(\theta) + v_{G,k}^C(\theta) \\ &= \alpha_k R_{w_k}^C(\theta \ominus \Theta_k) + \sum_{k'=1, k' \neq k}^K v_{MU,k'}^C(\theta) + v_{G,k}^C(\theta), \end{aligned} \quad (4.106)$$

$$v_{MU,k'}^C(\theta) = \alpha_{k'} X_{w_{k'}, w_k}^C(\theta \ominus \Theta_{k'}) \quad (4.107)$$

where for convenience we rewrite the expressions of  $R_{w_k}^C(\theta \ominus \Theta_k)$  Eq. 4.49 and  $X_{w_{k'}, w_k}^C(\theta \ominus \Theta_{k'})$  Eq. 4.50:

$$R_{w_k}^C(\theta \ominus \Theta_k) = \frac{E}{N_c} \sum_{i=0}^{N_s-1} L_i^{(k)} R_p(\theta - \theta_i^{(k)}) \quad (4.108)$$

$$X_{w_{k'}, w_k}^C(\theta \ominus \Theta_{k'}) = \frac{E}{N_c} \sum_{i=0}^{N_s-1} L_i^{(k',k)} R_p(\theta - \theta_i^{(k')}). \quad (4.109)$$

The covariance of  $v_{G,k}^C(\theta)$  is given by:

$$C_{v_{G,k}^C}(\theta) = \frac{N_0}{2} R_{w_k}^C(\theta) \theta \in [-\frac{T_h}{2}, \frac{T_h}{2}] \frac{N_0}{2} E R_p(\theta) \quad (4.110)$$

where we have taken into account in the right side of Eq. 4.110 that  $N_{0,C}^{(k)} = N_c$  (see Eq. 4.45). As  $\Theta_{k'}, k' \neq k$  is uniformly distributed in  $D_\Theta$ , the noise  $v_{MU,k'}^C(\theta)$

is weakly stationary. The mean and the covariance of  $v_{MU,k'}^C(\theta)$  are given by:

$$m_{MU,k'}^C(\theta) = \frac{1}{T} \int_{-\frac{T_h}{2}}^{T-\frac{T_h}{2}} v_{MU,k'}^C(\theta) d\Theta_{k'} \approx 0 \quad (4.111)$$

$$C_{MU,k'}^C(\theta) \approx \frac{1}{T} \int_{-\frac{T_h}{2}}^{T-\frac{T_h}{2}} v_{MU,k'}^C(\theta' + \theta) v_{MU,k'}^C(\theta') d\Theta_{k'}$$

$$\theta \in [-\frac{T_h}{2}, \frac{T_h}{2}] \quad \frac{1}{T} \alpha_{k'}^2 \frac{E^2}{N_c^2} \sum_{i=0}^{N_s-1} (L_i^{(k',k)})^2 R_{R_p}(\theta) \quad (4.112)$$

where

$$R_{R_p}(\theta) = \int_{-\infty}^{+\infty} R_p(t + \theta) R_p(t) dt \quad (4.113)$$

is the ACR of  $R_p(\theta)$ . Denote by  $E_{R_p} = R_{R_p}(0)$  the energy of  $R_p(\theta)$  ( $E_{R_p}$  is not like the energy of  $p(t)$  which is equal to one). Note that  $m_{MU,k'}^C(\theta)$  is approximately null only for oscillating pulses.

From Eq. 4.106, Eq. 4.108, Eq. 4.110 and Eq. 4.112, and taking into account that the delays of the interfering users are statistically independent, we can write the SINR of User  $k$  (the user of interest) as:

$$\rho_{G,MU}^{(k)} = \frac{[\alpha_k R_{w_k}^C(0)]^2}{C_{v_{G,k}}^C(0) + \sum_{k'=1, k' \neq k}^K C_{MU,k'}^C(0)} = \frac{\alpha_k^2 E}{\frac{N_0}{2} + \frac{E E_{R_p}}{T N_c^2} \sum_{k'=1, k' \neq k}^K \alpha_{k'}^2 E_d^{(k',k)}}$$

$$= \frac{1}{\frac{1}{\rho_k} + \frac{1}{\rho_{MU}^{(k)}}} \quad (4.114)$$

where

$$E_d^{(k',k)} = \sum_{i=0}^{N_s-1} (L_i^{(k',k)})^2 \geq N_c^2 \quad (4.115)$$

$$\rho_k = \frac{\alpha_k^2 E}{N_0/2} \quad (4.116)$$

$$\rho_{MU}^{(k)} = \frac{\alpha_k^2 T N_c^2}{E_{R_p} \sum_{k'=1, k' \neq k}^K \alpha_{k'}^2 E_d^{(k',k)}}. \quad (4.117)$$

We can see in Eq. 4.114 that  $\rho_{G,MU}^{(k)}$  approaches  $\rho_{MU}^{(k)}$  as  $\rho_k$  approaches infinity. In Eq. 4.115,  $E_d^{(k',k)}$  becomes equal to  $N_c^2$  for codes with minimum circular CCR (because  $L_i^{(k',k)} = 0$  or  $1, \forall i$ ). Accordingly, the maximum SINR is given by:

$$\rho_{G,MU,\max}^{(k)} = \frac{\alpha_k^2 E}{\frac{N_0}{2} + \frac{E E_{R_p}}{T} \sum_{k'=1, k' \neq k}^K \alpha_{k'}^2}. \quad (4.118)$$

Let us consider the same setup considered in Sec. 4.3. We have:

- $T = N_s T_h = 1.05 \times 10^{-8}$  s.
- $E_{R_p} \approx 8 \times 10^{-11}$  s.
- $E_d^{(k',k)} = N_c^2 = 9$ .
- $\rho_{MU}^{(k)} \approx 65 \approx 18$  dB.

In Fig. 4.12(a) we show the total SINR  $\rho_{G,MU}^{(k)}$  Eq. 4.114 with respect to the SNR  $\rho_k$  Eq. 4.116 (we have omitted the superscript  $^{(k)}$  and the subscript  $_k$ ). We can see that  $\rho_{G,MU}^{(k)}$  converges to  $\rho_{MU}^{(k)} \approx 18$  dB as expected from Eq. 4.114. From this result we can expect that the MSEs achieved asymptotically by both the MCE and the MME are equal to those achieved in the case of single-user at the SNR equal to the asymptotic SINR. We can see from Fig. 4.5(c) that the MSE achieved by both the MCE and the MME at  $\rho_k = 18$  dB is approximately equal to 9 ps<sup>2</sup>. We can deduce that the MSE achieved in the case of MUI depends on both the SINR and the MSE achieved at this SNR in the case of single-user. To be rigorous we have to say that this is true if the MUI comports as an AWGN.

In Fig. 4.12(b) we show the maximum MSE  $e_U$ , the CRLB  $c$ , the MSE  $e_{S,cr}$  of the MCE obtained by simulation (by randomly generating the AWGN and the delays of Waveforms 2 and 3), the MCE MSE approximation  $e_{1,cr}$ , the MSE  $e_{S,dm}$  of the MME obtained by simulation, the MME MSE approximation  $e_{1,dm}$ , and the asymptotic MUI MSE approximation  $e_{MU,as}$  Eq. 4.105 proposed in Case 6 Sec. 4.4.1.6, all with respect to the SNR  $\rho$ . Note that the MSE approximations of both the MCE and the MME are obtained from Eq. 4.70 by using the SINR instead of the SNR, and by replacing  $e_{x,i_k}^{(k)}$  by the CRLB. For the MME, we have computed the probability of error by simulation. We can observe that:

- The MCE MSE and the MME MSE converge to the constant values  $2 \times 10^{-20}$  s<sup>2</sup> and  $6.5 \times 10^{-20}$  s<sup>2</sup> respectively. This phenomenon is due to the average effect of the destructive collision with the user of interest.
- The MSE approximations  $e_{1,cr}$  and  $e_{1,dm}$  have the same behavior as the ones obtained by simulations (i.e. they converge to a constant value). However, they do not follow them closely.
- The asymptotic MUI MSE approximation  $e_{MU,as}$  proposed in Sec. 4.4.1.6 is very close to the asymptotic MUI MSE truly achieved. This value is totally different from that expected from the asymptotic SINR and the MSE achieved in the case of single-user. In fact, the effects of the MUI cannot be rigorously approximated by those of an AWGN. The single-user SNR achieving the MSE which is achieved here, is equal to  $\rho_k = 16$  dB instead of 18 dB (see Fig. 4.5(c)).
- The MCE slightly outperforms the MME.

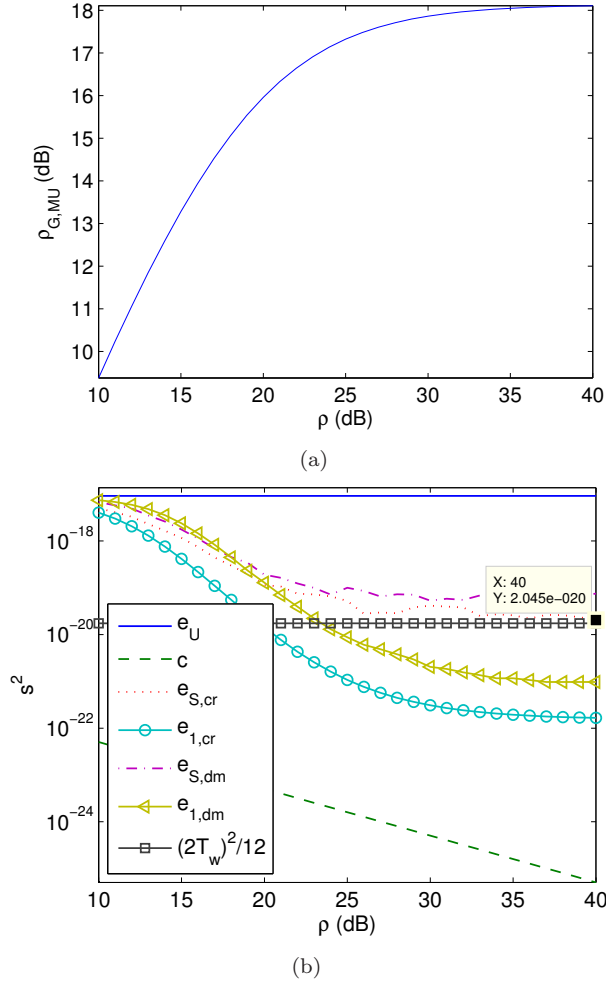


Fig. 4.12.: Random MUI: (a) SINR  $\rho_{G,MU}$  with respect to the SNR  $\rho$  (b) Maximum MSE  $e_U$ , CRLB  $c$ , MCE MSE obtained by simulation  $e_{S,cr}$ , MCE MSE approximation  $e_{1,cr}$ , MME MSE obtained by simulation  $e_{S,dm}$ , MME MSE approximation  $e_{1,dm}$ , and asymptotic MUI MSE approximation  $e_{MU,as}$ , with respect to the SNR  $\rho$ .

#### 4.5 THMA CODES WITH MINIMUM CCR AND SIDELobe ACR

In this section we propose some algorithms to generate time-hopping codes with minimum sidelobe ACR and minimum CCR. We consider two THMA codes structures: with chip separation (see Eq. 4.2, Eq. 4.3 and Eq. 4.4) and without

chip separation (see Eq. 4.3, Eq. 4.5 and Eq. 4.6). For both structures we consider the cases of non-periodic and periodic signals.

In Sec. 4.5.1, Sec. 4.5.2, Sec. 4.5.3 and Sec. 4.5.4 we consider the cases of THMA codes with chip separation for non-periodic signals, with chip separation for periodic signals, without chip separation for non-periodic signals, and without chip separation for periodic signals, respectively. In Sec. 4.5.5 we deal with the same codes considered in Sec. 4.5.1, Sec. 4.5.2, Sec. 4.5.3 and Sec. 4.5.4 but with variable code length. In Sec. 4.5.6 we show and discuss some codes generated using the proposed algorithms.

#### 4.5.1 THMA code with chip separation and minimum CCR and sidelobe ACR

We consider here THMA codes with chip separation for non-periodic signals.

For convenience we rewrite the normalized (with respect to  $\frac{E}{N_c}$ ) versions of Eq. 4.8 and Eq. 4.9:

$$X_{w_k, w_{k'}}(\tau) = \frac{E}{N_c} \sum_{n=0}^{N_c-1} \sum_{n'=0}^{N_c-1} R_p(\tau - [t_n^{(k)} - t_{n'}^{(k')}]) \quad (4.119)$$

$$R_{w_k}(\tau) = \frac{E}{N_c} \sum_{n=0}^{N_c-1} \sum_{n'=0}^{N_c-1} R_p(\tau - [t_n^{(k)} - t_{n'}^{(k)}]). \quad (4.120)$$

We can see from Eq. 4.120 that the global maximum of  $R_{w_k}(\theta)$  (equal to  $N_c$ ) is located at  $\tau = 0$ , and that  $N_c(N_c - 1)$  local maxima equal to 1 are located at  $\tau = t_n^{(k)} - t_{n'}^{(k)}$ ,  $\forall n \neq n'$ , if and only if, for each couple  $(n, n')$  the condition  $t_n^{(k)} - t_{n'}^{(k)} \neq t_m^{(k)} - t_{m'}^{(k)}$  is satisfied  $\forall (m, m') \neq (n, n')$ . However if we can find  $N_o \leq N_c - 1$  couples  $(n, n')$  having the same relative delay  $t_n^{(k)} - t_{n'}^{(k)}$ , then a local maximum equal to  $N_o$  will be located at  $\tau = t_n^{(k)} - t_{n'}^{(k)}$ . We can see from Eq. 4.119 that  $N_c^2$  local maxima equal to 1 are located at  $\tau = t_n^{(k)} - t_{n'}^{(k')}$ ,  $\forall (n, n')$ , if and only if, for each couple  $(n, n')$  the condition  $t_n^{(k)} - t_{n'}^{(k')} \neq t_m^{(k)} - t_{m'}^{(k')}$  is satisfied  $\forall (m, m') \neq (n, n')$ . However if we can find  $N_o \leq N_c$  couples  $(n, n')$  having the same relative delay  $t_n^{(k)} - t_{n'}^{(k')}$ , then a local maximum equal to  $N_o$  is located at  $\tau = t_n^{(k)} - t_{n'}^{(k')}$ . Accordingly, and by assuming that  $E_p = 1$ , we can write:

$$R_{\max}^{(k)} = \max_{\tau \notin [-\frac{T_h}{2}, \frac{T_h}{2}]} \{R_{w_k}(\tau)\} \in \{1, \dots, N_c - 1\} \quad (4.121)$$

$$X_{\max}^{(k, k')} = \max_{\tau} \{X_{w_k, w_{k'}}(\tau)\} \in \{1, \dots, N_c\} \quad (4.122)$$

where  $R_{\max}^{(k)}$  denotes the maximal local maximum of  $R_{w_k}(\tau)$  outside  $[-\frac{T_h}{2}, \frac{T_h}{2}]$ , and  $X_{\max}^{(k, k')}$  stands for the maximal local maximum of  $X_{w_k, w_{k'}}(\tau)$ . Note that

more local maxima may fall around the mentioned local maxima due to the oscillations in the used IR-UWB pulse.

Taking into account that  $R_{w_k}(\tau)$  is symmetric (i.e.  $t_n^{(k)} - t_{n'}^{(k)}$  and  $t_{n'}^{(k)} - t_n^{(k)}$  are both locations of local maxima), and that  $t_n^{(k)} - t_{n'}^{(k)} \neq t_m^{(k)} - t_{m'}^{(k)}$  is equivalent to  $t_n^{(k)} - t_m^{(k)} \neq t_{n'}^{(k')} - t_{m'}^{(k')}$ , the necessary and sufficient conditions for  $R_{\max}^{(k)} = \min_{(c_n^{(k)})} \{R_{\max}^{(k)}\} = 1$  and  $X_{\max}^{(k,k')} = \min_{(c_n^{(k)}), (c_{n'}^{(k')})} \{X_{\max}^{(k,k')}\} = 1$  can be written as:

$$d_{n,n'}^{(k)} \neq d_{m,m'}^{(k)}; \forall (n, n' > n); \forall (m, m' > m) \neq (n, n') \quad (4.123)$$

$$d_{n,n'}^{(k)} \neq d_{m,m'}^{(k')}; \forall (n, n' > n); \forall (m, m' > m) \quad (4.124)$$

where  $d_{n,n'}^{(k)}$  denotes the normalized relative delay between the  $n$ th and  $n'$ th pulses of  $w_k(t)$ , given by:

$$d_{n,n'}^{(k)} = \frac{t_{n'}^{(k)} - t_n^{(k)}}{T_h} = (n' - n)N_h + \Delta_{n,n'}^{(k)} \quad (4.125)$$

$$\Delta_{n,n'}^{(k)} = c_{n'}^{(k)} - c_n^{(k)} \in \{-N_h + 1, \dots, N_h - 1\}. \quad (4.126)$$

Note that Eq. 4.123 means that there are no different couples of pulses in  $w_k(t)$  having equal relative delays, whereas Eq. 4.124 means that the relative delay of any couple in any waveform  $w_k(t)$ , ( $k = 1, \dots, K$ ) is different from the relative delays of all other couples in the same waveform and in the other waveforms. Accordingly, Eq. 4.124 guarantees that both the minimum CCR and the minimum sidelobe ACR are satisfied. Denote by  $d_i^{(k)}$ , ( $i = 1, \dots, N_c - 1$ ) the row vector of  $N_c - i$  elements, containing the normalized relative delays between the pulses of  $w_k(t)$  separated by  $i$  chips:

$$d_i^{(k)} = (d_{n-i,n}^{(k)})_{n=i, \dots, N_c-1} = iN_h + \Delta_i^{(k)} \quad (4.127)$$

$$\Delta_i^{(k)} = (\Delta_{n-i,n}^{(k)})_{n=i, \dots, N_c-1}. \quad (4.128)$$

Using Eq. 4.127, we can write the necessary and sufficient conditions in Eq. 4.123 and Eq. 4.124 as:

$$x_j \neq x_{j'}; \forall j \neq j'; x_j, x_{j'} \in d^{(k)} \quad (4.129)$$

$$x_j \neq x_{j'}; \forall j \neq j'; x_j, x_{j'} \in d \quad (4.130)$$

where  $x_j$  and  $x_{j'}$  denote the  $j$ th and  $j'$ th elements in the row vectors

$$d^{(k)} = (d_1^{(k)} | \dots | d_{N_c-1}^{(k)}) \quad (4.131)$$

$$d = (d^{(1)} | \dots | d^{(K)}) \quad (4.132)$$

of  $\sum_{i=1}^{N_c-1} (N_c - i) = \frac{N_c(N_c-1)}{2}$  and  $\frac{KN_c(N_c-1)}{2}$  elements containing the normalized relative delays between all pulse couples in  $w_k(t)$ , and in all  $w_k(t)$ . By assuming that:

$$d_{n-i,n}^{(k)} \neq d_{n'-i',n'}^{(k')}; \forall (d_{n-i,n}^{(k)}, d_{n'-i',n'}^{(k')}) \in d_i \times d_{i' > i} \quad (4.133)$$

where

$$d_i = (d_i^{(1)} | \cdots | d_i^{(K)}) = \Delta_i + iN_h \quad (4.134)$$

$$\Delta_i = (\Delta_i^{(1)} | \cdots | \Delta_i^{(K)}). \quad (4.135)$$

We can write the necessary and sufficient conditions in Eq. 4.123 and Eq. 4.124 using Eq. 4.127 and Eq. 4.128 as:

$$x_j \neq x_{j'}; \forall j \neq j'; \forall i; x_j, x_{j'} \in \Delta_i^{(k)} \quad (4.136)$$

$$x_j \neq x_{j'}; \forall j \neq j'; \forall i; x_j, x_{j'} \in \Delta_i \quad (4.137)$$

where  $j, j' = 1, \dots, N_c - i$  in Eq. 4.136 ( $N_c - i$  is the length of  $\Delta_i^{(k)}$ ), and  $j, j' = 1, \dots, K(N_c - i)$  in Eq. 4.137 ( $K(N_c - i)$  is the length of  $\Delta_i$ ). Note that Eq. 4.136 and Eq. 4.137 mean that  $\forall i, \Delta_i^{(k)}$  (see the rows of  $\underline{\Delta}^{(k)}$  Eq. 4.138), as well as  $\Delta_i$  Eq. 4.135, should not contain equal elements:

$$\underline{\Delta}^{(k)} = \begin{pmatrix} \Delta_1^{(k)} \\ \vdots \\ \Delta_{N_c-1}^{(k)} \end{pmatrix} = \begin{pmatrix} \Delta_{0,1}^{(k)} & \cdots & \Delta_{N_c-2, N_c-1}^{(k)} \\ & \ddots & \vdots \\ & & \Delta_{0, N_c-1}^{(k)} \end{pmatrix}. \quad (4.138)$$

Note that Eq. 4.133 used to obtain Eq. 4.136 and Eq. 4.137 is satisfied  $\forall i' > i + 1$ , and for  $i' = i + 1$  only if  $\Delta_{n-i,n}^{(k)} - \Delta_{n'-i',n'}^{(k')} \neq N_h, \forall n, n', k, k', i$ . In fact,  $d_{n'-i',n'}^{(k')} - d_{n-i,n}^{(k)} = (i' - i)N_h + \Delta_{n'-i',n'}^{(k')} - \Delta_{n-i,n}^{(k)}$  with  $|\Delta_{n'-i',n'}^{(k')} - \Delta_{n-i,n}^{(k)}| \leq 2N_h - 2$  because  $|\Delta_{n-i,n}^{(k)}| \leq N_h - 1$  as  $c_n^{(k)} \in \{0, \dots, N_h - 1\}$ . Due to this fact we will set  $N_h = N_h + 1$  during the procedure described below until Eq. 4.133 becomes satisfied.

Let us now describe the algorithm proposed to generate the THMA code satisfying Eq. 4.124. We assume that only  $K$  and  $N_c$  are known:

1. Finding  $c^{(k)}$ , ( $k = 1, \dots, K$ ) that satisfy Eq. 4.151:
  - (a) Generate arbitrarily  $c_0^{(k)}$ , ( $k = 1, \dots, K$ ); generate the empty vectors  $\Delta_i$  Eq. 4.135, ( $i = 1, \dots, N_c - 1$ ).
  - (b) For  $n = 1, \dots, N_c - 1$ :  
For  $k = 1, \dots, K$ :
    - i. Set  $c_n^{(k)} = 0$ .
    - ii. Compute  $\Delta_{n-i,n}^{(k)}$ , ( $i = 1, \dots, n$ ) using Eq. 4.126.
    - iii. If  $\exists i$  s.t.  $\Delta_{n-i,n}^{(k)} \in \Delta_i$ , then set  $c_n^{(k)} = c_n^{(k)} + 1$  and repeat from Item 1(b)ii until  $\Delta_{n-i,n}^{(k)} \notin \Delta_i$ , ( $i = 1, \dots, n$ ).
    - iv. Put  $\Delta_{n-i,n}^{(k)}$  in  $\Delta_i$ , ( $i = 1, \dots, n$ ).
2. Finding  $N_h$  that satisfies Eq. 4.133:

- (a) Set  $N_h = \max_{k,n} \{c_n^{(k)}\} + 1$ .
- (b) Generate  $d = (d_1 | \cdots | d_{N_c-1})$ ,  $d_i = \Delta_i + iN_h$ .
- (c) If  $d$  contains equal elements, then set  $N_h = N_h + 1$  and repeat from Item 2b until  $d$  contains no equal elements.

Note that the value of  $N_h$  varies with the choice of  $c_0^{(k)}$  in Item 1a. We can reduce  $N_h$  by trying different values of  $c_0^{(k)}$ .

#### 4.5.2 THMA code with chip separation and minimum circular CCR and sidelobe ACR

In the code presented in Sec. 4.5.1 we have computed the CCR and the ACR by considering only one waveform for each user. As in practice waveforms are sent periodically, it is also interesting to consider the circular correlation. Accordingly, we have to verify now that the relative delays of the pulse couples in any non-repeated waveform  $w_k(t)$  are different from the relative delays of all other couples in the same waveform repeated twice  $w_k(t) + w_k(t-T)$  and in the other waveforms repeated twice.

In Sec. 4.5.1, we have considered the normalized relative delay  $d_{n,n'}^{(k)} = \frac{t_{n'}^{(k)} - t_n^{(k)}}{T_h}$  Eq. 4.125 with both  $t_n^{(k)}$  and  $t_{n'}^{(k)}$  Eq. 4.2 (positions of the pulses) in the same waveform ( $n, n' < N_c - 1, n' > n$ ). Now, we have to consider in addition:

$$\tilde{d}_{n,n'}^{(k)} = \frac{\tilde{t}_{n'}^{(k)} - t_n^{(k)}}{T_h} = (N_c + n' - n)N_h + \Delta_{n,n'}^{(k)} \quad (4.139)$$

where  $\Delta_{n,n'}^{(k)}$  is defined in Eq. 4.126, and

$$\tilde{t}_n^{(k)} = T + nT_c + c_n^{(k)}T_h = (N_c N_h + nN_h + c_n^{(k)})T_h \quad (4.140)$$

is the position of the  $n$ th pulse in the waveform  $w_k(t - T)$ . As for  $n' > n$ ,  $\tilde{d}_{n,n'}^{(k)}$  Eq. 4.139 becomes equal to  $d_{n,n'}^{(k)}$  Eq. 4.125 modulo  $N_s$  Eq. 4.4, we have to only consider  $n' < n$  in Eq. 4.139. We can see from Eq. 4.139 that to have two pulses distant by  $i$  chips, we should now have  $N_c + n' - n = i$ . Accordingly for the pulses distant by one chip we have to only consider the first pulse  $n' = 0$  in the second waveform with the last pulse  $n = N_c - 1$  in the first waveform, whereas for the pulses distant by  $N_c - 1$  chips we have to consider the pulses number  $n' = 0, \dots, N_c - 2$  in the second waveform with those number  $n = 1, \dots, N_c - 1$  in the first waveform. Accordingly we can write the duals of  $d_i^{(k)}$  Eq. 4.127,  $\Delta_i^{(k)}$  Eq. 4.128,  $d^{(k)}$  Eq. 4.131,  $d$  Eq. 4.132,  $d_i$  Eq. 4.134 and  $\Delta_i$  Eq. 4.135,

( $i = 1, \dots, N_c - 1$ ) as:

$$\tilde{d}_i^{(k)} = (\tilde{d}_{N_c+n-i,n}^{(k)})_{n=0,\dots,i-1} = iN_h + \tilde{\Delta}_i^{(k)} \quad (4.141)$$

$$\tilde{\Delta}_i^{(k)} = (\Delta_{N_c+n-i,n}^{(k)})_{n=0,\dots,i-1} \quad (4.142)$$

$$\tilde{d}^{(k)} = (\tilde{d}_1^{(k)} | \dots | \tilde{d}_{N_c-1}^{(k)}) \quad (4.143)$$

$$\tilde{d} = (\tilde{d}^{(1)} | \dots | \tilde{d}^{(K)}) \quad (4.144)$$

$$\tilde{d}_i = (\tilde{d}_i^{(1)} | \dots | \tilde{d}_i^{(K)}) \quad (4.145)$$

$$\tilde{\Delta}_i = (\tilde{\Delta}_i^{(1)} | \dots | \tilde{\Delta}_i^{(K)}) \quad (4.146)$$

with

$$\tilde{\underline{\Delta}}^{(k)} = \begin{pmatrix} \tilde{\Delta}_1^{(k)} \\ \vdots \\ \tilde{\Delta}_{N_c-1}^{(k)} \end{pmatrix} = \begin{pmatrix} \Delta_{N_c-1,0}^{(k)} & & & \\ & \vdots & \ddots & \\ & \Delta_{1,0}^{(k)} & \cdots & \Delta_{N_c-1,N_c-2}^{(k)} \end{pmatrix} \quad (4.147)$$

where the term in the first row in  $\tilde{\underline{\Delta}}^{(k)}$  Eq. 4.147 is the opposite of that in the last row in  $\underline{\Delta}^{(k)}$  Eq. 4.138 ( $\Delta_{N_c-1,0}^{(k)} = -\Delta_{0,N_c-1}^{(k)}$ ), and the terms in the last row in  $\tilde{\underline{\Delta}}^{(k)}$  Eq. 4.147 are the opposite of those in the first row in  $\underline{\Delta}^{(k)}$  Eq. 4.138 ( $\Delta_{1,0}^{(k)} = -\Delta_{0,1}^{(k)}, \dots, \Delta_{N_c-1,N_c-2}^{(k)} = -\Delta_{N_c-2,N_c-1}^{(k)}$ ). Note that unlike  $d_i^{(k)}$  Eq. 4.127 which contains  $N_c - i$  elements,  $\tilde{d}_i^{(k)}$  Eq. 4.141 contains  $i$  elements. However,  $\tilde{d}^{(k)}$  Eq. 4.143 and  $\tilde{d}$  Eq. 4.144 contain like  $d^{(k)}$  Eq. 4.131 and  $d$  Eq. 4.132,  $\sum_{i=1}^{N_c-1} i = \sum_{i=1}^{N_c-1} (N_c - i) = \frac{N_c(N_c-1)}{2}$  and  $\frac{KN_c(N_c-1)}{2}$  elements respectively.

The conditions in Eq. 4.129 and Eq. 4.130 can now be written as:

$$x_j \neq x_{j'}; \forall j \neq j'; x_j, x_{j'} \in \hat{d}^{(k)} = [\tilde{d}^{(k)} | d^{(k)}] \quad (4.148)$$

$$x_j \neq x_{j'}; \forall j \neq j'; x_j, x_{j'} \in \hat{d} = [\tilde{d} | d] \quad (4.149)$$

and those in Eq. 4.136 and Eq. 4.137 as:

$$x_j \neq x_{j'}; \forall j \neq j'; \forall i; x_j, x_{j'} \in \hat{\Delta}_i^{(k)} = [\tilde{\Delta}_i^{(k)} | \Delta_i^{(k)}] \quad (4.150)$$

$$x_j \neq x_{j'}; \forall j \neq j'; \forall i; x_j, x_{j'} \in \hat{\Delta}_i = [\tilde{\Delta}_i | \Delta_i] \quad (4.151)$$

under the assumption:

$$x \neq x'; \forall (x, x') \in \hat{d}_i \times \hat{d}_{i' > i} \quad (4.152)$$

where  $\hat{d}_i = [\tilde{d}_i | d_i]$ . Note that we can write  $\hat{\Delta}_i^{(k)}$  in Eq. 4.150 from Eq. 4.138 and Eq. 4.147 as:

$$\hat{\Delta}_i^{(k)} = [\tilde{\Delta}_i^{(k)} | \Delta_i^{(k)}] = [- \uparrow \Delta_i^{(k)} | \Delta_i^{(k)}] \quad (4.153)$$

where  $-\uparrow \underline{\Delta}^{(k)}$  denotes the opposite of the matrix  $\underline{\Delta}^{(k)}$  flipped in the up-down direction about a horizontal axis. Note that  $\hat{\Delta}^{(k)}$  is  $N_c \times N_c$  whereas  $\underline{\Delta}^{(k)}$  is  $N_c - 1 \times N_c - 1$  but empty below the diagonal and  $\tilde{\Delta}^{(k)}$  is  $N_c - 1 \times N_c - 1$  but empty above the diagonal.

Let us now describe the algorithm proposed to generate the THMA code satisfying Eq. 4.149:

1. Finding  $c^{(k)}$ , ( $k = 1, \dots, K$ ) that satisfy Eq. 4.137:
  - (a) Arbitrarily generate  $c_0^{(k)}$ , ( $k = 1, \dots, K$ ); generate the empty vectors  $\hat{\Delta}_i$  Eq. 4.146, ( $i = 1, \dots, N_c - 1$ ).
  - (b) For  $n = 1, \dots, N_c - 1$ :  
For  $k = 1, \dots, K$ :
    - i. Set  $c_n^{(k)} = 0$ .
    - ii. Compute  $\Delta_{n-i,n}^{(k)}$ , ( $i = 1, \dots, n$ ) using Eq. 4.126.
    - iii. If  $\exists i$  s.t.  $\Delta_{n-i,n}^{(k)} \in \hat{\Delta}_i$  or  $-\Delta_{n-i,n}^{(k)} \in \hat{\Delta}_{N_c-i}$ , then set  $c_n^{(k)} = c_n^{(k)} + 1$  and repeat from Item 1(b)ii until  $\Delta_{n-i,n}^{(k)} \notin \hat{\Delta}_i$  and  $-\Delta_{n-i,n}^{(k)} \notin \hat{\Delta}_{N_c-i}$ , ( $i = 1, \dots, n$ ).
    - iv. Put  $\Delta_{n-i,n}^{(k)}$  in  $\hat{\Delta}_i$  and  $-\Delta_{n-i,n}^{(k)}$  in  $\hat{\Delta}_{N_c-i}$ , ( $i = 1, \dots, n$ ).
2. Finding  $N_h$  that satisfies Eq. 4.133:
  - (a) Set  $N_h = \max_{k,n} \{c_n^{(k)}\} + 1$ .
  - (b) Generate  $\hat{d} = (\hat{d}_1 | \dots | \hat{d}_{N_c-1})$ ,  $\hat{d}_i = \hat{\Delta}_i + iN_h$ .
  - (c) If  $\hat{d}$  contains equal elements, then set  $N_h = N_h + 1$  and repeat from Item 2b until  $\hat{d}$  contains no equal elements.

#### 4.5.3 THMA code without chip separation and with minimum CCR and sidelobe ACR

Now we consider the generation of THMA codes without chip separation (see Eq. 4.3, Eq. 4.5 and Eq. 4.6) and with minimum CCR and sidelobe ACR.

The row vectors containing the normalized relative delays of the couples of pulses of  $w_k(t)$  separated by  $i$  pulses ( $i = 1, \dots, N_c - 1$ ,  $i = 1$  corresponds to adjacent pulses), of all couples of  $w_k(t)$ , and of all couples of all waveforms ( $k = 1, \dots, K$ ) are given by:

$$d_i^{(k)} = (d_{n-i,n}^{(k)})_{n=i,\dots,N_c-1} = \Delta_i^{(k)} \quad (4.154)$$

$$d^{(k)} = (d_1^{(k)} | \dots | d_{N_c-1}^{(k)}) \quad (4.155)$$

$$d = (d^{(1)} | \dots | d^{(K)}) \quad (4.156)$$

where

$$d_{n,n'}^{(k)} = \frac{t_{n'}^{(k)} - t_n^{(k)}}{T_h} = \Delta_{n,n'}^{(k)} \quad (4.157)$$

denotes the normalized relative delay between the  $n$ th and  $n'$ th pulses of  $w_k(t)$  with  $t_n^{(k)}$  given in Eq. 4.6 and  $\Delta_{n,n'}^{(k)}$  in Eq. 4.126.

The necessary and sufficient conditions for minimum sidelobe ACR and minimum CCR can now be written like in Eq. 4.123 and Eq. 4.124 as:

$$x_j \neq x_{j'}; \forall j \neq j'; x_j, x_{j'} \in d^{(k)} \quad (4.158)$$

$$x_j \neq x_{j'}; \forall j \neq j'; x_j, x_{j'} \in d \quad (4.159)$$

where  $x_j$  and  $x_{j'}$  denote the  $j$ th and  $j'$ th elements in the vectors  $d^{(k)}$  Eq. 4.155 and  $d$  Eq. 4.156 of  $\sum_{i=1}^{N_c-1} (N_c - i) = \frac{N_c(N_c-1)}{2}$  and  $\frac{KN_c(N_c-1)}{2}$  elements respectively.

Let us now describe the algorithm proposed to generate the THMA code satisfying Eq. 4.149:

1. Finding  $c^{(k)}$ , ( $k = 1, \dots, K$ ) that satisfy Eq. 4.159:
  - (a) Set  $c_0^{(k)} = 0$ , ( $k = 1, \dots, K$ ); generate the empty vector  $d$ .
  - (b) For  $n = 1, \dots, N_c - 1$ :
    - For  $k = 1, \dots, K$ :
      - i. Set  $c_n^{(k)} = c_{n-1}^{(k)} + 1$ .
      - ii. Compute  $\Delta_{n-i,n}^{(k)}$ , ( $i = 1, \dots, n$ ) using Eq. 4.126.
      - iii. If  $\exists i$  s.t.  $\Delta_{n-i,n}^{(k)} \in d$ , then set  $c_n^{(k)} = c_{n-1}^{(k)} + 1$  and repeat from Item 1(b)ii until  $\Delta_{n-i,n}^{(k)} \notin d$ , ( $i = 1, \dots, n$ ).
      - iv. Put  $\Delta_{n-i,n}^{(k)}$ , ( $i = 1, \dots, n$ ) in  $d$ .
2. Finding  $N_h$ :  $N_h = \max_{k,n} \{c_n^{(k)}\} + 1$ .

#### 4.5.4 THMA code without chip separation and with minimum circular CCR and sidelobe ACR

In this section we propose an algorithm to generate THMA codes without chip separation and with minimum circular CCR and sidelobe ACR.

We can write the normalized relative delay between the  $n'$ th pulse of the repeated waveform  $w_k(t - T)$  and the  $n$ th pulse of the non-repeated waveform  $w_k(t)$  as:

$$\tilde{d}_{n,n'}^{(k)} = \frac{\tilde{t}_{n'}^{(k)} - t_n^{(k)}}{T_h} = N_h + \Delta_{n,n'}^{(k)} \quad (4.160)$$

where  $\Delta_{n,n'}^{(k)}$  is defined in Eq. 4.126, and

$$\tilde{t}_n^{(k)} = T + c_n^{(k)}T_h = (N_h + c_n^{(k)})T_h \quad (4.161)$$

is the position of the  $n$ th pulse in the waveform  $w_k(t - T)$ . The row vectors containing the normalized relative delays of the couples of pulses of  $w_k(t)$  and  $w_k(t - T)$  (the first pulse in the first waveform and the second in the repeated one) separated by  $i$  pulses ( $i = 1, \dots, N_c - 1$ , where  $i = 1$  corresponds to adjacent pulses), of all couples between  $w_k(t)$  and  $w_k(t - T)$ , and of all couples between  $w_k(t)$  and  $w_k(t - T)$  for all users ( $k = 1, \dots, K$ ) can be expressed as:

$$\tilde{d}_i^{(k)} = (\tilde{d}_{N_c+n-i,n}^{(k)})_{n=0,\dots,i-1} = N_h + \tilde{\Delta}_i^{(k)} \quad (4.162)$$

$$\tilde{\Delta}_i^{(k)} = (\Delta_{N_c+n-i,n}^{(k)})_{n=0,\dots,i-1} \quad (4.163)$$

$$\tilde{d}^{(k)} = (\tilde{d}_1^{(k)} | \dots | \tilde{d}_{N_c-1}^{(k)}) \quad (4.164)$$

$$\tilde{d} = (\tilde{d}^{(1)} | \dots | \tilde{d}^{(K)}) \quad (4.165)$$

where the terms of  $\tilde{\Delta}_i^{(k)}$  Eq. 4.163 for a given  $i$  are the opposite of those of  $\Delta_{N_c-i}^{(k)}$  Eq. 4.154.

The minimum circular sidelobe ACR and CCR constraints can be written as:

$$x_j \neq x_{j'}; \forall j \neq j'; x_j, x_{j'} \in \hat{d}^{(k)} = [\tilde{d}^{(k)} | d^{(k)}] \quad (4.166)$$

$$x_j \neq x_{j'}; \forall j \neq j'; x_j, x_{j'} \in \hat{d} = [\tilde{d} | d]. \quad (4.167)$$

Let us now describe the algorithm proposed to generate the THMA code satisfying Eq. 4.167:

1. Finding  $c^{(k)}$ , ( $k = 1, \dots, K$ ) that satisfy Eq. 4.159:
  - (a) Set  $c_0^{(k)} = 0$ , ( $k = 1, \dots, K$ ); generate the empty vector  $d$  Eq. 4.156.
  - (b) For  $n = 1, \dots, N_c - 1$ :  
For  $k = 1, \dots, K$ :
    - i. Set  $c_n^{(k)} = c_{n-1}^{(k)} + 1$ .
    - ii. Compute  $\Delta_{n-i,n}^{(k)}$ , ( $i = 1, \dots, n$ ) using Eq. 4.126.
    - iii. If  $\exists i$  s.t.  $\Delta_{n-i,n}^{(k)} \in d$ , then set  $c_n^{(k)} = c_n^{(k)} + 1$  and repeat from Item 1(b)ii until  $\Delta_{n-i,n}^{(k)} \notin d$ , ( $i = 1, \dots, n$ ).
    - iv. Put  $\Delta_{n-i,n}^{(k)}$ , ( $i = 1, \dots, n$ ) in  $d$ .
2. Finding  $N_h$  so that the generated  $c^{(k)}$  satisfy Eq. 4.167:
  - (a) Set  $N_h = \max_{k,n} \{c_n^{(k)}\} + 1$ .
  - (b) Generate  $\hat{d} = [\tilde{d} | d] = [N_h - d | d]$ .
  - (c) If  $\hat{d}$  contains equal elements, then set  $N_h = N_h + 1$  and repeat from Item 2b until  $\hat{d}$  contains no equal elements.

#### 4.5.5 THMA codes with variable length

In this section we assume that we know the duration of the waveform in time-hops  $N_s$  Eq. 4.4, Eq. 4.5, and the minimum  $N_{c,\min}$  and maximum  $N_{c,\max}$  code lengths. We propose an algorithm to generate the maximum number of codewords (with variable length) of the codes presented in Sec. 4.5.1, Sec. 4.5.2, Sec. 4.5.3 and Sec. 4.5.4.

For the THMA codes in Sec. 4.5.1 and Sec. 4.5.2 we take  $N_h = \frac{N_s}{N_{c,\max}}$ , and for the THMA codes in Sec. 4.5.3 and Sec. 4.5.4 we have  $N_h = N_s$  Eq. 4.5. Remind that unlike the codes in Sec. 4.5.1 and Sec. 4.5.3, those in Sec. 4.5.2 and Sec. 4.5.4 consider the circular correlation.

Denote by  $K$  the number of generated codewords (size of codeword book),  $N_c = (N_{c,1} \cdots N_{c,K})$  the vector containing the number of pulses in each codeword,  $\tilde{c} = (\tilde{c}_0 \cdots \tilde{c}_{\tilde{N}_c-1})$  a candidate codeword (not necessarily added after to the codeword book) of instantaneous length  $\tilde{N}_c$ , and  $\tilde{c}_e$  an instantaneous candidate element to  $\tilde{c}$  (not necessarily added to it).

Let us first describe the algorithm proposed to generate codewords for the THMA code given in Sec. 4.5.4:

1. Generate the empty vectors  $\hat{d}$  and  $N_c$ ; set  $K = 0$ .
2. Set  $\tilde{c} = 0$ .
3. Set  $\tilde{c}_e = \tilde{c}_{\tilde{N}_c-1} + 1$ .
4. Compute  $\tilde{d} = \tilde{c}_e - \tilde{c}$ .
5. Set  $\hat{d} = (\tilde{d}|N_s - \tilde{d})$ .
6. If  $\{\hat{d}$  contains equal elements or  $\exists x \in \hat{d}_e; x \in \hat{d}\}$ , then set  $\tilde{c}_e = \tilde{c}_e + 1$  and repeat from Item 4 until either,  $\{\hat{d}$  contains no equal elements and  $\nexists x \in \hat{d}_e; x \in \hat{d}\}$ , or  $\{\tilde{c}_e = N_h\}$ .
7. If  $\tilde{c}_e \neq N_h$ , then set  $\tilde{c} = (\tilde{c}|\tilde{c}_e)$ ,  $\tilde{N}_c = \tilde{N}_c + 1$  and  $\hat{d} = (\hat{d}|\tilde{d})$  and proceed to Item 8, otherwise proceed to Item 9.
8. If  $\tilde{N}_c = N_{c,\max}$ , then set  $N_c = (N_c|\tilde{N}_c)$  and  $K = K + 1$ , add  $\tilde{c}$  to the codeword book, and proceed to Item 2.
9. If  $\tilde{N}_c \geq N_{c,\min}$ , then set  $N_c = (N_c|\tilde{N}_c)$  and  $K = K + 1$ , add  $\tilde{c}$  to the codeword book, and proceed to Item 2, otherwise stop the algorithm.

Now, for the THMA code in Sec. 4.5.1, we can generate  $\tilde{c}$  randomly in Item 2, we set  $\tilde{c}_e = 0$  in Item 3, we compute  $\tilde{d}$  as  $\tilde{d} = \tilde{c}_e - \tilde{c} + (\tilde{N}_c \cdots 1)N_h$  in Item 4, and we skip Item 5.

For the THMA code in Sec. 4.5.2, we do the same as for the code in Sec. 4.5.1 but we do not skip Item 5.

For the THMA code in Sec. 4.5.3, we just skip Item 5.

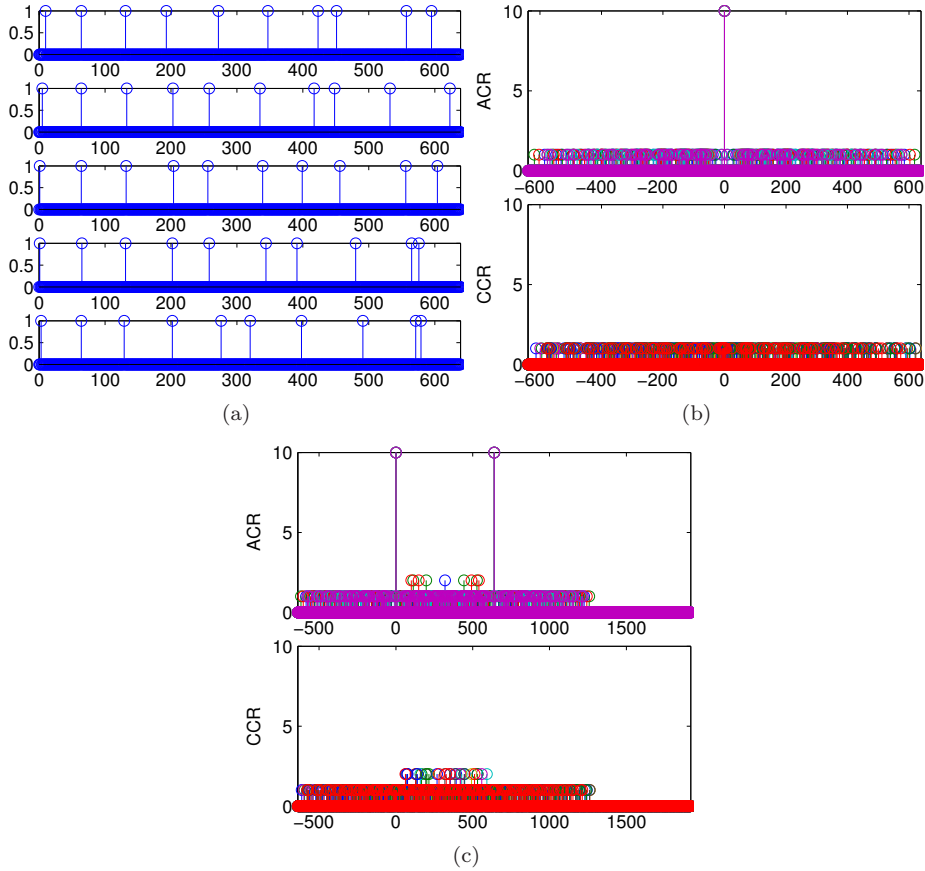


Fig. 4.13.: Code 1:  $K = 5$ ,  $N_c = 10$ ,  $N_s = 640$  and  $N_h = 64$  (a) Codewords (b) ACR and CCR (c) Circular ACR and CCR.

### 4.5.6 Numerical results

In this section we present some numerical results obtained using the algorithms proposed in Sec. Sec. 4.5.1, Sec. 4.5.2, Sec. 4.5.3, Sec. 4.5.4 and Sec. 4.5.5.

We denote by Code 1, Code 2, Code 3 and Code 4 the codes presented in Sec. 4.5.1, Sec. 4.5.2, Sec. 4.5.3, Sec. 4.5.4 respectively, and by Code 5.1, Code 5.2, Code 5.3 and Code 5.4 the codes with variable length presented in Sec. 4.5.5 and having the properties of Codes 1, 2, 3 and 4. We recall that for Codes 1, 2, 3 and 4, the number of codewords  $K$  and the length  $N_c$  of the code are both known and constant, whereas for Codes 5.1, 5.2, 5.3 and 5.4, the duration  $N_s$  of the waveform in time-hops is known as well as the minimum  $N_{c,\min}$  and maximum  $N_{c,\max}$  code lengths, but  $K$  is unknown and  $N_c$  is not the same for all codewords.

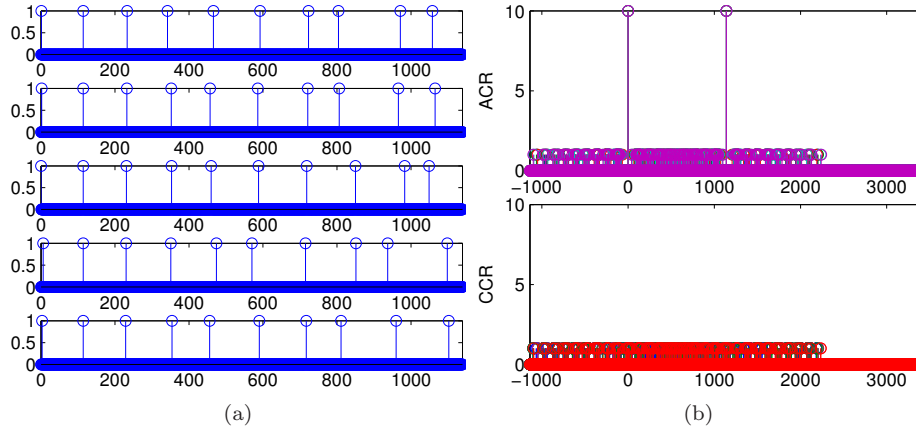


Fig. 4.14.: Code 2:  $K = 5$ ,  $N_c = 10$ ,  $N_s = 1140$  and  $N_h = 114$  (a) Codewords (b) Circular ACR and CCR.

Let us first consider Codes 1, 2, 3 and 4. We take  $K = 5$  and  $N_c = 10$ . We have obtained  $N_h = 64$  and  $N_s = 640$  for Code 1,  $N_h = 114$  and  $N_s = 1140$  for Code 2,  $N_s = N_h = 409$  for Code 3 and  $N_s = N_h = 789$  for Code 4. The codewords obtained for Codes 1, 2 and 3 are given below:

$$c = \begin{pmatrix} 10 & 0 & 3 & 1 & 16 & 27 & 39 & 3 & 45 & 19 \\ 5 & 0 & 5 & 11 & 2 & 15 & 33 & 0 & 20 & 47 \\ 1 & 0 & 4 & 12 & 0 & 19 & 15 & 8 & 44 & 28 \\ 1 & 1 & 3 & 10 & 2 & 24 & 7 & 32 & 53 & 0 \\ 3 & 0 & 1 & 10 & 20 & 0 & 14 & 43 & 59 & 3 \end{pmatrix}$$

$$c = \begin{pmatrix} 1 & 0 & 5 & 0 & 10 & 22 & 39 & 6 & 59 & 32 \\ 2 & 0 & 4 & 10 & 1 & 16 & 37 & 8 & 54 & 39 \\ 0 & 0 & 3 & 11 & 4 & 18 & 34 & 52 & 71 & 23 \\ 6 & 0 & 2 & 9 & 18 & 0 & 31 & 53 & 25 & 72 \\ 3 & 0 & 1 & 12 & 0 & 20 & 33 & 13 & 48 & 76 \end{pmatrix}$$

$$c = \begin{pmatrix} 0 & 1 & 17 & 26 & 65 & 85 & 165 & 228 & 332 & 402 \\ 0 & 2 & 15 & 29 & 62 & 98 & 153 & 219 & 322 & 395 \\ 0 & 3 & 10 & 31 & 54 & 89 & 126 & 171 & 261 & 358 \\ 0 & 4 & 12 & 34 & 53 & 105 & 145 & 233 & 275 & 383 \\ 0 & 5 & 11 & 43 & 61 & 118 & 142 & 220 & 296 & 408 \end{pmatrix}.$$

Note that the codewords of Codes 3 and 4 are equal as can be seen from the algorithms in Sec. 4.5.3 and Sec. 4.5.4. However, the waveform duration  $N_s$  is not the same for both. We can see that Codes 1 and 2 ( $N_s = 640$  and  $1140$ ) are longer than Codes 3 and 4 ( $N_s = 409$  and  $789$ ) respectively due to the chip  $T_c = N_h T_h$  separation between the consecutive pulses of Codes 1 and 2, and that

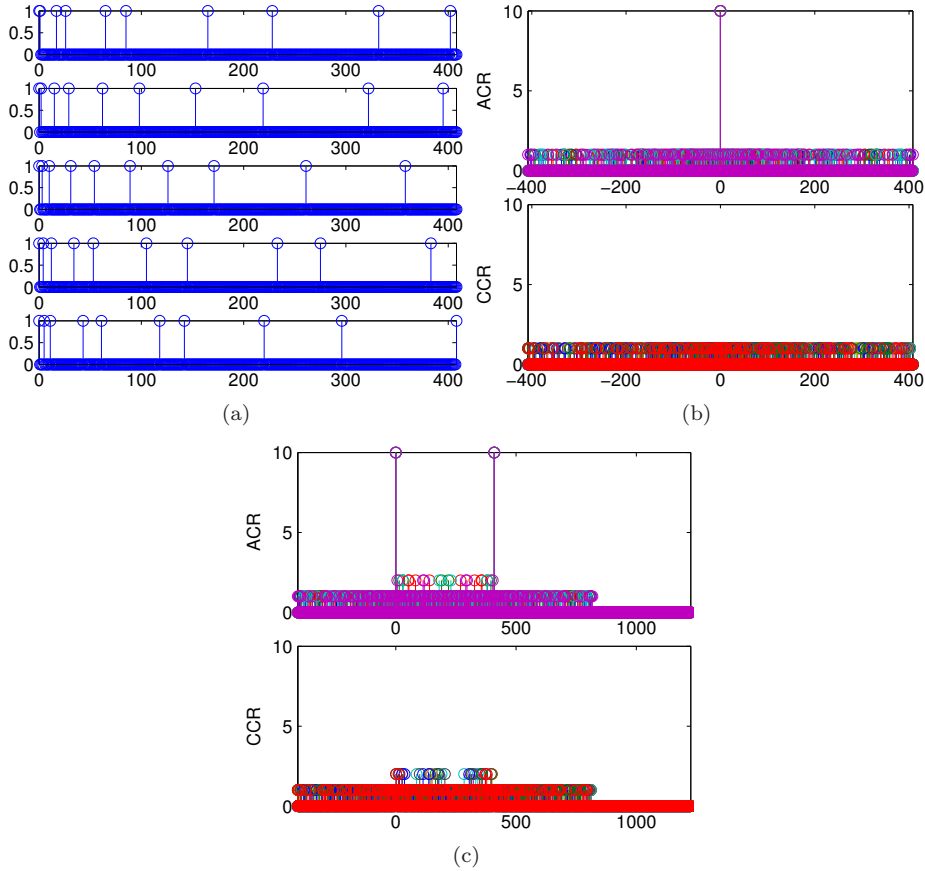


Fig. 4.15.: Code 3:  $K = 5$ ,  $N_c = 10$ ,  $N_s = N_h = 409$  (a) Codewords (b) ACR and CCR (c) Circular ACR and CCR.

Codes 2 and 4 are longer than Codes 1 and 3 respectively because they satisfy the circular correlation constraints.

Let us now consider Codes 5.1, 5.2, 5.3 and 5.4. We take  $N_s = 1000$ ,  $N_{c,\min} = 6$  and  $N_{c,\max} = 10$ . Different results have been obtained for Codes 5.1 and 5.2 because  $c_0^{(k)}$  is generated randomly. We have obtained  $K = 9$  with  $N_c = (10, 10, 10, 10, 10, 10, 10, 7, 6)$  for Code 1,  $K = 9$  with  $N_c = (10, 10, 10, 10, 8, 8, 6, 6, 6)$  for Code 2,  $K = 13$  with  $N_c = (10, 10, 10, 10, 10, 10, 9, 8, 7, 7, 6, 6, 6)$  for Codes 5.3, and  $K = 10$  with  $N_c = (10, 10, 10, 10, 10, 10, 10, 10, 10)$  for Codes 5.4.

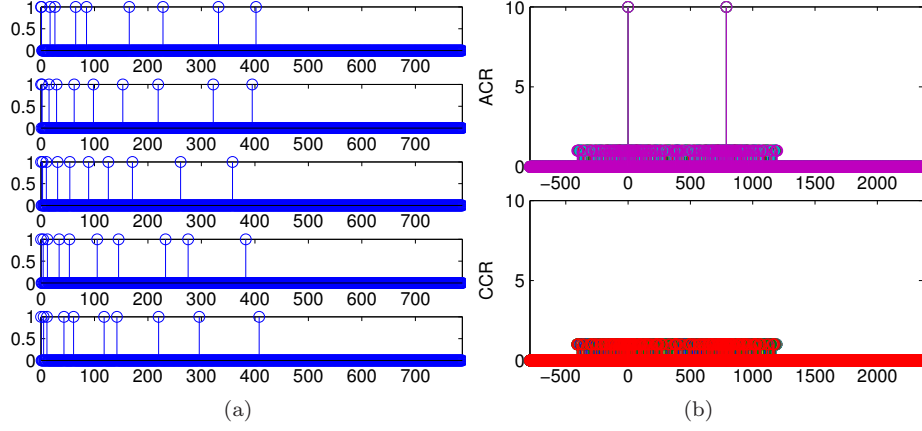


Fig. 4.16.: Code 4:  $K = 5$ ,  $N_c = 10$ ,  $N_s = N_h = 789$  (a) Codewords (b) Circular ACR and CCR.

Denote by:

$$w_k[j], j = 0, \dots, N_s - 1 \quad (4.168)$$

$$X_{w_k, w_{k'}}[j] = \sum_{\xi} w_k[\xi + j] w_{k'}[\xi] \quad (4.169)$$

the discrete waveform relative to  $w_k(t)$ , and the discrete CCR of  $w_k[j]$  and  $w_{k'}[j]$ , with  $w_k[j] = 1$  (resp. 0) if a pulse is (resp. is not) contained in  $[jT_h, (j+1)T_h)$ . The circular correlation can be obtained by correlating  $w_k[j]$  with  $w_{k'}[j] + w_{k'}[j - N_s]$ .

In Fig. 4.13(a) we show the discrete waveforms of all codewords of Code 1, in Fig. 4.13(b) the discrete ACR of all waveforms (figure on the top) and the discrete CCR of all different waveforms (figure on the bottom), and in Fig. 4.13(c) the discrete circular ACR and CCR. We can see that the constraint of minimum CCR and sidelobe ACR is satisfied (CCR and sidelobe ACR always lower than or equal to one) but not the constraint of minimum circular correlation (we have some points where the CCR and the sidelobe ACR are equal to two). Note that the ACR is always equal to  $N_c$  for a relative delay equal to a multiple of  $N_s$  (waveform duration in time-hops).

In Fig. 4.14(a) we show the obtained waveforms of Code 2, and in Fig. 4.14(b) the corresponding circular ACR and CCR. We can see that the constraint of minimum circular CCR and sidelobe ACR is satisfied.

In Fig. 4.15(a) we show the obtained waveforms of Code 3, in Fig. 4.15(b) the corresponding ACR and CCR, and in Fig. 4.15(c) the circular ACR and CCR. Like Code 1, we can see that the constraint of minimum CCR and sidelobe ACR is satisfied but not the constraint of minimum correlation.

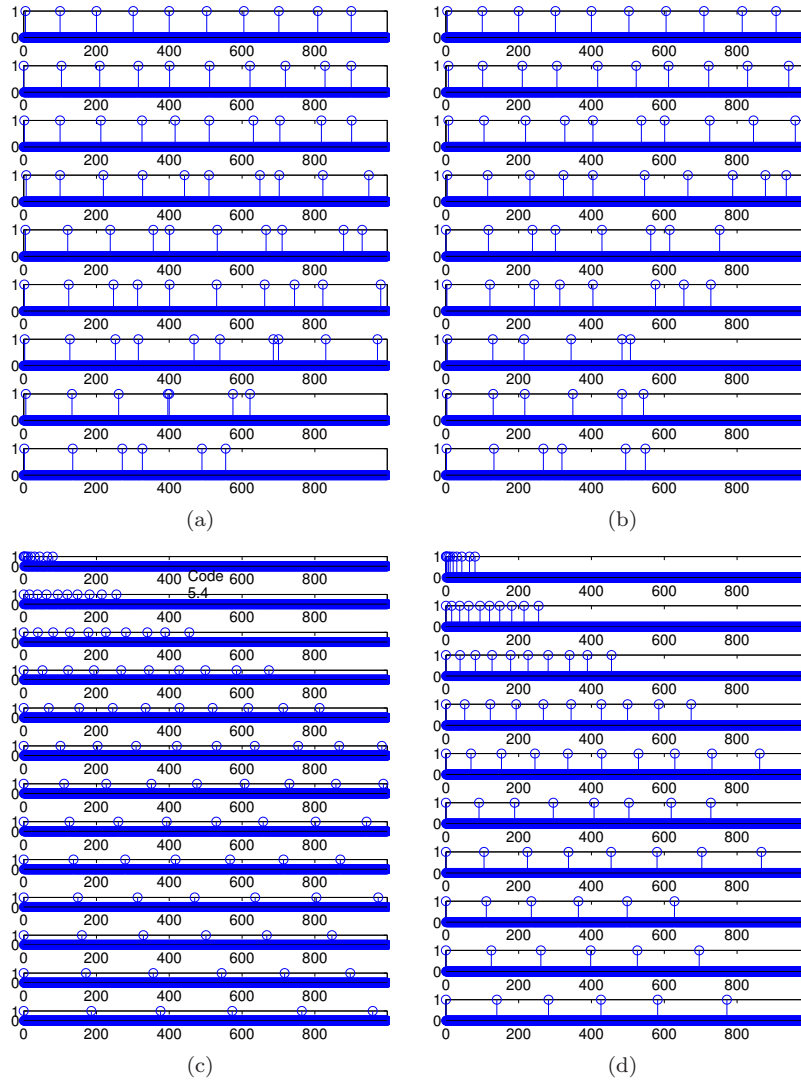


Fig. 4.17.:  $N_s = 1000$ ,  $N_{c,\min} = 6$  and  $N_{c,\max} = 10$  (a) Code 5.1 (b) Code 5.2 (c) Code 5.3 (d) Code 5.4

In Fig. 4.16(a) we show the obtained waveforms of Code 4, and in Fig. 4.16(b) the corresponding circular ACR and CCR. Like Code 2, the constraint of minimum circular CCR and sidelobe ACR is satisfied.

By comparing Codes 1 and 3 (resp. Codes 2 and 4), we can see that unlike Code 3 (resp. Code 4), the pulses of Code 1 (resp. Code 2) are approximately

equidistant thanks to the chip separation. However, the waveforms of Code 1 (resp. Code 2) are longer as already mentioned. By comparing Codes 3 and 4 we can see that a guard time (less than the duration of the waveforms of Code3) is added after the last pulse to satisfy the constraint of minimum circular CCR and sidelobe ACR.

In Fig. 4.17(a), Fig. 4.17(b), Fig. 4.17(c) and Fig. 4.17(d) we show the obtained waveforms for Codes 5.1, 5.2, 5.3 and 5.4 respectively. We can see that unlike Codes 5.1 and 5.2, the average relative delays between the consecutive pulses of the waveforms of Codes 5.3 and 5.4 increase with the waveform generation order (i.e. it is larger for a waveform generated later). This is due to the generation algorithms proposed in Sec. 4.5.5.

## 4.6 CONCLUSION

In this chapter we have considered TOA estimation based on TH-IR-UWB signals using both the MCE and the MME. We have derived based on the results of Chap. 2 and Chap. 3 some MSE approximations and approximate lower bounds for both estimators. The derived MSE approximations and approximate lower bounds are applied to TOA using TH-IR-UWB signals assuming single-user. We have seen that both the MCE and the MME approximately have the same global performances. We have considered TOA estimation with MUI. The cases of deterministic and random MUI are treated separately. We have presented some cases where the proposed MME outperforms the MCE. We have compared the MSE approximations to the MSE truly achieved with random MUI. The MCE slightly outperforms the MME in the case of random MUI. We have also presented some algorithms to generate THMA codes with minimum sidelobe ACR and minimum CCR.



## CHAPTER 5

---

# CRLBS FOR POSITION ESTIMATION AND JOINT TOA AND AOA ESTIMATION IN MIMO AND UWB SYSTEMS

---

THERE is a growing interest in UWB based positioning since the FCC has allowed in 2002 the unlicensed use of the UWB spectrum [1].

Different techniques, like the RSS, the TOA, the AOA, and the hybrid based methods, can be used, following the target application and the features of the transmitted and received signals.

The AOA estimation is based on the use of antenna arrays. An array of three non-collinear elements can determine the two-dimensional (2D) AOA without ambiguity. With RSS and TOA techniques, three reference nodes at least are needed to perform the 2D positioning without ambiguity. However, with the AOA technique, only two reference nodes are, in general, sufficient (see Sec. 5.1.8 for more details). By combining different techniques together (e.g. TOA and AOA), only one reference becomes sufficient.

In this chapter we consider positioning in UWB systems, TOA and AOA estimation in wideband (WB) SISO, SIMO, MISO and MIMO systems, and the estimation of the gain and the TOA in UWB MP channels.

In Sec. 5.1 we assume that UWB signals are transmitted. We derive the CRLB for position estimation based on the AOA technique, and for position estimation based on the TOA and AOA techniques simultaneously. The communication channel is supposed to be of the MP type, but with non-overlapping components.

The subject investigated in this section is based on our work published in [93, 107].

In Sec. 5.2 we investigate the problem of positioning in MISO and MIMO systems. We derive the CRLBs for the joint estimation of the TOA and the AOA. We assume that WB signals are transmitted. We consider both the cases of orthogonal and non-orthogonal signals. We compare the CRLBs obtained in SISO, SIMO, MISO and MIMO systems to each others under the assumption that the total transmitted energy is the same for all systems. We show that for TOA estimation, SIMO and MIMO systems are equivalent, and MISO and SISO systems are equivalent as well, when the transmitted signals are orthogonal. However, for non-orthogonal signals, MIMO systems are better than SIMO systems, and MISO systems are superior to SISO systems, in the regions where the received signals are constructive. For AOA estimation, we show that MIMO systems are better than SIMO systems, and that SIMO systems outperform MISO systems, when the transmitted signals are orthogonal. However, for non-orthogonal signals, MIMO systems become much more better in the regions where the received signals are constructive. The results presented in this section are already published in [108, 109].

As mentioned above, we consider in Sec. 5.1 UWB channels with non-overlapping MPCs. In order to study the impact of the overlapping among the neighboring MPCs on the performances of the estimation, we consider in Sec. 5.3 the problem of the joint estimation of the gains and the TOAs of all present MPCs, and derive the corresponding CRLBs. We have already treated this topic in [110, 111]. We compute the average CRLBs for the IEEE802.15.4a UWB channel model. The CRLBs obtained by averaging more than 80% of the possible cases of the considered channels, are very close to the CRLBs obtained under the non-overlapping assumption.

## 5.1 CRLBS FOR UWB-BASED POSITIONING USING AOA AND HYBRID TOA-AOA TECHNIQUES

UWB-based positioning has been mainly studied for the TOA method [112, 113]. Only few works can be found on CRLB for UWB-based AOA estimation [107, 114]. AOA is widely investigated in the literature for narrowband and WB signals but under the assumption of a narrowband signal [115–118]. In [116], the authors report the CRLB on the position for DS code division multiple access (CDMA) based positioning using simultaneously TOA and AOA whereas in [117], CRLBs are reported for joint AOA and TOA estimation in DS-CDMA systems.

In this section we consider the AOA method in a rigorous manner, that is, without the narrowband assumption. Furthermore we investigate a hybrid method by incorporating both the AOA and TOA information. The UWB signal under consideration is supposed to be composed from a train of pulses modulated by unknown data. The channel is supposed to be of the MP type; however

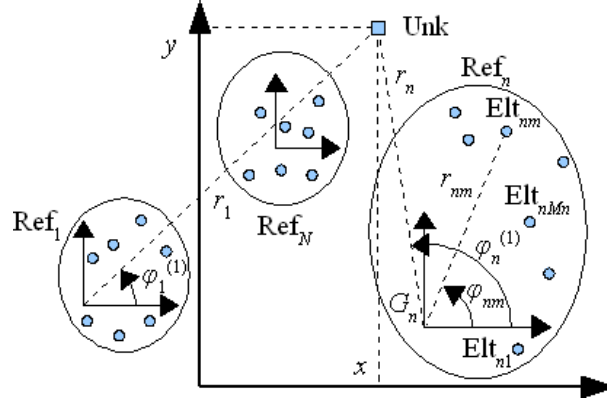


Fig. 5.1.: The unknown location node and the reference nodes arrays.

the impact of MP will be shown to be limited thanks to a realistic assumption (i.e. the non-overlapping assumption introduced in Sec. 5.1.2).

Our goal in this work is to evaluate the potential of a number of positioning techniques when a UWB signal is used. We do not focus however on implementation challenges.

In Sec. 5.1.1 we describe our system model. In Sec. 5.1.2 we introduce the non-overlapping assumption. In Sec. 5.1.3 we derive the CRLBs for the joint estimation of the direct path TOA and AOA. In Sec. 5.1.4 we propose a method that allows us to obtain the CRLBs for the joint estimation of a set of parameters, from the CRLBs of another set of parameters, that is function of the first set. In Sec. 5.1.5 we derive the CRLBs for AOA-based positioning. In Sec. 5.1.6 we derive the CRLBs for hybrid TOA-AOA based positioning. In Sec. 5.1.7 we compare the exact AOA CRLB to the approximated CRLB obtained using the narrowband approximation. In Sec. 5.1.8 we present and discuss the numerical results obtained for AOA-based positioning and hybrid positioning, considering some typical scenarios.

### 5.1.1 System model

In our reference scenario depicted in Fig. 5.1, we consider an unknown location node called Unk and  $N$  reference nodes called  $\text{Ref}_1, \dots, \text{Ref}_N$ . Unk is equipped with a one-element antenna for transmission, and each  $\text{Ref}_n$ , ( $n = 1, \dots, N$ ) equipped with a planar antenna array of  $M_n$  elements for reception. We call  $\text{Elt}_{n,m}$  the  $m^{\text{th}}$  element of  $\text{Ref}_n$ .

UWB channels are very challenging. One of the main channel impairment is the MP propagation. In view of this, several simplifying assumptions are introduced:

- The channel is assumed to contain a line of sight (LOS) component, to be non distorting and with AWGN.
- Unk and the scatterers leading to MP are sufficiently far away from all reference nodes, so that the received signals arrive as plane waves; this is equivalent to the far-field assumption.
- For a given element of the receive array, the contribution carried by the direct path in the received signal does not overlap with the replicas carried by the other paths. This condition is called the “non overlapping assumption” (NOLA).

We will show in Sec. 5.1.3 that once the NOLA is satisfied, the position estimate will not be impacted by the MP phenomenon. The NOLA will be discussed in Sec. 5.1.2.

The signal received at  $\text{Elt}_{n,m}$  can be written as:

$$r_{n,m}(t) = \sum_{l=1}^{L_n} \alpha_{n,m}^{(l)} s(t - \tau_{n,m}^{(l)}) + n_{n,m}(t) \quad (5.1)$$

$$= \sum_{l=1}^{L_n} \alpha_{n,m}^{(l)} s_{n,m}^{(l)}(t) + n_{n,m}(t) \quad (5.2)$$

where  $s(t)$  denotes the signal transmitted by Unk,  $L_n$  is the number of paths between Unk and any element  $\text{Ref}_n$ ,  $\alpha_{n,m}^{(l)}$  and  $\tau_{n,m}^{(l)}$  are the gain and the time delay introduced by the  $l^{\text{th}}$  path between Unk and  $\text{Elt}_{n,m}$ , and  $n_{n,m}(t)$  is the AWGN at  $\text{Elt}_{n,m}$ . Signals  $n_{n1}(t), \dots, n_{nM_n}(t)$  are independent and identically distributed with two-sided PSD of  $N_0/2$ .

The signal transmitted  $s(t)$  is given by:

$$s(t) = \sum_{k=1}^K a_k p(t - kT_s) \quad (5.3)$$

where  $a_1, \dots, a_K$  denote  $K$  unknown symbols belonging to a pulse amplitude modulation (PAM) constellation,  $T_s$  is the symbol period, and  $p(t)$  is the basic pulse waveform.

The far-field assumption allows us to write:

$$\alpha_{n,m}^{(l)} \approx \alpha_n^{(l)}, \forall m \quad (5.4)$$

$$\tau_{n,m}^{(l)} \approx \tau_n^{(l)} - \frac{r_{n,m}}{c} \cos(\varphi_n^{(l)} - \varphi_{n,m}) \quad (5.5)$$

where  $\tau_n^{(l)}$  denotes the delay corresponding to the  $l^{\text{th}}$  path between Unk and  $G_n$  (the geometric center of the  $n^{\text{th}}$  reference node),  $\varphi_n^{(l)}$  is the AOA with respect

to the  $x$  axis of the tap associated with the  $l^{\text{th}}$  scatterer,  $r_{n,m}$  and  $\varphi_{n,m}$  are the polar coordinates of  $\text{Elt}_{n,m}$  with respect to  $G_n$ , and  $c$  is the speed of light.

Denote by  $(x, y)$  and  $(x_n, y_n)$  the Cartesian coordinates of Unk and  $\text{Ref}_n$ , respectively, with respect to an absolute reference and by  $(r_n, \varphi_n)$  the polar coordinates of Unk with respect to the geometric center  $G_n$  of  $\text{Ref}_n$ . We can write  $r_n$  and  $\varphi_n$  as:

$$r_n = \sqrt{(x - x_n)^2 + (y - y_n)^2} \quad (5.6)$$

$$\varphi_n = 2 \arctan \left[ \frac{(y - y_n)}{(x - x_n) + \sqrt{(x - x_n)^2 + (y - y_n)^2}} \right] \quad (5.7)$$

where the expression of  $\varphi_n$  is valid  $\forall(x, y)$ , except the points with  $y - y_n = 0$  and  $x - x_n < 0$  simultaneously. Notice that  $r_n = \frac{\tau_n^{(1)}}{c}$  and  $\varphi_n = \varphi_n^{(1)}$  where  $\tau_n^{(1)}$  and  $\varphi_n^{(1)}$  are the time delay and the AOA associated with the direct path, respectively (see Eq. 5.5).

### 5.1.2 Non-overlapping assumption

In this subsection we analyze the impact of the NOLA and discuss whether this assumption is valid for realistic environments.

The following conditions are sufficient in order to benefit from the NOLA:

$$\begin{cases} \tau_n^{(2)} - \tau_n^{(1)} \geq T_w + \frac{D}{c} \\ \tau_n^{(L_n)} - \tau_n^{(1)} \leq T_s - T_w - \frac{D}{c} \end{cases} \quad (5.8)$$

where  $D$  denotes the diameter of the smallest circle centered on  $G_n$  and including all the elements of  $\text{Ref}_n$ , and  $T_w$  is the duration of  $p(t)$ . The first condition is associated with the possible overlapping between the direct path and the first replica, of a given transmitted pulse (we have  $K$  transmitted pulses, see Eq. 5.3); the second condition concerns the possible overlapping between the last replica of a given transmitted pulse, and the direct path of the next pulse.

Let us now consider a simplified version of the UWB channel model proposed for IEEE 802.15.4a in [9]. It has been assumed that the MP taps arrive grouped in consecutive clusters. The cluster TOA follows a Poisson process with conditional probability:

$$p(T_i | T_{i-1}) = \Delta \exp[-\Delta(T_i - T_{i-1})]$$

where  $T_i$  denotes the TOA of the  $i^{\text{th}}$  cluster and  $\Delta$  the average rate of arrival of clusters. Within a given cluster, the TOA of a given tap follows a mixture of two Poisson processes with conditional probabilities:

$$p(\tau_{j,i} | \tau_{j-1,i}) = \eta \delta_1 \exp[-\delta_1(\tau_{j,i} - \tau_{j-1,i})] + (1 - \eta) \delta_2 \exp[-\delta_2(\tau_{j,i} - \tau_{j-1,i})] \quad (5.9)$$

	Residential LOS	Office LOS
Range[m]	7 – 20	3 – 28
$\Delta^{-1}$ [ns]	21.28	62.5
$\Gamma$ [ns]	22.61	14.6
$\delta_1^{-1}, \delta_2^{-1}$ [ns]	0.65, 6.7	5.26, 0.34
$\eta$	0.095	0.0184
$\gamma$ [ns]	12.53	6.4
$\sigma$ [dB]	2.75	3

Table 5.1.: Parameters of the IEEE 802.15.4a channel model for LOS residential and LOS office environments.

where  $\tau_{j,i}$  denotes the TOA for the  $j^{\text{th}}$  tap of the  $i^{\text{th}}$  cluster and  $\delta_1$  and  $\delta_2$  tow average rates of arrival. The mean power corresponding to  $\tau_{j,i}$  is given by:

$$\mathcal{E}\{|\alpha_{j,i}|^2\} \propto \Omega_i \exp\left(-\frac{\tau_{j,i}}{\gamma}\right)$$

where  $\mathcal{E}\{\cdot\}$  denotes the expectation operator,  $\gamma$  is the intra-cluster time constant;  $\Omega_i$  follows a log-normal distribution:

$$10 \log(\Omega_i) = 10 \log \left[ \exp\left(-\frac{T_i}{\Gamma}\right) \right] + \mathcal{N}(0, \sigma^2). \quad (5.10)$$

$\Gamma$  denotes the inter-cluster time constant, and  $\mathcal{N}$  stands for a normal distribution with variance  $\sigma^2$ .

Table 5.1 shows the values taken by the model parameters for LOS residential and LOS office environments. From this table, the values of  $T_w$  and  $T_s$  can be chosen so that NOLA is approximately satisfied, that is to say the first tap overlaps rarely with next taps and the replicas of a certain impulse reach the next impulse with relatively small energy in average. The probability of overlapping is computed in Sec. 5.3 of this chapter, with respect to the pulse width and the average taps rate of arrival.

### 5.1.3 CRLBs for the joint estimation of the direct path TOA and AOA

In this subsection, we derive the CRLBs for the joint estimation of the parameters of the direct path (i.e.  $\tau_n^{(1)}$  and  $\varphi_n^{(1)}$ ). In Sec. 5.1.3.1 we assume that the symbols  $a_1, \dots, a_K$  modulating the transmitted signal are known (see Eq. 5.3), whereas

in Sec. 5.1.3.2 we assume that they should be jointly estimated with the the direct path parameters.

Denote by  $\underline{\Theta} = (\Theta_1 \cdots \Theta_{N_\Theta})^T$  ( $\cdot^T$  denotes the transpose operator) a vector of  $N_\Theta$  unknown parameters to estimate. The CRLBs of the elements of  $\underline{\Theta}$  are the diagonal elements of the CRLB matrix  $C$  given by [78]:

$$C = \text{FIM}^{-1} \quad (5.11)$$

$$F = (f^{\Theta_i, \Theta_{i'}})_{i, i'=1, \dots, N_\Theta} \quad (5.12)$$

$$f^{\Theta_i, \Theta_{i'}} = -\mathcal{E} \left\{ \frac{\partial^2 \Lambda}{\partial \theta_i \partial \theta_{i'}} \Big|_{\theta_i = \Theta_i, \theta_{i'} = \Theta_{i'}} \right\} \quad (5.13)$$

where  $F$  denotes the FIM and  $\Lambda$  the log-likelihood function for the joint estimation of  $\Theta_1, \dots, \Theta_{N_\Theta}$ .

### 5.1.3.1 Pilot aided case

Here, we assume that the modulating data  $a_1, \dots, a_K$  are pilot symbols known to the receiver. Accordingly, the unknown parameters present in our model, for a given  $\text{Ref}_n$ , are:

$$\alpha_n^{(1)}, \tau_n^{(1)}, \varphi_n^{(1)}, \dots, \alpha_n^{(L_n)}, \tau_n^{(L_n)}, \varphi_n^{(L_n)}$$

in which only  $\tau_n^{(1)}$  and  $\varphi_n^{(1)}$  are the useful parameters; all remaining parameters are nuisance parameters.

In order to find the CRLBs for the estimation of  $\tau_n^{(1)}$  and  $\varphi_n^{(1)}$ , we first consider the joint estimation of all channel parameters.

The log-likelihood function for the joint estimation of all channel parameters can be written from Eq. 5.2 as:

$$\Lambda = -\frac{1}{N_0} \sum_{m=1}^{M_n} \int_{t_1}^{t_2} \left[ r_{n,m}(t) - \sum_{l=1}^{L_n} \alpha_n^{(l)} s_{n,m}^{(l)}(t) \right]^2 dt \quad (5.14)$$

where  $[t_1, t_2]$  is the observation period.

Denote by  $\dot{x}(t)$  the derivative of a generic signal  $x(t)$ , and by  $E_x = \int_{t_1}^{t_2} x^2(t) dt$  its energy. From Eq. 5.12, Eq. 5.13 and Eq. 5.14, we can write the elements of

the FIM as:

$$f_{\varphi_n^{(1)}, \varphi_n^{(1)}} = \frac{2(\alpha_n^{(1)})^2}{N_0 c^2} E_s i_n(\varphi_n^{(1)}) \quad (5.15)$$

$$f_{\tau_n^{(1)}, \tau_n^{(1)}} = \frac{2M_n(\alpha_n^{(1)})^2}{N_0} E_s \quad (5.16)$$

$$f_{\varphi_n^{(1)}, \tau_n^{(1)}} = \frac{-2\alpha_n^{(1)2}}{N_0 c} E_s r_n^\perp = 0 \quad (5.17)$$

$$f_{\alpha_n^{(1)}, \omega_n^{(1)}} = s^2(t) \Big|_{t_1}^{t_2} \sum_{m=1}^{M_n} k_m^{\alpha_n^{(1)} \omega_n^{(1)}} = 0 \quad (5.18)$$

$$f_{\omega_n^{(l')}, \omega_n^{(1)}} = \sum_{m=1}^{M_n} k_m^{\omega_n^{(l')} \omega_n^{(1)}} \int_{t_1}^{t_2} \dot{s}_{n,m}^{(l')}(t) \dot{s}_{n,m}^{(1)}(t) dt = 0 \quad (5.19)$$

$$f_{\alpha_n^{(l')}, \omega_n^{(1)}} = \sum_{m=1}^{M_n} k_m^{\alpha_n^{(l')} \omega_n^{(1)}} \int_{t_1}^{t_2} s_{n,m}^{(l')}(t) \dot{s}_{n,m}^{(1)}(t) dt = 0 \quad (5.20)$$

where  $\omega_n^{(l')} \in \{\varphi_n^{(1)}, \tau_n^{(1)}\}$ ,  $l' \neq 1$ ,  $k_m^{\{\cdot\}}$  is a deterministic number, and

$$i_n(\varphi_n^{(1)}) = \sum_{m=1}^{M_n} r_{n,m}^2 \sin^2(\varphi_n^{(1)} - \varphi_{n,m}) \quad (5.21)$$

$$\begin{aligned} r_n^\perp &= \sum_{m=1}^{M_n} r_{n,m} \sin(\varphi_n^{(1)} - \varphi_{n,m}) = \sin(\varphi_n^{(1)}) \sum_{m=1}^{M_n} r_{n,m} \cos(\varphi_{n,m}) \\ &\quad - \cos(\varphi_n^{(1)}) \sum_{m=1}^{M_n} r_{n,m} \sin(\varphi_{n,m}) = 0. \end{aligned} \quad (5.22)$$

In Eq. 5.17 and Eq. 5.22,  $r_n^\perp$  is null because  $(r_{n,m}, \varphi_{n,m})$ ,  $(m = 1, \dots, M_n)$  are the polar coordinates of the elements of  $\text{Ref}_n$  with respect to their geometric center  $G_n$ , so  $\sum_{m=1}^{M_n} r_{n,m} \cos(\varphi_{n,m})$ , and  $\sum_{m=1}^{M_n} r_{n,m} \sin(\varphi_{n,m})$  are null directly from the definition of the geometric center. In Eq. 5.18, we have assumed that the observation interval  $[t_1, t_2]$  is sufficiently large so that  $s^2(t) \Big|_{t_1}^{t_2} = 0$ . In Eq. 5.19 and Eq. 5.20, both  $\int_{t_1}^{t_2} \dot{s}_{n,m}^{(l')}(t) \dot{s}_{n,m}^{(1)}(t) dt$  and  $\int_{t_1}^{t_2} s_{n,m}^{(l')}(t) \dot{s}_{n,m}^{(1)}(t) dt$  are null because the direct path does overlap with any MP replica, thanks to the NOLA.

The magnitude  $i_n(\varphi)$  in Eq. 5.21 can be seen as a kind of inertia in the direction  $\varphi_n - \frac{\pi}{2}$ . It becomes constant when the array of  $\text{Ref}_n$  is regular (i.e.  $r_{n,m} = r_{\text{Ref}_n}$ ,  $\forall m$ , and  $\varphi_{n,m} = \varphi_{n0} + \frac{2(m-1)\pi}{M_n}$ ), or when it is the superposition of regular arrays, all centered in  $G_n$ ; in Appendix B, we show that for regular arrays,  $i_n(\varphi)$  becomes independent of  $\varphi$  (i.e. omni-directional):

$$i_n(\varphi) = M \frac{r_{\text{Ref}_n}^2}{2} = i, \forall \varphi. \quad (5.23)$$

From Eq. 5.15, Eq. 5.16, Eq. 5.17, Eq. 5.18, Eq. 5.19 and Eq. 5.20 we can write the FIM for the estimation of the parameters relative to  $\text{Ref}_n$  as:

$$\mathbf{F}^{\text{Ref}_n} = \left( \begin{array}{cc|c} f\varphi_n^{(1)}\varphi_n^{(1)} & 0 & 0 \\ 0 & f\tau_n^{(1)}\tau_n^{(1)} & 0 \\ \hline 0 & 0 & \mathbf{F}^{\Omega_n^{\text{nuisance}}} \end{array} \right) \quad (5.24)$$

where  $\underline{\Omega}_n^{\text{nuisance}}$  is the nuisance parameters vector.

From Eq. 5.15 we can write the CRLB matrix  $\mathbf{C}^{\tau_n^{(1)}, \varphi_n^{(1)}}$  for the joint estimation of  $\varphi_n^{(1)}$  and  $\tau_n^{(1)}$  as:

$$\mathbf{C}^{\tau_n^{(1)}, \varphi_n^{(1)}} = \frac{N_0/2}{(\alpha_n^{(1)})^2 E_s} \begin{pmatrix} \frac{1}{M_n} & 0 \\ 0 & \frac{c^2}{i_n(\varphi_n^{(1)})} \end{pmatrix} = \frac{1}{\rho_n^{(1)} \beta_s^2} \begin{pmatrix} \frac{1}{M_n} & 0 \\ 0 & \frac{c^2}{i_n(\varphi_n^{(1)})} \end{pmatrix} \quad (5.25)$$

$$\rho_n^{(1)} = \frac{(\alpha_n^{(1)})^2 E_s}{N_0/2} \quad (5.26)$$

$$\beta_s^2 = \frac{E_s}{E_s} = \frac{\int_{-\infty}^{\infty} 4\pi^2 f^2 |S(f)|^2 df}{\int_{-\infty}^{\infty} |S(f)|^2 df} \quad (5.27)$$

where  $\rho_n^{(1)}$  denotes the SNR of the direct path at  $\text{Elt}_{n,m}$ ,  $\beta_s^2$  is the mean quadratic bandwidth of the transmitted signal,  $S(f)$  is the Fourier transform of  $s(t)$ , and  $f$  the frequency variable.

Two conclusions can be drawn:

- Under the NOLA, the CRLBs for the joint estimation of the direct path parameters do not depend on the parameters of the other paths. Accordingly, the accuracy achievable in such MP channels is the same as the accuracy achievable in AWGN channels.
- With an array of  $M_n$  elements, the CRLB for the estimation of the TOA is  $M_n$  times smaller than the CRLB with only one antenna. In fact, the signals received at the different elements of the array carry all the same information on  $\tau_n^{(1)}$ . Furthermore, these signals are corrupted by independent noise components.

### 5.1.3.2 Joint estimation of data and parameters

Here, we assume that the modulating data  $a_1, \dots, a_K$  are not known to the receiver, and have to be estimated jointly with the parameters of the direct path.

In order to compute the FIM for this joint estimation problem, we need to incorporate new terms into the FIM, which are of the form:

$$f^{a_k, \omega_n^{(1)}} = p^2(t) \Big|_{t_1}^{t_2} \sum_m k_m^{a_k \omega_n^{(1)}} = 0 \quad (5.28)$$

where  $k_m^{a_k \omega_n^{(1)}}$  denotes a deterministic number;  $f^{a_k, \omega_n^{(1)}}$  is null because  $p^2(t)|_{t_1}^{t_2} = 0$ .

The result in Eq. 5.28 also means that with unknown data, the achievable accuracy of the parameters is not impacted when joint estimation of parameters and data is performed.

#### 5.1.4 FIM transformation formula

In this subsection, we propose a method to obtain the FIM for the joint estimation of a set of parameters, from the FIM of another set of parameters, which is function of the first set. The obtained formula will be later used in Sec. 5.1.5 and Sec. 5.1.6 to find the CRLBs for the estimation of the position using the AOA technique, and using the hybrid TOA-AOA technique.

Denote by  $\underline{\Psi} = (\Psi_1 \cdots \Psi_J)^T$  and  $\underline{\Omega} = (\Omega_1 \cdots \Omega_J)^T$  two vectors of  $I$  and  $J$  parameters respectively. We assume that the FIM  $F^{\underline{\Omega}}$  of  $\underline{\Omega}$  is known. Our goal is to find the FIM  $F^{\underline{\Psi}}$  of  $\underline{\Psi}$  taking into account the fact that  $\underline{\Psi}$  and  $\underline{\Omega}$  are functions of each other.

It can be shown that:

$$\begin{aligned} \frac{\partial^2 \Lambda}{\partial \psi_{i'} \partial \psi_i} &= \sum_{j=1}^J \left\{ \frac{\partial \omega_j}{\partial \psi_i} \sum_{j'=1}^J \frac{\partial^2 \Lambda}{\partial \omega_{j'} \partial \omega_j} \frac{\partial \omega_{j'}}{\partial \psi_{i'}} \right\} + \frac{\partial \Lambda}{\partial \omega_j} \frac{\partial^2 \omega_j}{\partial \psi_{i'} \partial \psi_i} \\ &= \left( \frac{\partial \underline{\omega}}{\partial \psi_{i'}} \right)^T \frac{\partial^2 \Lambda}{\partial \underline{\omega}^2} \frac{\partial \underline{\omega}}{\partial \psi_i} + \frac{\partial \Lambda}{\partial \underline{\omega}} \frac{\partial}{\partial \psi_{i'}} \left( \frac{\partial \underline{\omega}}{\partial \psi_i} \right) \end{aligned} \quad (5.29)$$

where  $\Lambda$  denotes the log-likelihood function, and

$$\begin{aligned} \frac{\partial \underline{\omega}}{\partial \psi_i} &= \left( \frac{\partial \omega_1}{\partial \psi_i} \cdots \frac{\partial \omega_J}{\partial \psi_i} \right)^T \\ \frac{\partial \Lambda}{\partial \underline{\omega}} &= \left( \frac{\partial \Lambda}{\partial \omega_1} \cdots \frac{\partial \Lambda}{\partial \omega_J} \right) \\ \frac{\partial^2 \Lambda}{\partial \underline{\omega}^2} &= \left( \frac{\partial^2 \Lambda}{\partial \omega_j \partial \omega_{j'}} \right)_{j, j'=1, \dots, J} \end{aligned}$$

By applying the expectation operator to the negative of  $\frac{\partial^2 \Lambda}{\partial \psi_{i'} \partial \psi_i}$  in Eq. 5.29, in conjunction with the regularity condition  $\mathcal{E} \left[ \frac{\partial \Lambda}{\partial \underline{\omega}} \right] = 0$ , we obtain the generic element of the FIM of  $\underline{\Psi}$ :

$$f^{\psi_{i'} \psi_i} = \mathcal{E} \left[ - \frac{\partial^2 \Lambda}{\partial \psi_{i'} \partial \psi_i} \right] = \left( \frac{\partial \underline{\omega}}{\partial \psi_{i'}} \right)^T F^{\underline{\Omega}} \frac{\partial \underline{\omega}}{\partial \psi_i} \quad (5.30)$$

Finally, we can write the FIM of  $\underline{\Psi}$  from Eq. 5.30 as:

$$F^{\underline{\Psi}} = \left( J_{\underline{\Psi}}^{\underline{\omega}} \right)^T F^{\underline{\Omega}} J_{\underline{\Psi}}^{\underline{\omega}} \quad (5.31)$$

where

$$J_{\underline{\psi}}^{\underline{\omega}} = \frac{\partial \underline{\omega}}{\partial \underline{\psi}} = \left( \frac{\partial \omega_j}{\partial \psi_i} \right)_{i=1, \dots, I, j=1, \dots, J} \quad (5.32)$$

is the Jacobian of  $\underline{\omega}$  with respect to  $\underline{\psi}$ .

### 5.1.5 CRLBs for AOA-based positioning

In this subsection we derive the CRLBs for the estimation of the position, based on the information on the angles of arrival, at the different reference nodes, of the signal transmitted by the unknown location node. As already mentioned, the CRLBs will be computed using the FIM transformation formula derived in Sec. 5.1.4. As we only focus on the first path, we omit from now on index 1, for the sake of conciseness.

Given that the AOAs  $\varphi_1 \cdots \varphi_N$  at the different reference nodes are considered as independent parameters, we can write the FIM for the estimation of  $\underline{\varphi} = (\varphi_1 \cdots \varphi_N)^T$  from Eq. 5.15, Eq. 5.26 and Eq. 5.27 as:

$$F_{\underline{\varphi}} = \text{diag}\{f^{\varphi_1, \varphi_1} \dots f^{\varphi_N, \varphi_N}\} = \frac{\beta_s^2}{c^2} \text{diag}\{\rho_1 \dot{\mathbf{i}}_1(\varphi_1) \cdots \rho_N \dot{\mathbf{i}}_N(\varphi_N)\} \quad (5.33)$$

where  $\text{diag}(\cdot)$  denotes the diagonal matrix.

From Eq. 5.31, we can write the FIM for the joint estimation of the Cartesian coordinates  $(x, y)$  of Unk using the AOA technique as:

$$F^{x,y} = \left( J_{x,y}^{\underline{\varphi}} \right)^T F_{\underline{\varphi}} J_{x,y}^{\underline{\varphi}} \quad (5.34)$$

where  $J_{x,y}^{\underline{\varphi}}$  is the Jacobian of  $\underline{\varphi}$  with respect to  $(x, y)$  given from Eq. 5.32 and Eq. 5.7 by:

$$J_{x,y}^{\underline{\varphi}} = \begin{pmatrix} -\frac{\sin \varphi_1}{r_1} & \dots & -\frac{\sin \varphi_N}{r_n} \\ \frac{\cos \varphi_1}{r_1} & \dots & \frac{\cos \varphi_N}{r_n} \end{pmatrix}^T. \quad (5.35)$$

From Eq. 5.34, Eq. 5.34 and Eq. 5.35, we have:

$$F^{x,y} = \frac{\beta_s^2}{c^2} \sum_{n=1}^N \frac{\rho_n \dot{\mathbf{i}}_n(\varphi_n)}{r_n^2} \begin{pmatrix} \sin^2 \varphi_n & -\frac{\sin(2\varphi_n)}{2} \\ -\frac{\sin(2\varphi_n)}{2} & \cos^2 \varphi_n \end{pmatrix}. \quad (5.36)$$

By inverting  $F^{x,y}$ , the CRLB matrix becomes:

$$C^{x,y} = \frac{c^2}{\beta_s^2 \Delta^{x,y}} \sum_{n=1}^N \frac{\rho_n \dot{\mathbf{i}}_n(\varphi_n)}{r_n^2} \begin{pmatrix} \cos^2 \varphi_n & \frac{\sin(2\varphi_n)}{2} \\ \frac{\sin(2\varphi_n)}{2} & \sin^2 \varphi_n \end{pmatrix} \quad (5.37)$$

where

$$\Delta^{x,y} = \sum_{n=1}^{N-1} \sum_{n'=n+1}^N \frac{\rho_n \dot{\mathbf{i}}_n(\varphi_n)}{r_n^2} \frac{\rho_{n'} \dot{\mathbf{i}}_{n'}(\varphi_{n'})}{r_{n'}^2} \sin^2(\varphi_n - \varphi_{n'}). \quad (5.38)$$

Denote by  $c^x$  and  $c^y$  the CRLBs of  $x$  and  $y$ , respectively. They are the diagonal elements of  $C^{x,y}$ .

### 5.1.6 CRLBs for hybrid TOA-AOA based positioning

In this subsection we derive the CRLBs for the estimation of the position, based on the information on the angles and the times of arrival, at the different reference nodes, of the signal transmitted by the unknown location node. Like for the case of AOA-based positioning considered in Sec. 5.1.5, the CRLBs will be computed here using the FIM transformation formula derived in Sec. 5.1.4.

In Sec. 5.1.6.1, we consider the problem of hybrid positioning based on only one array. In Sec. 5.1.6.2, we consider the same problem but based on  $N$  arrays.

#### 5.1.6.1 Hybrid positioning with one array

As mentioned above, we consider here the case of one array.

For the polar coordinates  $(r_n, \varphi_n)$  of the position of the Unk with respect to the center  $G_n$  of Ref $_n$ , the FIM can be easily deduced from Eq. 5.24, and the CRLB matrix from Eq. 5.25:

$$F^{r_n, \varphi_n} = \frac{\rho_n \beta_s^2}{c^2} \begin{pmatrix} M_n & 0 \\ 0 & i_n(\varphi_n) \end{pmatrix} \quad (5.39)$$

$$C^{r_n, \varphi_n} = \frac{c^2}{\rho_n \beta_s^2} \begin{pmatrix} \frac{1}{M_n} & 0 \\ 0 & \frac{1}{i_n(\varphi_n)} \end{pmatrix}. \quad (5.40)$$

Denote by  $c^{r_n}$  and  $c^{\varphi_n}$  the CRLBs of  $r_n$  and  $\varphi_n$  respectively. Then,  $c^{r_n}$  and  $c^{\varphi_n}$  are the diagonal elements of  $C^{r_n, \varphi_n}$ . We want now to find the CRLBs for the estimation of  $(x, y)$ . We first compute the Jacobian  $J_{x,y}^{r_n, \varphi_n}$  and then use the FIM transformation formula derived in Sec. 5.1.4 to find the FIM of  $(x, y)$ ;  $J_{x,y}^{r_n, \varphi_n}$  is given from Eq. 5.32, Eq. 5.6 and Eq. 5.7 by:

$$J_{x,y}^{r_n, \varphi_n} = \begin{pmatrix} \cos \varphi_n & \sin \varphi_n \\ -\frac{\sin \varphi_n}{r_n} & \frac{\cos \varphi_n}{r_n} \end{pmatrix}. \quad (5.41)$$

About the FIM,

$$F_{x,y}^{x,y} = (J_{x,y}^{r_n, \varphi_n})^T F^{r_n, \varphi_n} J_{x,y}^{r_n, \varphi_n} = \frac{\rho_n \beta_s^2}{c^2} \begin{pmatrix} d_n^{x,x} & d_n^{x,y} \\ d_n^{x,y} & d_n^{y,y} \end{pmatrix} \quad (5.42)$$

where,

$$\begin{aligned} d_n^{x,x} &= M_n \cos^2 \varphi_n + i_n(\varphi_n) \frac{\sin^2 \varphi_n}{r_n^2} \\ d_n^{y,y} &= M_n \sin^2 \varphi_n + i_n(\varphi_n) \frac{\cos^2 \varphi_n}{r_n^2} \\ d_n^{x,y} &= \frac{\sin(2\varphi_n)}{2} \left( M_n - \frac{i_n(\varphi_n)}{r_n^2} \right) \end{aligned}$$

By inverting  $F_{x,y}^{x,y}$  Eq. 5.42 we obtain the CRLB matrix of  $(x, y)$ :

$$C^{x,y} = \frac{c^2 r_n^2}{M_n \rho_n \beta_s^2 i_n(\varphi_n)} \begin{pmatrix} d_n^{y,y} & -d_n^{x,y} \\ -d_n^{x,y} & d_n^{x,x} \end{pmatrix}. \quad (5.43)$$

### 5.1.6.2 Hybrid positioning with $N$ arrays

As already mentioned, we consider here the case of  $N$  arrays.

For simplicity reasons, we assume that the  $N$  arrays are identical and regular. Accordingly, the inertia becomes omni-directional (i.e.  $M_n = M$ ,  $i_n(\varphi) = i$ ,  $\forall \varphi$ ,  $\forall n$ , see Eq. 5.23).

The total FIM is equal to the sum of the  $N$  elementary FIMs in Eq. 5.42. This is due to the statistical independence between signals observed at different arrays. We can write:

$$\mathbf{F}^{x,y} = \sum_{n=1}^N \mathbf{F}_n^{x,y} = \frac{\beta_s^2}{c^2} \sum_{n=1}^N \rho_n \begin{pmatrix} d_n^{x,x} & d_n^{x,y} \\ d_n^{x,y} & d_n^{y,y} \end{pmatrix}.$$

Hence, the CRLB matrix becomes:

$$\mathbf{C}^{x,y} = \frac{c^2}{\beta_s^2} \frac{1}{\Delta^{x,y}} \sum_{n=1}^N \rho_n \begin{pmatrix} d_n^{y,y} & -d_n^{x,y} \\ -d_n^{x,y} & d_n^{x,x} \end{pmatrix}$$

where,

$$\begin{aligned} \Delta^{x,y} = & \sum_{n=1}^N \rho_n^2 \frac{M i}{r_n^2} + \sum_{n=1}^{N-1} \sum_{n'=n+1}^N \rho_n \rho_{n'} \left\{ \sin^2(\varphi_n - \varphi_{n'}) \left( M^2 + \frac{i^2}{r_n^2 r_{n'}^2} \right) \right. \\ & \left. + i M \cos^2(\varphi_n - \varphi_{n'}) \left( \frac{1}{r_n^2} + \frac{1}{r_{n'}^2} \right) \right\}. \end{aligned}$$

### 5.1.7 Comparison of the exact AOA CRLB and the CRLB obtained with the narrowband assumption

In this subsection we compare the exact value of the CRLB for AOA estimation with the approximated value obtained when the narrowband approximation is made (i.e. when the transmitted signal is assumed to be a monochromatic sine wave around the central frequency). Obviously, the signal used in both cases is the same: a UWB signal.

The purpose here is not to compare the potential of narrowband with that of UWB-based positioning, but to compare the bounds obtained by considering the true UWB structure with those computed by making a narrowband approximation.

Under the narrowband approximation, the mean quadratic bandwidth in Eq. 5.27 becomes:

$$\beta_s^2 \approx \beta_{NB}^2 = 4\pi^2 f_c^2 \quad (5.44)$$

where  $f_c$  denotes the central frequency of the spectrum of the transmitted signal (subscript  $_{NB}$  denotes ‘‘narrowband’’). Denote by NWR the narrowband to

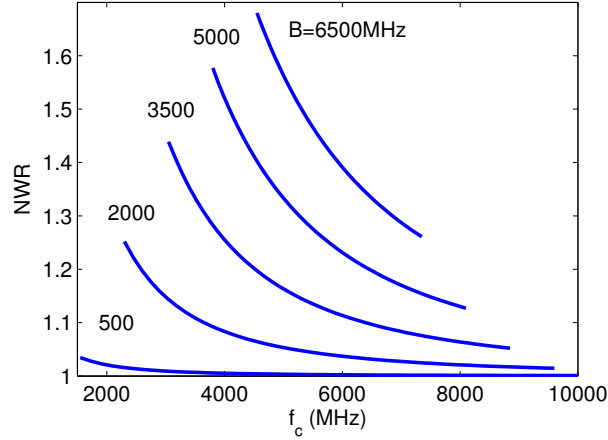


Fig. 5.2.: The narrowband to UWB, AOA CRLBs ratio, with respect to the central frequency  $f_c$  and the bandwidth  $B$ .

UWB CRLBs ratio, and by  $f_l$ ,  $f_h$ , and  $B = f_h - f_l$  the lowest frequency, the highest frequency, and the bandwidth of the transmitted signal, respectively. From Eq. 5.25, we can write NWR as:

$$\text{NWR} = \frac{c_{NB}^{\varphi_n}}{c^{\varphi_n}} = \frac{\beta_s^2}{\beta_{NB}^2} = \frac{\int_{f_l}^{f_h} f^2 |S(f)|^2 df}{f_c^2 \int_{f_l}^{f_h} |S(f)|^2 df} \quad (5.45)$$

where  $c^{\varphi_n}$  denotes the exact value of the CRLB and  $c_{NB}^{\varphi_n}$  the approximated one. Eq. 5.45 shows that  $c_{NB}^{\varphi_n}$  is greater than  $c^{\varphi_n}$  because in general  $\int_{f_c}^{f_h} f^2 |S(f)|^2 df$  is larger than  $\int_{f_l}^{f_c} f^2 |S(f)|^2 df$ .

When  $|S(f)|$  is constant in the interval  $[f_l, f_h]$ , NWR becomes:

$$\text{NWR} = 1 + \frac{B^2}{3f_c^2}. \quad (5.46)$$

Fig. 5.2 shows the values of NWR for different values of  $f_c$  and  $B$  when  $|S(f)|$  is constant inside  $[f_l, f_h]$ . We can see that, as can be expected from Eq. 5.46, that NWR increases as the fractional bandwidth  $\frac{B}{f_c}$  increases. Obviously, as the CRLBs ratio is very close to one, we can deduce that for relatively low fractional bandwidths, narrowband and UWB signals theoretically achieve the same accuracy for AOA estimation. However, this does not mean that both systems are equivalent. In fact, UWB signals may outperform narrowband signals for ambiguity issues.

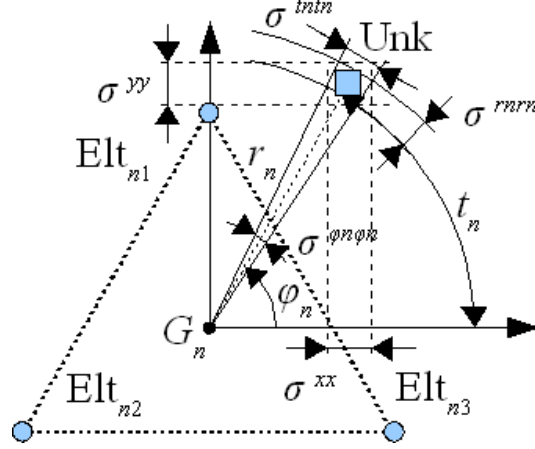


Fig. 5.3.: The triangular array in use and, the polar and Cartesian bounds.

### 5.1.8 Numerical results and discussion

In this subsection we consider a special scenario for which we provide numerical values for the CRLBs. In Sec. 5.1.8.1 we describe the considered scenario, and in Sec. 5.1.8.2 and Sec. 5.1.8.3 we present and discuss the results obtained for AOA-based positioning and hybrid positioning, respectively.

#### 5.1.8.1 Illustration scenario

As mentioned above, we describe here our illustration scenario.

The transmitted signal  $s(t)$  is supposed to have the following characteristics: Cardinal sine pulse (in order to have a flat spectrum) modulated by carrier with  $[f_c, B] = [6.85, 7.5]$  GHz (i.e.  $[f_l, f_h] = [3.1, 10.6]$  GHz),  $\gamma_s(f) = \gamma_s = -41.3$  dBm/MHz (PSD) and  $T = 1 \mu\text{s}$  (time of observation). The pulse mainlobe width (from zero to zero) is given by  $T_w = \frac{2}{B} \approx 0.27$  ns.

From Eq. 5.9 we can approximate the average rate of arrival of replicas within clusters by  $\delta^{-1} = \eta\delta_1^{-1} + (1 - \eta)\delta_2^{-1}$ . From Table 5.1 we obtain  $\delta^{-1} \approx 0.43$  ns (resp.  $\delta^{-1} \approx 6.1$  ns) for LOS office (resp. LOS residential) environments. As  $T_w = 0.27$  ns, we can suppose that the first condition of the NOLA (see Eq. 5.8) is satisfied for LOS office environments. Furthermore, we can see from Eq. 5.10 that the time constant  $\Gamma$  ( $\Gamma = 14.6$  ns for LOS office environments, see Table 5.1) determines the vanishment of the average power of clusters. Therefore, if we consider a symbol period  $T_s$  sufficiently larger than 14.6 ns, we can suppose that the second condition of the NLOA (see Eq. 5.8) is also satisfied.

We consider identical arrays of three elements built from an equilateral triangle (see Fig. 5.3). Accordingly,  $i_n(\varphi)$  Eq. 5.21, Eq. 5.23 is omni-directional thanks to the array regularity. Denote by  $e$  the length of one side of the triangle. For

$e = 25$  cm, we obtain  $D \approx 29$  cm (diameter of the smallest circle containing the array) and  $i = 0.0312$  m<sup>2</sup>. We suppose that the far field assumption is satisfied beyond  $d_{ff} = 2\frac{D^2}{\lambda_h} \approx 5.9$  m ( $\lambda_h = \frac{c}{f_h}$  denotes the wavelength of the highest frequency).

For convenience, we recall the expression of the SNR in Eq. 5.26:

$$\rho = \frac{\alpha^2 E_s}{N_0/2} \quad (5.47)$$

where  $\alpha$  denotes now the gain (i.e. attenuation) of the channel including all the undesired effects, and  $E_s$  the energy of the transmitted signal. We can write  $E_s$  and  $\alpha^2$  as:

$$E_s = \gamma_s(f)BT \quad (5.48)$$

$$\alpha^2 = \frac{\lambda_c^2}{4\pi} \frac{1}{4\pi d^2} \frac{1}{\eta_{il}\eta_{nf}} \quad (5.49)$$

where  $\frac{\lambda_c^2}{4\pi}$  is the aperture of the receive antenna evaluated with respect to the central frequency  $f_c$  ( $\lambda_c$  is the corresponding wavelength),  $\frac{1}{4\pi d^2}$  the attenuation due to the propagation,  $\eta_{il} = 2.5$  dB the implementation loss and  $\eta_{nf} = 6.6$  dB the noise figure. We take  $N_0 = -110$  dBm/MHz.

In Sec. 5.1.8 we denote by  $\sigma^{r_n}$ ,  $\sigma^{\varphi_n}$ ,  $\sigma^x$  and  $\sigma^y$  the square roots of the CRLBs  $c^{\varphi_n}$ ,  $c^{r_n}$ ,  $c^x$  and  $c^y$ , respectively.

### 5.1.8.2 AOA-based positioning

Here, we present and discuss the results obtained for AOA-based positioning.

We consider the two following setups:

1. Setup with two reference nodes located at  $(-10, 0)$  m (Cartesian coordinates) and  $(10, 0)$  m, respectively.
2. Setup with four reference nodes located at  $(-10, -10)$  m,  $(-10, 10)$  m,  $(10, -10)$  m and  $(10, 10)$  m, respectively.

Let us start with the first setup. Fig. 5.4(a) and Fig. 5.4(b) show the square roots of the CRLBs of  $x$  and  $y$  with respect to the position of Unk, respectively. Fig. 5.4(c) shows the SNRs at Ref<sub>1</sub> and Ref<sub>2</sub> with respect to the position of Unk. The positions of Ref<sub>1</sub> and Ref<sub>2</sub> correspond to the maxima of the corresponding SNR curves. In Fig. 5.4(a) we see that  $\sigma^x$  approaches infinity when Unk approaches the axis joining the geometric centers of the two used arrays. This result can be expected from the expression of the CRLBs in Eq. 5.37. We can deduce that, in order to be able to locate Unk everywhere using the AOA technique, two reference nodes are insufficient. We can see from Fig. 5.4(a) and Fig. 5.4(b) that for  $(x, y) = (-30, -15)$  m, we have  $\sigma^x \approx 0.65$  m and  $\sigma^y \approx 0.46$

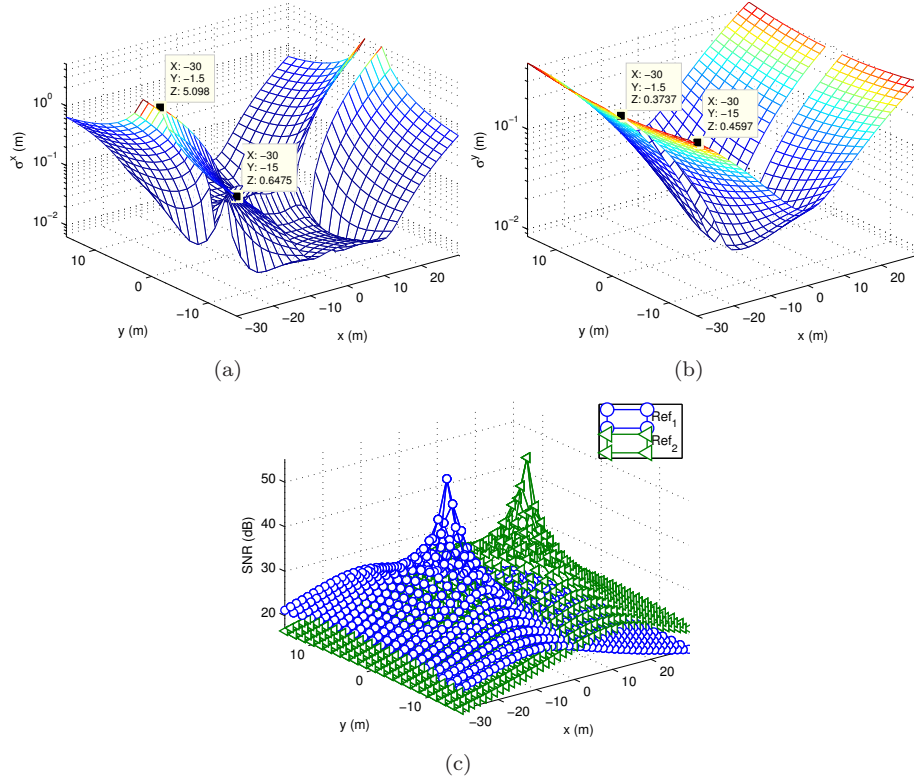


Fig. 5.4.: AOA-based positioning: setup with two arrays located at  $(-10, 0)$  m and  $(10, 0)$  m (a) Square root of the CRLB of  $x$  with respect to the position  $(x, y)$  of Unk (b) Square root of the CRLB of  $y$  with respect to  $(x, y)$  (c) SNR at Ref<sub>1</sub> and Ref<sub>2</sub> with respect to  $(x, y)$ .

m, whereas for  $(x, y) = (-30, -1.5)$  m (near the axis joining the two arrays), we have  $\sigma^x \approx 5.1$  m (very high) and  $\sigma^y \approx 0.37$  m.

Consider now the second setup. Fig. 5.4(a) and Fig. 5.4(b) show the standard deviations corresponding to the CRLBs of  $x$  and  $y$ , and Fig. 5.4(c) the SNRs at Ref<sub>1</sub>, Ref<sub>2</sub>, Ref<sub>3</sub> and Ref<sub>4</sub>, all with respect to the position of Unk. We can see that the CRLBs of both  $x$  and  $y$  are much smaller with the actual setup of four arrays, than with the previous setup of only two arrays. We can see that for  $(x, y) = (0, 0)$  m, we have  $(\sigma^x, \sigma^y) \approx (1.6, 1.6)$  cm, whereas for  $(x, y) = (-30, -30)$  m, we rather have  $(\sigma^x, \sigma^y) \approx (37, 37)$  cm.

### 5.1.8.3 Hybrid positioning

Here, we present and discuss the results obtained for hybrid positioning.

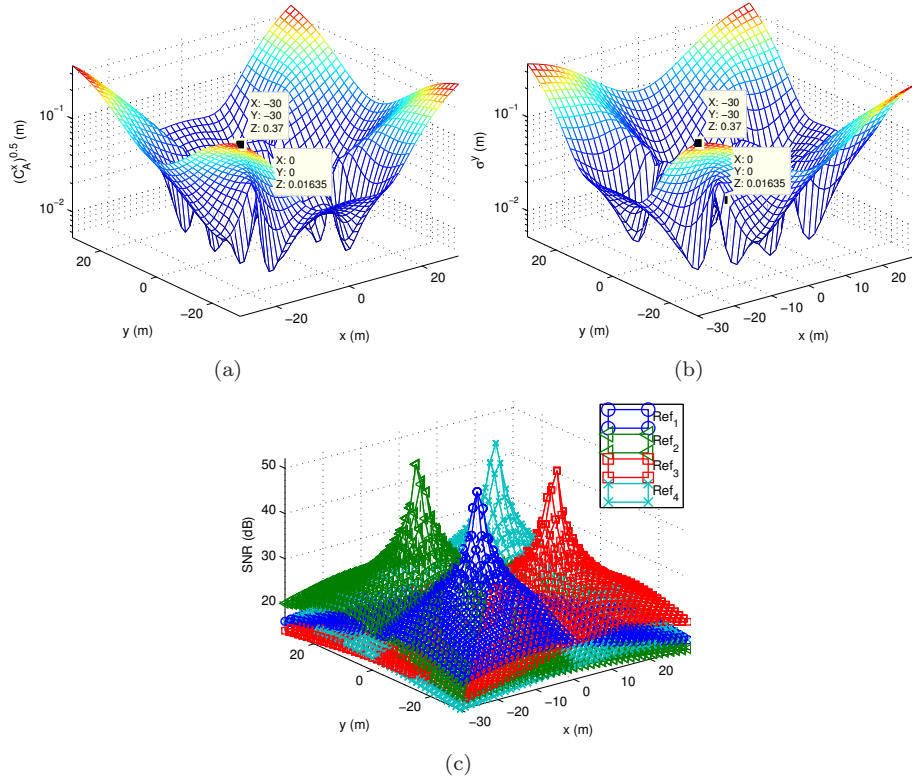


Fig. 5.5.: AOA-based positioning: setup with four arrays located at  $(-10, -10)$  m,  $(-10, 10)$  m,  $(10, -10)$  m and  $(10, 10)$  m (a) Square root of the CRLB of  $x$  with respect to the position  $(x, y)$  of Unk (b) Square root of the CRLB of  $y$  with respect to  $(x, y)$  (c) SNR at Ref<sub>1</sub>, Ref<sub>2</sub>, Ref<sub>3</sub> and Ref<sub>4</sub> with respect to  $(x, y)$ .

We consider the two following setups:

1. Setup with one reference node located at  $(0, 0)$  m.
2. Setup with four reference nodes located at  $(-10, -10)$  m,  $(-10, 10)$  m,  $(10, -10)$  m and  $(10, 10)$  m, respectively (the same as the second setup considered for AOA-based positioning).

Let us consider the first setup.

Before discussing the obtained results, let us denote by  $t_n = r_n \varphi_n$  the curvilinear abscissa (or tangential abscissa) of Unk with respect to Ref <sub>$n$</sub>  ( $t_n$  is depicted in Fig. 5.3). From Eq. 5.40, we can write the CRLB of  $t_n$  as:

$$c^{t_n} = r_n^2 c^{\varphi_n} = \frac{c^2 r_n^2}{\rho_n \beta_s^2 i_n(\varphi_n)}. \quad (5.50)$$

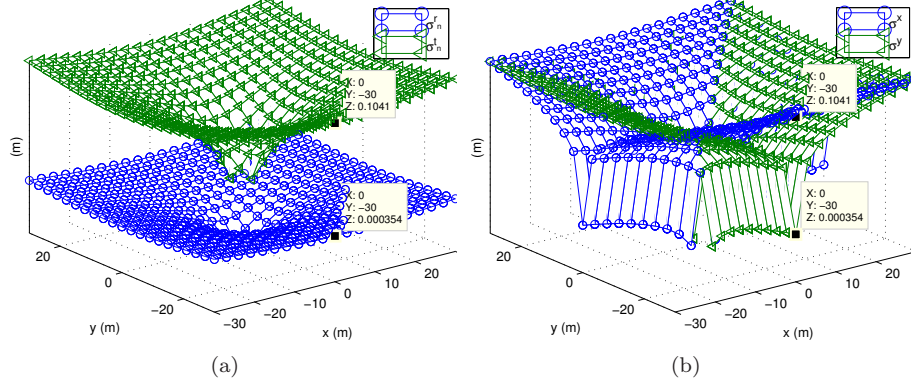


Fig. 5.6.: Hybrid positioning: setup with one array located at  $(0, 0)$  m (a) Square roots of the CRLBs of  $r_n$  and  $t_n$  with respect to the position  $(x, y)$  of Unk (b) Square roots of the CRLBs of  $x$  and  $y$  with respect to  $(x, y)$ .

We also denote by  $\sigma^{t_n}$  the square root of  $c^{t_n}$ .

From Fig. 5.3 (where  $\sigma^{xx} = \sigma^x$ ,  $\sigma^{yy} = \sigma^y$ ,  $\sigma^{r_n r_n} = \sigma^{r_n}$ ,  $\sigma^{t_n t_n} = \sigma^{t_n}$ ,  $\sigma^{\varphi_n \varphi_n} = \sigma^{\varphi_n}$ ), we can see that  $\sigma^{xx}$  (resp.  $\sigma^{yy}$ ) is mainly determined by  $\sigma^{r_n r_n}$  when Unk is closer to the  $x$  axis (resp.  $y$  axis) than the  $y$  axis (resp.  $x$  axis). However, when Unk moves away from the  $x$  axis (resp.  $y$  axis),  $\sigma^{xx}$  (resp.  $\sigma^{yy}$ ) becomes mainly determined by  $\sigma^{t_n t_n}$ .

Consider now Fig. 5.6(a) and Fig. 5.6(b) where are shown the square roots of the CRLBs of  $r_n$  and  $t_n$ , and those of  $x$  and  $y$  with respect to the position of Unk, respectively. We see in Fig. 5.6(a) that  $\sigma^{r_n}$  is much smaller than  $\sigma^{t_n}$ . For  $(x, y) = (0, -30)$  m, we have  $\sigma^{r_n} \approx 0.35$  mm and  $\sigma^{t_n} \approx 10.4$  cm. This result could be expected from Eq. 5.40 and Eq. 5.50. In Fig. 5.6(b), we see that  $\sigma^x$  (resp.  $\sigma^y$ ) reaches its lowest values along the  $x$  axis (resp.  $y$  axis). This result could be expected from our comments above Fig. 5.3 in conjunction with the fact (already observed in Fig. 5.6(a)) that  $\sigma^{r_n}$  is much smaller than  $\sigma^{t_n}$ . It also could be expected from the expressions of the CRLBs in Eq. 5.43. For  $(x, y) = (0, -30)$  m (the same considered above), we have  $\sigma^x \approx 10.4$  cm and  $\sigma^y \approx 0.35$  mm. Notice that, as Unk is now located at the  $y$  axis, we have  $\sigma^x \approx \sigma^{t_n}$  and  $\sigma^y \approx \sigma^{r_n}$ .

Consider now the second setup with four reference nodes. Fig. 5.7(a) and Fig. 5.7(b) show the standard deviations corresponding to the CRLBs of  $x$  and  $y$ , respectively. Thanks to the information about the position contained in the TOA information, we can see that the CRLBs are now highly much smaller than those obtained with the same setup but using the AOA technique. We can see that for  $(x, y) = (-30, -30)$  m (the same point considered above in the setup of four reference nodes with the AOA technique, see Fig. 5.5(a) and Fig. 5.5(b)), we have  $(\sigma^x, \sigma^y) \approx (0.85, 0.85)$  mm.

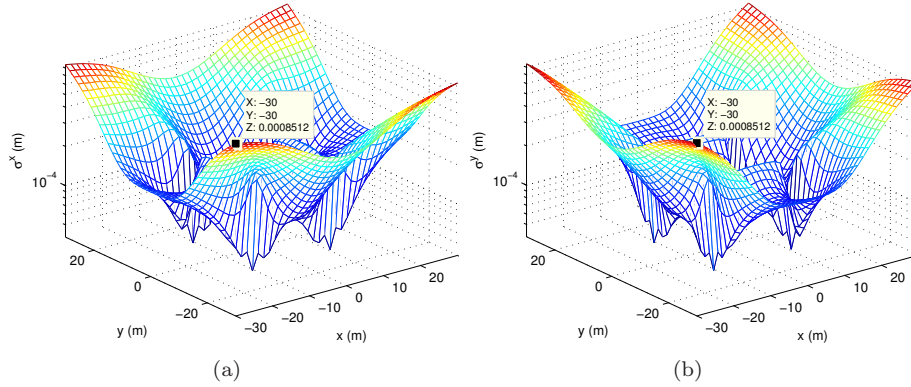


Fig. 5.7.: Hybrid positioning: setup with four arrays located at  $(-10, -10)$  m,  $(-10, 10)$  m,  $(10, -10)$  m and  $(10, 10)$  m (a) Square root of the CRLB of  $x$  with respect to the position  $(x, y)$  of Unk (b) Square root of the CRLB of  $y$  with respect to  $(x, y)$ .

## 5.2 CRLBS FOR JOINT TOA AND AOA ESTIMATION IN WIDEBAND MISO AND MIMO SYSTEMS: COMPARISON WITH SISO AND SIMO SYSTEMS

MIMO technology has been widely investigated in the literature for communication systems in order to exploit the spatial diversity in fading channels. In this paper we aim to see if we can benefit from MISO and MIMO configurations for positioning purpose. To do so, we derive the CRLBs for the joint estimation of the TOA and the AOA at the receiver. This matter has already been investigated for target detection in MIMO Radar systems [119–124]. The main two differences between the two scenarios are that in MIMO Radar we locate the target instead of the receiver or the transmitter like in our case and that the received signals are the reflection of the transmitted signals by the target instead of being received directly from the transmitter.

In [122] the CRLB of the target position  $(x, y)$  is computed assuming orthogonal signals. In [121, 123, 124] the CRLB for direction estimation is computed using the same array for both transmission and reception. In [121] arbitrary signals are considered, unlike [123, 124] where signals are supposed to be orthogonal. In [119] it has been shown that the CRLB for direction estimation is the same in  $1 \times 2$  and  $2 \times 1$  setups when orthogonal signals are used which has also been shown in [120] for  $1 \times 3$ ,  $2 \times 2$  and  $3 \times 1$  setups. However, in [119, 120] the energy captured by each one of SIMO antennas is supposed to be the same as the energy received from each one of the MISO transmit antennas which means that the total radiated energy in the  $N \times 1$  MISO setup is  $N$  times the energy radiated in a  $1 \times N$  SIMO setup.

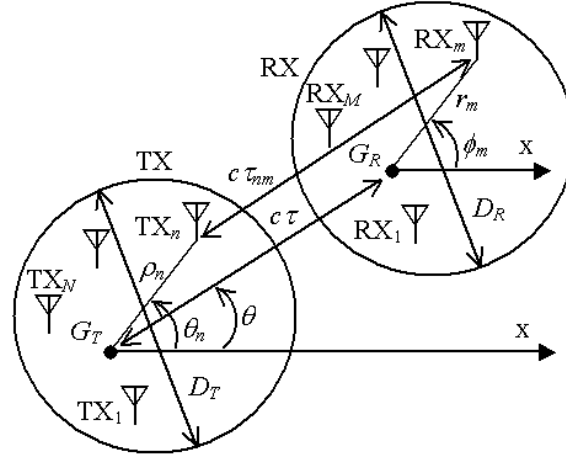


Fig. 5.8.: MIMO model: Tx and Rx are sufficiently far away so that the rays coming from Tx can be considered parallel at Rx.

We first consider arbitrary signals. Then we show that, constrained to the total radiated energy, SISO is equivalent to MISO and SIMO is equivalent to MIMO for TOA estimation when the signals are orthogonal. For non-orthogonal signals, MISO performs better than SISO, and MIMO outperforms SIMO in the regions where the received signals are constructive. For AOA estimation we show that for orthogonal signals MIMO is the best, then SIMO, then MISO. For non-orthogonal signals, we show that in constructive regions, MIMO is better than orthogonal MIMO, and MISO is worse than orthogonal MISO.

In Sec. 5.2.1 the system model is described. In Sec. 5.2.2 the expressions of the CRLBs for the estimation of the TOA and AOA are derived. In Sec. 5.2.3 the CRLBs of the TOA and AOA are compared in SISO, SIMO, MISO and MIMO systems. In Sec. 5.2.4 a typical scenario is considered and numerical results are provided and discussed.

### 5.2.1 System model

In this subsection we describe our MIMO system model. Given that MISO is a special case of MIMO, we derive the CRLBs in MIMO systems and then deduce those of MISO conditions.

In our model depicted in Fig. 5.8, we consider an antenna array Tx of  $N$  elements for transmission and an array Rx of  $M$  elements for reception. Let  $(\rho_n, \theta_n)$  and  $(r_m, \phi_m)$  be the polar coordinates of  $Tx_n$  ( $n^{\text{th}}$  element of Tx) and  $Rx_m$  ( $m^{\text{th}}$  element of Rx) with respect to  $G_T$  (geometric center of Tx) and  $G_R$  (geometric center of Rx), respectively. Given the definition of  $(\rho_n, \theta_n)$  and

$(r_m, \phi_m)$  we can write:

$$\sum_{n=1}^N \rho_n \sin(\theta - \theta_n) = 0, \forall \theta \quad (5.51)$$

$$\sum_{m=1}^M r_m \sin(\theta - \phi_m) = 0, \forall \theta \quad (5.52)$$

where  $\theta$  denotes the angle of departure measured with respect to the geometric centers of Tx and Rx. In Fig. 5.8,  $D_T$  and  $D_R$  denote the diameters of the smallest circles containing the arrays Tx and Rx, respectively.

Assume that the communication channel between Tx and Rx is AWGN. Even if this assumption is not realistic especially in WB systems, it allows us to obtain the lowest reachable CRLBs and to compare with SISO and SIMO configurations. Assume also that Tx and Rx are sufficiently far from each other so that:

$$\begin{cases} \alpha_{n,m} \approx \alpha \\ \tau_{n,m} \approx \tau - \frac{\rho_n}{c} \cos(\theta - \theta_n) + \frac{r_m}{c} \cos(\theta - \phi_m) \end{cases} \forall (n, m) \quad (5.53)$$

where  $\alpha$  and  $\tau$  (resp.  $\alpha_{n,m}$  and  $\tau_{n,m}$ ) denote the gain and the time delay of the channel between  $G_T$  and  $G_R$  (resp. Tx<sub>*n*</sub> and Rx<sub>*m*</sub>), and  $c$  the speed of light.

Let  $s_n(t)$  be the complex envelope of the signal transmitted by Tx<sub>*n*</sub>;  $s_n(t)$  can be written as:

$$s_n(t) = \sum_{i=-\infty}^{+\infty} d_{n,i} \sum_{j=0}^{N_c-1} c_{n,j} p(t - iT_s - jT_c) \quad (5.54)$$

where  $(d_{n,i})$  are the modulating symbols associated to Tx<sub>*n*</sub>,  $(c_{n,j})$  the code of length  $N_c$  associated to Tx<sub>*n*</sub>,  $T_s$  the symbol period,  $T_c$  ( $T_s = N_c T_c$ ) the chip period and  $p(t)$  the used waveform.

Let  $v_m(t)$  be the complex envelope of the signal received by Rx<sub>*m*</sub>; we can write:

$$v_m(t) = \alpha \sum_{n=1}^N e^{-j\omega_0 \tau_{n,m}} s_n(t - \tau_{n,m}) + n_m(t) \quad (5.55)$$

$$= \sum_{n=1}^N u_{n,m}(t) + n_m(t) \quad (5.56)$$

where  $\omega_0$  is the angular frequency of the carrier, and  $u_{n,m}(t)$  and  $n_m(t)$  are the complex envelopes of the useful signal received by Rx<sub>*m*</sub> from Tx<sub>*n*</sub> and the background noise at Rx<sub>*m*</sub> respectively. Assume that  $n_1(t), \dots, n_M(t)$  are independent and identically distributed, and that  $2N_0$  is their PSD ( $\frac{N_0}{2}$  is the PSD of the real bandpass noise). Denote by  $\dot{x}(t)$  the derivative of the generic signal  $x(t)$ ,  $X(f)$  its Fourier transform,  $E_x = \int |x(t)|^2 dt$  its energy and  $\beta_x^2 = \frac{E_{\dot{x}}}{E_x} = \frac{\int 4\pi^2 f^2 |X(f)|^2 df}{\int |X(f)|^2 df}$  its mean quadratic bandwidth. We assume that the energy and the mean quadratic bandwidth are the same for all transmit antennas (i.e.  $E_{s_n} = E_s, \forall n$ , and  $\beta_{s_n}^2 = \beta_s^2, \forall n$ ).

### 5.2.2 CRLBs for the joint estimation of the TOA and the AOA

In this subsection we derive the FIM and the CRLBs for the joint estimation of the TOA and the AOA in MIMO and MISO systems. We assume that the unknown parameters are  $\tau$  and  $\theta$  only.

The part of interest in the log-likelihood function can be written from Eq. 5.56 as:

$$\Lambda^{\tau,\theta} = \frac{-1}{2N_0} \sum_{m=1}^M \int_{-\infty}^{+\infty} \left| v_m(t) - \sum_{n=1}^N u_{n,m}(t) \right|^2 dt. \quad (5.57)$$

Denote by  $x^*(t)$  the complex conjugate of  $x(t)$ ,  $X_{x,y}(\tau) = \int x(t+\tau)y^*(t)dt$  the cross-correlation function of  $x(t)$  and  $y(t)$ ,  $\nu = \alpha^2 E_s/N_0$  the signal to noise ratio (SNR) per one transmitted signal,  $\nu_t = N\nu$  the total SNR,  $i_T = \sum_{n=1}^N \rho_n^2 \sin^2(\theta - \theta_n)$  and  $i_R = \sum_{m=1}^M r_m^2 \sin^2(\theta - \phi_m)$  the inertias (the inertia of an array has been already defined in Sec. 5.1, see Eq. 5.21) of Tx and Rx (remind that Tx and Rx are arrays) in the direction  $\theta$  (remind that  $i_T$  and  $i_R$  are independent of  $\theta + \frac{\pi}{2}$  in the case of regular arrays, see Eq. 5.23),  $\sum_{n \neq n'} \{\cdot\} = \sum_n \sum_{n' \neq n+1} \{\cdot\}$ ,  $A_n = \rho_n \sin(\theta - \theta_n)$ , and  $\Delta\tau_{n',n}$  the delay between  $u_{n'm}(t)$  and  $u_{n,m}(t)$ . Note that  $i_T$ ,  $i_R$ ,  $A_n$  and  $\Delta\tau_{n',n}$  are all functions of  $\theta$ . However, we omit  $\theta$  for sake of conciseness. From Eq. 5.53, we can write  $\Delta\tau_{n',n}$  as:

$$\begin{aligned} \Delta\tau_{n',n} &= \tau_{n'm} - \tau_{n,m} \\ &= \frac{1}{c} [\rho_n \cos(\theta - \theta_n) - \rho_{n'} \cos(\theta - \theta_{n'})]. \end{aligned} \quad (5.58)$$

Given that we are in the far-field assumption,  $\Delta\tau_{n',n}$  is independent of  $m$ , the shape of Rx and the distance between Tx and Rx; it just depends on the shape of Tx and the angle  $\theta$ .

Taking the negatives of the expectations of the second partial derivatives of  $\Lambda^{\tau,\theta}$  Eq. 5.57 with respect to  $\tau$  and  $\theta$  and taking account of Eq. 5.51 and Eq. 5.52, the elements of the FIM of  $\tau$  and  $\theta$  (see the definition of the FIM in Eq. 5.12)

$$\mathbf{F}^{\tau,\theta} = \begin{pmatrix} \mathfrak{f}^{\tau,\tau} & \mathfrak{f}^{\tau,\theta} \\ \mathfrak{f}^{\theta,\tau} & \mathfrak{f}^{\theta,\theta} \end{pmatrix} \quad (5.59)$$

can be written as:

$$f^{\tau,\tau} = M\nu \left\{ \beta_s^2 (N + \Gamma_s^{\omega_0}) + \omega_0^2 (N + \Gamma_s^{\omega_0}) - 2\omega_0 \beta_s \Gamma_{\dot{s},s}^{\omega_0} \right\} \quad (5.60)$$

$$f^{\theta,\theta} = \frac{\nu}{c^2} \left\{ \beta_s^2 \left[ i_R (N + \Gamma_s^{\omega_0}) + M(i_T + I_s^{\omega_0}) \right] + \omega_0^2 \left[ i_R (N + \Gamma_s^{\omega_0}) + M(i_T + I_s^{\omega_0}) \right] - 2\omega_0 \beta_s \left[ i_R \Gamma_{\dot{s},s}^{\omega_0} + M I_{\dot{s},s}^{\omega_0} \right] \right\} \quad (5.61)$$

$$f^{\tau,\theta} = f^{\theta,\tau} = \frac{M\nu}{c} \left\{ \beta_s^2 J_s^{\omega_0} + \omega_0^2 J_s^{\omega_0} - 2\omega_0 \beta_s J_{\dot{s},s}^{\omega_0} \right\} \quad (5.62)$$

where the expressions of  $\Gamma_s^{\omega_0}$ ,  $I_s^{\omega_0}$  and  $J_s^{\omega_0}$  are given below, whereas those of  $\Gamma_{\dot{s},s}^{\omega_0}$ ,  $I_{\dot{s},s}^{\omega_0}$ ,  $J_{\dot{s},s}^{\omega_0}$  and  $J_{\dot{s},s}^{\omega_0}$  in Appendix C since they will be shown below to be negligible. We have:

$$\Gamma_s^{\omega_0} = 2 \sum_{n \neq n'} \hat{X}_{s_n s_{n'}}^{\omega_0} \quad (5.63)$$

$$I_s^{\omega_0} = 2 \sum_{n \neq n'} A_n A_{n'} \hat{X}_{s_n s_{n'}}^{\omega_0} \quad (5.64)$$

$$J_s^{\omega_0} = \sum_{n \neq n'} (A_n + A_{n'}) \hat{X}_{s_n s_{n'}}^{\omega_0} \quad (5.65)$$

where

$$\hat{X}_{s_n s_{n'}}^{\omega_0} = \Re \left\{ e^{j\omega_0 \Delta\tau_{n',n}} \frac{X_{s_n s_{n'}}(\Delta\tau_{n',n})}{E_s} \right\}. \quad (5.66)$$

$\hat{X}_{s_n s_{n'}}^{\omega_0}$  denotes the correlation coefficient between  $u_{n,m}(t)$  and  $u_{n',m}(t)$  (i.e. the signals received by Rx<sub>m</sub> from Tx<sub>n</sub> and Tx<sub>n'</sub> respectively). We have  $|\hat{X}_{s_n s_{n'}}^{\omega_0}| \leq 1$  because it is normalized with respect to  $E_s$  ( $E_s$  is the energy of  $s_n(t)$ ,  $\forall n$ ). Given the expression of  $\Delta\tau_{n',n}$  (see Eq. 5.58),  $\hat{X}_{s_n s_{n'}}^{\omega_0}$  is the same for all reception elements. It just depends on the transmitted signals, the shape of Tx and the direction (i.e the angle of departure  $\theta$ ) of Rx. Note that  $\Gamma_s^{\omega_0}$  is a number like  $\hat{X}_{s_n s_{n'}}^{\omega_0}$ ,  $I_s^{\omega_0}$  a squared distance like  $i_T$  and  $i_R$ , and  $J_s^{\omega_0}$  is a distance.

For narrowband and WB signals where the carrier frequency  $f_0$  is much larger than the bandwidth  $B$ ,  $\beta_s^2$  (mean quadratic bandwidth of the baseband transmitted signal) can be neglected with respect to  $\omega_0^2$ . If  $|U(f)|$  is constant along the band,  $\beta_s^2$  reaches its maximum  $\pi^2 B^2$ . For  $B = 20$  MHz and  $f_0 = 2.4$  GHz, we have  $\frac{\beta_s}{\omega_0} = \frac{B}{2f_0} \approx 0.0042$  (note that even for UWB signals we can neglect the envelope mean quadratic bandwidth, see Sec. 5.1.7, and our comments to Eq. 2.28 in Sec. 2.1.1.2). Accordingly,  $f^{\tau,\tau}$ ,  $f^{\theta,\theta}$  and  $f^{\tau,\theta}$  can be approximated

from Eq. 5.60, Eq. 5.61 and Eq. 5.62 by:

$$f^{\tau,\tau} = M\nu\omega_0^2(N + \Gamma_s^{\omega_0}) \quad (5.67)$$

$$f^{\theta,\theta} = \frac{\nu\omega_0^2}{c^2} \left[ i_R(N + \Gamma_s^{\omega_0}) + M(i_T + I_s^{\omega_0}) \right] \quad (5.68)$$

$$f^{\tau,\theta} = \frac{M\nu\omega_0^2}{c} J_s^{\omega_0}. \quad (5.69)$$

In the computation of  $f^{\tau,\tau}$ ,  $f^{\theta,\theta}$  and  $f^{\tau,\theta}$  we have assumed that we are able to know the phase of the carrier at Tx and Rx; otherwise the accuracy on the estimation of  $\tau$  will be much lower and  $\omega_0^2$  must be replaced by  $\beta_s^2$  in Eq. 5.67. We have also to note that, due to the ambiguity phenomenon studied in Chap. 1, the accuracy associated with  $\omega_0^2$  cannot be in general achieved with WB signals except at very high SNRs. The accuracy on the estimation of the angle is always dependent on  $\omega_0^2$  since  $\theta$  is function of the time difference of arrival of the signals received at Rx rather than the absolute time delay between Tx and Rx.

We have already seen in the definition of the CRLB in Eq. 5.11 in Sec. 5.1.3 that the CRLBs are the diagonal elements of the inverse of the FIM. Accordingly, when the FIM  $F^{\tau,\theta}$  Eq. 5.59 of  $\tau$  and  $\theta$  is diagonal (i.e.  $f^{\tau,\theta} = f^{\theta,\tau} = 0$ ), then the CRLBs of  $\tau$  and  $\theta$  will be given by  $c^\tau = \frac{1}{f^{\tau,\tau}}$  and  $c^\theta = \frac{1}{f^{\theta,\theta}}$ , respectively. In the general case, the expressions of  $c^\tau$  and  $c^\theta$  are much more complicated and difficult to interpret. Below, we analyze the expressions of  $f^{\tau,\tau}$ ,  $f^{\theta,\theta}$  and  $f^{\tau,\theta}$  (the elements of the FIM) and compute  $c^\tau$  and  $c^\theta$  in some special cases.

In Eq. 5.67 and Eq. 5.68,  $\Gamma_s^{\omega_0}$  is a measure of the correlation among  $u_{1m}(t), \dots, u_{Nm}(t)$  (the useful signals received by Rx<sub>m</sub> from Tx<sub>1}, \dots, Tx\_N respectively). From now on, received signal components will stand for the useful components  $u_{1m}(t), \dots, u_{Nm}(t)$  of an arbitrary received signal  $v_m(t)$  (see Eq. 5.56) instead of  $v_1(t), \dots, v_M(t)$  (the signals received at Rx<sub>1}, \dots, Rx\_M). From Eq. 5.63 and Eq. 5.66, we can see that  $\Gamma_s^{\omega_0}$  is the same for all Rx<sub>m}; it depends on  $s_1(t), \dots, s_N(t)$ , the shape of the array Tx, and  $\theta$ . It belongs into the interval  $[-N, N(N-1)]$ . Note that it is not necessary that  $\Gamma_s^{\omega_0}$  takes all its possible values in every scenario.</sub></sub></sub>

$\Gamma_s^{\omega_0}$  is positive (resp. negative) when the received signal components are constructive (resp. destructive) and null when they are orthogonal. Note that the energy of the sum of constructive (resp. destructive) signals is greater (resp. less) than the sum of their energies, and that the energy of the sum of orthogonal signals is equal to the sum of their energies.  $\Gamma_s^{\omega_0}$  reaches its upper bound when the received signal components are completely correlated (i.e.  $\hat{X}_{s_n s_{n'}}^{\omega_0} = 1, \forall(n, n')$ ) and reaches its lower bound when the sum of the received signal components is null. Given that  $\Gamma_s^{\omega_0}$  is function of  $\theta$ , the received signal components cannot be constructive, destructive or orthogonal for all positions.

When  $\Gamma_s^{\omega_0}$  is equal to  $N(N-1)$ , then  $I_s^{\omega_0}$  Eq. 5.64 is equal to  $-i_T(\theta)$ ,  $J_s^{\omega_0}$  Eq. 5.65 and  $f^{\tau,\theta}$  Eq. 5.69 are equal to zero (diagonal FIM), and  $f^{\tau,\tau}$  Eq. 5.67 is

accordingly maximal, so  $c^\tau$  becomes minimal. The expressions of the CRLBs of  $\tau$  and  $\theta$  are given in this case by:

$$c_{MIMO,c}^\tau = \frac{1}{MN^2\nu\omega_0^2} = \frac{1}{MN\nu_t\omega_0^2} \quad (5.70)$$

$$c_{MIMO,c}^\theta = \frac{c^2}{N^2\nu\omega_0^2 i_R} = \frac{c^2}{N\nu_t\omega_0^2 i_R} \quad (5.71)$$

where the subscript  $c$  denotes that the received signal components are constructive. In Eq. 5.70 and Eq. 5.71 the term  $N^2$  highlights the fact that the energy of the sum of  $N$  identical signals is equal to  $N^2$  times the energy of each one of them. In the expression of  $c_{MIMO,c}^\theta$  we do not see  $i_T$  (the inertia of the array Tx) because receiving the sum of identical signals coming from different transmission elements is equivalent to having only one transmission element. For the same reason we will see below in Eq. 5.73 that in MISO systems,  $c^\theta$  approaches infinity when the received signals are identical.

The expressions of the CRLBs of  $\tau$  and  $\theta$  in MISO systems, in the case of constructive received signal components, can be deduced from those (i.e. Eq. 5.70 and Eq. 5.71) in MIMO systems by taking  $M = 1$  and  $i_R = 0$ :

$$c_{MISO,c}^\tau = \frac{1}{N\nu_t\omega_0^2} \quad (5.72)$$

$$c_{MISO,c}^\theta = \infty. \quad (5.73)$$

When  $\Gamma_s^{\omega_0}$  is equal to  $-N$  (received signal components completely destructive), then  $c^\tau$  approaches infinity in MIMO and MISO systems whereas  $c^\theta$  becomes a function of the shape of the array Tx and the distribution of the transmitted signals on the transmission elements.

In both cases considered above (i.e.  $\Gamma_s^{\omega_0} = N(N-1)$  and  $\Gamma_s^{\omega_0} = -N$ ),  $c^\tau$  and  $c^\theta$  are very sensitive to the value of the angle; they are subject to strong oscillations with the variation of  $\theta$ . To illustrate this fact, we consider a uniform linear array (ULA) of two elements transmitting the same signal; the ULA is supposed to be orthogonal to the  $x$  axis. The signal received by an element located on the  $x$  axis is the sum of two identical signals, so  $\Delta\tau_{1,2} = 0$  and  $\hat{X}_{s_1 s_2}^{\omega_0} = 1$ . If we move the receiver so that  $\Delta\tau_{1,2}$  becomes equal to half the period of the carrier, then  $u_1(t)$  and  $u_2(t)$  become destructive (in phase opposition) and their sum becomes quasi null ( $\hat{X}_{s_1 s_2}^{\omega_0} \approx -1$ , we say ‘‘quasi’’ because the corresponding envelopes are not 100% equal because they are delayed from each other). For the first position,  $c^\tau$  reaches its minimum, whereas for the second position it becomes quasi infinite.

Assume now that the codes  $(c_{n,j})$  and  $(c_{n',j})$  used in transmission (see Eq. 5.54) are orthogonal,  $\forall n \neq n'$ . We have already mentioned that the received signal components are not necessarily orthogonal at the receiver, even if they are orthogonal at the transmitter. The maximum possible delay between two different received signal components is given by  $\Delta\tau_{n',n}^{\max} = \frac{D_T}{c}$  (see Eq. 5.58,

$D_T$  has been already defined as the diameter of the smallest circle containing Tx). Given that the array inter-element spacing is in general smaller than half the carrier wavelength,  $\Delta\tau_{n',n}^{\max}$  will be in the order of a few periods of the carrier. Furthermore, given that the chip period  $T_c$  (see Eq. 5.54) is much larger, in WB signals, than the carrier period,  $\Delta\tau_{n',n}^{\max}$  will be much smaller than  $T_c$ , so the received signal components can be considered orthogonal for all values of  $\theta$ . It follows that  $\hat{X}_{s_n s_{n'}}^{\omega_0}$ ,  $\Gamma_s^{\omega_0}$ ,  $I_s^{\omega_0}$  and  $J_s^{\omega_0}$  are all quasi null  $\forall\theta$ . The CRLBs of  $\tau$  and  $\theta$  obtained in this case, can be approximated from Eq. 5.67, Eq. 5.68 and Eq. 5.69 by:

$$c_{MIMO,o}^{\tau} = \frac{1}{MN\nu\omega_0^2} = \frac{1}{M\nu_t\omega_0^2} \quad (5.74)$$

$$c_{MIMO,o}^{\theta} = \frac{c^2}{\nu\omega_0^2 [Ni_R + Mi_T]} = \frac{c^2}{\nu_t\omega_0^2 [i_R + \frac{M}{N}i_T]} \quad (5.75)$$

where the subscript  $_o$  indicates that the transmitted signals are orthogonal. In Eq. 5.74 and Eq. 5.75, the term  $N$  highlights the fact that the energy of the sum of  $N$  identical orthogonal signals is equal to  $N$  times the energy of each one of them. The term  $M$  highlights the fact that the Fisher information contained in the  $M$  signals received at the  $M$  elements of Rx, is  $M$  times the Fisher information contained in each one of them, because they are statistically independent, and separately contain equal information.

The expressions of the CRLBs of  $\tau$  and  $\theta$  in MISO systems, in the case of orthogonal transmitted signals, can be deduced from those (i.e. Eq. 5.74 and Eq. 5.75) in MIMO systems by taking  $M = 1$  and  $i_R = 0$ :

$$c_{MISO,o}^{\tau} = \frac{1}{\nu_t\omega_0^2} \quad (5.76)$$

$$c_{MISO,o}^{\theta} = \frac{Nc^2}{\nu_t\omega_0^2 i_T}. \quad (5.77)$$

### 5.2.3 Comparison of SISO, SIMO, MISO and MIMO configurations

In this subsection we compare the CRLBs of the SISO, SIMO, MISO and MIMO configurations. We assume that the total transmitted energy is the same in all systems. We also assume that the arrays Tx and Rx are identical and have the same orientation so that  $M = N$  and  $i_R = i_T$ ,  $\forall\theta$ .

Let us first give the expressions (easily deduced from the expressions obtained in MIMO systems) of  $c^\tau$  in SISO and SIMO systems, and  $c^\theta$  in SIMO systems:

$$c_{SISO}^\tau = \frac{1}{\nu_t \omega_0^2} \quad (5.78)$$

$$c_{SIMO}^\tau = \frac{1}{M \nu_t \omega_0^2} \quad (5.79)$$

$$c_{SIMO}^\theta = \frac{c^2}{\nu_t \omega_0^2 i_R}. \quad (5.80)$$

Consider first the TOA estimation. We can deduce from the expressions established above that the smallest value of  $c^\tau$ , which is also insensitive to the angle, is obtained in SIMO and orthogonal MIMO configurations; it is  $M$  times lower than the smallest value obtained in SISO and orthogonal MISO configurations. However, MIMO can do better than SIMO, and MISO can do better than SISO in the regions where the received signal components are constructive. When the received signal components are completely correlated, the value of  $c^\tau$  obtained in MIMO configurations is  $N$  times lower than that obtained in SIMO configurations, and the value of  $c^\tau$  obtained in MISO configurations is  $N$  times lower than that obtained in SISO configurations.

Consider now the AOA estimation. The smallest value of  $c^\theta$ , which is also insensitive to the angle, is obtained in orthogonal MIMO configurations, then in SIMO configurations, then in orthogonal MISO configurations. The smallest value of  $c^\theta$  obtained in orthogonal MIMO configurations is half (for identical Tx and Rx) of that obtained in SIMO configurations, and this latter is  $N$  times lower than that obtained in orthogonal MISO configurations. However, MIMO can do better than orthogonal MIMO in the regions where the received signal components are constructive. When the received signal components are completely correlated, the value of  $c^\theta$  obtained in MIMO configurations is  $N$  times lower (instead of being equal to the half) than that obtained in SIMO configurations (for identical Tx and Rx), whereas it approaches infinity in MISO configurations.

#### 5.2.4 Numerical results and discussion

In this section we show and discuss some numerical results obtained in some typical scenarios.

The considered setups are:

- SISO:  $1 \times 1$ .
- SIMO:  $1 \times 2$  and  $1 \times 4$ .
- MISO:  $2 \times 1$  and  $4 \times 1$ .
- MIMO:  $2 \times 2$  and  $4 \times 4$

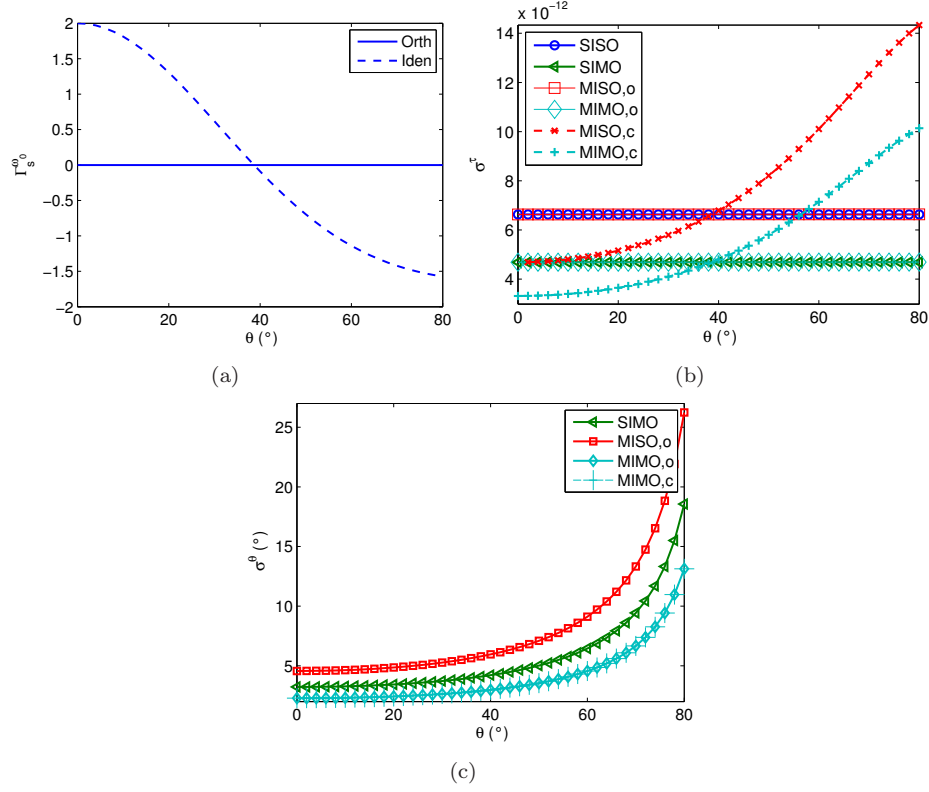


Fig. 5.9.: SISO  $1 \times 1$ , SIMO  $1 \times 2$ , MISO  $2 \times 1$  and MIMO  $2 \times 2$  systems (a)  $\Gamma_s^{\omega_0}$  with respect to the angle  $\theta$  (b) Square root  $\sigma^\tau$  of the CRLB of  $\tau$  with respect to  $\theta$  (c) Square root  $\sigma^\theta$  of the CRLB of  $\theta$  with respect to  $\theta$ .

In  $2 \times 1$ ,  $2 \times 2$ ,  $4 \times 1$  and  $4 \times 4$ , both orthogonal transmitted signals, and identical transmitted signals have been considered. When orthogonal signals are considered, Alamouti code [125] is used in  $2 \times 1$  and  $2 \times 2$ , and Hadamard (4) code in  $4 \times 1$  and  $4 \times 4$ . ULAs are used in transmission and reception. Tx and Rx are orthogonal to the  $x$  axis. The modulating symbols  $(\pm 1 \pm j)$  (20 symbols) are generated randomly and shaped by a root raised cosine of roll-off equal to 0.5. We take  $f_0 = 2.4$  GHz (carrier),  $R_c = 20$  MHz (chip rate),  $\nu_t = 20$  dB (total SNR, the same for all systems) and  $d = 5$  cm  $< 6.25$  cm  $= \frac{\lambda_0}{2}$  ( $d$  denotes the array inter-element spacing, and  $\lambda_0$  the wavelength of the carrier). We denote by  $\sigma^\tau$  and  $\sigma^\theta$  the square roots of  $c^\tau$  and  $c^\theta$  respectively.

Consider first the systems SISO  $1 \times 1$ , SIMO  $1 \times 2$ , MISO  $2 \times 1$  and MIMO  $2 \times 2$ .

In Fig. 5.9(a) we show  $\Gamma_s^{\omega_0}$  with respect to the angle  $\theta$ , for MISO and MIMO, for both the orthogonal and identical transmitted signals cases. We can see that  $\Gamma_s^{\omega_0}$  is quasi null for the case of orthogonal signals. For the case of identical signals, we can see the regions where the received signal components are constructive (for  $\theta \in [0, 38]^\circ$  where  $\Gamma_s^{\omega_0} > 0$ ) and destructive (for  $\theta \in [39, 80]^\circ$  where  $\Gamma_s^{\omega_0} < 0$ ). We can also see that as  $N = 2$ , we have  $\Gamma_s^{\omega_0} \in [-2, 2]$ . It has been already noticed that  $\Gamma_s^{\omega_0} \in [-N, N(N-1)]$ .

In Fig. 5.9(b) we show the square root  $\sigma^\tau$  of the CRLB of  $\tau$  with respect to the angle  $\theta$ , for SISO, SIMO, MISO and MIMO, for both the orthogonal and identical transmitted signals cases. We can see that, like it has been expected, the smallest  $\sigma^\tau$  is obtained with MIMO in the constructive region, then with SIMO and orthogonal MIMO, then with MISO in the constructive region and MIMO in the region where the received signal components are not very destructive (i.e. for  $\theta \in [39, 56]^\circ$ ), then with SISO and orthogonal MISO, then with MISO in the destructive region and MIMO in the region where the received signal components are very destructive (i.e. for  $\theta \in [57, 80]^\circ$ ).

In Fig. 5.9(c) we show the square root  $\sigma^\theta$  of the CRLB of  $\theta$  with respect to the angle  $\theta$ , for SIMO, MISO and MIMO, for both the orthogonal and identical transmitted signals cases. We can see that the smallest  $\sigma^\theta$  is obtained with MIMO (for both orthogonal and identical transmitted signals), then with SIMO, then with orthogonal MISO. The value of  $\sigma^\theta$  is increasing with  $\theta$  because  $i_T$  and  $i_R$  are decreasing with  $\theta$ ;  $i_T$  and  $i_R$  are maximal for  $\theta = 0$  and approach infinity (because linear arrays) for  $\theta = \pi/2$ . We do not show  $\sigma^\theta$  for identical transmitted signals because it approaches infinity when  $\theta$  approaches zero (see Eq. 5.73). In Sec. 5.2.3 we have seen that  $\sigma^\theta$  is the lowest in constructive MIMO but is very sensitive to  $\theta$ . However,  $\sigma^\theta$  is the same here in constructive and orthogonal MIMO. In fact, in this special case where we consider a MIMO  $2 \times 2$  with two identical arrays, we can prove that  $i_R \Gamma_s^{\omega_0} + M I_s^{\omega_0} = 0, \forall \theta$  (see Eq. 5.68) which leads to the obtained result.

Consider now the systems SISO  $1 \times 1$ , SIMO  $1 \times 4$ , MISO  $4 \times 1$  and MIMO  $4 \times 4$ .

We can see in Fig. 5.10(a) that  $\Gamma_s^{\omega_0}$  varies now, in the case of identical transmitted signals, from  $-N = -4$  to  $N(N-1) = 16$ . For  $\theta \approx 38^\circ$ , we have  $\Gamma_s^{\omega_0} \approx -4$  which means that the received signal components are quasi, completely destructive; we can see in Fig. 5.10(b) that in this region of strong destruction,  $\sigma^\tau$  approaches infinity in both MIMO and MISO systems, as has been already expected; however, we can see in Fig. 5.10(c) that unlike  $\sigma^\tau$ ,  $\sigma^\theta$  is not singular in this region. As now  $i_R \Gamma_s^{\omega_0} + M I_s^{\omega_0} \neq 0$  (unlike the case of MIMO  $2 \times 2$  considered above), we can see in Fig. 5.10(c) that  $\sigma^\theta$  is, as expected, the lowest in MIMO systems in the constructive region than in orthogonal MIMO systems.

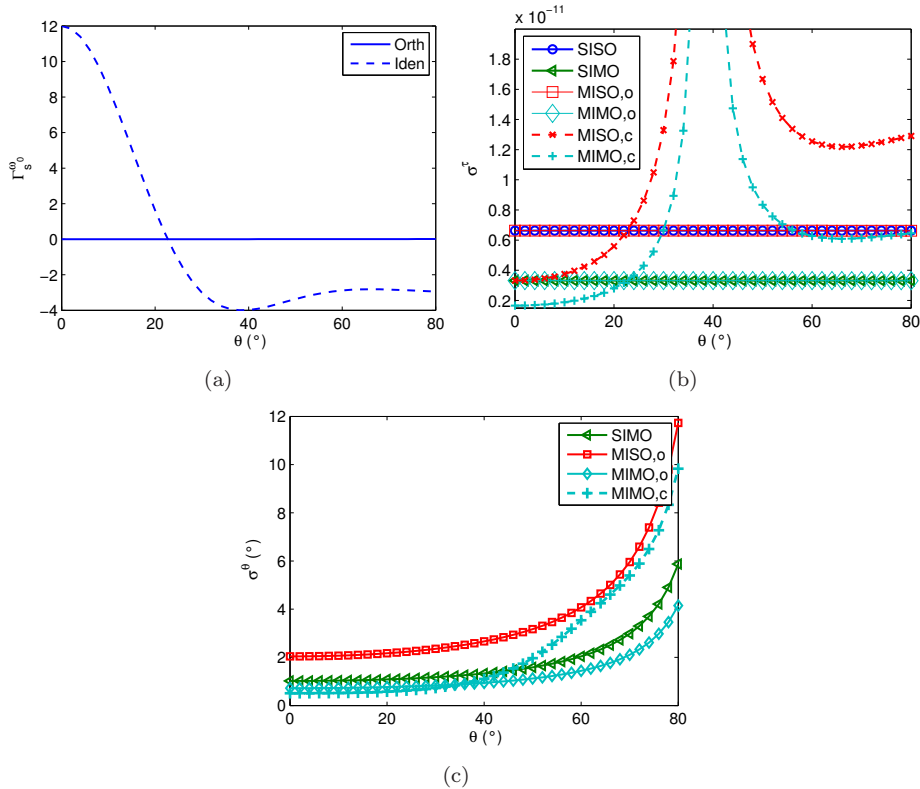


Fig. 5.10.: SISO  $1 \times 1$ , SIMO  $1 \times 4$ , MISO  $4 \times 1$  and MIMO  $4 \times 4$  systems (a)  $\Gamma_s^{\omega_0}$  with respect to the angle  $\theta$  (b) Square root  $\sigma^\tau$  of the CRLB of  $\tau$  with respect to  $\theta$  (c) Square root  $\sigma^\theta$  of the CRLB of  $\theta$  with respect to  $\theta$ .

### 5.3 CRLBS FOR UWB CHANNEL ESTIMATION: IMPACT OF THE OVERLAPPING OF THE MPCS ON THE JOINT GAIN AND TOA ESTIMATION

UWB signals can serve for very accurate positioning thanks to their high frequency components and large bandwidth. One of the most severe challenges is the parameter estimation in MP channels. CRLBs for UWB MP channel estimation have been widely studied in the literature assuming non overlapping MPCs [93, 126]. In [127] the overlapping between the different MPCs is investigated. It has been shown that the smallest CRLBs are obtained under the NOLA and more MPCs leads in general to higher CRLBs and less performance.

In this section we study the impact of the overlapping on the performance of the estimation. We compute the probability of the overlapping between neighbor-

ing MPCs with respect to the pulse width to average MPC rate of arrival ratio. We consider the IEEE802.15.3a [7] and IEEE802.15.4a [9] UWB channel models. We show that for a pulse width sufficiently smaller than the average MPC rate of arrival, the probability to have more than three overlapping MPCs is relatively small. We show also that instead of considering all MPCs together we can split the received signal into consecutive non-overlapping blocks and study each block separately. We compute the CRLBs for MPC gain and TOA estimation in blocks of up to three overlapping MPCs and compute the average bounds. We show that for a pulse width to average rate of arrival ratio equal to 0.3824 and an SNR of zero dB, the bounds obtained by averaging more than 80% of cases are very close to the smallest reachable bounds (i.e. the ones obtained in AWGN channels, and in MP channels under the non-overlapping assumption).

In Sec. 5.3.1 we describe our system model. In Sec. 5.3.2 we present the considered channel statistical model. In Sec. 5.3.3 we compute the probability of overlapping between neighboring MPCs. In Sec. 5.3.4 we derive the FIM for the joint estimation of the MPCs gains and TOAs. In Sec. 5.3.5 we compute the CRLBs corresponding to blocks of up to three MPCs. In Sec. 5.3.6 we compute the average CRLBs.

### 5.3.1 System model

In this subsection we describe our system model. We consider a LOS MP AWGN communication channel. The signal received by the receiver (Rx) can be written as:

$$r(t) = \sum_{l=1}^L \alpha^{(l)} s(t - \tau^{(l)}) + n(t) \quad (5.81)$$

where  $s(t)$  is the signal sent by the transmitter (Tx),  $\alpha^{(l)}$  and  $\tau^{(l)}$  the gain and the time delay of MPC<sup>(l)</sup> (the  $l^{\text{th}}$  MPC),  $L$  the number of MPCs and  $n(t)$  the AWGN. Let  $\gamma_n = \nu_{nf} \frac{N_0}{2}$  be the bilateral PSD of  $n(t)$  where  $\nu_{nf}$  is the noise figure and  $\frac{N_0}{2}$  the PSD at the room temperature.

The transmitted signal  $s(t)$  is an IR-UWB signal. Both PAM and PPM modulations can be used, and both DS and TH spreading and multiple access codes as well. Signal  $s(t)$  can be written as:

$$s(t) = \sum_{i=-\infty}^{+\infty} a_i \sum_{j=0}^{N_c-1} c_j p_{T_w}(t - iT_s - jT_c - d_j T_h - b_i \epsilon) \quad (5.82)$$

where  $p_{T_w}(t)$  is the used pulse and  $T_w$  its width,  $a_i$  and  $b_j$  the PAM and PPM symbols respectively,  $(c_j)$  and  $(d_j)$  the DS and TH codes,  $N_c$  the code length,  $T_s$  the symbol period,  $T_c$  ( $T_s = N_c T_c$ ) the chip period,  $T_h$  the time hop and  $\epsilon$  the PPM time shift. We say that  $s(t)$  is invariant with respect to the time to pulse

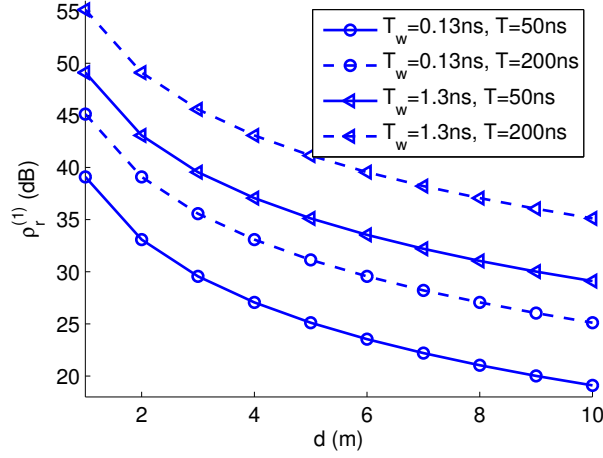


Fig. 5.11.: SNR  $\rho_r^{(1)}$  in dB with respect to the distance  $d$ .

width ratio ( $t/T_w$ ) if  $p_{T_w}(t)$  can be written as:

$$p_{T_w}(t) = p\left(\frac{t}{T_w}\right), \forall T_w. \quad (5.83)$$

Gaussian pulse and its multiple derivatives are an example of pulses satisfying Eq. 5.83. In this section we consider a doublet (second derivative of the Gaussian pulse) for numerical illustration:

$$p_{T_w}(t) \propto \left[1 - 4\pi\left(\frac{t}{T_w}\right)^2\right] e^{-2\pi\left(\frac{t}{T_w}\right)^2}.$$

Denote by  $\gamma_s(f)$  and  $P_s = \int_0^{+\infty} \gamma_s(f) df$  the unilateral PSD and the power of  $s(t)$ ,  $T$  the integration time,  $\nu_p^{(l)}$  the loss due to the propagation through the  $l^{th}$  path ( $\nu_p^{(1)} = 4\pi d^2$  where  $d$  is the distance between Tx and Rx),  $A = c^2/4\pi f_c^2$  ( $f_c$  the central frequency) the aperture of Rx,  $\nu_{il}$  the implementation loss,  $\rho_t$  the transmitted signal to received noise ratio, and  $\rho_r^{(l)}$  the SNR of MPC $^{(l)}$ . We can write  $\rho_t$  ( $\rho_t$  is independent of  $d$ ) and  $\rho_r^{(l)}$  as:

$$\begin{aligned} \rho_t &= \frac{P_s T}{\gamma_n} \\ \rho_r^{(l)} &= \frac{P_s T A}{\nu_p^{(l)} \nu_{il} \gamma_n}. \end{aligned}$$

In Fig. 5.11 we show  $\rho_r^{(1)}$  with respect to  $d$  when a doublet is used. We take  $\gamma_s^{peak} = -41.3$  dBm/MHz,  $T_w = 0.13$  and  $1.3$  ns,  $T = 50$  and  $200$  ns,  $N_0/2 =$

	Residential LOS	Office LOS	Outdoor LOS	0-4 LOS
Range (m)	7 – 20	3 – 28	5 – 17	0 – 4
$1/\Lambda$ (ns)	21.28	62.5	208.3	42.92
$1/\lambda_1$ (ns)	0.65	5.26	3.7	0.4
$1/\lambda_2$ (ns)	6.67	0.34	0.41	
$1/\lambda$ (ns)	6.1	0.43	0.44	0.4

Table 5.2.: Parameters of UWB channels in some types of environments.

$-114$  dBm/MHz,  $\nu_{nf} = 6.6$  dB and  $\nu_{il} = 2.5$  dB. For  $T_w = 0.13$  ns,  $T = 50$  ns and  $d = 9$  m, we obtain  $\rho_r^{(1)} \approx 20$  dB and  $\rho_t \approx 90$  dB.

### 5.3.2 Channel statistical model

In this subsection we describe the statistical model of our UWB MP channel.

Based on the IEEE 802.15.3a and IEEE 802.15.4a models [7, 9], we assume that the MPCs arrive to Rx in consecutive clusters. The TOA of a cluster follows a Poisson process of average-rate-of-arrival of  $1/\Lambda$  while the TOA of a MPC within a cluster follows a mixture of two Poisson processes of average-rates-of-arrival  $1/\lambda_1$  and  $1/\lambda_2$ . We can write:

$$T_{\tau_{i,1}|\tau_{i-1,1}} = \Lambda e^{-\Lambda(\tau_{i,1}-\tau_{i-1,1})} \quad (5.84)$$

$$T_{\tau_{i,j}|\tau_{i,j-1}} = \kappa\lambda_1 e^{-\lambda_1(\tau_{i,j}-\tau_{i,j-1})} + (1-\kappa)\lambda_2 e^{-\lambda_2(\tau_{i,j}-\tau_{i,j-1})} \quad (5.85)$$

where  $T_{\{\cdot\}}$  denotes the probability density function (PDF),  $\tau_{i,j}$  the TOA (taking as reference the time of transmission) of the  $j^{th}$  MPC within the  $i^{th}$  cluster, and  $\kappa \in [0, 1]$ .

We define the average of the MPC average-rates-of-arrival (within a cluster) as:

$$1/\lambda = \kappa/\lambda_1 + (1-\kappa)/\lambda_2. \quad (5.86)$$

Unless otherwise mentioned, we mean from now on by average-rate-of-arrival the magnitude  $1/\lambda$  defined above.

In Table 5.2 we show for some environments the cluster average-rate-of-arrival  $1/\Lambda$ , the MPC average-rates-of-arrival  $1/\lambda_1$  and  $1/\lambda_2$ , and the average-rate-of-arrival  $1/\lambda$ .

### 5.3.3 Probability of overlapping between neighboring MPCs

In this subsection we compute the probability of overlapping between neighboring MPCs.

Assuming that the chip period  $T_c$  in Eq. 5.82 is larger than the time delay corresponding to the last MPC, we can consider without loss of generality the transmission of only one pulse. From the channel statistical model presented in Sec. 5.3.2, we can assume that if the pulse width is sufficiently smaller than the average-rate-of-arrival, then the received signal can be split into consecutive non overlapping blocks, of overlapping pulses (i.e. the blocks are not overlapping while the MPCs within a given block are overlapping).

Denote by  $P_{\Delta\tau}^{t_0}$  the probability that  $\Delta\tau^{(l,l-1)} = (\tau^{(l')} - \tau^{(l)}) \leq t_0$ . Assuming that MPC<sup>( $l-1$ )</sup> and MPC<sup>( $l$ )</sup> fall in the same cluster, we can write:

$$\begin{aligned} P_{\Delta\tau}^{t_0} &= \int_0^{t_0} \{\kappa\lambda_1 e^{-\lambda_1 t} + (1-\kappa)\lambda_2 e^{-\lambda_2 t}\} dt \\ &= \kappa(1 - e^{-\lambda_1 t_0}) + (1-\kappa)(1 - e^{-\lambda_2 t_0}). \end{aligned} \quad (5.87)$$

Denote by  $P_{L_b}^{l_b}$  the probability that the number  $L_b$  of the MPCs falling in the first block, is equal to  $l_b$ . Assuming that BK<sub>1</sub> (BK <sub>$i$</sub>  denotes the  $i^{th}$  block) falls in the first cluster, we can write:

$$\begin{aligned} P_{L_b}^{l_b} &= P\{L_b = l_b\} = P\left\{\left(\Delta\tau^{(l,l-1)} \leq T_w, l = 2, l_b\right) \& \left(\Delta\tau^{(l_b+1,l_b)} > T_w\right)\right\} \\ &= (P_{\Delta\tau}^{T_w})^{l_b-1} (1 - P_{\Delta\tau}^{T_w}) \end{aligned} \quad (5.88)$$

where  $P\{\cdot\}$  denotes the probability operator.

Note that even if BK<sub>1</sub> does not fall in the first cluster, Eq. 5.88 can be considered as a good approximation if the pulse width  $T_w$  and  $1/\lambda$  are sufficiently smaller than  $1/\Lambda$ . However, the probability that an arbitrary block contains  $l_b$  MPCs is slightly different from that given in Eq. 5.88.

Let us define the pulse width to average-rate-of-arrival ratio as:

$$\lambda T_w \quad (5.89)$$

where  $1/\lambda$  is the average-rate-of-arrival defined in Eq. 5.86.

In Fig. 5.12 we show  $P_{L_b}^{l_b}$  with respect to the pulse width to average-rate-of-arrival ratio  $\lambda T_w$  for  $l_b = 1, 2, 3$  and for  $l_b \leq 3$ . We vary  $\lambda T_w$  from 0.1 to 2. Residential LOS and office LOS environments have been considered. We can see that  $P_{L_b}^1 > P_{L_b}^2 > P_{L_b}^3, \forall \lambda T_w$ ; this result could be expected from Eq. 5.88. We can also see that for  $\lambda T_w = 0.5$ , the probability to have no more than three MPCs in the first block, is greater than 0.9 for both residential LOS and office LOS environments.

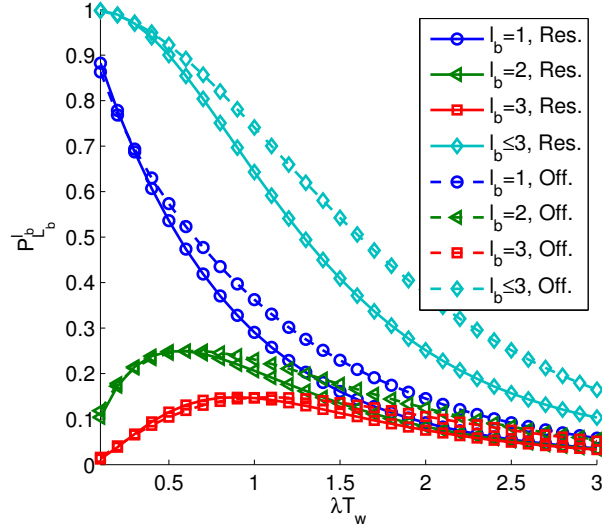


Fig. 5.12.:  $P_{L_b}^{l_b}$  with respect to  $\lambda T_w$  for  $l_b = 1, 2, 3$  and for  $l_b \leq 3$  in residential LOS (Res.) and office LOS (Off.) environments.

We will see in Sec. 5.3.4 that non-overlapping blocks can be studied separately. In addition, by taking into consideration the small probability to have more than three MPCs per block, we can simplify our study by only considering blocks of one, two and three MPCs instead of considering the whole channel impulse response. When the pulse width becomes larger than the average-rate-of-arrival, blocks of more than three MPCs should be considered. In this work, we only consider blocks of up to three MPCs.

### 5.3.4 Fisher information matrix for multipath channel parameter estimation

In this subsection we derive the FIM for the joint estimation of the channel parameters.

We assume that the unknown parameters to estimate are  $\alpha^{(1)}, \tau^{(1)}, \dots, \alpha^{(L)}, \tau^{(L)}$ . Denote by  $J^{\underline{\alpha}, \underline{\tau}}$  the FIM for the joint estimation of  $\underline{\alpha} = (\alpha^{(1)} \dots \alpha^{(L)})^T$  and  $\underline{\tau} = (\tau^{(1)} \dots \tau^{(L)})^T$ , and by  $c^{\alpha^{(l)}}$  and  $c^{\tau^{(l)}}$  the CRLBs of  $\alpha^{(l)}$  and  $\tau^{(l)}$  respectively.

From Eq. 5.81 we can write the log likelihood function for the joint estimation of  $\underline{\alpha}$  and  $\underline{\tau}$  as:

$$\Lambda^{\underline{\alpha}, \underline{\tau}} = K - \frac{1}{2\gamma_n} \int_T \left\{ r(t) - \sum_{l=1}^L \alpha^{(l)} s(t - \tau^{(l)}) \right\}^2 dt \quad (5.90)$$

where  $K$  denotes a constant.

Denote by  $\dot{x}(t)$ ,  $X(f)$ ,  $E_x = \int_T x^2(t)dt$ ,  $\beta_x^2 = E_{\dot{x}}/E_x = \int 4\pi^2 f^2 |X(f)|^2 df / \int |X(f)|^2 df$  and  $R_x(\tau) = \int_T x(t+\tau)x(t)dt$  the derivative, Fourier transform, energy (in  $T$ ), mean quadratic bandwidth, and auto-correlation function of  $x(t)$  respectively,  $X_{x,y}(\tau) = \int_T x(t+\tau)y(t)dt$  the cross-correlation function of  $x(t)$  and  $y(t)$ , and  $\hat{R}_x(\tau) = R_x(\tau)/E_x$  and  $\hat{X}_{x,y}(\tau) = X_{x,y}(\tau)/\sqrt{E_x E_y}$  the normalized auto and cross correlation functions ( $|\hat{R}_x(\tau)| \leq 1$  and  $|\hat{X}_{x,y}(\tau)| \leq 1$ ). We can prove that when  $x(t)$  satisfies Eq. 5.83, then  $\hat{R}_x(\tau)$  satisfies it as well, and  $\beta_x^2$  becomes inversely proportional to the squared pulse width  $T_w^2$  (i.e.  $\beta_x^2 T_w^2$  is constant), and when both  $x(t)$  and  $y(t)$  satisfy it, then  $\hat{X}_{x,y}(\tau)$  satisfies it as well.

Taking the negatives of the expectations of the second partial derivatives of  $\Lambda^{\alpha,\tau}$  leads to the following elements of the FIM  $J^{\alpha,\tau}$ :

$$f^{\alpha^{(l)},\alpha^{(l')}} = \frac{R_s^{(l',l)}}{\gamma_n} = \rho_t \hat{R}_s^{(l',l)} \quad (5.91)$$

$$f^{\tau^{(l)},\tau^{(l')}} = \frac{\alpha^{(l)}\alpha^{(l')}R_s^{(l',l)}}{\gamma_n} = \sqrt{\rho_r^{(l)}\rho_r^{(l')}}\beta_s^2 \hat{R}_s^{(l',l)} \quad (5.92)$$

$$f^{\alpha^{(l)},\tau^{(l')}} = \frac{-\alpha^{(l')}X_{s\dot{s}}^{(l',l)}}{\gamma_n} = -\sqrt{\rho_t\rho_r^{(l')}}\beta_s \hat{X}_{s\dot{s}}^{(l',l)} \quad (5.93)$$

where  $x^{(l',l)}$  denotes  $x(\Delta\tau^{(l',l)})$ , and  $f^{\alpha^{(l)},\tau^{(l')}} = f^{\tau^{(l')},\alpha^{(l)}}$ . Taking  $l = l'$  and assuming that  $s^2(t)|_T = 0$ , we obtain the elements of  $J^{\alpha,\tau}$  corresponding to MPC<sup>(l)</sup>:

$$f^{\alpha^{(l)},\alpha^{(l)}} = \rho_t \quad (5.94)$$

$$f^{\tau^{(l)},\tau^{(l)}} = \rho_r^{(l)}\beta_s^2 \quad (5.95)$$

$$f^{\alpha^{(l)},\tau^{(l)}} = 0. \quad (5.96)$$

therefore, we can write  $J^{\alpha,\tau}$  as:

$$J^{\alpha,\tau} = \begin{pmatrix} J^{(1,1)} & | & J^{(1,2)} & | & \dots \\ \hline J^{(2,1)} & | & J^{(2,2)} & | & \ddots \\ \vdots & | & \ddots & | & \ddots \end{pmatrix} \quad (5.97)$$

where,

$$J^{(l,l')} = \begin{pmatrix} f^{\alpha^{(l)},\alpha^{(l')}} & f^{\alpha^{(l)},\tau^{(l')}} \\ f^{\tau^{(l)},\alpha^{(l')}} & f^{\tau^{(l)},\tau^{(l')}} \end{pmatrix}.$$

Note that for  $l' \neq l$ , the matrix  $J^{(l,l')}$  is diagonal because  $f^{\alpha^{(l)},\tau^{(l)}} = 0$  (see Eq. 5.96). Furthermore, if MPC<sup>(l)</sup> does not overlap with any other MPC, then  $J^{(l,l')}$  becomes null for all  $l' \neq l$  (see Eq. 5.91, Eq. 5.92 and Eq. 5.93, and take into account that  $X_{x,y}(\tau) = 0$  if  $x(t+\tau)$  and  $y(t)$  do not overlap). As the CRLBs of the parameters to estimate correspond to the diagonal elements of the FIM inverse  $(J^{\alpha,\tau})^{-1}$ , we can easily show that when MPC<sup>(l)</sup> does not overlap with any other MPC, then the CRLBs  $c^{\alpha^{(l)}}$  and  $c^{\tau^{(l)}}$  of  $\alpha^{(l)}$  and  $\tau^{(l)}$  are the inverses of  $f^{\alpha^{(l)},\alpha^{(l)}}$  Eq. 5.94 and  $f^{\tau^{(l)},\tau^{(l)}}$  Eq. 5.95 respectively. The CRLBs obtained in this case are the smallest that can be reached. They correspond to the CRLBs obtained in an AWGN channel.

We have seen in Sec. 5.3.3 that the received signal can be split into non-overlapping blocks of overlapping MPCs when the pulse width is sufficiently smaller than the average-rate-of-arrival. Let us denote by  $J_{b_i}^{\alpha,\tau}$  the FIM corresponding to the block BK<sub>i</sub>. As the Fisher information  $f^{\alpha^{(l)},\alpha^{(l')}}$  Eq. 5.91,  $f^{\tau^{(l)},\tau^{(l')}}$  Eq. 5.92 and  $f^{\alpha^{(l)},\tau^{(l')}}$  Eq. 5.93 are null if MPC<sup>(l)</sup> and MPC<sup>(l')</sup> belong into two different blocks (because they do not overlap), we can write the FIM in Eq. 5.97 as:

$$J^{\alpha,\tau} = \begin{pmatrix} \frac{J_{b_1}^{\alpha,\tau} \mid \underline{0} \mid \cdots}{\underline{0} \mid J_{b_2}^{\alpha,\tau} \mid \ddots} \\ \vdots \mid \ddots \mid \ddots \end{pmatrix}. \quad (5.98)$$

We can deduce from the structure of  $J^{\alpha,\tau}$  in Eq. 5.98 that the CRLBs of the parameters of a given block can be obtained by only inverting the sub-FIM corresponding to the concerned block. This means that different blocks can be considered separately and that by studying all possible cases of an arbitrary block, we can characterize the whole channel. We have already mentioned that only blocks of up to three MPCs will be considered in this work.

### 5.3.5 CRLBs for channel parameter estimation

In this subsection we compute the CRLBs of the gains and the TOAs of the MPCs belonging to blocks of one (Sec. 5.3.5.1), two (Sec. 5.3.5.2) and three MPCs (Sec. 5.3.5.3). From now on, we denote by MPC<sup>(l)</sup> the  $l^{\text{th}}$  MPC in the considered block.

#### 5.3.5.1 CRLBs for blocks of one MPC

Here we consider blocks of one MPC. Given that the considered MPC does not overlap with any other MPC, the CRLBs of  $\alpha^{(1)}$  and  $\tau^{(1)}$  are given from Eq. 5.94,

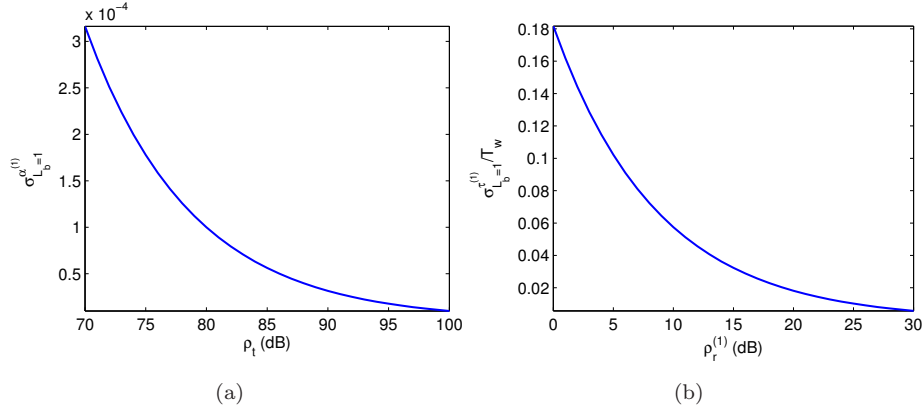


Fig. 5.13.: Block of one MPC (a) Square root  $\sigma_{L_b=1}^{\alpha^{(1)}}$  of the CRLB of  $\alpha^{(1)}$  with respect to  $\rho_t$  (b) Normalized square root  $\sigma_{L_b=1}^{\tau^{(1)}}/T_w$  of the CRLB of  $\tau^{(1)}$  with respect to  $\rho_r^{(1)}$ .

Eq. 5.95 and Eq. 5.96 by:

$$c_{L_b=1}^{\alpha^{(1)}} = \frac{1}{f_{\alpha^{(1)}, \alpha^{(1)}}} = \frac{1}{\rho_t} \quad (5.99)$$

$$c_{L_b=1}^{\tau^{(1)}} = \frac{1}{f_{\tau^{(1)}, \tau^{(1)}}} = \frac{1}{\rho_r^{(1)} \beta_s^2}. \quad (5.100)$$

We can see in Eq. 5.99 and Eq. 5.100 that  $c_{L_b=1}^{\alpha^{(1)}}$  is, unlike  $c_{L_b=1}^{\tau^{(1)}}$ , independent of  $\alpha^{(1)}$ ; it depends just on the transmitted signal to received noise ratio  $\rho_t$ . Given that  $\beta_s^2 T_w^2$  is constant for pulses satisfying Eq. 5.83, it seems more significant to evaluate  $c_{L_b=1}^{\tau^{(1)}}/T_w^2$  instead of  $c_{L_b=1}^{\tau^{(1)}}$ .

Remember that all the numerical results provided in this paper are obtained using a doublet. In Fig. 5.13(a) we show  $\sigma_{L_b=1}^{\alpha^{(1)}}$  (the square root of the CRLB  $c_{L_b=1}^{\alpha^{(1)}}$  of  $\alpha^{(1)}$ ) with respect to  $\rho_t$ .  $\rho_t$  is varying from 70 to 100 dB. For  $\rho_t = 90$  dB, we obtain  $\sigma_{L_b=1}^{\alpha^{(1)}} = 0.3 \times 10^{-4}$ .

In Fig. 5.13(b) we show the normalized square root  $\sigma_{L_b=1}^{\tau^{(1)}}/T_w$  of the CRLB  $c_{L_b=1}^{\tau^{(1)}}$  of  $\tau^{(1)}$  with respect to  $\rho_r^{(1)}$ . We vary  $\rho_r^{(1)}$  from 0 to 30 dB. Remember that the difference of 70 dB between  $\rho_t$  and  $\rho_r^{(1)}$  corresponds to  $T_w = 0.13$  ns,  $d = 9$  m and  $\nu_{il} = 2.5$  dB. We can see that for  $\rho_r^{(1)} = 20$  dB, we have  $\sigma_{L_b=1}^{\tau^{(1)}} = 0.0182 T_w$ .

### 5.3.5.2 CRLBs for blocks of two MPCs

Here, we consider blocks of two MPCs.

The FIM  $J_{b_i}^{\alpha, \tau}$  corresponding to the block  $BK_i$  has the same structure as the FIM in Eq. 5.97. Accordingly, the CRLBs  $c_{L_b=2}^{\alpha^{(l)}}$  and  $c_{L_b=2}^{\tau^{(l)}}$ ,  $l = 1, 2$ , of  $\alpha^{(l)}$  and  $\tau^{(l)}$ , respectively, can be obtained by inverting  $J_{b_i}^{\alpha, \tau}$  then taking the corresponding diagonal elements. Using Eq. 5.91, Eq. 5.92 and Eq. 5.93 we obtain:

$$c_{L_b=2}^{\alpha^{(l)}} = \frac{1 - \left[ \hat{X}_{s\dot{s}}^{(2,1)} \right]^2 - \left[ \hat{R}_{\dot{s}}^{(2,1)} \right]^2}{\rho_t \Delta} \quad (5.101)$$

$$c_{L_b=2}^{\tau^{(l)}} = \frac{1 - \left[ \hat{X}_{s\dot{s}}^{(2,1)} \right]^2 - \left[ \hat{R}_{\dot{s}}^{(2,1)} \right]^2}{\rho_r^{(l)} \beta_s^2 \Delta} \quad (5.102)$$

where

$$\Delta = 1 - 2 \left[ \hat{X}_{s\dot{s}}^{(2,1)} \right]^2 - \left[ \hat{R}_{\dot{s}}^{(2,1)} \right]^2 - \left[ \hat{R}_{\dot{s}}^{(2,1)} \right]^2 + \left( \hat{R}_{\dot{s}}^{(2,1)} \hat{R}_{\dot{s}}^{(2,1)} + \left[ \hat{X}_{s\dot{s}}^{(2,1)} \right]^2 \right).$$

In Eq. 5.101 and Eq. 5.102, we can see that  $c_{L_b=2}^{\alpha^{(l)}}$  does not depend on any MPC gain whereas  $c_{L_b=2}^{\tau^{(l)}}$  only depends on the gain of  $\text{MPC}^{(l)}$ . This property is true with blocks of any size. Both  $c_{L_b=2}^{\alpha^{(l)}}$  and  $c_{L_b=2}^{\tau^{(l)}}$  depend on the transmitted signal and the inter-MPC delay  $\Delta\tau^{(2,1)}$ . Thanks to the symmetry in blocks of two MPCs, we have  $c_{L_b=2}^{\alpha^{(1)}} = c_{L_b=2}^{\alpha^{(2)}}$  regardless the values taken by  $\alpha^{(1)}$  and  $\alpha^{(2)}$ , whereas  $c_{L_b=2}^{\tau^{(1)}} = c_{L_b=2}^{\tau^{(2)}}$  only if  $\alpha^{(1)} = \alpha^{(2)}$ .

Notice that both  $c_{L_b=2}^{\alpha^{(l)}}$  and  $c_{L_b=2}^{\tau^{(l)}}$  approach infinity when  $\Delta\tau^{(2,1)}$  approaches zero. This just means that we are unable, due to the background noise, to distinguish between two neighboring MPCs when they are very close to each other. However, we are always able (if  $\text{MPC}^{(1)}$  and  $\text{MPC}^{(2)}$  are not destructive) to estimate  $\alpha^{(l)}$  and  $\tau^{(l)}$  with high accuracy by doing marginal estimation and treating  $\text{MPC}^{(1)}$  and  $\text{MPC}^{(2)}$  as one MPC. The optimal solution consists on choosing the joint estimation when it is more accurate and the marginal estimation when it is more accurate. Since the CRLBs of marginal estimation are not computed here, we assume that we are unable to distinguish between  $\text{MPC}^{(1)}$  and  $\text{MPC}^{(2)}$  when the CRLB  $c_{L_b=2}^{\tau^{(1)}}$  of the TOA of  $\text{MPC}^{(1)}$  is larger than the squared inter-MPC delay  $(\Delta\tau^{(2,1)})^2$ . Denote by  $\Delta\tau_{L_b=2}^{\min}$  the value of  $\Delta\tau^{(2,1)}$  for which, we have  $c_{L_b=2}^{\tau^{(1)}} = (\Delta\tau^{(2,1)})^2$ .

Given that Eq. 5.83 holds for  $\hat{R}_s(\tau)$ ,  $\hat{R}_{\dot{s}}(\tau)$  and  $\hat{X}_{s\dot{s}}(\tau)$  if it holds for  $p_{T_w}(t)$ , it seems more significant to evaluate  $c^{\alpha^{(l)}}$  and  $c^{\tau^{(l)}}$  with respect to  $\Delta\tau^{(2,1)}/T_w$  instead of  $\Delta\tau^{(2,1)}$ . In Fig. 5.14(a) we show  $\sigma_{L_b=1}^{\alpha^{(1)}}$  (the square root of the CRLB obtained in the case of blocks with one MPC) and  $\sigma_{L_b=2}^{\alpha^{(l)}}$  (the same for  $l = 1, 2$ ) with respect to  $\Delta\tau^{(2,1)}/T_w$ . We take  $\rho_t = 90\text{dB}$ . For  $\Delta\tau^{(2,1)} = 0.1T_w$ , we obtain  $\sigma_{L_b=2}^{\alpha^{(l)}} \approx 0.0027 \approx 85\sigma_{L_b=1}^{\alpha^{(1)}}$ .

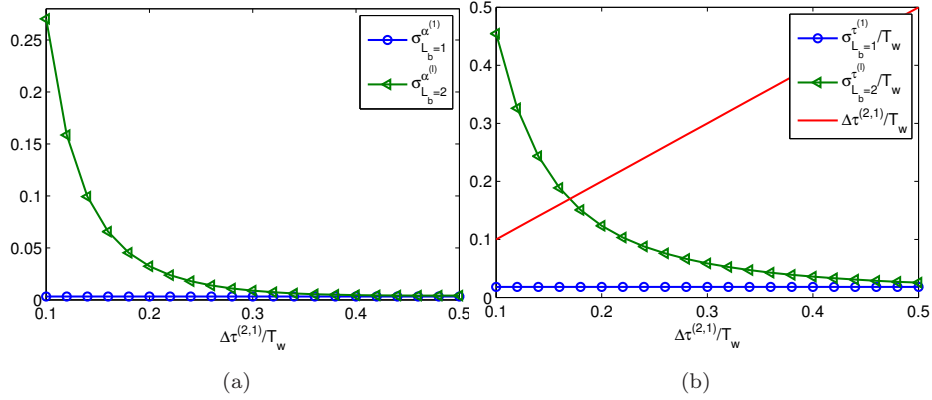


Fig. 5.14.: Block of two MPCs (a)  $\sigma_{L_b=1}^{\alpha^{(1)}}$  (one MPC per block) and  $\sigma_{L_b=2}^{\alpha^{(l)}}$  with respect to  $\Delta\tau^{(2,1)}/T_w$  (b)  $\sigma_{L_b=1}^{\tau^{(1)}}$  (one MPC per block),  $\sigma_{L_b=2}^{\tau^{(l)}}$  and  $\Delta\tau^{(2,1)}/T_w$  (first bisector) with respect to  $\Delta\tau^{(2,1)}/T_w$ .

In Fig. 5.14(b) we show  $\sigma_{L_b=1}^{\tau^{(1)}}$  (corresponding to the case of one MPC per block),  $\sigma_{L_b=2}^{\tau^{(l)}}$  (the same for  $l = 1, 2$  if we consider equal SNRs) and  $\Delta\tau^{(2,1)}/T_w$  (first bisector) with respect to  $\Delta\tau^{(2,1)}/T_w$ . We take  $\rho_r^{(l)} = 20\text{dB}$ . We can see that  $\sigma_{L_b=2}^{\tau^{(l)}}$  becomes larger than  $\Delta\tau^{(2,1)}$  for  $\Delta\tau^{(2,1)} < \Delta\tau_{L_b=2}^{\min} = 0.16T_w$ . Note that  $\Delta\tau_{L_b=2}^{\min}$  decreases as the SNR  $\rho_r^{(l)}$  increases. For  $\Delta\tau^{(2,1)} = 0.1T_w$ , we obtain  $\sigma_{L_b=2}^{\tau^{(l)}} \approx 0.45T_w \approx 25\sigma_{L_b=1}^{\tau^{(1)}}$ .

We can see from Fig. 5.14(a) and Fig. 5.14(b) that  $\sigma_{L_b=2}^{\alpha^{(l)}}$  becomes approximately equal to  $\sigma_{L_b=1}^{\alpha^{(1)}}$ , and  $\sigma_{L_b=2}^{\tau^{(l)}}$  approximately equal to  $\sigma_{L_b=1}^{\tau^{(1)}}$  for  $\Delta\tau^{(2,1)} = 0.5T_w$ .

### 5.3.5.3 CRLBs for blocks of three MPCs

Here, we consider blocks of three MPCs.

As  $c_{L_b=3}^{\alpha^{(l)}}$  and  $c_{L_b=3}^{\tau^{(l)}}$  do not have closed form in this case, we compute them numerically. Given the non-symmetry of blocks of more than two MPCs, the CRLBs of the parameters of the different MPCs are not equal even if the MPC gains are equal. For this reason, we only consider here the first MPC.

In Fig. 5.15(a) we show  $\sigma_{L_b=1}^{\alpha^{(1)}}$  (the case of one MPC per block) and  $\sigma_{L_b=3}^{\alpha^{(1)}}$  with respect to both  $\Delta\tau^{(2,1)}/T_w$  (normalized relative delay between MPC<sup>(1)</sup> and MPC<sup>(2)</sup>) and  $\Delta\tau^{(3,2)}/T_w$  (normalized relative delay between MPC<sup>(2)</sup> and MPC<sup>(3)</sup>). We can see that for  $\Delta\tau^{(2,1)} = \Delta\tau^{(3,2)} = 0.1T_w$ , we have  $\sigma_{L_b=3}^{\alpha^{(1)}} \approx 0.0072 \approx 226\sigma_{L_b=1}^{\alpha^{(1)}}$ .

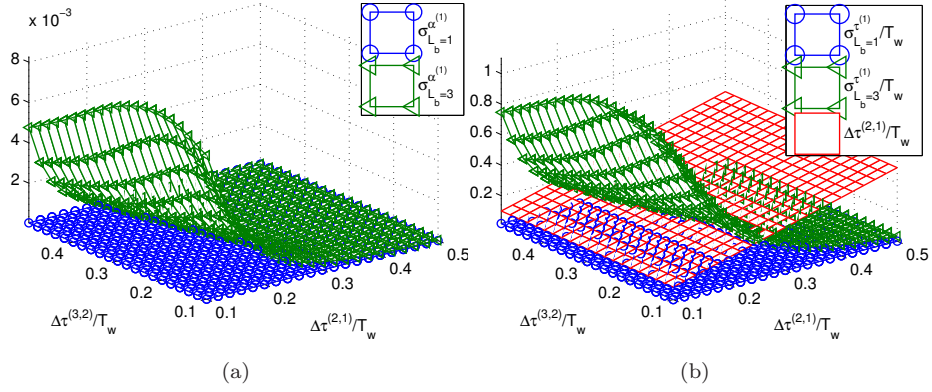


Fig. 5.15.: Block of three MPCs (a)  $\sigma_{L_b=1}^{\alpha^{(1)}}$  (one MPC per block) and  $\sigma_{L_b=3}^{\alpha^{(1)}}$  with respect to  $\Delta\tau^{(2,1)}/T_w$  and  $\Delta\tau^{(3,2)}/T_w$  (b)  $\sigma_{L_b=1}^{\tau^{(1)}}$  (one MPC per block),  $\sigma_{L_b=3}^{\tau^{(1)}}$  and  $\Delta\tau^{(2,1)}/T_w$  (bisector) with respect to  $\Delta\tau^{(2,1)}/T_w$  and  $\Delta\tau^{(3,2)}/T_w$ .

In Fig. 5.15(b) we show  $\sigma_{L_b=1}^{\tau^{(1)}}$  (the case of one MPC per block),  $\sigma_{L_b=3}^{\tau^{(1)}}$  and  $\Delta\tau^{(2,1)}/T_w$  (bisector) with respect to  $\Delta\tau^{(2,1)}/T_w$  and  $\Delta\tau^{(3,2)}/T_w$ . We can see that for  $\Delta\tau^{(2,1)}$  and  $\Delta\tau^{(3,2)}$  larger than  $\Delta\tau_{L_b=3}^{\min} = 0.24T_w$ ,  $\sigma_{L_b=3}^{\tau^{(1)}}$  becomes larger than  $\Delta\tau^{(2,1)}$ .

We can also see from Fig. 5.15(a) and Fig. 5.15(b) that  $\sigma_{L_b=3}^{\alpha^{(1)}}$  becomes close to  $\sigma_{L_b=1}^{\alpha^{(1)}}$ , and  $\sigma_{L_b=3}^{\tau^{(1)}}$  close to  $\sigma_{L_b=1}^{\tau^{(1)}}$ , for  $\Delta\tau^{(2,1)} = 0.5T_w$  even if  $\Delta\tau^{(3,2)} = 0.1T_w$ .

### 5.3.6 Average CRLBs

In this subsection we compute the averages of the square roots of the CRLBs of the gain and the TOA of the first MPC, when the square root of the CRLB of the TOA is smaller than the inter-MPC delay, in blocks of up to three MPCs. Since the considered average does not take account of all possible cases, we also compute the probability of the averaged cases.

The average of the square root of the CRLB of  $\theta \in \{\alpha^{(1)}, \tau^{(1)}\}$  is given by:

$$\langle \sigma^\theta \rangle = \frac{\sum_{i=1}^3 P_i \langle \sigma_i^\theta \rangle}{\sum_{i=1}^3 P_i} \quad (5.103)$$

where

$$\begin{aligned}
 P_1 &= P\{L_b = 1\} = 1 - P_{\Delta\tau}^{T_w} \\
 P_2 &= P\{(L_b = 2) \& (\Delta\tau^{(2,1)} > \Delta\tau_{L_b=2}^{\min})\} = (P_{\Delta\tau}^{T_w} - P_{\Delta\tau}^{\Delta\tau_{L_b=2}^{\min}})(1 - P_{\Delta\tau}^{T_w}) \\
 P_3 &= P\{(L_b = 3) \& (\Delta\tau^{(2,1)}, \Delta\tau^{(3,2)} > \Delta\tau_{L_b=3}^{\min})\} \\
 &= (P_{\Delta\tau}^{T_w} - P_{\Delta\tau}^{\Delta\tau_{L_b=3}^{\min}})^2(1 - P_{\Delta\tau}^{T_w})
 \end{aligned}$$

and

$$\langle \sigma_{L_b=1}^\theta \rangle = \sigma_{L_b=1}^\theta \quad (5.104)$$

$$\langle \sigma_{L_b=2}^\theta \rangle = \frac{\int_{\Delta\tau_{L_b=2}^{\min}}^{T_w} \sigma_{L_b=2}^\theta T_{\Delta\tau}^{t_1} dt_1}{\int_{\Delta\tau_{L_b=2}^{\min}}^{T_w} T_{\Delta\tau}^{t_1} dt_1} \quad (5.105)$$

$$\langle \sigma_{L_b=3}^\theta \rangle = \frac{\int_{\Delta\tau_{L_b=3}^{\min}}^{T_w} \int_{\Delta\tau_{L_b=3}^{\min}}^{T_w} \sigma_{L_b=3}^\theta T_{\Delta\tau}^{t_1} T_{\Delta\tau}^{t_2} dt_1 dt_2}{\int_{\Delta\tau_{L_b=3}^{\min}}^{T_w} \int_{\Delta\tau_{L_b=3}^{\min}}^{T_w} T_{\Delta\tau}^{t_1} T_{\Delta\tau}^{t_2} dt_1 dt_2}. \quad (5.106)$$

with  $t_1 = \Delta\tau^{(2,1)}$ ,  $t_2 = \Delta\tau^{(3,2)}$ , and  $T_{\Delta\tau}^t$  the PDF given in Eq. 5.85. Note that  $\sigma_{L_b=2}^\theta$  and  $\sigma_{L_b=3}^\theta$  are functions of  $t_1$  and  $(t_1, t_2)$  respectively.

We can easily show that the average of all possible cases approaches infinity. This does not mean that we are not able to estimate the MPC parameters with good accuracy. It just says that we can not distinguish between neighboring MPCs when they are very close to each other. The probability of the cases averaged in Eq. 5.103 is given by:

$$P = P_1 + P_2 + P_3.$$

In Fig. 5.16(a), we show the square root bound of  $\alpha^{(1)}$  in blocks of one MPC  $\sigma_{L_b=1}^{\alpha^{(1)}}$ , the average square root bounds in blocks of two and three MPCs  $\langle \sigma_{L_b=l_b}^{\alpha^{(1)}} \rangle$ ,  $l_b = 2, 3$ , and the average square root bound in blocks of up to three MPCs  $\langle \sigma^{\alpha^{(1)}} \rangle$  with respect to the transmit SNR  $\rho_t$ . We consider a doublet of  $T_w = 0.13$  ns, and office LOS environments, so the pulse width to average-rate-of-arrival ratio is equal to  $\lambda T_w = 0.3824$ .

In Fig. 5.16(b), we show the square root bound of  $\tau^{(1)}$  in blocks of one MPC  $\sigma_{L_b=1}^{\tau^{(1)}}$ / $T_w$ , the average square root bound in blocks of two and three MPCs  $\langle \sigma_{L_b=l_b}^{\tau^{(1)}} \rangle$ / $T_w$ ,  $l_b = 2, 3$ , the average square root bound in blocks of up to three MPCs  $\langle c^{\tau^{(1)}} \rangle$ / $T_w$  and the minimum inter-MPC delay  $\Delta\tau_{L_b=l_b}^{\min}$ / $T_w$ , all with respect to the SNR of the first MPC  $\rho_r^{(1)}$ .

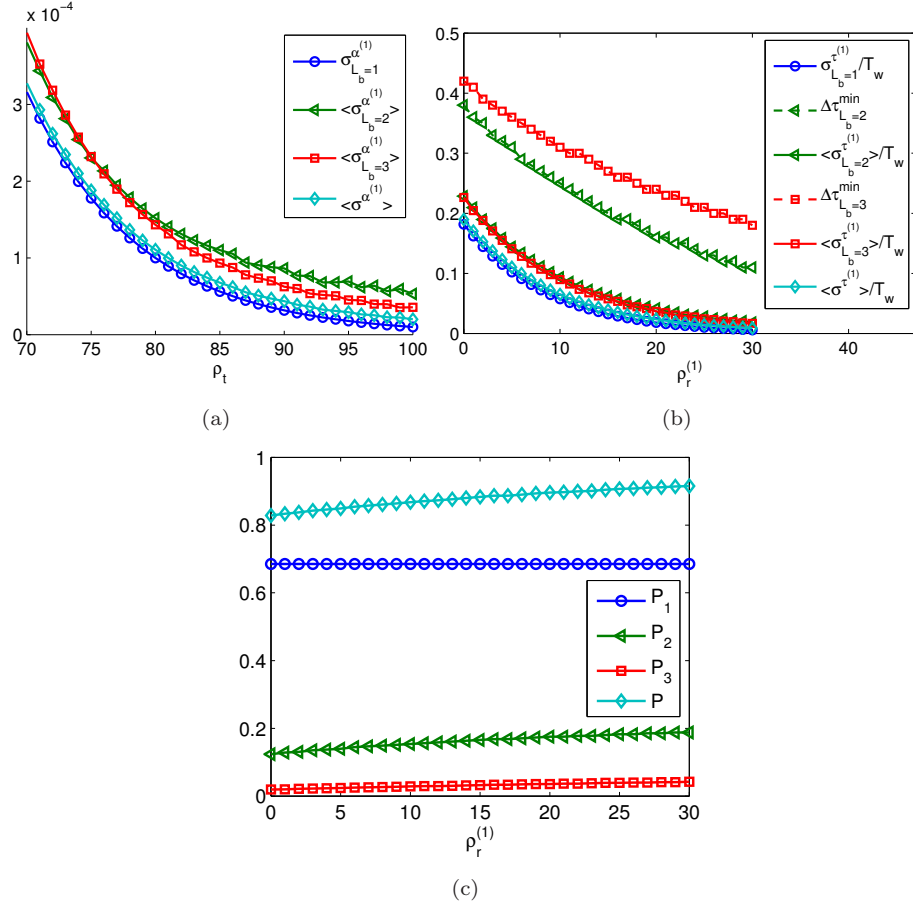


Fig. 5.16.: (a)  $\sigma_{L_b=1}^{\alpha(1)}$  (one MPC per block),  $\langle \sigma_{L_b=l_b}^{\alpha(1)} \rangle$  for  $l_b = 2, 3$  (average bounds), and  $\langle \sigma^{\alpha(1)} \rangle$  (average bound) with respect to the transmit SNR  $\rho_t$  (b)  $\sigma_{L_b=1}^{\tau(1)}/T_w$  (one MPC per block),  $\langle \sigma_{L_b=l_b}^{\tau(1)} \rangle/T_w$  for  $l_b = 2, 3$  (average bounds),  $\langle \sigma^{\tau(1)} \rangle/T_w$  (average bound), and  $\Delta\tau_{L_b=l_b}^{\min}/T_w$  (minimum inter-MPC delay) with respect to the SNR of the first MPC  $\rho_r^{(1)}$  (c) Probabilities to have one  $P_1$ , two  $P_2$ , three  $P_3$ , and up to three  $P$  MPCs per block, with respect to  $\rho_r^{(1)}$ .

In Fig. 5.16(c) we show the probabilities to have blocks with one MPC  $P_1$ , two MPCs  $P_2$ , three MPCs  $P_3$ , and up to three MPCs  $P$ , with respect to the SNR of the first MPC  $\rho_r^{(1)}$ .

We can see that the average bounds for both gain and TOA estimation are very close to the bounds obtained under the non-overlapping assumption (which are the smallest reachable bounds). We can also see that the probability of the averaged cases is greater than 0.8 (resp. 0.9) for  $\rho_r^{(1)} = 0$  dB (resp.  $\rho_r^{(1)} \geq 23$  dB). This means that, in the case where the CRLBs can be achieved (i.e. in the asymptotic region), good accuracy can be often achieved by joint estimation in the considered environments. Note that by performing marginal estimation when the neighboring MPCs are very close to each other, and joint estimation when they are sufficiently far, we can then average all the possible cases to obtain small bounds instead of infinite bounds.

## 5.4 CONCLUSION

In this chapter we have considered the derivation of performance limits for parameter estimation for positioning in WB and UWB systems, assuming AWGN and MP channels.

We have considered UWB-based positioning using the AOA-based method and the hybrid TOA-AOA based method. For both methods, we have derived the CRLBs for position estimation. We have first derived the CRLBs for the joint estimation of the direct path TOA and AOA, assuming an UWB MP channel. We have shown, that under the non-overlapping assumption, the estimation is not impacted by the MP aspect of the channel. We have compared the exact AOA CRLB and the approximated one obtained by assuming a narrowband signal. The analytical results obtained for the CRLBs have been illustrated by numerical results for some typical scenarios.

We have derived the CRLBs for the joint estimation of the TOA and the AOA in WB MISO and MIMO systems. For TOA estimation, SIMO and MIMO are equivalent, and MISO and SISO as well when the transmitted signals are orthogonal. For non-orthogonal signals, MIMO is better than SIMO, and MISO is better than SISO when the received signals are constructive. For AOA estimation, MIMO is better than SIMO, and SIMO is better than MISO when the transmitted signals are orthogonal. For non-orthogonal signals, MIMO is much better when the received signals are constructive. However, the CRLBs obtained in MISO and MIMO systems when the transmitted signals are not orthogonal are very sensitive to the angle. As AWGN channels have been assumed, the CRLBs for the joint estimation of the TOA and the AOA should be investigated in realistic MIMO configurations where MP fading channels are considered.

We have considered parameter estimation in UWB MP channels. We have studied the impact of the overlapping of the MPCs on the joint MPC gain and

TOA estimation. Instead of considering the estimation of the total channel impulse response, we can split the received signal into non-overlapping blocks of overlapping MPCs, then estimate the parameters of these blocks separately. We have considered the IEEE802.15.3a and IEEE802.15.4a UWB channel models. For sufficiently small pulse width to average-rate-of-arrival ratio, the probability to have more than three MPCs per block is relatively small. Accordingly, we have computed the CRLBs for the joint MPC gain and TOA estimation in blocks of up to three overlapping MPCs. Based on the obtained results we have computed the average CRLBs. It appears that the CRLBs obtained by averaging more than 80% of possible cases are very close to the CRLBs obtained under the non-overlapping assumption.

## CHAPTER 6

---

# TESTBED FOR IR-UWB BASED RANGING AND POSITIONING: EXPERIMENTAL AND THEORETICAL PERFORMANCES

---

TESTING the algorithms and estimators proposed in the literature on measurement data is a fundamental step in the development of positioning systems.

IR-UWB based positioning faces many challenges including multipath conditions where the detection of the first MPC which is not always the strongest one becomes a hard problem especially at low SNRs. Many TOA estimators has been proposed for dense multipath channels. In [22], the authors have studied the threshold and energy based estimators and evaluated their performances. They have also obtained some results based on experimental measurements in an indoor residential environment. In [33], the authors have considered a threshold-based estimator and some suboptimal estimators based on peak detection and tested them on data collected in a typical office building.

In this chapter we describe a testbed for IR-UWB based ranging and positioning. The testbed is realized at UCL. It consists of a FPGA with high speed serial module used as pulse generator, four UWB antennas, and either a sampling oscilloscope or realtime oscilloscope used as receiver. Two setups have been considered, one for ranging with one transmit antenna and one receive antenna, and another one for positioning with one transmit antenna and three receive antennas. The results presented in this chapter are based on the work published in [96, 128].

In order to estimate the distances and the position we first estimate the TOA by either using the MLE, or a threshold-based estimator. Based on the collected data, we compute the variances for range and position estimation and compare them to the corresponding CRLBs. We discuss the impact of the shape of the autocorrelation of the transmitted pulse, and that of the multipath aspect of the channel on the estimation accuracy.

When the TOA is estimated using the MLE, the variances for ranging and positioning are very close to the corresponding CRLBs if the first MPC is the strongest one, and if the mainlobe of the autocorrelation of the received pulse is stronger than the sidelobes. However, when a given MPC is stronger than the first one due to the channel, or when a given sidelobe is stronger than the mainlobe due to the additive noise and/or the channel fading, the estimation performances deteriorate drastically. In fact, a false MPC (resp. sidelobe) detection easily leads to an error of 60 cm (resp. 21 cm) in ranging and 14 cm (resp. 7 cm) in positioning.

By estimating the TOA using a threshold-based estimator, we can detect the first MPC even if it is not the strongest one, so the estimation errors due to false MPC detection can be removed. However, the errors due to sidelobe detection cannot be removed using threshold-based estimators. We will also see from experimental results that, even in the presence of errors due to false MPC detection, the positioning accuracy can be improved by increasing the number of receivers.

In Sec. 6.1 we describe the TH-IR-UWB generator. In Sec. 6.2 we describe the realized testbed. In Sec. 6.3 we present the characteristics of the generated, transmitted and received signals. In Sec. 6.4 we describe the channel model adopted in this work and the considered TOA estimator. We show and discuss the results obtained for ranging in Sec. 6.5 and those obtained for positioning in Sec. 6.6.

## 6.1 TH-IR-UWB GENERATOR

Many UWB pulse generators have been proposed in the literature. It will suffice to mention the step recovery diode pulse generators [129–132], the tunnel diode pulsers [8], the emitter coupled logic [8], the Scholtz’s monocycle generator [133], the programmable Complementary metal-oxide semiconductor (CMOS) pulse generator [134], and the voltage controlled ring oscillator (VCRO) based generator [135, 136].

The main goal of the research activities in this field is to design integrated low-consumption generators, that respect the emission masks, and that can be integrated in future UWB transceivers. However, our objective in this work is restricted to design a multiuser TH-IR-UWB generator for experimentation purposes.



Fig. 6.1.: Xilinx ML505 development board.

The proposed generator is based on a FPGA with high-speed serial module. The main issues considered in this work are the generation of monopulses (i.e. pulses of one positive lobe), the generation of shaped pulses (i.e. oscillating pulses), and the generation of TH-IR-UWB waveforms for single-user and for multiuser.

In Sec. 6.1.1 we will describe the monopulse generator and the TH-IR-UWB generator for single-user. In Sec. 6.1.2 we will describe the multi-user TH-IR-UWB generator. In Sec. 6.1.3 we will describe the methods proposed to obtain shaped pulses from the unshaped generated monopulses.

### 6.1.1 Monopulse and single-user TH-IR-UWB generation

We will describe here how an FPGA with a high-speed serial module can serve as a monopulse generator and a TH-IR-UWB generator.

In our experimentations we have considered the following three Xilinx development boards, each of them containing an FPGA and a high-speed serial module:

1. The ML505 board (see Fig. 6.1) based on the Virtex 5XC5VLX50T FPGA and a single-channel GTP RocketIo serial module of maximum line rate of  $R_b = 3.75$  Gb/s.
2. The ML507 board based on the Virtex XC5VFX70T FPGA and a single-channel GTX RocketIo serial module of maximum line rate of  $R_b = 6.5$  Gb/s.
3. The ML523 board based on the Virtex XC5VFXT100 FPGA and 16 channels GTX RocketIo serial module of maximum line rate of  $R_b = 6.5$  Gb/s.

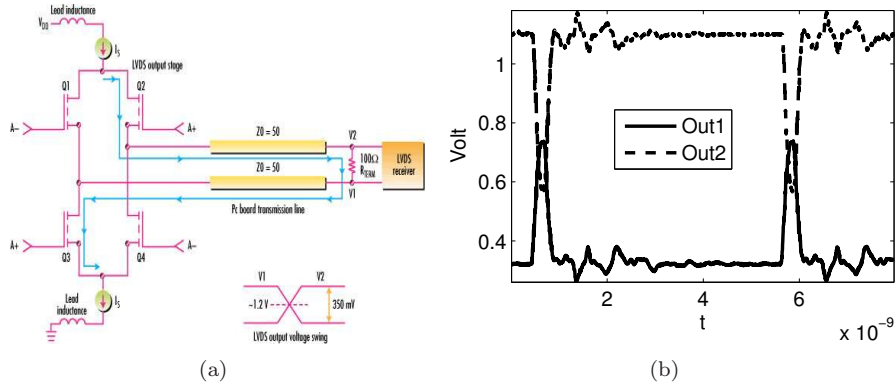


Fig. 6.2.: (a) LVDS driver with two complementary outputs (Out 1 and Out 2) (b) The TH-IR-UWB waveforms observed at Out 1 and Out 2 for the pattern “00000000000000000001”.

In order to generate our monopulse we use the Xilinx’s Integrated bit error ratio tester (IBERT) application which allows the serial module to send periodically a pattern of  $N_b = 20$  bits ( $N_b$  is the number of bits per pattern) at the rate  $R_b = 1/T_b$  ( $T_b$  is the duration of one bit). By setting 19 bits to “0” and one bit to “1” we obtain a periodic monopulse with pulse width of  $T_w \approx 1/R_b$  and repetition period of  $T_r = 20T_b$ .

On the electronic level, the predefined patterns are sent using a low voltage differential signaling (LVDS) driver (see Fig. 6.2(a)), containing two complementary outputs (Out 1 and Out 2) accessible on SubMiniature version A (SMA) connectors.

By increasing the rate  $R_b$  of the serial module, we decrease the pulse duration until it reaches a given threshold determined by the present low-pass filtering effects. In the latter case, the pulse width is no longer equal to the bit duration (i.e.  $T_w > T_b$ ). The repetition period is always given by  $T_r = N_b T_b$ .

The main drawback of the IBERT application is its very short pattern of  $N_b = 20$  bits. Assume for example that a given repetition period is required to guarantee that the last MPC (due to the multipath channel where the measurement campaign will be carried out) corresponding to a given transmitted pulse, is received before sending the next pulse. Then, to increase the repetition period  $T_r = 20T_b$  we have to decrease the rate  $R_b$ , which makes the generated pulses wider.

To solve this problem we have used another application which allows us to define, in the memory of the FPGA, patterns with the required lengths. By using this application, the pulse duration  $T_w$  can be chosen by tuning the rate  $R_b$  of

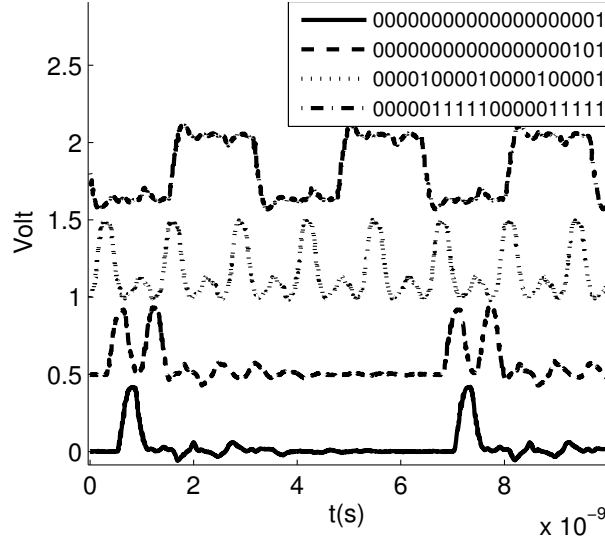


Fig. 6.3.: TH-IR-UWB waveforms corresponding to different patterns.

the serial module, and the repetition period  $T_r$  by varying the length  $N_b$  of the predefined pattern.

The generated signal can be written as:

$$s(t) = \sum_{i=0}^{\infty} w(t - iN_bT_b) = \sum_{i=0}^{\infty} \sum_{j=0}^{N_b-1} a_j p_g(t - iN_bT_b - jT_b)$$

where  $p_g(t)$  denotes the generated monopulse,  $w(t)$  the TH-IR-UWB waveform corresponding to the defined pattern,  $N_b$  the length of the pattern, and  $a_j$  the value of the  $j$ th bit in the pattern. By setting  $a_j$  to either “0” or “1” we obtain the wanted waveform.

In Fig. 6.2(b) we show the TH-IR-UWB waveforms obtained at the complementary outputs Out 1 and Out 2 of the LVDS driver (see Fig. 6.2(a)), for the pattern “00000000000000000001”, at the rate  $R_b = 3.75$  GHz, using the board ML505.

In Fig. 6.3 we show the TH-IR-UWB waveforms corresponding to the following patterns: “00000000000000000001”, “100000000000000000101”, “00001000010000100001” and “00000111110000011111”.

### 6.1.2 Multiuser TH-IR-UWB waveforms generation

In Sec. 6.1.1 we have described how TH-IR-UWB waveforms for single-user can be generated by setting the bits of the available pattern to either “0” or “1”.

Here we will describe the methods proposed to generate multiuser TH-IR-UWB waveforms.

TH is a particular type of multiple-access techniques. The  $k$ th user TH waveform can be written as ( $k = 1, \dots, K$ ):

$$w^{(k)}(t) = \sum_{n=0}^{N_c-1} p_g(t - nT_c - c_n^{(k)}T_h) \quad (6.1)$$

where  $T_c$  denotes the chip period,  $N_c$  the number of chips per waveform ( $N_c$  is also the length of the TH code),  $T_h = \frac{T_c}{N_h}$  the time-hop equal to the bit duration  $T_b$ , and  $(c_0^{(k)}, \dots, c_{N_c-1}^{(k)})$ ,  $c_n^{(k)} \in \{0, \dots, N_h - 1\}$  the code of the  $k$ th user.

In order to generate multiuser TH-IR-UWB waveforms, both single-channel (e.g. ML505 and ML507) and multi-channel (e.g. ML523) boards can be used.

With multi-channel boards, multiuser waveforms can be generated by assigning a channel to each user, then defining for each channel its own pattern. The TH-IR-UWB waveforms in Eq. 6.1 are obtained by considering patterns of  $N_b = N_c N_h$  bits, then setting the bits of number  $nN_h + c_n^{(k)} + 1$ , ( $n = 0, \dots, N_c - 1$ ) to “1” and the remaining bits to “0”. For  $N_c = 3$ ,  $N_h = 4$  and  $K = 2$  ( $K$  denotes the number of users), the codes  $c^{(1)} = (0, 0, 1)$  and  $c^{(2)} = (1, 3, 1)$  are obtained by the patterns  $p^{(1)} = 100010000100$  and  $p^{(2)} = 010000010100$  respectively. The main advantage of this approach is its simple implementation. However, its main two drawbacks are that:

- The number of users is limited to the number of available channels.
- Multi-channel boards are more expensive than single-channel boards.

In Fig. 6.4 we show the normalized TH-IR-UWB waveforms corresponding to the codes  $c^{(1)}$  and  $c^{(2)}$ . Note that we have successfully generated multiuser TH-IR-UWB waveforms using the ML523 board. However, the waveforms shown in Fig. 6.4 are obtained by simulation.

With single-channel boards, multi-user waveforms can be generated by defining one pattern of  $N_b = KN_c N_h$  bits obtained by concatenating the patterns of the different users. For the same example considered above, the pattern to define is  $p^{(1,2)} = p^{(1)}|p^{(2)} = 100010000100010000010100$ . Now, to separate the waveforms corresponding to the different users from each others, we have to demultiplex the output of our single-channel at the frequency  $\frac{1}{N_b} = \frac{1}{N_c N_h}$ . The demultiplexer can easily be fabricated from low-cost switches. For  $2^l$  users, we need  $1 + 2 + 4 + \dots + 2^{l-1} = 2^l - 1$  switches. The major drawback of this approach is that the waveforms at the output of the demultiplexer are  $K$  times longer than the required waveform length. In contrast, the main advantage is that there is no limitation regarding the total number of users.

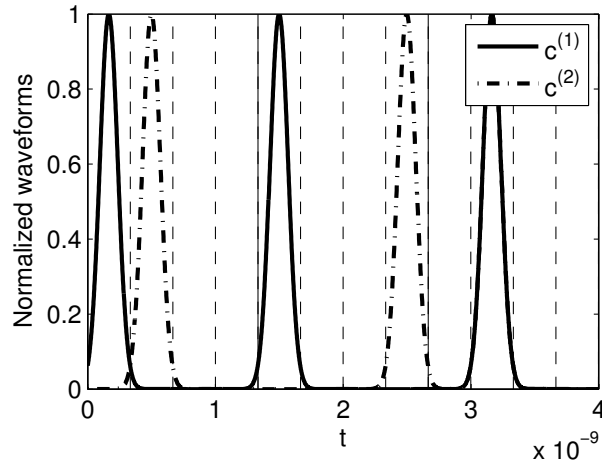


Fig. 6.4.: TH-IR-UWB waveforms corresponding to the TH codes  $c^{(1)} = (0, 0, 1)$  and  $c^{(2)} = (1, 3, 1)$ .

### 6.1.3 Pulse shaping

In Sec. 6.1.1 and Sec. 6.1.2 the generated waveforms are based on monopulses (i.e. pulses of one lobe, we also call them unshaped pulses). As the spectra of such pulses fall around the DC frequency, the generated monopulses should be shaped in order to make their spectra falling in higher frequency bands.

In order to obtain pure IR-UWB waveforms, we have considered two shaping methods, the antenna based shaping method and the complementary-output based shaping method, both without modulating by a carrier. In Sec. 6.1.3.1 we present the antenna-based shaping method, and in Sec. 6.1.3.2 the complementary-output based shaping method.

#### 6.1.3.1 Antenna based shaping

We describe here the shaping method based on the use of the transmit antenna.

This method simply consists on sending the generated monopulse directly to the transmit antenna. Therefore, the received pulse is shaped by both the transmit and the receive antennas.

In Fig. 6.5(a), we show the normalized monopulse  $p(t)$  generated by the board ML523 at the rate  $R_b = 6.5$  Gb/s, the normalized received pulse  $p_1(t)$  shaped by an UWB antenna having the same shape as the antenna (called Antenna 1) described in [137] and shown in Fig. 6.6(a), but 4 times smaller, and the normalized received pulse  $p_2(t)$  shaped by a 2.4 GHz dipole antenna (called Antenna 2). The widths of  $p(t)$ ,  $p_1(t)$  and  $p_2(t)$  are equal to  $T_w = 368$  ps,  $T_{w,1} = 1.2$  ns and  $T_{w,2} = 3.6$  ns, respectively.

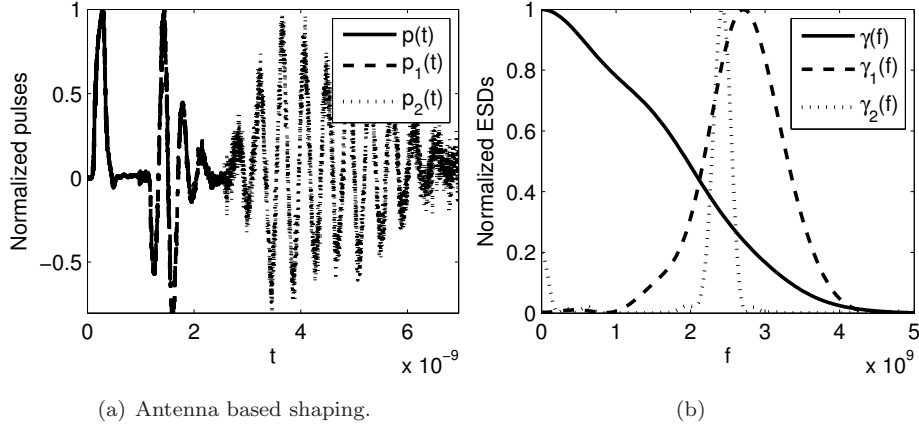


Fig. 6.5.: (a) Normalized monopulse  $p(t)$ , and normalized pulses  $p_1(t)$  and  $p_2(t)$  shaped by Antenna 1 and Antenna 2 (b) Normalized ESDs  $\gamma(f)$ ,  $\gamma_1(f)$  and  $\gamma_2(f)$  of  $p(t)$ ,  $p_1(t)$  and  $p_2(t)$ .

In Fig. 6.5(b), we show the normalized energy spectral densities (ESDs)  $\gamma(f)$ ,  $\gamma_1(f)$  and  $\gamma_2(f)$  corresponding to  $p(t)$ ,  $p_1(t)$  and  $p_2(t)$  respectively. The bandwidth at -10 dB of  $p(t)$  is equal to  $B = 2f_h = 6.7$  GHz ( $f_h$  denotes the highest frequency). The bandwidths and central frequencies corresponding to  $p_1(t)$  and  $p_2(t)$  are equal to  $(f_{c,1}, B_1) = (2.67, 2.35)$  GHz and  $(f_{c,2}, B_2) = (2.41, 0.48)$  GHz, respectively.

The energy  $E_g$  of the generated monopulse is measured by connecting Out 1 directly to the oscilloscope (Out 2 is connected to the transmit antenna); we can write  $E_g = \int_{-\infty}^{+\infty} \frac{p_g^2(t)}{R} dt = 0.36$  pJ where  $p_g(t)$  denotes the voltage signal observed by the oscilloscope and  $R = 50 \Omega$  the impedance of the oscilloscope. The received energy  $E_r$  is measured by connecting the receive antenna to the oscilloscope; we can write  $E_r = \int_{-\infty}^{+\infty} \frac{p_r^2(t)}{R} dt$  where  $p_r(t)$  denotes the signal observed by the oscilloscope. Denote by  $P_r(f)$  the Fourier transform of  $p_r(t)$ , and  $\gamma_t^e(f)$  and  $\gamma_r^e(f) = \frac{|P_r(f)|^2}{R}$  the transmitted and received ESDs respectively. The transmitted energy is given by:

$$E_t = \int_{-\infty}^{+\infty} \gamma_t^e(f) df \quad (6.2)$$

Using the Friis transmission formula, we can write:

$$\gamma_t^e(f) = \frac{\gamma_r^e(f)}{\nu(f)} \quad (6.3)$$

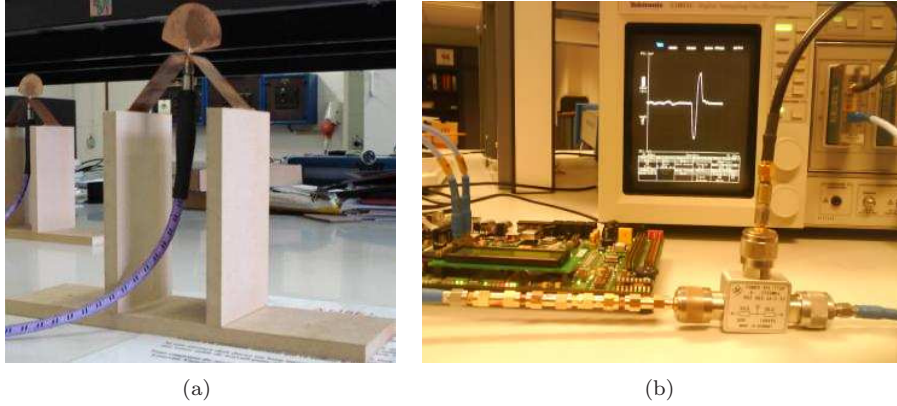


Fig. 6.6.: (a) UWB antenna (b) ML507 board with two complementary outputs, chain of connectors used to introduce delay, power combiner, and sampling oscilloscope visualizing the shaped pulse.

where

$$\nu(f) = G_t G_r \frac{1}{4\pi d^2} \frac{c^2}{4\pi f^2} = G_t G_r \left( \frac{c}{4\pi d f} \right)^2 \quad (6.4)$$

with  $G_t$  and  $G_r$  representing the gains (approximately constant in the considered frequency bands) of the transmit and receive antennas respectively (non-isotropic antennas),  $d$  the distance between transmit and receive antennas (we have considered  $d = 30$  cm),  $\frac{1}{4\pi d^2}$  the loss due to free-space propagation, and  $\frac{c^2}{4\pi f^2}$  the aperture of the receive antenna around the frequency  $f$ .

By computing  $E_t$  and dividing it by  $E_g$  we have found that 1/4 and 1/30 of the generated energy is radiated by Antenna 1 and Antenna 2 respectively (i.e. 3/4 and 29/30 dissipated). For the antenna described in [137], shown in Fig. 6.6(a) and used later in Sec. 6.2 we have found that 1/13 of the energy is radiated. Note that for the antenna in [137] we have  $G_t = G_r = 2.15$  dB whereas for Antenna 1 and Antenna 2 we have assumed that the antennas are isotropic (i.e.  $G_t = G_r = 0$  dB) because we do not know their specifications (this means that the values of corresponding radiated energies are lower than the obtained ones).

The main weaknesses of antenna based shaping lie in the fact that:

- Most generated energy is dissipated in the transmit antenna, and only a small portion is radiated.
- The bandwidth of the shaped pulse is much smaller than that of the unshaped one.

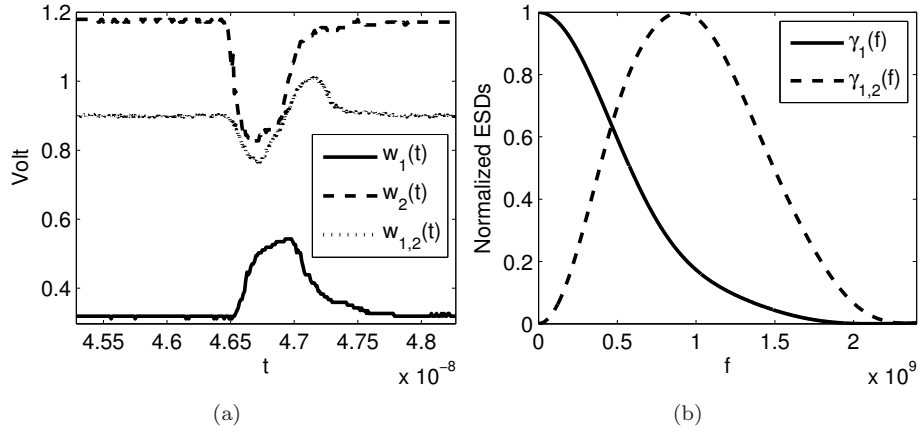


Fig. 6.7.: (a) Complementary monopulses  $w_1(t)$  and  $w_2(t)$  and shaped pulse  $w_{1,2}(t)$  (b) Normalized ESDs  $\gamma_1(f)$ ,  $\gamma_{1,2}(f)$  of  $w_1(t)$  and  $w_{1,2}(t)$ .

- The required transmission frequency band (i.e. that of the shaped pulse) should totally fall in the frequency band of the generated pulse. This also means that the monopulse should be highly short.

### 6.1.3.2 Complementary-output based shaping

We describe here the shaping method based on the use of the complementary outputs of the LVDS driver.

As pointed out in Sec. 6.1.1, we have two complementary outputs per channel thanks to the LVDS driver (see Fig. 6.2(a) and Fig. 6.2(b)). The second shaping method consists on exploiting these outputs in the shaping procedure. To do so, we apply a time delay approximately equal to the monopulse width to one of the two outputs, then add both outputs.

To validate our idea, we have used a chain of connectors to introduce the necessary delay and the R&S RVZ 0-2700 MHz power splitter (and combiner) to add the two outputs. In Fig. 6.6(b), we can see the ML507 board used to generate the monopulse with the two complementary outputs, the chain of connectors, the combiner and the shaped pulse on the oscilloscope.

In Fig. 6.7(a) we show the complementary generated monopulses  $w_1(t)$  and  $w_2(t)$ , and their sum  $w_{1,2}(t)$  after shifting  $w_1(t)$ . In Fig. 6.7(b) we show the normalized ESDs  $\gamma_1(f)$  and  $\gamma_{1,2}(f)$  corresponding to  $w_1(t)$  and  $w_{1,2}(t)$  respectively. The unshaped pulse (generated using the ML507 board at the rate  $R_b = 3$  Gb/s) has a width of  $T_w = 600$  ps and a bandwidth of  $B = 2.44$  GHz, whereas the shaped pulse has a width of  $T_w = 950$  ps, a central frequency of  $f_c = 1.45$  GHz, and a bandwidth of  $B = 1.79$  GHz. The energy loss due to the power combiner is equal to 4.5 dB.

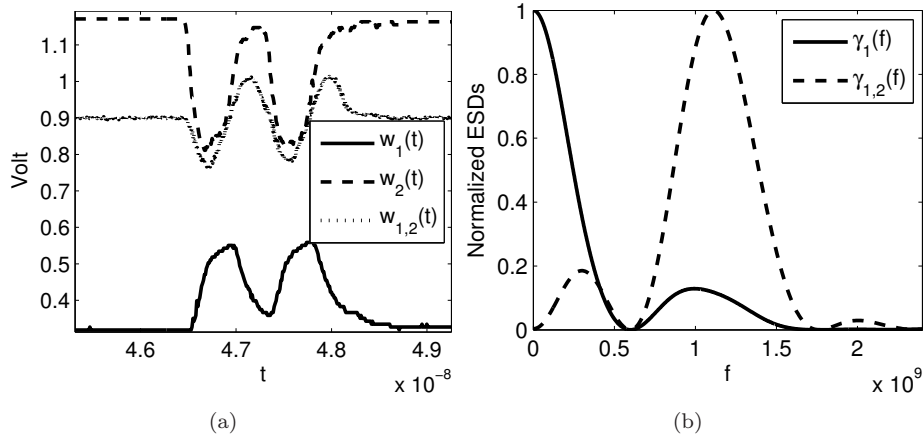


Fig. 6.8.: (a) Complementary waveforms  $w_1(t)$  (two consecutive monopulses) and  $w_2(t)$  and shaped waveform  $w_{1,2}(t)$  (b) Normalized ESDs  $\gamma_1(f)$ ,  $\gamma_{1,2}(f)$  of  $w_1(t)$  and  $w_{1,2}(t)$ .

In Fig. 6.8(a) we show the complementary generated waveforms  $w_1(t)$  and  $w_2(t)$  when two consecutive monopulses have been generated, and the shaped waveform  $w_{1,2}(t)$ . In Fig. 6.8(b) we show the normalized ESDs corresponding to  $w_1(t)$  and  $w_{1,2}(t)$ .

The main advantage of this shaping method is that the energy loss is relatively small because it is only due to the component introducing the delay and to the combiner. However, like the antenna based shaping method, the required transmission frequency band should totally fall in the frequency band of the generated pulse.

## 6.2 THE TESTBED

In this section we describe the testbed realized at UCL in order to perform ranging and positioning based on IR-UWB signals.

We have already mentioned that the testbed is composed of a FPGA with high speed serial module as IR-UWB pulse generator, four UWB antennas, one (Tx) for transmission and three (Rx $i$ ,  $i = 1, 2, 3$  for reception, and an oscilloscope used as receiver.

The IR-UWB pulse generator has been considered in detail in Sec. 6.1. In the measurement campaigns presented in this chapter, we have used the Xilinx single-channel ML507 development board as pulse generator. Now, instead of combining the two outputs Out 1 and Out 2 together to obtain a shaped pulse, we

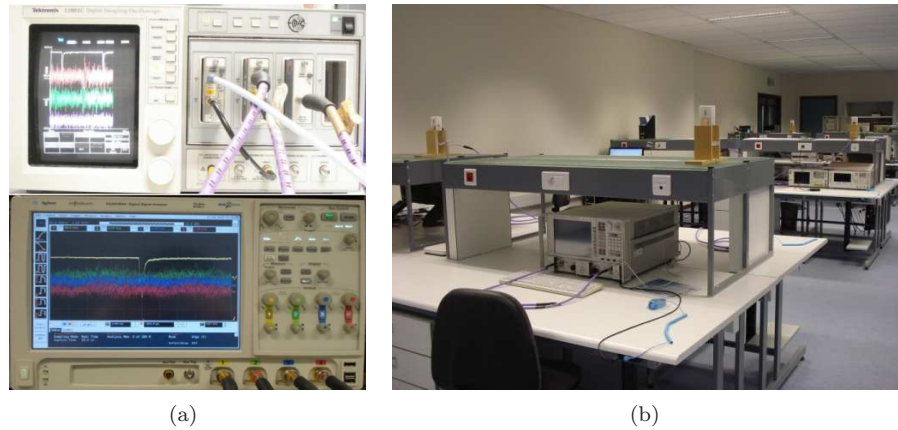


Fig. 6.9.: (a) Tektronix (top) and Agilent (bottom) oscilloscopes (b) Characterization room.

have connected Out 1 to the transmit antenna Tx, and Out 2 to the oscilloscope in order to be used as a reference for TOA estimation.

The RocketIo output Out 1 is matched to  $50 \Omega$  impedance such that it can be connected to Tx. The UWB antennas ( $3 \times 10 \times 8 \text{ cm}^3$ , see Fig. 6.6(a)) are designed and fabricated at UCL [137].

Either the Tektronix 11801C digital sampling oscilloscope, or the Agilent DSA91304A Digital Signal Analyzer, have been used in the carried out measurement campaigns. The Tektronix 11801C Digital Sampling Oscilloscope shown in Fig. 6.9(a) (the one on the top) has a bandwidth from DC to 50 GHz and a sampling interval equal to 0.01 ps. It contains 4 heads with up to 2 channels per head. The Agilent DSA91304A Digital Signal Analyzer shown in Fig. 6.9(a) (the one on the bottom) has a bandwidth of 13 GHz and a sampling frequency of 40 GS/s. It contains 4 channels.

Gore phaseflex cables [138] of 4 and 8 meters are used to connect the FPGA to the transmit antenna and the oscilloscope, and the receive antennas to the oscilloscope. An amplifier is also used to compensate the losses in the cables.

Two setups have been considered: one for ranging and one for positioning. In the first setup, we have used one transmit antenna and one receive antenna, whereas in the second setup, we have used one transmit antenna and three receive antennas. For both setups, the measurement phase is preceded by a phase of calibration. The main roles of the phase of calibration are:

- Finding the characteristics of the generated, transmitted and received pulses.

- Estimating the noise corrupting the acquisition.
- Estimating the delays introduced by the cables.

The measurement campaigns are carried out in a wide characterization room ( $33 \times 9 \times 2.8 \text{ m}^3$ ) containing many tables with many electronics equipments (see Fig. 6.9(b)).

### 6.3 SIGNALS CHARACTERISTICS

In this section we present the characteristics of the generated, transmitted and received signals.

Denote by  $p_g(t)$  the generated pulse,  $p_{gc}(t)$  the clean generated pulse obtained by bandpass filtering  $p_g(t)$  between 0.2 and 2 GHz then keeping the main lobe of the filtered pulse,  $p_r(t)$  the received pulse, and  $p_{rc}(t)$  the clean received pulse obtained by bandpass filtering  $p_r(t)$  between 0.5 and 2 GHz then keeping five main lobes of the filtered pulse. The generated  $p_g(t)$  and clean generated  $p_{gc}(t)$  pulses are shown in Fig. 6.10(a), and the received  $p_r(t)$  and clean received  $p_{rc}(t)$  pulses in Fig. 6.10(b). Note that we have defined the clean generated and received pulses in order to remove the ringing present at the output of the FPGA, and to obtain smooth spectra that can be used below in the computation of the frequency response of the antenna. Note that we have defined the clean generated and received pulses in order to remove the ringing present at the output of the FPGA, and to obtain smooth spectra that can be used below in the computation of the frequency response of the antenna.

Denote by  $\gamma_g^p(f)$ ,  $\gamma_{gc}^p(f)$ ,  $\gamma_r^p(f)$  and  $\gamma_{rc}^p(f)$  the power spectral densities (PSD) corresponding to the pulses  $p_g(t)$ ,  $p_{gc}(t)$ ,  $p_r(t)$  and  $p_{rc}(t)$ , respectively. The PSD  $\gamma_x^p(f)$  of a given voltage signal  $x(t)$ , that is measured using the oscilloscope (such as  $p_g(t)$  and  $p_r(t)$ ), is given by:

$$\gamma_x^p(f) = \frac{|X(f)|^2}{RT_r} \quad (6.5)$$

where  $X(f)$  denotes the Fourier transform of  $x(t)$  and  $T_r$  the repetition period. In Fig. 6.10(c) we show  $\gamma_g^p(f)$  and  $\gamma_{gc}^p(f)$ , and in Fig. 6.10(d)  $\gamma_r^p(f)$  and  $\gamma_{rc}^p(f)$ .

For later use in Sec. 6.4 (see Eq. 6.8 and Eq. 6.10) we denote by  $h(t)$  and  $H(f)$  the normalized (with respect to  $\nu(f)$  in Eq. 6.4 so that the effects of  $\nu(f)$  will be contained in  $\alpha^{(l)}$  in Eq. 6.9) impulse and frequency responses counting for all effects between the input of the transmit antenna and the output of the receive antenna. We can write:

$$p_{rc}(t) = p_{gc}(t) \otimes h(t) \quad (6.6)$$

$$H(f) = \begin{cases} \frac{P_{rc}(f)}{\sqrt{\nu(f)P_{gc}(f)}} & |f| \in [0.5, 2] \text{ GHz} \\ 0 & \text{elsewhere.} \end{cases} \quad (6.7)$$

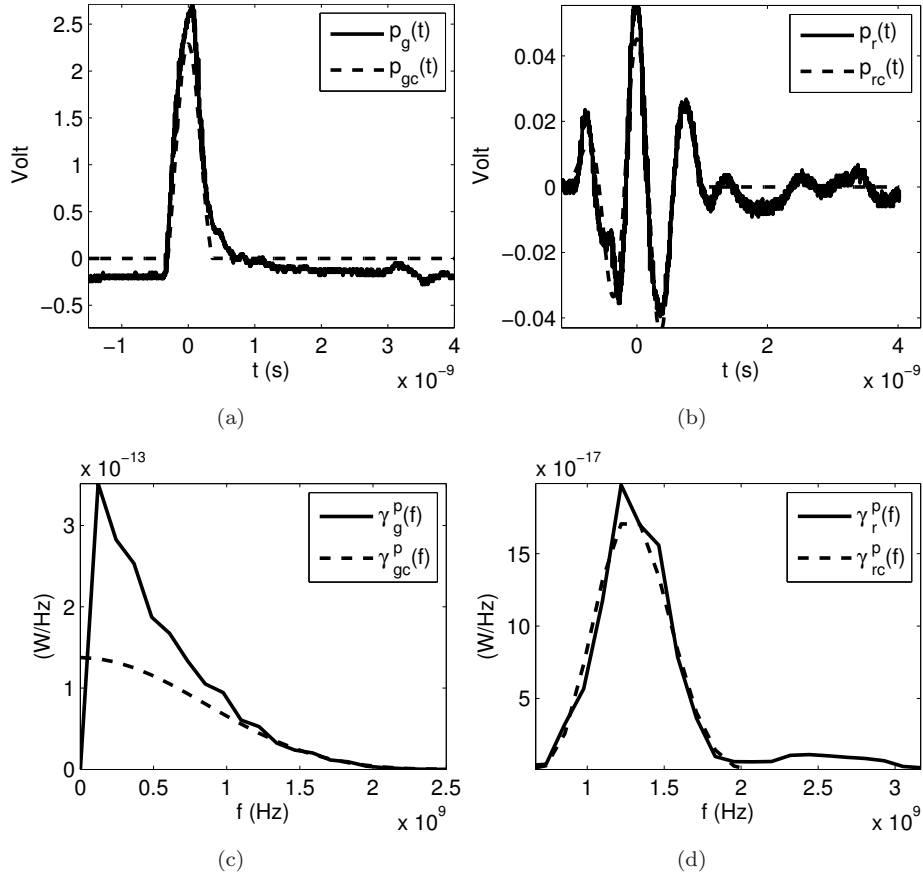


Fig. 6.10.: (a) Generated  $p_g(t)$  and clean generated  $p_{gc}(t)$  pulses (b) Received  $p_r(t)$  and clean received  $p_{rc}(t)$  pulses (c) PSDs  $\gamma_g^p(f)$  and  $\gamma_{gc}^p(f)$  of  $p_g(t)$  and  $p_{gc}(t)$  (d) PSDs  $\gamma_r^p(f)$  and  $\gamma_{rc}^p(f)$  of  $p_r(t)$  and  $p_{rc}(t)$ .

In Fig. 6.11, we show  $|H_{Norm}(f)|$ , the normalized module of  $H(f)$ .

The characteristics of the clean generated pulse  $p_{gc}(t)$  are as follows:

- Pulse duration (from zero to zero):  $T_{gc} = 672$  ps.
- Bandwidth (at -10 dB from the PSD peak [1]):  $B_{gc} = 3.7$  GHz.

The characteristics of the clean received pulse  $p_{rc}(t)$  are given by:

- Pulse duration:  $T_{rc} = 2.1$  ns
- Lowest frequency, highest frequency, mean frequency and bandwidth:  $f_l = 0.73$  GHz,  $f_h = 1.7$  GHz,  $f_m = 1.29$  GHz and  $B_{rc} = 0.97$  GHz.

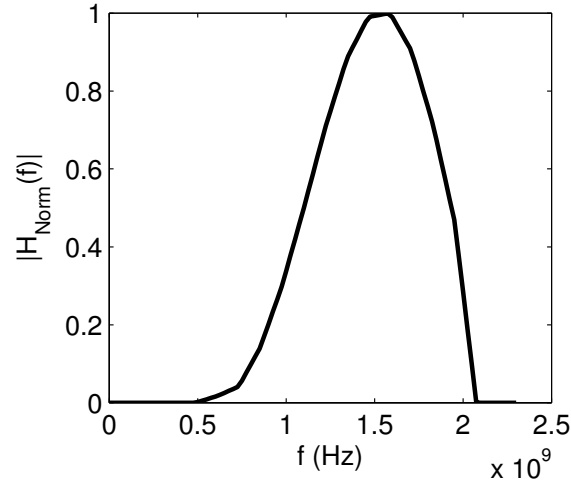


Fig. 6.11.: Normalized module  $|H_{Norm}(f)|$  of the frequency response between the generated and the received pulses.

- Mean quadratic bandwidth:  $\beta^2 = 6.86 \times 10^{19} \text{ s}^{-2}$ .

Regarding the radiated power and energy, we have obtained (without taking into account the attenuation in the cables connecting the FPGA to Tx, and RXs to the oscilloscope):

- Transmitted energy per bit:  $E_t = 3 \text{ pJ}$ . We have computed  $E_t$  using Eq. 6.2, Eq. 6.3 and Eq. 6.4 by considering a distance of  $d = 30 \text{ cm}$ .
- Power:  $0.0281 \text{ mW}$ ; this value is below the limit set by the US Federal Communications Commission (FCC) and the European Commission (EC) to approximately  $0.5 \text{ mW}$  and  $0.167 \text{ mW}$ , respectively. We have considered a repetition period of  $T_r = 106.666 \text{ ns}$ .
- Mean PSD:  $1.11 \times 10^{-14} \text{ W/Hz}$ ; this value is below the limit set by the FCC and the EC to  $7.4 \times 10^{-14} \text{ (-41.3 dBm/MHz)}$ . Given that we radiate between  $0.5$  and  $2 \text{ GHz}$ , we should upconvert our signals into the band located between  $3.1$  and  $10.6$  (resp.  $6$  and  $8.5$ )  $\text{GHz}$  in order to be compliant with the FCC (resp. EC) emission masks.
- PSD peak:  $1.97 \times 10^{-14} \text{ W/Hz}$ ; this value is below the limit set by the EC to  $2 \times 10^{-11} \text{ W/Hz}$  ( $0 \text{ dBm/50MHz}$ ).

#### 6.4 CHANNEL MODEL AND TOA ESTIMATOR

In this section we describe the channel model adopted in this work and the considered TOA estimator.

Denote by  $s(t)$  the generated signal and  $r(t)$  the signal received through a multipath AWGN channel. Signal  $s(t)$  consists of a burst of the monopulses  $p_g(t)$  (presented in Sec. 6.3). We can write  $r(t)$  as:

$$r(t) = s(t) \otimes h(t) \otimes c(t) + n(t) = \sum_{l=1}^L \alpha^{(l)} s_r(t - \tau^{(l)}) + n(t) \quad (6.8)$$

with

$$c(t) = \sum_{l=1}^L \alpha^{(l)} \delta(t - \tau^{(l)}) \quad (6.9)$$

$$s_r(t) = s(t) \otimes h(t) \quad (6.10)$$

where  $n(t)$  denotes the AWGN of bilateral PSD of  $N_0/2$ ,  $\alpha^{(l)}$  and  $\tau^{(l)}$  the gain and the time delay of the  $l$ th MPC,  $L$  the number of MPCs,  $c(t)$  the channel impulse response, and  $s_r(t)$  the generated signal filtered by the transmit and receive antennas. We recall that  $h(t)$  is given in Eq. 6.6.

By assuming the first MPC (containing the information about the distance) the strongest one, we can estimate the time delay  $\tau = \tau^{(1)}$  using the MLE:

$$\hat{\tau} = \underset{t}{\operatorname{argmax}} \{z(t)\} \quad (6.11)$$

where

$$z(t) = r(t) \otimes s_r(-t) \quad (6.12)$$

is the cross-correlation of  $r(t)$  and  $s_r(t)$ .

Note that in Eq. 6.12 we have filtered the received signal by the filter matched to  $s_r(t)$  Eq. 6.10, and not to the generated signal  $s(t)$  (see Eq. 6.8). In fact, we have seen in Sec. 6.3 that the pulses  $p_g(t)$  (the unshaped generated monopulse) and  $p_r(t)$  composing the signals  $s(t)$  and  $r(t)$  do not have the same shape. By contrast, the pulses of  $r(t)$  Eq. 6.8 and  $s_r(t)$  Eq. 6.10 have the same shape. Note also that on the oscilloscope, we only get the samples of  $s(t)$  and  $r(t)$ . So, in order to use the MLE in Eq. 6.11, we have to filter  $s(t)$  twice by  $h(t)$  according to Eq. 6.10 to obtain  $s_r(t)$ .

We have seen in Chap. 5 that when the first MPC does not overlap with the following MPCs, the CRLB for TOA estimation can be written as:

$$C_\tau = \frac{N_0/2}{(\alpha^{(1)})^2 E_t \beta_s^2} = \frac{1}{\rho \beta_s^2} \quad (6.13)$$

where  $E_t$  denotes the transmitted energy (i.e. energy of  $s_r(t)$  in Eq. 6.10), and  $E_r = (\alpha^{(1)})^2 E_t$  and  $\rho = \frac{E_r}{N_0/2}$  the useful received energy and the SNR of the first MPC.

## 6.5 RANGING

In this section we show and discuss the results obtained for ranging. We consider one transmit antenna (Tx) and one receive antenna (RX). The distance between Tx and RX belongs to the range 1 to 6 meters.

In order to get an accurate estimation of the TOA we must estimate the delays introduced by the cables connecting the FPGA to the oscilloscope and to the transmit antenna, and the cables connecting the receive antennas to the oscilloscope. In this setup, where only one receive antenna is used, we have to estimate only one delay ( $\tau_c$ ), while in the positioning setup in Sec. 6.6 below where three receive antennas will be used, we have to estimate three delays ( $\tau_{c1}$ ,  $\tau_{c2}$  and  $\tau_{c3}$ ).

In order to estimate  $\tau_c$ , we put Rx at a known distance ( $d_c = 30$  cm) from Tx, estimate the observed time delay  $\tau_{co}$  (we mean by “observed” the time delay containing both the time of flight and the cables delay) by using Eq. 6.11, and subtract the time of flight  $d_c/c$  from  $\hat{\tau}_{co}$  (estimate of  $\tau_{co}$ ):

$$\hat{\tau}_c = \hat{\tau}_{co} - d_c/c.$$

The estimate  $\hat{\tau}_c$  of  $\tau_c$  relies on one transmitted pulse. Given that we have transmitted 50 pulses per acquisition, the final estimate of  $\tau_c$  is the mean  $\mu_{\hat{\tau}_c}$  of the 50 estimates  $\hat{\tau}_c$ . We have found  $\mu_{\hat{\tau}_c} = -0.32$  ns.

Once the delay introduced by the cables is estimated, the distance between Tx and Rx can be estimated by:

$$\hat{d} = c(\hat{\tau}_o - \mu_{\hat{\tau}_c})$$

where  $\hat{\tau}_o$  is the observed time delay estimated by using Eq. 6.11.

Denote by  $\sigma_d$ ,  $\mu_d$  and  $b_d = \mu_d - d$  the standard deviation, mean and bias of  $\hat{d}$  obtained over the 50 transmitted pulses, respectively. The CRLB for the estimation of  $d$  can be obtained from Eq. 6.13 as:

$$C_d = C_\tau c^2 = \frac{c^2}{\rho \beta_s^2} = \frac{c^2 N_0/2}{E_r \beta_s^2}.$$

In order to compute  $C_d$ , we should know the values of  $N_0/2$  and  $E_r$  ( $\beta_s^2$  corresponds to the mean quadratic bandwidth of the clean received pulse  $p_{rc}(t)$ , see Sec. 6.3).

We have estimated  $N_0/2$  as the average over the 50 received pulses of the average of the PSD  $\gamma_r^p(f)$  of the received signal (computed using Eq. 6.5) in the frequency band between  $f_1 = 6$  GHz and  $f_2 = 250$  GHz (there are no useful signal components in this band). We have found that  $N_0/2$  is in the order of  $10^{-19}$  W/Hz (-100 dBm/MHz).

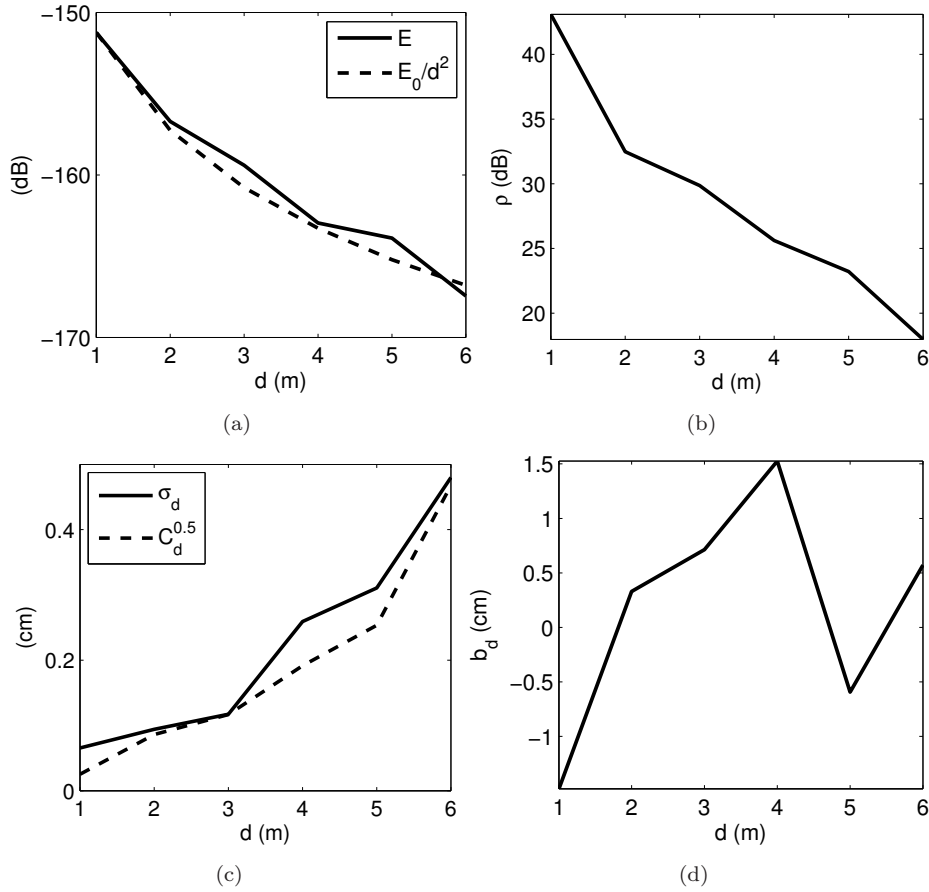


Fig. 6.12.: (a) Energy of the first MPC in dB (with respect to Joule) with respect to the distance  $d$  (b) SNR of the first MPC with respect to  $d$  (c) Standard deviation  $\sigma_d$  and square root of the CRLB in centimeters with respect to  $d$  (d) Bias  $b_d$  in centimeters with respect to  $d$ .

By assuming the energy of the first MPC to be inversely proportional to the squared distance, we have estimated  $E_r$  by  $E_0/d^2$ , where  $E_0$  denotes the measured received energy per pulse at  $d = 1$  m. In Fig. 6.12(a) we show the estimated energy  $E_0/d^2$  in dB (with respect to Joule) versus the distance  $d$  (in meters), and the energy  $E$  of the first MPC measured at each distance. We have already mentioned that  $d$  belongs to the range 1 to 6 meters. We can see that  $E$  closely follows  $E_0/d^2$ . For  $d = 6$  m, we have  $E = 1.8 \times 10^{-17}$  J and  $E_0/d^2 = 2.1 \times 10^{-17}$  J.

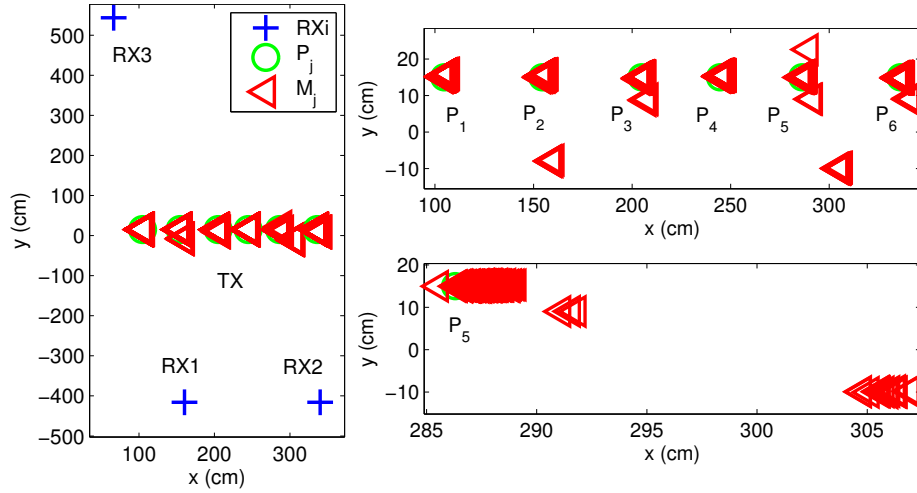


Fig. 6.13.: (left) Rx1, Rx2 and Rx3, positions occupied by Tx ( $P_1, \dots, P_6$ ), and estimated positions of Tx ( $M_1, \dots, M_6$ ) (right top) Zoom around  $P_1, \dots, P_6$  (right bottom) Zoom around  $P_5$ .

In Fig. 6.12(b) we show the SNR  $\rho$  in dB, obtained from the measured  $E$  and  $N_0/2$ , with respect to the distance. For  $d = 6$  m, we have  $\rho = 18$  dB.

In Fig. 6.12(c) we show the standard deviation and the square root of the CRLB in centimeters with respect to the distance. The variance and the CRLB are very close thanks to the good SNR and the shape of the transmitted pulse. For  $d = 6$  m, we have  $\sigma_d = 0.4798$  cm and  $\sqrt{C_d} = 0.4676$  cm ( $\rho = 18$  dB).

In Fig. 6.12(d) we show the bias in centimeters with respect to the distance. It seems to be random with respect to the distance. The minimum and maximum values of the bias are found at  $d = 1$  m ( $b_d = -1.48$  cm) and  $d = 4$  m ( $b_d = 1.53$  cm) respectively. From our point of view, this bias is due to the fact that we have measured the distances using a measuring tape. Given that the measured variance is very small, we are more confident in the estimated values of the distance than the ones obtained using the measuring tape.

## 6.6 POSITIONING

In this section we present and discuss the results obtained for positioning.

We have considered one transmitter Tx as unknown location node and three receivers Rx1, Rx2 and Rx3 as reference nodes. As depicted in Fig. 6.13 (left), Rx1, Rx2 and Rx3 are located at (160.2, -416) cm, (340, -416) cm and (66.4, 543.4) cm, respectively, and Tx at one of the following six posi-

tions:  $P_1(104.7, 15)$  cm,  $P_2(154.5, 15)$  cm,  $P_3(204.8, 15)$  cm,  $P_4(244.6, 15)$  cm,  $P_5(286.3, 15)$  cm, and  $P_6(336.1, 15)$  cm.

Like for ranging, we have first estimated the delays  $\tau_{c1}$ ,  $\tau_{c2}$  and  $\tau_{c3}$  introduced by the cables connecting Rx1, Rx2 and Rx3 to the oscilloscope, respectively. The average values obtained based on 185 transmitted pulses are equal to  $\mu_{\hat{\tau}_{c1}} = -0.39$  ns,  $\mu_{\hat{\tau}_{c2}} = -0.26$  ns and  $\mu_{\hat{\tau}_{c3}} = -0.29$  ns.

In order to estimate the position of Tx, we first estimate the distance  $d_i$  between Tx and Rx $i$  ( $i = 1, 2, 3$ ), then we estimate the position of Tx by triangulation. The method of triangulation used here consists in minimizing the following objective function:

$$(\hat{x}, \hat{y}) = \underset{(x,y)}{\operatorname{argmin}} \sum_{i=1}^3 \frac{\left( \hat{d}_i - \sqrt{(x-x_i)^2 + (y-y_i)^2} \right)^2}{2\sigma_{\hat{d}_i}^2}$$

where  $(x, y)$  and  $(x_i, y_i)$  denote the cartesian coordinates of Tx and Rx $i$  respectively,  $(\hat{x}, \hat{y})$  the estimated coordinates of Tx,  $\hat{d}_i$  the estimated distance and  $\sigma_{\hat{d}_i}^2$  the variance of  $\hat{d}_i$ .

Using the formula of transformation relative to the Fisher information matrix established in Chap. 5, we can write the CRLB matrix for the estimation of  $(x, y)$  as:

$$C_{x,y} = \frac{c^2}{\beta^2 \Delta_\rho} \sum_{i=1}^3 \rho_i \begin{pmatrix} \sin^2 \varphi_i & -\sin \varphi_i \cos \varphi_i \\ -\sin \varphi_i \cos \varphi_i & \cos^2 \varphi_i \end{pmatrix} \quad (6.14)$$

where  $\varphi_i$  denotes the angle between the axis joining Tx to Rx $i$  and the x axis,  $\rho_i$  the SNR at Rx $i$ ,  $C_{d_i}$  the CRLB for the estimation of  $d_i$ , and  $\Delta_\rho$  is given by  $\Delta_\rho = \sum_{i=1}^3 \sum_{i'=i+1}^3 \rho_i \rho_{i'} \sin^2(\varphi_i - \varphi_{i'})$ . The CRLBs  $C_x$  and  $C_y$  of  $x$  and  $y$  are the diagonal elements of  $C_{x,y}$ :  $C_x = C_{x,y}(1, 1)$  and  $C_y = C_{x,y}(2, 2)$ . Assuming that  $\rho_i = \rho \forall i$ , we can write:

$$C_{x,y} = \frac{C_d}{\Delta} \sum_{i=1}^3 \begin{pmatrix} \sin^2 \varphi_i & -\sin \varphi_i \cos \varphi_i \\ -\sin \varphi_i \cos \varphi_i & \cos^2 \varphi_i \end{pmatrix}$$

where  $\Delta = \sum_{i=1}^3 \sum_{i'=i+1}^3 \sin^2(\varphi_i - \varphi_{i'})$ .

In Fig. 6.13 (left) we show the positions of Rx1, Rx2 and Rx3, the different positions  $P_j$  ( $j = 1, \dots, 6$ ) occupied by Tx, and the estimated positions ( $M_j$ ) of Tx. For each  $P_j$ , we have 185  $M_j$  based on 185 transmitted pulses. In order to visualize the estimation errors, we make a zoom around  $P_1, \dots, P_6$  in Fig. 6.13 (right top) and around  $P_5$  in Fig. 6.13 (right bottom).

In Fig. 6.13 (right bottom), we can see that the estimates of  $P_5$  are distributed among three sets. For each set, the different estimates have approximately the same ordinate but different abscissas which means that the ordinate is estimated

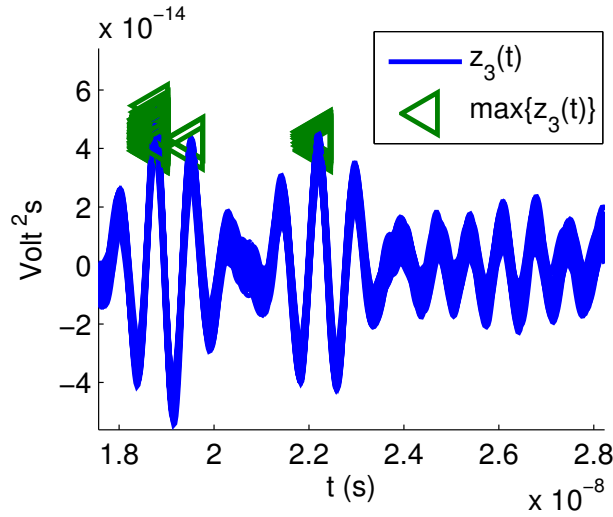


Fig. 6.14.: Cross-correlations (for 185 transmitted pulses) of the transmitted signal and the signals received at Rx3, and the ML estimates of the TOA when Tx is located at  $P_5$ .

more accurately than the abscissa. This is due to the geometry of our setup where the axis joining Tx to Rx $i$  ( $i = 1, 2, 3$ ) is more aligned with the y axis than the x axis ( $\cos^2 \varphi_i < \sin^2 \varphi_i$ ). This result can be expected from Eq. 6.14 showing that the ratio between the CRLBs of  $x$  and  $y$  can be written as:  $C_x/C_y = \sum_{i=1}^3 \rho_i \sin^2 \varphi_i / \sum_{i=1}^3 \rho_i \cos^2 \varphi_i \gg 1$ .

In Fig. 6.13 (right top), we can see that some estimates of  $P_2$  (resp.  $P_3$  and  $P_6$ ) fall at around 23 cm (resp. 7 cm) from the true position. This error results from an error in the estimation of the distance between Tx to Rx3. For  $P_2$ , the ranging error is due to a MPC in the signal received by Rx3 stronger than the first MPC, whereas for  $P_3$  and  $P_6$ , it is due to a sidelobe in the first MPC stronger than the mainlobe. For  $P_5$  (see Fig. 6.13 (right bottom)), we can see both the MPC errors and the sidelobe errors. For  $P_1$  and  $P_4$ , we have only the usual error due to the AWGN which is also the most recurrent type of error for the other positions.

In Fig. 6.14, we show, for the 185 transmitted pulses, the cross-correlation  $z_3(t) = r_3(t) \otimes s_r(-t)$  (see Eq. 6.12) of the signal  $r_3(t)$  received at Rx3 and the reference signal  $s_r(t)$  Eq. 6.10, when Tx is located at  $P_5$ . We can see that most estimates correspond to the mainlobe of the first MPC, whilst some estimates correspond to the mainlobe of the second MPC, and others to a sidelobe in the first MPC.

When the second MPC (resp. the first sidelobe of the first MPC) is detected we have an error on the estimation of the TOA equal to 3.1 ns (resp. 0.7 ns) which

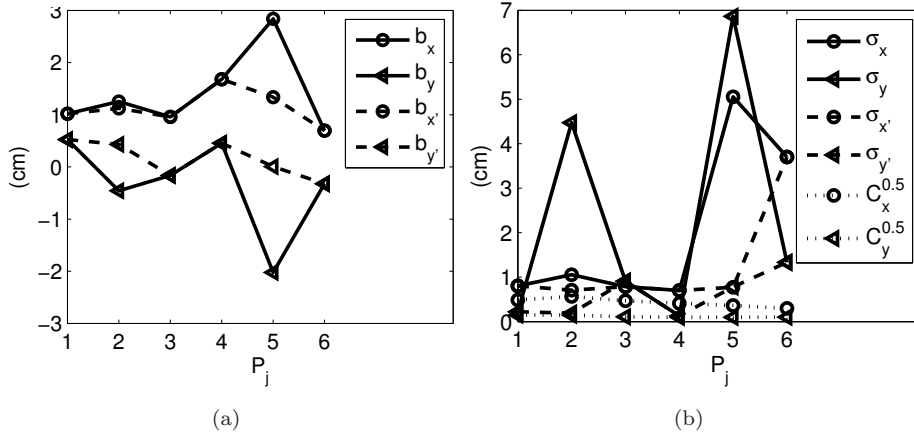


Fig. 6.15.: (a) Bias of the estimators of  $x$  and  $y$  in centimeters with respect to  $P_1, \dots, P_6$  for TOA MLE ( $b_{\hat{x}}$  and  $b_{\hat{y}}$ ) and threshold based estimator ( $b_{\hat{x}'}$  and  $b_{\hat{y}'}$ ) (b) Standard deviations of the estimators of  $x$  and  $y$  in centimeters for TOA MLE ( $\sigma_{\hat{x}}$  and  $\sigma_{\hat{y}}$ ) and threshold based estimator ( $\sigma_{\hat{x}'}$  and  $\sigma_{\hat{y}'}$ ), and square roots of the CRLBs of  $x$  and  $y$ .

corresponds to a ranging error of 93 cm (resp. 21 cm). These ranging errors lead to errors in positioning (distance between true and estimated positions) which are much smaller (23 cm for false MPC detection and 7 cm for false sidelobe detection). In fact, Rx1 and Rx2 will pull the estimated position toward the true position. The positioning error can be even more reduced if we have more receivers with accurate estimated distance. Suppose now that all receivers overestimate the distance. In this case, the position obtained by triangulation will again fall close to the true position. We can deduce that the positioning accuracy can be highly improved and the errors due to false MPC and sidelobe detection can be highly mitigated by increasing the number of receivers.

In Fig. 6.15(a) we show the measured bias of  $\hat{x}$  and  $\hat{y}$  ( $b_x$  and  $b_y$  respectively) with respect to the positions  $P_1, \dots, P_6$  occupied by Tx. In Fig. 6.15(b) we show the standard deviations of  $\hat{x}$  and  $\hat{y}$  ( $\sigma_x$  and  $\sigma_y$ ) and the square roots of the CRLBs ( $C_x^{0.5}$  and  $C_y^{0.5}$ ) of  $x$  and  $y$ . We can see that  $b_x$  and  $b_y$  are relatively small, and that  $\sigma_x$  and  $\sigma_y$  are very close to  $C_x^{0.5}$  and  $C_y^{0.5}$ , respectively, when neither false MPC detection nor false sidelobe detection occur. For  $P_4$  (neither false MPC detection nor false sidelobe detection occur), we have  $(b_x, b_y) = (1.68, 0.46)$  cm,  $(\sigma_x, \sigma_y) = (0.7, 0.13)$  cm and  $(C_x^{0.5}, C_y^{0.5}) = (0.41, 0.1)$  cm, whereas for  $P_5$  (both false MPC detection and false sidelobe detection occur), we have  $(b_x, b_y) = (2.84, -2.02)$  cm,  $(\sigma_x, \sigma_y) = (5.05, 6.86)$  cm and  $(C_x^{0.5}, C_y^{0.5}) = (0.36, 0.1)$  cm.

In order to solve the problem of false MPC detection, we consider a threshold-based TOA estimator. This estimator consists on waiting until the cross-

correlation  $z_i(t)$ , ( $i = 1, 2, 3$ ) Eq. 6.12 crosses a given threshold, then searching within an interval equal to the pulse width for the maximum of  $z_i(t)$ . The threshold should be carefully chosen with respect to the noise level and the useful signal level in order to minimize the probability of early detection due to the AWGN, the probability of late detection due to the channel MPCs, and the probability of non detection.

In Fig. 6.15(a) and Fig. 6.15(b) we show the bias terms ( $b_{x'}$  and  $b_{y'}$ ) and the standard deviations ( $\sigma_{x'}$  and  $\sigma_{y'}$ ) when the threshold-based estimator is used. The estimation error is highly reduced for  $P_2$  and  $P_5$ . For  $P_5$ , we have now  $(b_{x'}, b_{y'}) = (1.34, 0.005)$  cm and  $(\sigma_{x'}, \sigma_{y'}) = (0.77, 0.78)$  cm when the threshold-based estimator is used compared to  $(b_x, b_y) = (2.84, -2.02)$  cm and  $(\sigma_x, \sigma_y) = (5.05, 6.86)$  cm when the MLE is used. Note that the errors due to the false sidelobe detection are still present at  $P_3$ ,  $P_5$  and  $P_6$  with the threshold-based estimator.

## 6.7 CONCLUSION

A testbed for IR-UWB based ranging and positioning is described and a TH-IR-UWB generator is presented. The characteristics of the generated, transmitted and received signals are analyzed.

Based on the collected data, the variances for ranging and positioning are computed. Those obtained using the TOA MLE are found to be close to the CRLBs when the first MPC is the strongest MPC and the pulse mainlobe is stronger than the sidelobes. In realistic multipath environments where the last assumption is not often true, the MLE can lead to false MPC and sidelobe detection and to non-negligible estimation errors.

By using threshold based estimators, the errors due to false MPC detection can be corrected. It has been also shown that the impact of the ranging errors on the positioning accuracy can be mitigated by increasing the number of receivers.



## CHAPTER 7

---

## CONCLUSIONS

---

To conclude, we summarize the main contributions of this thesis and draw out some interesting problems for future investigation.

We consider the problem of nonlinear estimation for deterministic parameters. Both the threshold and the ambiguity phenomena are studied. Some approximations of the statistics of the MLE are proposed by making use of the subdomain method initiated by Wozencraft [89] and improved by McAulay [70]. Some approximate upper and lower bounds are also derived. The main approximate lower bounds rely on the Bayesian ZZLB [58] and BTLB [60]. The numerical results obtained by considering the example of TOA estimation via IR-UWB signals, show that the proposed MSE approximations are highly accurate and that the derived approximate bounds are very tight.

Utilizing one of the resulting MSE approximations, the thresholds of the begin-ambiguity, end-ambiguity and asymptotic regions are computed with respect to the IFBW of the transmitted signal. Also, analytic expressions are derived. Some thresholds depend on the shape of the ACR of the transmitted signal, while others depend on the shape of its envelope.

Based on the results related to the asymptotic threshold, we propose a very simple method to optimize the spectrum of the transmitted pulse with respect

to the available SNR, so that the achieved MSE can be the lowest attainable MSE at that SNR.

We propose a new receiver (the DM receiver) for TH-IR-IWB signals and a new TOA estimator (the MME) based on that receiver. The statistics and the local and global probabilities of error are derived for both the DM and the CR receivers. Using the subdomain method introduced in Chap. 2, we approximate the local and the global MSEs of the MME and the MCE. The performances of the MME and the MCE are similar for single-user and for multiuser with random MUI. With deterministic MUI, the MME (resp. MCE) remarkably outperforms the MCE (resp. MME) for constructive (resp. destructive) MUI. This result is very interesting because one can combine the MME and the MCE together to obtain an estimator that outperforms both of them.

We propose some TOA estimators for AWGN and MP channels based on the phase of the DFT of received signal, and compute their achieved MSEs. They achieve the CRLB asymptotically. We compare them with the MLE.

We study the performance limits of positioning and parameter estimation in UWB systems, and wideband MIMO and MISO systems. We consider UWB systems with MP channels and derive the CRLBs for positioning employing either the AOA technique, or the hybrid TOA-AOA technique. Built on typical scenarios, some numerical results are presented and discussed.

We study the impact of the overlapping of the components of an UWB channel on the estimation of the gain and the TOA. The probability of overlapping is calculated for the IEEE802.15.3a and the IEEE802.15.4a statistical channel models. By evaluating the average CRLBs, it turns out that the theoretical performances achievable in MP channels are very close to those achievable in AWGN channels, in more than 80% of the possible cases.

We deal with the estimation of the TOA and the AOA in wideband MIMO and MISO systems. The cases of orthogonal and non-orthogonal signals are investigated, and the CRLBs obtained in SISO, SIMO, MISO and MIMO configurations are compared.

A testbed for IR-UWB based ranging and positioning is presented. We describe the implemented TH-IR-UWB generator and the investigated shaping methods. Positioning is performed by making use of the TOA technique. We study the impact of the channel and the pulse shape on the achieved performances. The potential of the threshold estimators in the detection of the first MPC is demonstrated, and the improvement insured by increasing the number of the reference nodes is highlighted.

Some topics of interest for future research are:

- The effects of the threshold and the ambiguity phenomena on two-step and direct positioning.

- Low-cost TOA estimators for MU systems with MP channels: design, implementation and experimenting in realistic channels.
- Data-fusion methods for NLOS environments: design and testing.



# APPENDIX A

## CURVATURES OF THE AUTOCORRELATION FUNCTION AND OF ITS ENVELOPE

---

In this appendix we show that for

$$R_s(\theta, \Theta) = \Re \left\{ e^{j2\pi\varphi_c(\theta-\Theta)} e_{R_s}(\theta, \Theta) \right\} \quad (\text{A.1})$$

$$\varphi_c = \frac{\int_0^{+\infty} \varphi \Re \{ \mathcal{F}_{R_s}(\varphi) \} d\varphi}{\int_0^{+\infty} \Re \{ \mathcal{F}_{R_s}(\varphi) \} d\varphi} \quad (\text{A.2})$$

$$\mathcal{F}_{R_s}(\varphi) = \int_{\Theta_1}^{\Theta_2} R_s(\theta, \Theta) e^{-j2\pi\varphi(\theta-\Theta)} d\theta \quad (\text{A.3})$$

we have:

$$-\ddot{R}_s(\Theta, \Theta) = -\Re \{ \ddot{e}_{R_s}(\Theta, \Theta) \} + 4\pi^2 \varphi_c^2 E_s. \quad (\text{A.4})$$

From the definition of the complex envelope and the Fourier transform in Eq. A.1 and Eq. A.3 respectively we can write the Fourier transform of the complex envelope  $e_{R_s}(\theta, \Theta)$  as:

$$\mathcal{F}_{e_{R_s}}(\varphi) = 2\mathcal{F}_{R_s}^+(\varphi + \varphi_c) \quad (\text{A.5})$$

where  $z^+(\varphi) = z(\varphi)$  for  $\varphi > 0$  and  $z^+(\varphi) = 0$  for  $\varphi \leq 0$ .

From Eq. A.1 we can write:

$$\ddot{R}_s(\theta, \Theta) = \Re \left\{ e^{j2\pi\varphi_c(\theta-\Theta)} \left[ \ddot{e}_{R_s}(\theta, \Theta) - 4\pi^2 \varphi_c^2 e_{R_s}(\theta, \Theta) + j4\pi\varphi_c \dot{e}_{R_s}(\theta, \Theta) \right] \right\} \quad (\text{A.6})$$

For  $\theta = \Theta$  we can write Eq. A.1 and Eq. A.6 as:

$$R_s(\Theta, \Theta) = E_s = \Re\{e_{R_s}(\Theta, \Theta)\} \quad (\text{A.7})$$

$$\begin{aligned} \ddot{R}_s(\Theta, \Theta) &= \Re\{\ddot{e}_{R_s}(\Theta, \Theta)\} - 4\pi^2\varphi_c^2\Re\{e_{R_s}(\Theta, \Theta)\} \\ &+ 4\pi\varphi_c\Re\{j\dot{e}_{R_s}(\Theta, \Theta)\}. \end{aligned} \quad (\text{A.8})$$

Using Eq. A.7 we can write Eq. A.8 as:

$$\ddot{R}_s(\Theta, \Theta) = \Re\{\ddot{e}_{R_s}(\Theta, \Theta)\} - 4\pi^2\varphi_c^2E_s + 4\pi\varphi_c\Re\{j\dot{e}_{R_s}(\Theta, \Theta)\}. \quad (\text{A.9})$$

In order to prove Eq. A.4 we have to show that  $\Re\{j\dot{e}_{R_s}(\Theta, \Theta)\} = 0$  in Eq. A.9. To do so we write  $\dot{e}_{R_s}(\theta, \Theta)$  with respect to the Fourier transform  $\mathcal{F}_{e_{R_s}}(\varphi)$  Eq. A.5 of  $e_{R_s}(\theta, \Theta)$  using the inverse Fourier transform as:

$$\begin{aligned} \dot{e}_{R_s}(\theta, \Theta) &= \int_{-\infty}^{+\infty} j2\pi\varphi\mathcal{F}_{e_{R_s}}(\varphi)e^{j2\pi\varphi(\theta-\Theta)}d\varphi \\ &= \int_{-\infty}^{+\infty} j4\pi\varphi\mathcal{F}_{R_s}^+(\varphi + \varphi_c)e^{j2\pi\varphi(\theta-\Theta)}d\varphi \\ &= \int_{-\infty}^{+\infty} j4\pi(\phi - \varphi_c)\mathcal{F}_{R_s}^+(\phi)e^{j2\pi(\phi-\varphi_c)(\theta-\Theta)}d\phi \\ &= \int_0^{+\infty} j4\pi(\phi - \varphi_c)\mathcal{F}_{R_s}(\phi)e^{j2\pi(\phi-\varphi_c)(\theta-\Theta)}d\phi \end{aligned} \quad (\text{A.10})$$

where  $\phi = \varphi + \varphi_c$ . From Eq. A.10 we can write  $\dot{e}_{R_s}(\Theta, \Theta)$  as:

$$\dot{e}_{R_s}(\Theta, \Theta) = \int_0^{+\infty} j4\pi(\varphi - \varphi_c)\mathcal{F}_{R_s}(\varphi)d\varphi. \quad (\text{A.11})$$

From Eq. A.2 and Eq. A.11 we can write  $\Re\{j\dot{e}_{R_s}(\Theta, \Theta)\}$  in Eq. A.9 as:

$$\Re\{j\dot{e}_{R_s}(\Theta, \Theta)\} = - \int_0^{+\infty} 4\pi(\varphi - \varphi_c)\Re\{\mathcal{F}_{R_s}(\varphi)\}d\varphi = 0$$

so Eq. A.4 is proved.

# APPENDIX B

## INERTIA OF A REGULAR ANTENNA ARRAY

---

In this appendix we show that the inertia

$$i_n(\varphi) = \sum_{m=1}^{M_n} r_{n,m}^2 \sin^2(\varphi - \varphi_{n,m}) = \sum_{m=1}^{M_n} \frac{r_{n,m}^2}{2} (1 - \cos[2(\varphi - \varphi_{n,m})])$$

of an antenna array becomes independent of  $\varphi$  (i.e. omni-directional) if the array is regular. As for regular arrays,  $r_{n,m} = r_{\text{Ref}_n}$ ,  $\forall m$ , and  $\varphi_{n,m} = \varphi_{n0} + \frac{2(m-1)\pi}{M_n}$ ,  $i_n(\varphi)$  becomes:

$$i_n(\varphi) = \frac{r_{\text{Ref}_n}^2}{2} \left\{ M_n - \sum_{m=1}^{M_n} \cos \left[ 2 \left( \varphi - \varphi_{n0} - \frac{2(m-1)\pi}{M_n} \right) \right] \right\}.$$

Define  $S$  as:

$$S = \sum_{m=1}^{M_n} \left\{ \cos \left[ 2 \left( \varphi - \varphi_{n0} - \frac{2(m-1)\pi}{M_n} \right) \right] + i \sin \left[ 2 \left( \varphi - \varphi_{n0} - \frac{2(m-1)\pi}{M_n} \right) \right] \right\}.$$

The use of Euler's formula leads to:

$$S = e^{i2(\varphi - \varphi_{n0})} \sum_{m=1}^{M_n} e^{-i\frac{4(m-1)\pi}{M_n}} = e^{i2(\varphi - \varphi_{n0})} \frac{1 - e^{-i4\pi}}{1 - e^{-i\frac{4\pi}{M_n}}} = 0, M_n > 2$$

where it has been taken into account that  $S$  is the sum of a geometric series. Finally,

$$i_n(\varphi) = \frac{M_n r_{\text{Ref}_n}^2}{2}.$$



# APPENDIX C

## FIM FOR JOINT TOA AND AOA ESTIMATION IN MIMO SYSTEMS

---

In this appendix we give the expressions of the magnitudes  $\Gamma_{\hat{s}}^{\omega_0}$ ,  $\Gamma_{\hat{s},s}^{\omega_0}$ ,  $I_{\hat{s}}^{\omega_0}$ ,  $I_{\hat{s},s}^{\omega_0}$ ,  $J_{\hat{s}}^{\omega_0}$  and  $J_{\hat{s},s}^{\omega_0}$ , that appear in the expressions of the elements of the FIM in Eq. 5.60, Eq. 5.61 and Eq. 5.62 and that are neglected. We can show that:

$$\begin{aligned}
 \Gamma_{\hat{s}}^{\omega_0} &= 2 \sum_{n \neq n'} \hat{X}_{\hat{s}_n \hat{s}_{n'}}^{\omega_0} \\
 \Gamma_{\hat{s},s}^{\omega_0} &= 2 \sum_{n \neq n'} \hat{X}_{\hat{s}_n s_{n'}}^{\omega_0} \\
 I_{\hat{s}}^{\omega_0} &= 2 \sum_{n \neq n'} A_n A_{n'} \hat{X}_{\hat{s}_n \hat{s}_{n'}}^{\omega_0} \\
 I_{\hat{s},s}^{\omega_0} &= 2 \sum_{n \neq n'} A_n A_{n'} \hat{X}_{\hat{s}_n s_{n'}}^{\omega_0} \\
 J_{\hat{s}}^{\omega_0} &= \sum_{n \neq n'} (A_n + A_{n'}) \hat{X}_{\hat{s}_n \hat{s}_{n'}}^{\omega_0} \\
 J_{\hat{s},s}^{\omega_0} &= \sum_{n \neq n'} (A_n + A_{n'}) \hat{X}_{\hat{s}_n s_{n'}}^{\omega_0}
 \end{aligned}$$

where

$$\begin{aligned}
 \hat{X}_{\hat{s}_n \hat{s}_{n'}}^{\omega_0} &= \Re \left\{ e^{j\omega_0 \Delta\tau_{n',n}} \frac{X_{\hat{s}_n \hat{s}_{n'}}(\Delta\tau_{n',n})}{E_s \beta_s^2} \right\} \\
 \hat{X}_{\hat{s}_n s_{n'}}^{\omega_0} &= \Re \left\{ j e^{j\omega_0 \Delta\tau_{n',n}} \frac{X_{\hat{s}_n s_{n'}}(\Delta\tau_{n',n})}{E_s \beta_s} \right\}.
 \end{aligned}$$



## Bibliography

- [1] Federal Communications Commission (FCC), “Revision of part 15 of the commission rules regarding ultra-wideband transmission systems,” in *FCC 02-48*, April 2002.
- [2] Commission of the European Communities (EC), “Commission decision of 21/ii/2007 on allowing the use of the radio spectrum for equipment using ultra-wideband technology in a harmonised manner in the community,” February 2007.
- [3] —, “Final report from CEPT in response to EC mandates on the harmonized introduction of radio applications based on ultra-wideband (UWB) technology,” March 2007.
- [4] I. Oppermann, M. Hämäläinen, and J. Iinatti, Eds., *Optimum Array Processing: Part IV of Detection, Estimation, and Modulation Theory*. Wiley, 2004.
- [5] S. Gezici and H. Poor, “Position Estimation via Ultra-Wide-Band Signals,” *Proceedings of the IEEE*, vol. 97, no. 2, pp. 386–403, February 2009.
- [6] M. Ghavami, L. Michael, and R. Kohno, *Ultra Wideband Signals and Systems in Communication Engineering*. Wiley, 2004.
- [7] M.-G. Di Benedetto and G. Giancola, *Understanding ultra wide band radio fundamentals*. Prentice Hall PTR, 2004.
- [8] H. R. Jeffery, Ed., *An Introduction to Ultra Wideband Communication Systems*. Prentice Hall, June 2005.
- [9] A. Molisch, K. Balakrishnan, D. Cassioli, C.-C. Chong, S. Emami, A. Fort, J. Karedal, J. Kunisch, H. Schantz, and K. Siwiak, “A comprehensive model for ultrawideband propagation channels,” in *IEEE Global Telecommunications Conference (GLOBECOM 2005)*, vol. 6, December 2005, pp. 3648–3653.
- [10] F. Gustafsson and F. Gunnarsson, “Mobile positioning using wireless networks: possibilities and fundamental limitations based on available wireless network measurements,” *IEEE Signal Processing Magazine*, vol. 22, no. 4, pp. 41–53, July 2005.
- [11] A. Sayed, A. Tarighat, and N. Khajehnouri, “Network-based wireless location: challenges faced in developing techniques for accurate wireless location information,” *IEEE Signal Processing Magazine*, vol. 22, no. 4, pp. 24–40, July 2005.
- [12] N. Patwari, J. Ash, S. Kyperountas, A. Hero, R. Moses, and N. Correal, “Locating the nodes: cooperative localization in wireless sensor networks,” *IEEE Signal Processing Magazine*, vol. 22, no. 4, pp. 54–69, July 2005.

- [13] G. Sun, J. Chen, W. Guo, and K. J. R. Liu, "Signal processing techniques in network-aided positioning: a survey of state-of-the-art positioning designs," *IEEE Signal Processing Magazine*, vol. 22, no. 4, pp. 12–23, July 2005.
- [14] S. Zafer, S. Gezici, and I. Guvenc, *Ultra-wideband Positioning Systems: Theoretical Limits, Ranging Algorithms, and Protocols*. Cambridge University Press, 2008.
- [15] D. Dardari, A. Conti, U. Ferner, A. Giorgetti, and M. Win, "Ranging with ultrawide bandwidth signals in multipath environments," *Proceedings of the IEEE*, vol. 97, no. 2, pp. 404–426, February 2009.
- [16] W. Namgoong, "A channelized digital ultrawideband receiver," *IEEE Transactions on Wireless Communications*, vol. 2, no. 3, pp. 502–510, May 2003.
- [17] S. Hoyos, B. Sadler, and G. Arce, "Monobit digital receivers for ultrawideband communications," *IEEE Transactions on Wireless Communications*, vol. 4, no. 4, pp. 1337–1344, July 2005.
- [18] M.-W. Chen and R. Brodersen, "A subsampling UWB radio architecture by analytic signaling," in *IEEE International Conference on Acoustics, Speech, and Signal Processing (ICASSP 2004)*, vol. 4, May 2004, pp. iv–533–iv–536.
- [19] Y. Vanderperren, W. Dehaene, and G. Leus, "A flexible low power subsampling UWB receiver based on line spectrum estimation methods," in *IEEE International Conference on Communications (ICC 2006)*, vol. 10, June 2006, pp. 4694–4699.
- [20] I. Guvenc and Z. Sahinoglu, "Threshold-based TOA estimation for impulse radio UWB systems," in *IEEE International Conference on Ultra-Wideband (ICUWB 2005)*, 2005, pp. 420–425.
- [21] I. Guvenc, Z. Sahinoglu, A. Molisch, and P. Orlik, "Non-coherent TOA estimation in IR-UWB systems with different signal waveforms," in *2nd International Conference on Broadband Networks (BroadNets 2005)*, vol. 2, October 2005, pp. 1168–1174.
- [22] D. Dardari, C.-C. Chong, and M. Win, "Threshold-based time-of-arrival estimators in UWB dense multipath channels," *IEEE Transactions on Communications*, vol. 56, no. 8, pp. 1366–1378, August 2008.
- [23] A. Rabbachin and I. Oppermann, "Synchronization analysis for UWB systems with a low-complexity energy collection receiver," in *International Workshop on Ultra Wideband Systems Joint with Conference on Ultrawideband Systems and Technologies (Joint UWBST IWUWBS 2004)*, May 2004, pp. 288–292.

- [24] C. Carbonelli and U. Mengali, "Synchronization of energy capture receivers for UWB applications," in *Proceedings 13th European Signal Processing Conference (EUSIPCO-2005)*, 2005, pp. 4–8.
- [25] A. D'Amico, U. Mengali, and L. Taponecco, "Energy-based TOA estimation," *IEEE Transactions on Wireless Communications*, vol. 7, no. 3, pp. 838–847, March 2008.
- [26] W. Shaohua, Z. Qinyu, and Z. Naitong, "A two-step TOA estimation method for IR-UWB ranging systems," in *Fifth Annual Conference on Communication Networks and Services Research (CNSR 2007)*, May 2007, pp. 302–310.
- [27] M. Ho, V. Somayazulu, J. Foerster, and S. Roy, "A differential detector for an ultra-wideband communications system," in *IEEE 55th Vehicular Technology Conference (VTC 2002)*, vol. 4, 2002, pp. 1896–1900.
- [28] L. Yang and G. Giannakis, "Timing ultra-wideband signals with dirty templates," *IEEE Transactions on Communications*, vol. 53, no. 11, pp. 1952–1963, November 2005.
- [29] G. Tchere, P. Uolkosold, S. Knedlik, and O. Loffeld, "Communication and TOA estimation with differential impulse radio UWB systems," in *4th Workshop on Positioning, Navigation and Communication (WPNC 2007)*, 2007, pp. 87–95.
- [30] Y. Ying, M. Ghogho, and A. Swami, "Analysis of code-assisted blind synchronization for UWB systems," in *IEEE International Conference on Communications (ICC 2007)*, June 2007, pp. 4293–4298.
- [31] A. D'Amico, U. Mengali, and L. Taponecco, "Synchronization for differential transmitted reference UWB receivers," *Wireless Communications, IEEE Transactions on*, vol. 6, no. 11, pp. 4154–4163, 2007.
- [32] J.-Y. Lee and R. Scholtz, "Ranging in a dense multipath environment using an UWB radio link," *IEEE Journal on Selected Areas in Communications*, vol. 20, no. 9, pp. 1677–1683, December 2002.
- [33] C. Falsi, D. Dardari, L. Mucchi, and M. Z. Win, "Time of arrival estimation for UWB localizers in realistic environments," *EURASIP Journal on Advances in Signal Processing*, vol. 2006, no. 1, pp. 1–13, 2006.
- [34] S. Gezici, Z. Sahinoglu, A. Molisch, H. Kobayashi, and H. Poor, "Two-step time of arrival estimation for pulse-based ultra-wideband systems," *EURASIP Journal on Advances in Signal Processing*, vol. 2008, no. 1, p. 529134, 2008. [Online]. Available: <http://asp.eurasipjournals.com/content/2008/1/529134>

- [35] A. Mallat, J. Louveaux, L. Vandendorpe, M. Di Dio, and M. Luise, "Discrete fourier transform-based TOA estimation in UWB systems," *EURASIP Journal on Wireless Communications and Networking*, vol. 2012, no. 1, pp. 1–9, 2012. [Online]. Available: <http://dx.doi.org/10.1186/1687-1499-2012-3>
- [36] A. Mallat, J. Louveaux, and L. Vandendorpe, "TOA estimators operating in the frequency domain," in *Satellite and Terrestrial Radio Positioning Techniques: A signal processing perspective*, D. Dardari, M. Luise, and E. Falletti, Eds. Elsevier, 2012.
- [37] Z. Sahinoglu and I. Guvenc, "Multiuser interference mitigation in noncoherent UWB ranging via nonlinear filtering," *EURASIP Journal on Wireless Communications and Networking*, vol. 2006, no. 1, pp. 1–10, 2006.
- [38] D. Dardari, A. Giorgetti, and M. Win, "Time-of-arrival estimation of UWB signals in the presence of narrowband and wideband interference," in *IEEE International Conference on Ultra-Wideband (ICUWB 2007)*, September 2007, pp. 71–76.
- [39] M. Win and R. Scholtz, "Impulse radio: how it works," *IEEE Communications Letters*, vol. 2, no. 2, pp. 36–38, 1998.
- [40] W. Lovelace and J. Townsend, "Chip discrimination for large near far power ratios in UWB networks," in *IEEE Military Communications Conference (MILCOM 2003)*, vol. 2, 2003, pp. 868–873.
- [41] E. Fishler and H. Poor, "Low-complexity multiuser detectors for time-hopping impulse-radio systems," *IEEE Transactions on Signal Processing*, vol. 52, no. 9, pp. 2561–2571, 2004.
- [42] S. Gezici, H. Kobayashi, and H. Poor, "A comparative study of pulse combining schemes for impulse radio UWB systems," in *2004 IEEE/Sarnoff Symposium on Advances in Wired and Wireless Communication*, 2004, pp. 7–10.
- [43] S. Gezici, H. Kobayashi, H. Poor, and A. Molisch, "Optimal and suboptimal linear receivers for time-hopping impulse radio systems," in *International Workshop on Ultra Wideband Systems Joint with Conference on Ultrawideband Systems and Technologies (Joint UWBST IWUWBS 2004)*, 2004, pp. 11–15.
- [44] A. Naanaa, Z. Ben Jemaa, and S. Belghith, "Performance of multiple-access TH-UWB system: chaotic vs classical codes sequences," in *3rd International Conference on Signals, Circuits and Systems (SCS 2009)*, November 2009, pp. 1–5.

- [45] I. Hosseini and N. Beaulieu, "Bit error rate of TH-BPSK UWB receivers in multiuser interference," *IEEE Transactions on Wireless Communications*, vol. 8, no. 10, pp. 4916–4921, October 2009.
- [46] Z. Zhang, F. Zeng, and L. Ge, "Correlation properties of time-hopping sequences for impulse radio," in *IEEE International Conference on Acoustics, Speech, and Signal Processing (ICASSP 2003)*, vol. 4, April 2003, pp. 141–144.
- [47] J. J. Metzner and U. Tunttoolavest, "Pulse time hopping for multiaccess communications with a concatenated code," in *The 2002 45th Midwest Symposium on Circuits and Systems (MWSCAS 2002)*, vol. 1, 2002, pp. 172–176.
- [48] A. Amigo, A. Mallat, and L. Vandendorpe, "Multiuser and multipath interference mitigation in UWB TOA estimation," in *IEEE International Conference on Ultra-Wideband (ICUWB 2011)*, September 2011, pp. 465–469.
- [49] X.-G. Xia and K. Liu, "A generalized chinese remainder theorem for residue sets with errors and its application in frequency determination from multiple sensors with low sampling rates," *IEEE Signal Processing Letters*, vol. 12, no. 11, pp. 768–771, November 2005.
- [50] C. Towers, D. Towers, and J. Jones, "Time efficient chinese remainder theorem algorithm for full-field fringe phase analysis in multi-wavelength interferometry," *Opt Express.*, vol. 12, no. 6, pp. 1136–1143, March 2004.
- [51] I. Sahin and N. Yilmazer, "Reducing computational complexity of time delay estimation method using frequency domain alignment," in *43rd Annual Conference on Information Sciences and Systems (CISS 2009)*, 2009, pp. 43–46.
- [52] L. Blancoa, J. Serraa, and M. Nájara, "Minimum variance time of arrival estimation for positioning," *Special Sect. Process. Anal. High Dimens. Masses Image Signal Data*, vol. 90, no. 8, pp. 2611–2620, 2010.
- [53] W. L. S Wang, D Sen, "Subband analysis of time delay estimation in STFT domain," in *Proceedings of the 11th Australian International Conference on Speech Science and Technology*, 2006, pp. 211–215.
- [54] B. Jiang and F. H. Chen, "High precision time delay estimation using generalised mvdr cross spectrum," *Electronics Letters*, vol. 43, no. 2, pp. 131–133, January 2007.
- [55] —, "Short pulse multi-frequency phase-based time delay estimation," *Journal of the Acoustical Society of America*, vol. 127, no. 1, pp. 309–315, 2010.

- [56] X. Li and K. Pahlavan, "Super-resolution TOA estimation with diversity for indoor geolocation," *IEEE Transactions on Wireless Communications*, vol. 3, no. 1, pp. 224–234, January 2004.
- [57] H. L. V. Trees, *Ultra Wideband Signals and Systems in Communication Engineering*. Wiley, 2002.
- [58] J. Ziv and M. Zakai, "Some lower bounds on signal parameter estimation," *IEEE Transactions on Information Theory*, vol. 15, no. 3, pp. 386–391, May 1969.
- [59] L. Seidman, "Performance limitations and error calculations for parameter estimation," *Proceedings of the IEEE*, vol. 58, no. 5, pp. 644–652, May 1970.
- [60] S. Bellini and G. Tartara, "Bounds on error in signal parameter estimation," *IEEE Transactions on Communications*, vol. 22, no. 3, pp. 340–342, March 1974.
- [61] S.-K. Chow and P. Schultheiss, "Delay estimation using narrow-band processes," *IEEE Transactions on Acoustics, Speech and Signal Processing*, vol. 29, no. 3, pp. 478–484, June 1981.
- [62] A. Weiss and E. Weinstein, "Fundamental limitations in passive time delay estimation—part I: Narrow-band systems," *IEEE Transactions on Acoustics, Speech and Signal Processing*, vol. 31, no. 2, pp. 472–486, April 1983.
- [63] E. Weinstein and A. Weiss, "Fundamental limitations in passive time-delay estimation—part II: Wide-band systems," *IEEE Transactions on Acoustics, Speech and Signal Processing*, vol. 32, no. 5, pp. 1064–1078, October 1984.
- [64] A. Zeira and P. Schultheiss, "Realizable lower bounds for time delay estimation," *IEEE Transactions on Signal Processing*, vol. 41, no. 11, pp. 3102–3113, November 1993.
- [65] —, "Realizable lower bounds for time delay estimation. 2. threshold phenomena," *IEEE Transactions on Signal Processing*, vol. 42, no. 5, pp. 1001–1007, May 1994.
- [66] B. Sadler and R. Kozick, "A survey of time delay estimation performance bounds," in *Fourth IEEE Workshop on Sensor Array and Multichannel Processing*, July 2006, pp. 282–288.
- [67] B. Sadler, L. Huang, and Z. Xu, "Ziv-zakai time delay estimation bound for ultra-wideband signals," in *IEEE International Conference on Acoustics, Speech and Signal Processing (ICASSP 2007)*, vol. 3, April 2007, pp. III-549–III-552.
- [68] A. Renaux, "Contribution à l'analyse des performances d'estimation en traitement statistique du signal," Ph.D. dissertation, ENS CACHAN, 2006.

- [69] L. Seidman, "An upper bound on average estimation error in nonlinear systems," *IEEE Transactions on Information Theory*, vol. 14, no. 2, pp. 243–250, March 1968.
- [70] R. McAulay and D. Sakrison, "A PPM/PM hybrid modulation system," *IEEE Transactions on Communication Technology*, vol. 17, no. 4, pp. 458–469, August 1969.
- [71] H. L. Van Trees, *Detection, Estimation and Modulation Theory*. Wiley, 1968.
- [72] B. Bobrovsky and M. Zakai, "A lower bound on the estimation error for certain diffusion processes," *IEEE Transactions on Information Theory*, vol. 22, no. 1, pp. 45–52, January 1976.
- [73] B. Bobrovsky, E. Mayer-Wolf, and M. Zakai, "Some classes of global cramer rao bounds," *The Annals of Statistics*, vol. 15, no. 4, pp. 1421–1438, 1987.
- [74] A. Weiss and E. Weinstein, "A lower bound on the mean-square error in random parameter estimation (corresp.)," *IEEE Transactions on Information Theory*, vol. 31, no. 5, pp. 680–682, September 1985.
- [75] D. Chazan, M. Zakai, and J. Ziv, "Improved lower bounds on signal parameter estimation," *IEEE Transactions on Information Theory*, vol. 21, no. 1, pp. 90–93, January 1975.
- [76] E. Weinstein, "Relations between belini-tartara, chazan-zakai-ziv, and wax-ziv lower bounds," *IEEE Transactions on Information Theory*, vol. 34, no. 2, pp. 342–343, March 1988.
- [77] K. Bell, Y. Steinberg, Y. Ephraim, and H. Van Trees, "Extended ziv-zakai lower bound for vector parameter estimation," *IEEE Transactions on Information Theory*, vol. 43, no. 2, pp. 624–637, March 1997.
- [78] S. Kay, *Fundamentals of Statistical Signal Processing Estimation Theory*. Prentice-Hall, 1993.
- [79] E. W. Barankin, "Locally best unbiased estimators," *The Annals of Mathematical Statistics*, vol. 20, pp. 477–501, December 1949.
- [80] R. McAulay and L. Seidman, "A useful form of the barankin lower bound and its application to PPM threshold analysis," *IEEE Transactions on Information Theory*, vol. 15, no. 2, pp. 273–279, March 1969.
- [81] R. McAulay and E. Hofstetter, "Barankin bounds on parameter estimation," *IEEE Transactions on Information Theory*, vol. 17, no. 6, pp. 669–676, November 1971.

- [82] P. Swerling, "Parameter estimation for waveforms in additive gaussian noise," *Journal of the Society for Industrial and Applied Mathematics*, vol. 7, no. 2, pp. 152–166, June 1959.
- [83] L. Knockaert, "The barankin bound and threshold behavior in frequency estimation," *IEEE Transactions on Signal Processing*, vol. 45, no. 9, pp. 2398–2401, September 1997.
- [84] L. Seidman, "The performance of a PPM/PM hybrid modulation system," *IEEE Transactions on Communication Technology*, vol. 18, no. 5, pp. 697–698, October 1970.
- [85] D. Dardari, C.-C. Chong, and M. Win, "Improved lower bounds on time-of-arrival estimation error in realistic UWB channels," in *The 2006 IEEE 2006 International Conference on Ultra-Wideband (ICUWB 2006)*, September 2006, pp. 531–537.
- [86] B. Sadler, L. Huang, and Z. Xu, "Ziv-zakai time delay estimation bound for ultra-wideband signals," in *IEEE International Conference on Acoustics, Speech and Signal Processing (ICASSP 2007)*, vol. 3, April 2007, pp. III–549–III–552.
- [87] R. Kozick and B. Sadler, "Bounds and algorithms for time delay estimation on parallel, flat fading channels," in *IEEE International Conference on Acoustics, Speech and Signal Processing, (ICASSP 2008)*, April 2008, pp. 2413–2416.
- [88] D. Dardari and M. Win, "Ziv-zakai bound on time-of-arrival estimation with statistical channel knowledge at the receiver," in *IEEE International Conference on Ultra-Wideband (ICUWB 2009)*, September 2009, pp. 624–629.
- [89] J. M. Wozencraft and I. M. Jacobs, *Principles of Communication Engineering*. Wiley, 1965.
- [90] L. Seidman, "A class of signals for analog telemetry over a coherent channel," *IEEE Transactions on Aerospace and Electronic Systems*, vol. AES-5, no. 4, pp. 645–653, July 1969.
- [91] D. Rife and R. Boorstyn, "Single tone parameter estimation from discrete-time observations," *IEEE Transactions on Information Theory*, vol. 20, no. 5, pp. 591–598, September 1974.
- [92] F. Athley, "Threshold region performance of maximum likelihood direction of arrival estimators," *IEEE Transactions on Signal Processing*, vol. 53, no. 4, pp. 1359–1373, April 2005.
- [93] A. Mallat, J. Louveaux, and L. Vandendorpe, "UWB based positioning in multipath channels: CRBs for AOA and for hybrid TOA-AOA based

- methods,” in *IEEE International Conference on Communications (ICC 2007)*, June 2007, pp. 5775–5780.
- [94] H. I. Jacobson, “The maximum variance of restricted unimodal distributions,” *The Annals of Mathematical Statistics*, vol. 40, no. 5, pp. 1746–1752, October 1969.
- [95] S. W. Dharmadhikari and K. Joag-Dev, “Upper bounds for the variances of certain random variables,” *Communications in Statistics - Theory and Methods*, vol. 18, no. 9, pp. 3235–3247, 1989.
- [96] A. Mallat, P. Gerard, M. Drouguet, F. Keshmiri, C. Oestges, C. Craeye, D. Flandre, and L. Vandendorpe, “Testbed for IR-UWB based ranging and positioning: Experimental performance and comparison to CRLBs,” in *5th IEEE International Symposium on Wireless Pervasive Computing (ISWPC 2010)*, May 2010, pp. 163–168.
- [97] A. Genz, “Numerical computation of multivariate normal probabilities,” *Journal of Computational and Graphical Statistics*, vol. 1, no. 2, pp. 141–149, June 1992.
- [98] —, “On a number-theoretical integration method,” *Aequationes Mathematicae*, vol. 8, no. 3, pp. 304–311, October 1972.
- [99] —, “Randomization of number theoretic methods for multiple integration,” *SIAM Journal on Numerical Analysis*, vol. 13, no. 6, pp. 904–914, December 1976.
- [100] D. Nuyens and R. Cools, “Fast component-by-component construction, a reprise for different kernels,” *H. Niederreiter and D. Talay editors, Monte-Carlo and Quasi-Monte Carlo Methods*, pp. 371–385, 2004.
- [101] E. Cinlar, *Introduction to Stochastic Process*. Englewood Cliffs, NJ: Prentice Hall, 1975.
- [102] G. Marsaglia, “Ratios of normal variables and ratios of sums of uniform variables,” *Journal of the American Statistical Association*, vol. 60, no. 309, pp. 193–204, March 1965.
- [103] —, “Ratios of normal variables,” *Journal of Statistical Software*, vol. 16, no. 4, May 2006.
- [104] D. V. HINKLEY, “On the ratio of two correlated normal random variable,” *Biometrika*, vol. 56, no. 3, pp. 635–639, December 1969.
- [105] B. P. Lathi, *Modern Digital and Analog Communication Systems*, 3rd ed. Oxford University Press, 1998.
- [106] H. Gudbjartsson and S. Patz, “The rician distribution of noisy MRI data,” *Magn Reson Med.*, vol. 34, no. 6, pp. 910–914, 1995.

- [107] A. Mallat, J. Louveaux, and L. Vandendorpe, "UWB based positioning: Cramer rao bound for angle of arrival and comparison with time of arrival," in *2006 Symposium on Communications and Vehicular Technology*, November 2006, pp. 65–68.
- [108] A. Mallat and L. Vandendorpe, "CRBS for the joint estimation of TOA and AOA in wideband MISO and MIMO systems: Comparison with SISO and SIMO systems," in *IEEE International Conference on Communications (ICC 2009)*, June 2009, pp. 1–6.
- [109] —, "CRB for the joint estimation of TOA and AOA in MIMO systems," in *Satellite and Terrestrial Radio Positioning Techniques: A signal processing perspective*, D. Dardari, M. Luise, and E. Falletti, Eds. Elsevier, 2012.
- [110] A. Mallat, C. Oestges, and L. Vandendorpe, "CRBs for UWB multipath channel estimation: Impact of the overlapping between the MPCs on MPC gain and TOA estimation," in *IEEE International Conference on Communications (ICC 2009)*, June 2009, pp. 1–6.
- [111] —, "CRBs for for UWB multipath channel estimation: Impact of the overlapping pulses," in *Satellite and Terrestrial Radio Positioning Techniques: A signal processing perspective*, D. Dardari, M. Luise, and E. Falletti, Eds. Elsevier, 2012.
- [112] R. Cardinali, L. De Nardis, P. Lombardo, and M. Di Benedetto, "UWB ranging accuracy for applications within IEEE 802.15.3a," in *2nd International Workshop Networking with Ultra Wide Band and Workshop on Ultra Wide Band for Sensor Networks*, July 2005, pp. 65–69.
- [113] J. Montillet, G. T. F. De Abreu, H. Saarnisaari, and I. Oppermann, "Comparison of UWB and WCDMA positioning accuracies," in *IEEE 61st Vehicular Technology Conference (VTC 2005)*, vol. 4, May, pp. 2260–2263.
- [114] G. T. F. De Abreu, "Performance of parameter estimation from UWB-IR signals with an array of orthonormal correlators," in *IEEE International Conference on Ultra-Wideband (ICUWB 2005)*, September 2005, pp. 542–547.
- [115] J.-P. Delmas and H. Abeida, "Cramer-rao bounds of DOA estimates for BPSK and QPSK modulated signals," *IEEE Transactions on Signal Processing*, vol. 54, no. 1, pp. 117–126, January.
- [116] C. Botteron, A. Host-Madsen, and M. Fattouche, "Cramer-rao bound for location estimation of a mobile in asynchronous DS-CDMA systems," in *IEEE International Conference on Acoustics, Speech, and Signal Processing (ICASSP 2001)*, vol. 4, 2001, pp. 2221–2224.
- [117] G. Zhenghui and E. Gunawan, "Cramer-rao bound for joint direction of arrival, time delay estimation in DS-CDMA systems," in *21st Century*

- Military Communications Conference Proceedings (MILCOM 2000)*, vol. 1, 2000, pp. 614–618.
- [118] P. Stoica and A. Nehorai, “MUSIC, maximum likelihood, and cramer-rao bound: further results and comparisons,” *IEEE Transactions on Acoustics, Speech and Signal Processing*, vol. 38, no. 12, pp. 2140–2150, December 1990.
- [119] H. Messer, G. Singal, and L. Bialy, “On the achievable DF accuracy of two kinds of active interferometers,” *IEEE Transactions on Aerospace and Electronic Systems*, vol. 32, no. 3, pp. 1158–1164, July 1996.
- [120] R. Nielsen, “Performance of combinations of projectors and receivers,” *IEEE Journal of Oceanic Engineering*, vol. 27, no. 3, pp. 753–759, July 2002.
- [121] I. Bekkerman and J. Tabrikian, “Target detection and localization using MIMO radars and sonars,” *IEEE Transactions on Signal Processing*, vol. 54, no. 10, pp. 3873–3883, October 2006.
- [122] H. Godrich, A. Haimovich, and R. Blum, “Cramer rao bound on target localization estimation in MIMO radar systems,” in *42nd Annual Conference on Information Sciences and Systems (CISS 2008)*, March 2008, pp. 134–139.
- [123] H. Xu, S. Yi, H. Chunlin, M. Lu, and H. Wang, “Estimation of direction-of-arrival by an active array,” in *Congress on Image and Signal Processing (CISP 2008)*, vol. 5, May 2008, pp. 277–280.
- [124] X. H. Wu, A. A. KISHK, and A. W. Glisson, “Antenna effects on a MIMO radar for angle estimation: A cramer-rao lower bound analysis,” in *IEEE Antennas and Propagation Society International Symposium (AP-S 2008)*, July 2008, pp. 1–4.
- [125] S. Alamouti, “A simple transmit diversity technique for wireless communications,” *IEEE Journal on Selected Areas in Communications*, vol. 16, no. 8, pp. 1451–1458, October 1998.
- [126] S. Gezici, Z. Tian, G. Giannakis, H. Kobayashi, A. Molisch, H. Poor, and Z. Sahinoglu, “Localization via ultra-wideband radios: a look at positioning aspects for future sensor networks,” *IEEE Signal Processing Magazine*, vol. 22, no. 4, pp. 70–84, July 2005.
- [127] J. Zhang, R. A. Kennedy, and T. D. Abhayapala, “Cramer-rao lower bounds for the time delay estimation of UWB signals,” in *IEEE International Conference on Communications (ICC 2004)*, vol. 6, June 2004, pp. 3424–3428.

- [128] A. Mallat, P. Gerard, and L. Vandendorpe, "Multi-user time-hopping IR-UWB generator based on FPGA with high-speed serial module," in *2011 18th IEEE International Conference on Electronics, Circuits and Systems (ICECS 2011)*, December 2011, pp. 615–618.
- [129] H. Packard, *Pulse and waveform generation with step recovery diodes*, ser. Application note 918, October 1984.
- [130] R. Tielert, "Subnanosecond-pulse generator employing 2-stage pulse step sharpener," *Electronics Letters*, vol. 12, no. 3, pp. 84–85, February 1976.
- [131] J.-S. Lee, C. Nguyen, and T. Scullion, "New uniplanar subnanosecond monocycle pulse generator and transformer for time-domain microwave applications," *IEEE Transactions on Microwave Theory and Techniques*, vol. 49, no. 6, pp. 1126–1129, June 2001.
- [132] J. Han and C. Nguyen, "A new ultra-wideband, ultra-short monocycle pulse generator with reduced ringing," *IEEE Microwave and Wireless Components Letters*, vol. 12, no. 6, pp. 206–208, June 2002.
- [133] H. Kim, D. Park, and Y. Joo, "Design of CMOS scholtz's monocycle pulse generator," in *2003 IEEE Conference on Ultra Wideband Systems and Technologies*, November 2003, pp. 81–85.
- [134] K. Marsden, H.-J. Lee, D.-S. Ha, and H.-S. Lee, "Low power CMOS re-programmable pulse generator for UWB systems," in *2003 IEEE Conference on Ultra Wideband Systems and Technologies*, November 2003, pp. 443–447.
- [135] W. Tang, A. Andreou, and E. Culurciello, "A low-power silicon-on-sapphire tunable ultra-wideband transmitter," in *IEEE International Symposium on Circuits and Systems (ISCAS 2008)*, May 2008, pp. 1974–1977.
- [136] M. Jazairli, A. Mallat, L. Vandendorpe, and D. Flandre, "An ultra-low-power frequency-tunable UWB pulse generator using 65nm CMOS technology," in *IEEE International Conference on Ultra-Wideband (ICUWB 2010)*, vol. 1, September 2010, pp. 1–4.
- [137] F. Keshmiri, R. Chandra, and C. Craeye, "Design of a UWB antenna with stabilized radiation pattern," in *IEEE Antennas and Propagation Society International Symposium (AP-S 2008)*, July 2008, pp. 1–4.
- [138] [Online]. Available: [www.gore.com](http://www.gore.com)